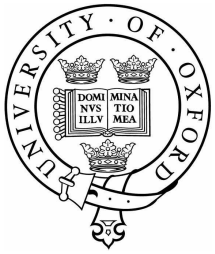
BCC metals in extreme environments: Modelling the structure and evolution of defects

Mark R. Gilbert
Linacre College

Hilary Term, 2009

Department of Materials, University of Oxford, Oxford, UK
EURATOM/CCFE Fusion Association, Culham Science Centre, Abingdon, UK





ABSTRACT

Designing materials for fusion applications is a very challenging problem, requiring detailed understanding of the behaviour of materials under the kinds of extreme conditions expected in a fusion environment. During the lifetime of fusion-reactor components, materials will be subjected to high levels of neutron irradiation, but must still perform effectively at high operating temperatures and under significant loading conditions.

Body-centred cubic (bcc) transition metals are some of the most promising candidates for structural materials in fusion because of their relatively high density, which allows for effective neutron-shielding with the minimum volume and mass of material. In this work we perform atomistic simulations on two of the most important of these, Fe and W.

In this thesis we describe atomic-scale simulations of defects found in bcc systems. In part I we consider the vacancy and interstitial loop defects that are produced and accumulated as a result of irradiation-induced displacement cascades. We show that vacancy dislocation loops have a critical size below which they are highly unstable relative to planar void defects, and thus offer an explanation as to why they are so rarely seen in TEM observations of irradiated bcc metals. Additionally, we compare the diffusion rates of these vacancy loops to their interstitial counterparts and find that, while interstitial loops are more mobile, the difference in mobility is not as significant as might have been expected.

In part II we study screw dislocations, which, as the rate limiting carriers of plastic deformation, are significantly responsible for the strength of materials. We present results from large-scale finite temperature molecular dynamics simulations of screw dislocations under stress and observe the thermally-activated kink-pair formation regime at low stress, which appears to be superseded by a frictional regime at higher stresses. The mobility functions fitted to the results are vital components in simulations of dislocation networks and other large-scale phenomena.

Lastly, we develop a multi-string Frenkel-Kontorova model that allows us to study the core structure of screw dislocations. Subtle changes in the form of the interaction laws used in this model demonstrate the difference between the non-degenerate and degenerate core structures. We provide simple criteria to guarantee the correct structure when developing interatomic potentials for bcc metals.

ACKNOWLEDGEMENTS

I would like to thank my supervisors Sergei, David, and Peter for all their help and support. Thanks to Dr Sergei Dudarev for guidance, tutelage, and enthusiasm, and also for being available for discussions on a daily basis! Thank you to Prof. David Pettifor for helpful discussions and suggestions, and for guiding me through the complexities of the Oxford University system. Many thanks to Dr Peter Derlet for providing the underlying molecular dynamics code used for much of the work in chapters 3, 4, and 6, and for answering numerous questions on the theoretical aspects of molecular simulation.

Thanks to Drs Zhongwen Yao and Mike Jenkins for the explanation and discussion of their experimental results, which motivated and complimented much of the work presented in chapters 3 and 4. Thanks also to Prof. Steve Roberts and the rest of the Oxford Materials fusion group for the discussions and stimulating environment at the Friday morning meetings.

I am also grateful to Dr Jaime Marian for hosting my visits to the Lawrence Livermore Laboratory and for inviting me back each summer. Thanks for the suggestions, help, and collaboration that lead to the research presented in chapter 5. I also acknowledge Drs Alfredo Caro and Vasily Bulatov for their helpful discussions whilst in Livermore. We thank Diana Farcas for kindly providing the simulation time on the System X supercomputer at Virginia Tech University.

The work presented in this thesis has been jointly funded by the United Kingdom Engineering and Physical Sciences Research Council and by the European Communities under the contract of Association between EURATOM and CCFE (formerly UKAEA). Thanks to all of these. In particular I am grateful to CCFE for allowing me to undertake this thesis, and thanks to all my friends and colleagues at Culham for making it such a pleasant place to work.

Finally, I would like to thank my parents, family, friends and, most of all, my wife Sarah, for their support and understanding, without which the work presented in this thesis would not have been possible.

CONTENTS

1. Introduction: Fusion materials 1
1.1 Materials for a fusion environment 4
1.1.1 Materials options 7
1.2 Materials research 8
1.2.1 Neutronics 9
1.2.2 Activation calculations 11
1.2.3 The role of materials modelling 16
1.3 Summary of thesis 17

2. Computational methods 20
2.1 Molecular dynamics (and statics) 20
2.1.1 The early history of MD 21
2.1.2 Time-integration algorithms 23
2.1.3 Neighbour lists 29
2.1.4 Derivation of the Parrinello-Rahman equations of motion 33
2.2 Conjugate gradient energy-minimisation 40
2.3 The nudged elastic band method 43
2.4 Interatomic potentials 45

Part I Irradiation induced defects 55

3. The structure and stability of vacancy defects in Fe and W 56
3.1 Introduction 56
3.2 Vacancy defects in bcc Fe 64
3.2.1 $\frac{1}{2}\langle 111\rangle$ Vacancy loops at 0K 65
3.2.2 Transformation at finite temperature 72
3.2.3 Origin of the energy differences 78
3.2.4 $\langle 001\rangle$ Vacancy loops 85
3.2.5 Rectangular vacancy-dislocation loops 90
3.3 Vacancy defects in bcc W at 0K 93
3.4 Comparison with experiment 97
3.5 Concluding remarks 103

4. Thermally activated mobility of vacancy and interstitial loops in Fe and W . . . 105
4.1 Introduction . . . 105
4.2 Structural comparison of loops . . . 109
4.3 Finite-temperature MD simulations . . . 115
4.3.1 Simulation results . . . 119
4.4 Calculation of the diffusion coefficient . . . 123
4.4.1 Diffusion results . . . 127
4.5 Comparison with recent experiments . . . 139
4.5.1 Migration of vacancy loops to surfaces . . . 141
4.6 Coherent motion of interstitial loops . . . 143
4.7 Concluding remarks and further work . . . 151

Part II Screw dislocations: the carriers of plastic deformation 154

5. Molecular dynamics simulations of screw-dislocation motion in Fe . 155
5.1 Introduction . . . 155
5.2 Simulation set-up and computational requirements . . . 161
5.3 Results . . . 172
5.4 Mobility laws . . . 183
5.5 Summary and future work . . . 191

6. Multi-string Frenkel-Kontorova model for $\frac{1}{2}\langle 111\rangle$ screw dislocations 194
6.1 Introduction . . . 195
6.2 The multi-string Frenkel-Kontorova model . . . 199
6.2.1 The inter-string interaction law . . . 202
6.2.2 Interaction laws derived from interatomic potentials . . 210
6.3 The core structure of a screw dislocation . . . 215
6.3.1 Shape of the U_1 curves . . . 222
6.3.2 Analytical representations for U_1 . . . 229
6.4 The Peierls barrier . . . 233
6.5 Conclusions and further work . . . 238

7. Conclusions . . . 241

Appendix 247

A. The bcc metal structure . . . 248
A.1 A Coordinate system with $z = [111]$ . . . 250

B. Handbook of activation data 253

C. Additional derivations 264
C.1 The derivative of $\dot{\mathbf{s}}_i^T \mathbf{G} \dot{\mathbf{s}}_i$ 264
C.2 The derivative $\partial r_{ij}/\partial \mathbf{s}_l$ 265
C.3 The Parrinello-Rahman equation of motion for $\ddot{\mathbf{h}}$ 267

D. Correspondence between nearest neighbour strings and atoms . . . 272

E. Correction to the diffusion coefficient D 275

List of Figures 278

List of Tables 287

Bibliography 288

1. INTRODUCTION: FUSION MATERIALS

One of the greatest challenges for the scientific community during the current century is, and will continue to be, to find a solution to the problem of how to meet our ever-growing energy demands in a safe, sustainable, economical, and, as much as possible, environmentally-friendly way [**1**, **2**]. There are many alternative energy sources (*i.e.,* different to the dominant sources of the past and present) currently being researched and developed in the world today to try and meet these requirements, and the future energy landscape will probably be made up of a diverse mixture of energy solutions. Under such circumstances we will avoid the current political and economic (and environmental) problems associated with the over-reliance on a single energy source, namely fossil fuels.

Nuclear fusion is one such alternative energy source. The principle is to generate power by harnessing the energy released when two light atomic nuclei 'fuse' to form a heavier one. It is this very process which takes place in the Sun, and therefore already accounts for most of our current energy resources, including fossil fuels (*i.e.,* derived from dead organic matter whose creation relies primarily on photosynthesis). Thus, the ability to control and concentrate such nuclear fusion power is a very desirable problem to solve.

Historically, research into nuclear fusion has focussed on developing the theory and technology required to initiate and confine the fusion reaction itself. Even in the next phase of development for so-called *confinement*

fusion, where a large new experimental reactor called ITER [**3**] is to be built, the primary focus is on demonstrating the steady-state confinement of an energy-producing plasma (the ionized gas of reactants) for significant lengths of time (between 300 and 500s) [**4**]. This was the natural choice because it was, and still is, vital for the issues surrounding the reaction to be solved comprehensively during the experimental phase of fusion research - failure in this respect would remove fusion as a potential energy generator. However, if, as expected, current experimental devices, such as the Joint European Torus (JET), and future ones like ITER are able to address the outstanding issues related to the control of the fusion reaction, then it is time to consider the requirements for turning fusion into a commercially viable power source.

More recently, there has been a developing interest in an alternative to confinement fusion, where a hot plasma of reactants is confined using magnetic fields. In *inertial* fusion, a solid pellet of fuel will be compressed and heated, most likely using lasers, sufficiently to induce a fusion reaction. To produce a sustained power output several fuel pellets must be 'burnt' every second, and so, although inertial fusion does not have to contend with the same engineering difficulties associated with plasma confinement, there are still significant challenges associated with the accurate injection and compression of fuel into the system. Research into confinement fusion is at a much more advanced stage than inertial, but both may eventually lead to commercial power generation.

Just as in nuclear fission, which is the opposite process involving the splitting of heavy nuclei into lighter ones to release energy, a significant proportion of the energy released in a fusion (or fission) event is contained in the form of the kinetic energy of the neutron produced during the

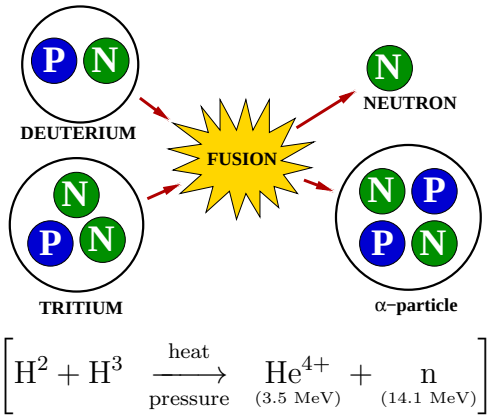


Fig. 1.1: Schematics of the Deuterium-Tritium fusion reaction. The resulting neutron carries 14.1 MeV of the excess energy.

reaction. For a fusion reactor one of the most favourable reactions under consideration is the Deuterium-Tritium (DT) reaction. The two input ions combine to produce an α-particle (*i.e.*, a He^4 nucleus) and a neutron carrying 14.1 MeV of energy (the α-particle has just 3.5 MeV of energy by comparison [**5**]), see Figure 1.1. Having a lot of the energy in the form of a fast-moving neutron is both fortuitous and problematic. In confinement fusion it is beneficial because a neutron, having neutral charge, is not obstructed by the powerful magnetic fields required to contain the ionized gas (plasma) of fusion nuclei. Therefore a neutron escapes the immediate vicinity of the fusion reaction and its energy can be absorbed and harnessed as it slows down and interacts with the vacuum vessel surrounding the plasma. However, these very interactions, which cannot be avoided, cause damage to the materials where they take place. Designing materials to withstand this neutron irradiation, as well as the other extremes associated with the fusion environment, presents a serious scientific problem.

1.1 Materials for a fusion environment

Any structural materials designed for fusion environments must operate reliably and safely (*i.e.,* without failure) at a range of elevated temperatures (for example the blanket shield of ITER is expected to operate at temperatures in excess of 300°C [**3**, section 2.3]) for extended periods, while at the same time being subject to the high-energy neutron fluxes described above. They must also withstand high loading stresses, as well as experiencing localised high surface energy fluxes, and being exposed to high-temperature, high-pressure coolants and tritium breeding materials [**1**, **6**]. Therefore, one of the most crucial barriers for fusion is the development and demonstration of materials that will tolerate these extreme environments for the sufficiently long timescales required to give a commercial reactor high availability (*i.e.,* time when it produces power) [**7**]. If a reactor is off-line for too high a percentage of possible operation time, due to the replacement of components, then the electricity generation costs become less competitive when compared to other power sources.

The reliability and lifetime concerns are of chief importance for the areas of a fusion power plant that are in closest proximity to the fusion reaction (*i.e.,* the plasma) itself. These are the components inside the toroidal vacuum vessel of the 'Tokamak' common to current confinement fusion plant designs (see for example [**8**]). As indicated in the plans for the 'next-step' device, ITER, shown in Figure 1.2, these plasma-exposed in-vessel components are the shielding blanket containing the first wall, and also the divertor, where there is a particularly high flux of exhaust particles [**3**, **4**, **7**]. Cost calculations have suggested that it is desirable for the divertor, which will suffer from the greatest heat load due to the impact of exhaust particles (α-particles, *etc.*) as they escape the plasma, to last for

around two full power years before replacement in a commercial reactor [**7**, **8**], while blanket modules with operational lifetimes of around five years are expected [**8**, **9**]. However, other components, in particular the vacuum vessel walls (see Figure 1.2), should ideally last for as long as a reactor is in service, which may be 25 years, since replacing them would be prohibitively expensive and would require a long shutdown of the power plant.

The problem of materials design is complicated further by the need, at the end of a component's lifetime, to be able to remove and dispose of the constituent materials safely and in an environmentally acceptable way. The neutron bombardment (irradiation) that in-vessel components are subjected to may not only cause changes in structural properties but can also cause the material to become radioactive, as the atoms of the original material are transformed via various neutron capture reactions into other, possibly radioactive, element isotopes. While this activated material may not be structurally compromised, and so may not impact on energy production, it would still be of concern to power generation companies who would have to meet the cost of disposal of any radioactive waste.

Finally, the vessel components, as well as being structural, must also function efficiently as a neutron shield. It is vital that the neutron energy flux beyond a reactor's vessel walls is minimised to almost zero. This protects not only power plant components exterior to the vacuum vessel from neutron irradiation, but also the human workers in the vicinity of the reactor. For plasma-facing materials the design criteria are also influenced by the need to reduce erosion rates under irradiation and keep the resulting plasma contamination effects to a minimum.

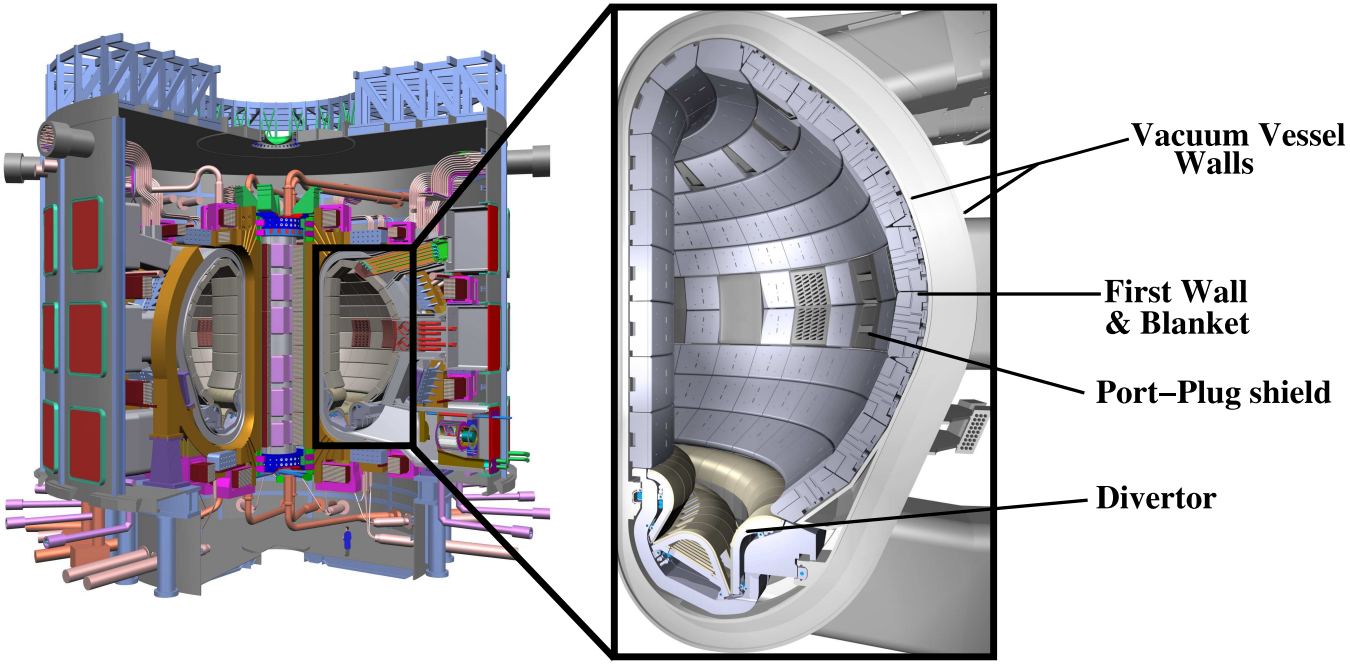


Fig. 1.2: Diagrams of the planned ITER experiment [**3**, **4**]. The device dwarfs all previous fusion experiments (see the human scale indicator in the bottom right-hand corner of the main diagram). The plasma is contained within the toroidal vacuum vessel (see expanded view) using magnetic confinement. The first wall and blanket must function as both a neutron shield and heat sink to absorb the generated power, and, in a commercial reactor, would also need to breed Tritium fuel. © ITER organization.

1.1.1 Materials options

The constraints placed on materials due to the fusion environment, as discussed above, are severely limiting when it comes to deciding what materials to use. Body-centred-cubic (bcc) (see Appendix A) transition metals (the refractory metals of groups VB and VIB, together with Fe) are good candidates for structural fusion applications because they have good neutron shielding and collimation properties [**10**]. It is largely expected that, in common with similar applications, industrially available steels will be acceptable for the vacuum vessel walls in experimental reactors like ITER [**4**], demonstration plants ('DEMO'), and actual power plants. Only minor composition changes will be required to meet radioactivity restrictions, such as a reduction in Co [**3**, section 2.13]. Indeed, there has been significant progress in recent years in designing and improving the strength and radiation-resistance of ferritic-martensitic steels [**1**]. However, for the in-vessel components there is still significant research and debate about what materials should be used, with some high-density, but expensive, options such as SiC ceramic composites [**6**] being proposed along with the bcc transition metals and their alloys.

In current designs and concepts, the plasma-facing armour material of the first wall - representing 80% of the total exposed surface in ITER [**3**] - could be constructed from Be, as proposed in the original plans for ITER, because of its low effect on plasma performance when present as a contaminant [**3**]. Alternatively, a W alloy with improved erosion resistance compared to Be or pure W may be used, or perhaps even some, as yet unknown, steel [**8**]. For the divertor of a fusion reactor W is one of the main candidates, perhaps as the major constituent of an alloy, with some small sections of carbon-fibre-composites in areas where there is high

heat-flux [**3**, **8**]. For the majority of the remaining in-vessel components (excluding the heat sinks and coolants) the shielding and structural requirements predominate. For these reasons steels, with bcc Fe as the major constituent, are currently the materials of choice in the design of experimental facilities, including ITER. However, the exact choice in the design of a commercial power plant is still unclear, with the list of possibilities also including alloys of the other bcc metals, such as V [**1**], as well as advanced materials like SiC [**8**].

1.2 Materials research

The current research effort in fusion materials programs around the world is mainly focused on the development and understanding of structural materials because it is their reliability and lifetime that, above all others, have the greatest impact on the commercial feasibility of fusion power [**1**]. The computational research presented in this thesis is also directed toward these structural materials, and more specifically at the bcc transition metals, such as Fe and W, which are the main candidate materials (both as pure metals and as part of alloys) for the majority of components in both ITER and future devices [**3**, **8**, **9**]. However, the present work, which is motivated by a need to understand the changes in material behaviour under the neutron-irradiated, high-temperature, high-stress conditions of a fusion environment, has taken place within the framework of the Culham Centre for Fusion Energy's (CCFE's - formerly the UKAEA) research efforts into all issues related to materials for fusion applications. To appreciate this wider outlook, it is worth discussing two other areas of CCFE's materials research, particularly as they address issues of neutron shielding and material activation, neither of which are immediately approachable using

the kind of theory and simulation described in this thesis.

1.2.1 Neutronics

Neutronics is primarily concerned with tracking the path of neutrons, such as those produced by a fusion reaction, from their point of origin as they move through, and interact with, the surrounding materials. In particular, neutronics calculations can be used to assess the quality of attenuation in a particular structure, not only in terms of how well neutrons are absorbed by the constituent materials, but also how neutrons are focussed and diverted by a particular structural geometry (*i.e.,* collimation, *etc.*). The most commonly used and widely validated neutronics code is that developed at the Los Alamos National Laboratory, known as the Monte-Carlo N-Particle or MCNP transport code [**11**–**13**]. As input it takes cross-sectional data for the interaction of neutrons with every possible atomic species. A neutron source is then defined together with a geometry and materials specification, which, for example, might be the design of a new experimental reactor such as ITER, or perhaps a model of a current reactor with a proposed new component added. The transport code then generates and propagates neutrons (one at a time) from the source, which may produce neutrons with random spacial, directional, and energy coordinates. Statistical probabilities or weights (hence Monte-Carlo) are then used to determine what happens as a particular neutron travels through the geometry. For example, it could be 'destroyed' in an neutron-capture reaction, or it may bounce around and gradually lose its initial energy. The events which take place are entirely determined by the structure and material composition of the given geometry. By tracking the path and evolution of many randomly generated neutrons (perhaps tens of millions of neutrons) the code is able

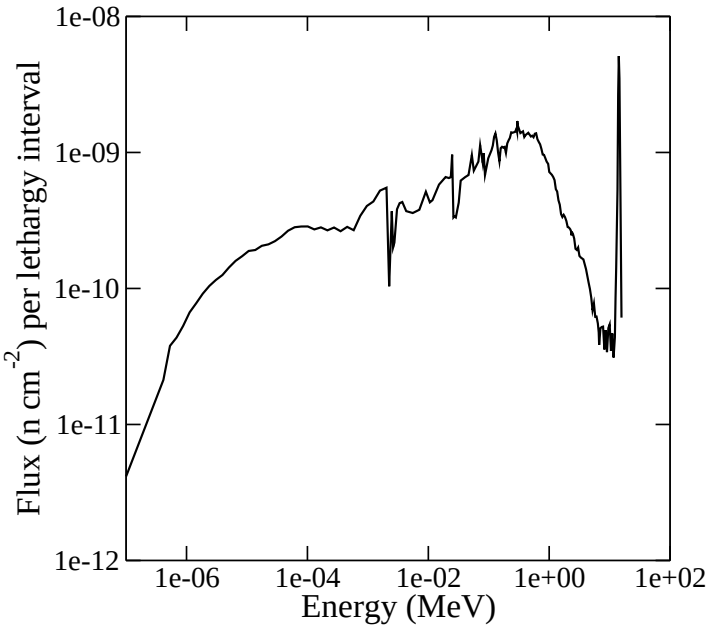


Fig. 1.3: The neutron spectrum of energies incident on the primary mirror of an equatorial diagnostic port being designed as part of the ITER experiment. Calculations performed using MCNP version 4C3 [**11**].

to build up a statistical picture of neutron flux at various points and surfaces in the system. In this way it is possible to assess the quality of shielding (attenuation) produced by a given geometry and material set-up, which may indicate that more shielding is required, or it may provide information as to whether a particular region near to a neutron-producing device is a safe working environment for humans.

Figure 1.3 shows a typical MCNP-calculated neutron spectrum. In this case it is the spectrum of neutrons hitting a mirror inside one of the equatorial port-plugs of the ITER geometry. The mirror is directly exposed to the plasma via an opening in the port-plug shield (see Figure 1.2). Thus, in this graph of neutron flux per lethargy interval against energy, there is a pronounced peak at 14.1 MeV associated with fusion neutrons hitting the mirror directly from the plasma. Additionally, there is also a broad

spectrum of lower energy neutrons that have been attenuated by the nearby vessel components. Note that a lethargy interval at a given energy is the natural logarithm of that energy (upper bound) divided by the energy data point below it (lower bound).

Unfortunately, even when many millions of neutrons are tracked, this may still only represent the neutrons produced in a fraction of a second in a fusion plasma, and so codes like MCNP are unable to investigate the material changes caused by the neutron fluence. Consequently, the neutron fluxes and energy spectrum determined from these calculations are often passed forward into other analysis tools. In particular, the fluxes and spectrums can be used in materials activation calculations (see below) to determine how a particular material composition would respond, *i.e.,* by becoming radioactive, due to the flux. Neutronics results can also be compared to experimental neutron irradiations to get an idea of the level of damage in the scale-up of flux from the experiment to the reactor environment.

1.2.2 Activation calculations

CCFE has long-established expertise in the area of activation calculations as a result of the inventory code FISPACT, which has been developed and maintained over the past 20 years by R. Forrest. FISPACT [**14**, **15**] was created to perform calculations of the activation induced by neutrons (and more recently deuterons and protons [**14**]) for materials in fusion devices. It calculates the number of atoms and the activity in a material after a particular neutron irradiation. Together with external libraries of reaction cross-sections and decay data of all relevant nuclides, FISPACT forms the European Activation System (EASY) [**16**]. The libraries are used by

FISPACT to find the inventory of nuclides (atoms) produced during the irradiation of a starting material composition with a specified flux and spectrum of neutrons [**15**]. As well as giving the numbers of each nuclide species, it also gives details of production pathways, (*i.e.,* what reactions, such as neutron capture or radioactive decays, took place in order to produce a given nuclide), and activity levels for the final material, including the relative contribution from the different radioactive elements contained in the final composition. This information enables a determination of many useful quantities, including the radioactive lifetime of a material after irradiation, the cooling time required before a material can be handled, and the radiation dose that would be received during accidental or intended exposure to a material both during and after irradiation.

The inventory calculations in FISPACT are performed by solving a set of coupled differential equations, with the equation for each possible nuclide i defined as

$$\frac{\mathrm{d}N_i}{\mathrm{d}t} = -N_i(\lambda_i + \sigma_i\phi) + \sum_{j\neq i} N_j(\lambda_{ij} + \sigma_{ij}\phi) + S_i, \tag{1.1}$$

where N_i is the amount of nuclide i at time t, λ_i (s^{-1}) is the decay constant of i, λ_{ij} is the decay constant producing i from j, σ_i is the total cross-section for reactions (with neutrons) on i (cm^2), σ_{ij} is the total reaction cross-section for reactions on j producing i, S_i is the additional atoms of nuclide i produced by fission (where fission reactants are present in the material), and ϕ is the neutron flux (neutrons $\mathrm{cm}^{-2}\mathrm{s}^{-1}$) [**15**].

While FISPACT, as part of EASY, can be used to directly assess the activation properties of a given material composition, such as a newly-devised steel, it is also able to produce extensive data on the response

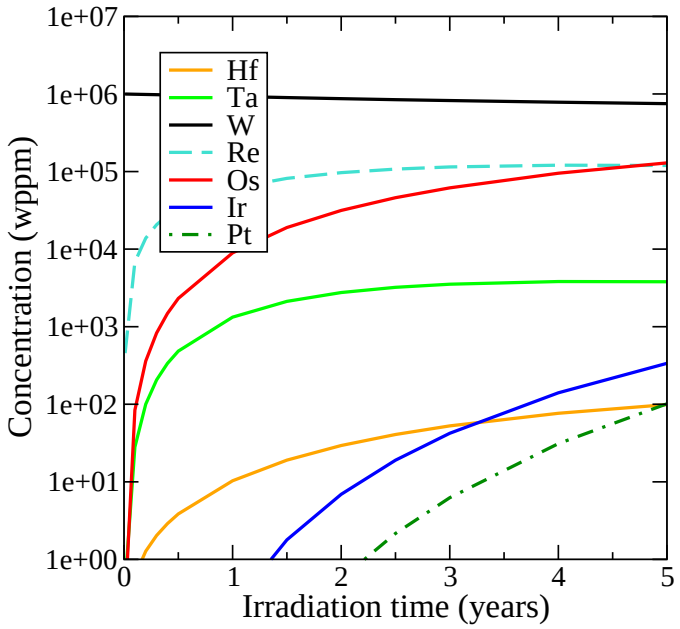


Fig. 1.4: The transmutation (burn-up) of pure W as a result of exposure to the 1×10^{15} neutrons $\mathrm{cm}^{-2}\mathrm{s}^{-1}$ neutron flux expected in the first wall of a fusion power plant for five years. The concentration of each element in the system, as it is burnt-up or created, is given in weight parts per million (wppm). Data taken from the *Handbook of Activation Data Calculated Using EASY-2003* [**17**, pg 431] © United Kingdom Atomic Energy Authority.

of pure elements. For example, irradiating a pure sample of naturally occurring W, *i.e.,* with the correct abundances of its 180, 182, 183, 184 (most abundant), and 186 isotopes (see [**17**, page 424]), with a typical neutron flux for the first wall of a conceptual fusion reactor (where W may be used) leads to the transmutation or burn-up of the element. Figure 1.4 shows how W is transformed into other elements by neutron irradiation during the expected five-year lifetime [**8**] of first wall components [**17**].

In Figure 1.4, where concentrations of each element are presented in weight parts per million (wppm), we can see that there are significant quantities (around 10% of total weight of material after 5 years) of both Re (Rhenium) and Os (Osmium) produced during the irradiation. Such a

transformation may affect the properties of any material containing W, particularly if it results in the formation of brittle, σ-phase precipitates [**18**]. Note that error bars are not given in this and subsequent transmutation graphs (see Appendix B for explanation).

More significantly for fusion research, transmutation calculations like these are able to predict the production of both He and H. The build-up of He in particular, because of its unreactive nature, is likely to be a severe life-limiting factor for components in a fusion reactor, where it may lead to swelling and fracture. To appreciate the production of these elements, whose atomic masses are tiny compared to those of W and the other transmutation products, we need to recalculate the concentrations and produce them in atomic parts per million (appm). The graph shown in Figure 1.5 shows the same transmutation results as in Figure 1.4, but this time the concentrations are given in appm. As a result, both He and H now appear significantly in the graph (in wppm their concentrations barely reached 1 after five years of irradiation). The amount of He produced after five years is around 30 appm, while about 80 appm H is produced.

Transmutation calculations like these and detailed material-activation analyses have been performed for all of the naturally occurring elements in the periodic table, and the results are collated into a 'Handbook of activation data' [**17**]. This extensive source of data is a useful reference tool to determine if a particular element under consideration for a fusion component, perhaps as an alloying element, has an acceptable activation response. In Appendix B, more details of the data contained in this handbook are given, and we also present the results for pure Fe (including a more detailed transmutation graph in appm), which is the most relevant metal for the present research.

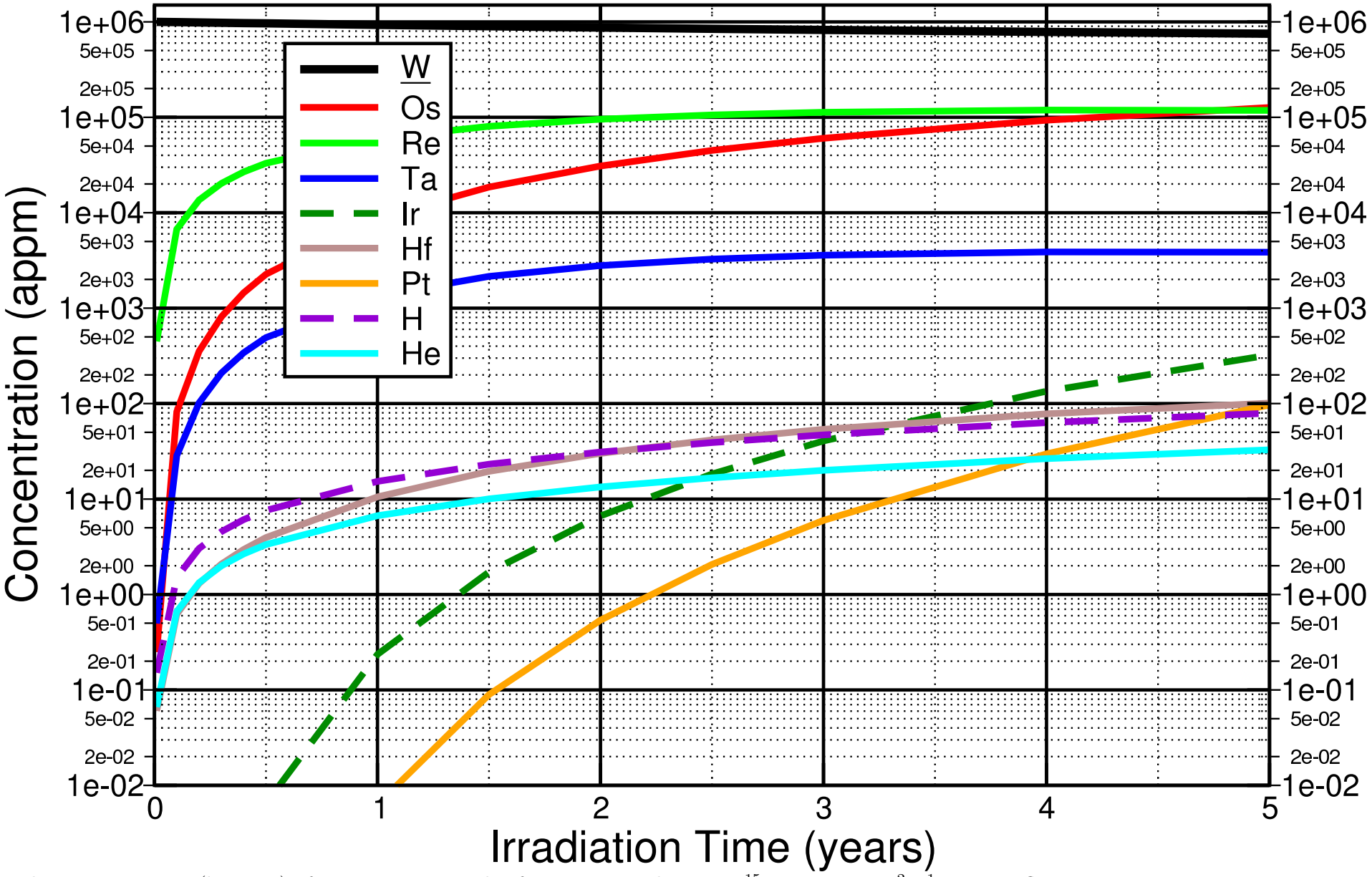


Fig. 1.5: The transmutation (burn-up) of pure W as a result of exposure to the 1×10^{15} neutrons $cm^{-2}s^{-1}$ neutron flux expected in the first wall of a fusion power plant for five years. In this graph concentrations are given in atomic parts per million (appm). Calculated Using EASY-2003 [**19**]. For more details see [**20**] © 2010 United Kingdom Atomic Energy Authority.

Note that all of the results obtained from either neutronics or activation calculations are only as accurate as the cross-section data. There is significant effort in Europe and elsewhere to improve such data, either by direct experiments or by improved theoretical modelling.

1.2.3 The role of materials modelling

While the two techniques discussed above are vital tools in the design process and materials selection for fusion reactor components, they do not remove the uncertainty surrounding how the properties and behaviour of materials, particularly those in structural components, will change as a result of the neutron damage accumulated during plasma burning. Nor do they give any clue as to how materials may perform under high operating temperatures or extreme loading conditions, such as those caused by the magnetic fields surrounding the plasma. Current conceptual fusion power plant designs often rely on assumptions of performance based on existing materials [**21**], which may only have been tested in existing fusion experiments, where neutron flux is low and the magnetic fields are relatively weak, or in fission reactors, where the neutron energy is low. Theoretical and computer modelling of materials at the atomic scale can help to address this uncertainty and may also guide experimentalists toward 'advanced' materials with more desirable properties, which are needed in order to make commercial fusion power a reality.

Although computer simulation and theoretical models like those presented in this thesis are not currently able to reproduce the full complexity of a real material system, such as steel, they still have a vital role to play in describing the fundamental processes taking place due to extreme environmental conditions. In particular, as we shall see in this

work, simulations are already able to explain some of the observations seen in irradiation experiments on the bcc transition metals. As our understanding improves, and as the power of computational techniques increases, we will be able to model ever-more realistic systems. However, this future work can only be successful if it is able to build on a detailed understanding of behaviour at the more basic level.

The present research, as described in this thesis, is motivated by a desire to explain changes in pure bcc metals as if they were being used directly in a fusion-like environment. It forms part of a larger body of research both at CCFE and around the world directly aimed at developing the necessary understanding of material processes, in expectation of modelling more complex systems in the future.

Below we give a brief summary of the structure of this thesis.

1.3 Summary of thesis

The work presented in this thesis is split into two main parts, comprising chapters 3 and 4, and chapters 5 and 6, respectively. Before these, in chapter 2, we begin by discussing the computational techniques used throughout the project, including some historical background. In particular, we discuss the development and current status of the numerical descriptions of atomic interactions, which are needed for all of the simulations discussed in the thesis.

In the first part we will consider the structure and behaviour of the atomic defects produced in materials as a result of the impact of neutrons during irradiation. When the displacement cascades caused by this bombardment collapse they can lead to the production of dislocation defects. Here we focus primarily on vacancy defects (*i.e.,* a defect caused by

the absence of one of more atoms from the normal bcc lattice structure), since these are, as we shall see in chapter 4, less mobile (but not immobile) than interstitial defects (the presence of extra atoms), and so have greater residence times in any material in which they occur. This, in turn, implies that they will have more of an effect on the mechanical properties of the material. In chapter 3 we characterise the size dependent structure of vacancy defects and relate these observations to experimental studies of bcc metals under irradiation. Then, in chapter 4, we compare the structure and mobility (diffusion) of these vacancy dislocation loops with equivalent interstitial loops.

In the second part we investigate the mobility and structure of screw dislocations. It is well known that these defects, which are often present in materials, are the rate-limiting carriers of plastic deformation (see, for example, Hull and Bacon [**22**, chapter 3]). Consequently, their behaviour and mobility will be the significant factors determining the strength and structural integrity of materials as they are subjected to the high-stress, high-temperature conditions in a fusion device. In chapter 5 we perform simulations to measure the temperature-dependent motion of screw dislocation in Fe as a result of high applied stresses, and calculate the mobility laws that are a vital component in computational studies of these defects. Meanwhile, in chapter 6, we develop a Frenkel-Kontorova [**23**] model to describe the core structure of the screw dislocations. We use this research to answer one of the fundamental questions in molecular dynamics simulation of screw dislocations: how do you design an interatomic potential so that it reproduces the correct core structure? We also consider whether a potential producing the correct core will necessarily reproduce the Peierls energy barrier for translation of a dislocation through the

lattice. In the final chapter we present a brief summary of the main conclusions from the thesis.

2. COMPUTATIONAL METHODS

The simulations performed during the course of the research, the results of which are presented in subsequent chapters, have employed a number of different computational techniques. Below we present a description of the fundamentals of these methods, together with some historical background.

2.1 Molecular dynamics (and statics)

Molecular dynamics, or MD, is the name given to the technique by which the dynamic properties of many-particle systems may be obtained [**24**]. The basic principle of the method is to evolve a system of interacting particles by integrating their equations of motion [**25**]. In normal circumstances, *i.e.,* in the absence of external forces, *etc.*, the particles or atoms are free to move around under conditions of constant energy or temperature. In the related technique of Molecular Statics (MS), by comparison, the motion of particles is more controlled. The aim in this latter case is to evolve the system towards a potential energy minimum. This can be achieved in several ways, but the general idea is to stop the system from moving to areas of higher potential energy (*i.e.,* the wrong way), thus forcing it to fall down to a minimum.

Note that here we use Molecular Statics to refer to the relaxation method implemented in the main atomistic program **moldyPSI** [**26**] (see later) used in the present research, whereas by some definitions it could be

thought of as a dynamic *quenching* process because the particles move dynamically between periodic adjustments to the kinetic energy of the system (see section 2.1.2). In many cases, true 'static' methods, such as conjugate-gradient relaxation (see section 2.2), are computationally less expensive than the MS discussed here, although we have found that MS can still be useful when the minimum energy configuration is very different from the initial system.

2.1.1 The early history of MD

Whilst the need to find the solution to a many-body problem has been appreciated for several centuries, for example by Laplace in the early 19th century [**27**], it was not until the advent of digital computers that any progress in this matter was made [**28**].

The first steps were taken at the beginning of the 1950s when Metropolis *et al.* [**29**] devised their 'Metropolis Monte-Carlo' technique, which is still the basis of many modern Monte-Carlo (MC) simulations [**24**], particularly those used to calculate time-independent properties of systems in thermal equilibrium. A few years later, in the late 1950s, the first MD simulations were performed by Alder and Wainwright for a system of hard spheres [**30**–**32**]. They simulated a few dozen, and then later a few hundred, particles in a rectangular box [**30**]. The concept of periodic boundary conditions, which had been devised as part of the development of MC (see [**29**, **33**]), was included to create an effectively infinite sample. The particles moved with constant velocity between perfectly elastic collisions [**24**]. The calculations, as described in [**30**], demonstrated the transition between the solid and liquid phases in the hard sphere system, as well as allowing for the calculation of both equilibrium and non-equilibrium

properties [**31**].

In the years that followed, the techniques of MD improved, in particular through the development of better descriptions for the interactions between the particles. In the calculations of Alder and Wainwright [**25**] the particles travelled as free particles between collisions, whereas in a realistic system particles should influence each other as a function of their distance apart. Interatomic potentials, which are expressions for the potential energy of interaction of two particles as a function of their separation, had already been used in MC calculations, for example by Wood and Parker in 1957 [**34**], where they performed calculations on three-dimensional Lennard-Jones molecules.

However, it was not until Gibson *et al.* in 1960 [**35**], following on from earlier theoretical work by Vineyard [**36**, **37**], that an article was published describing the first MD calculations performed with a continuous interatomic potential. The simulations, which investigated the creation of defects as a result of radiation damage in a face-centred cubic (fcc) metal, used a simple repulsive pairwise potential (*i.e.,* the potential describes the force between pairs of atoms) with the necessary cohesion in the system provided by a constant inward force applied to the boundary atoms.

In 1964, Rahman [**38**] improved matters further by studying liquid Argon using the Lennard-Jones pairwise potential, which incorporates a repulsive core and an attractive tail [**35**], on a system containing 864 atoms. The functional form of the Lennard-Jones potential is given by:

$$V(r) = 4\epsilon \left[\left(\frac{\sigma}{r}\right)^{12} - \left(\frac{\sigma}{r}\right)^{6} \right], \tag{2.1}$$

where ϵ and σ are parameters that vary according to the material under investigation, and r is the distance between the pairs of particles. Rahman

calculated diffusion constants at different temperatures, which agreed well with the experimental measurements in [**39**]. In addition, pair-correlation curves and their Fourier transforms were produced from the simulation output, and these had the same profiles (for example, in terms of peak positions) as curves produced by X-ray scattering experiments, such as those of Eisenstein and Gingrich [**40**]. The algorithms and methods employed by Rahman in his computer experiments form the fundamentals upon which many of the current MD programs are based [**25**].

Since this famous 1964 paper by Rahman the properties of the Lennard-Jones potential have been thoroughly investigated, for example by Verlet in his 1967 and 1968 Physical Review papers [**41**, **42**]. Verlet was also concerned with Ar, in particular its phase diagram, and this was later extended by Hansen and Verlet in 1969 [**43**], who studied the phase transition of the same system. More recent developments in the area of interatomic potentials, particularly for bcc metals, will be discussed in section 2.4.

2.1.2 Time-integration algorithms

A time-integration algorithm, which is the engine of any MD program [**25**], is the method used to advance (in time) the solution of the ordinary differential equations that describe a system of interacting particles.

In what we call Molecular Statics (MS) the evolution of the system during each time-step (or, more appropriately, iteration since the system does not evolve freely in time) occurs in the same way as for MD. The only difference comes between steps, where, for MS, some or all of the atomic velocities are 'zeroed' depending on whether the particles are decelerating.

Deceleration means that kinetic energy is falling, and hence implies that

potential energy must be increasing, which is undesirable if a potential energy minimum is sought, and so by removing the kinetic energy (*i.e.,* by setting velocities to zero) the overall system energy falls. Then in the next iteration of MS the atoms interact and move off again, which only happens by converting some of the remaining potential energy into kinetic. In this way the system gets closer to the required minimum. In **moldyPSI**, kinetic energy is removed in one of two ways: either all velocities are set to zero because the global kinetic energy has fallen ('global KE quench'); or the velocities of individual atoms are reset depending on whether or not they are decelerating ('local quench'). This stop-start approach in MS, which essentially 'freezes' the system down to zero kelvin, is commonly known as 'relaxation' or 'quenching' of a system of particles.

In modern MD simulations the integration algorithms used are generally based on a finite-differences approach. The basic scheme involves starting from the positions, velocities, and other dynamic properties of the particles in the system at a time t and finding the same quantities at a later time $t + \Delta t$ to a sufficient degree of accuracy [**24**]. In the simplest case, where the system evolves under constant volume and energy, the advancement is achieved by using Newton's second law ($\mathbf{f} = m\mathbf{a}$) to find the accelerations from the forces on each particle, which are in turn calculated from the potential function (see section 2.4). Iterating this procedure allows the time evolution of a system to be followed for long times [**25**].

The classic time-integration algorithm used in many MD programs is known as the Verlet algorithm, so-called because it was first implemented by Loup Verlet in the late 1960s [**41**, **42**]. The equation used to advance the

particle positions in this method is given in [**41**] as:

$$\mathbf{r}_i(t+h) = -\mathbf{r}_i(t-h) + 2\mathbf{r}_i(t) + \sum_{j \neq i} \mathbf{f}\left(r_{ij}(t)\right) h^2, \tag{2.2}$$

where h is the time increment (*i.e.,* Δt) and $\mathbf{r}_i$ is the position vector of particle i. Here we note that the summed force-terms on the right-hand side of (2.2) represent the acceleration of particle i. The parameters of the Lennard-Jones potential (see section 2.4) used in [**41**] to describe the interaction between particles were chosen so that when the forces, and hence the accelerations, were calculated, the mass of the particles, which would have otherwise appeared in (2.2) as a consequence of Newton's second law, cancelled with the differentiated potential. In other words, the potential was re-scaled so that mass no longer appeared in the equations of motion.

The Verlet algorithm is popular because it is simple to implement, accurate, and stable [**25**]. It is also symmetrical about $\mathbf{r}(t)$ making it time-reversible [**24**]. However, it does have the disadvantage that the velocities are not calculated automatically as part of the algorithm. They can be derived from the $t + \Delta t$ and $t - \Delta t$ positions, but this is both inconvenient and subject to large errors, and so several modifications to the basic Verlet scheme have been suggested to try and overcome these problems.

The 'leap-frog' algorithm is another commonly used integration scheme. It is algebraically equivalent to the Verlet algorithm, and was actually the first of the two to be described; by Feynman *et al.* in 1963 (see [**44**]). However, it was not until the later publications by Hockney in 1970 [**45**] and by Potter in 1972 [**46**] that it was fully detailed and named. The

algorithm has the form:

$$\begin{aligned} \mathbf{v}\left(t + \tfrac{1}{2}\Delta t\right) &= \mathbf{v}\left(t - \tfrac{1}{2}\Delta t\right) + \Delta t\, \mathbf{a}(t), \\ \mathbf{r}(t + \Delta t) &= \mathbf{r}(t) + \Delta t\, \mathbf{v}\left(t + \tfrac{1}{2}\Delta t\right). \end{aligned} \tag{2.3}$$

Here $\mathbf{r}, \mathbf{v}$, and $\mathbf{a}$ have their usual meanings of position, velocity, and acceleration, respectively. Elimination of the velocities from the equations (2.3) confirms that they are the same as (2.2). This system has the advantage that the velocities appear explicitly, though not at time t, and so is not subject to the same errors as the Verlet-algorithm [**24**] (the improvement in computers since the early simulations has made precision less of an issue even for the original Verlet scheme).

However, there is a Verlet algorithm that does store the positions, velocities, and accelerations all at the same time t [**24**]. It was first suggested by Swope *et al.* in 1982 [**47**], and is often called the 'velocity-Verlet' algorithm. It has the following form:

$$\begin{aligned} \mathbf{r}(t + \Delta t) &= \mathbf{r}(t) + \Delta t \mathbf{v}(t) + \tfrac{1}{2}(\Delta t)^2 \mathbf{a}(t), \\ \mathbf{v}(t + \Delta t) &= \mathbf{v}(t) + \tfrac{1}{2}\Delta t \left[\mathbf{a}(t) + \mathbf{a}(t + \Delta t)\right], \end{aligned} \tag{2.4}$$

from which the original Verlet equation can be recovered again. It has the benefit that there is no requirement to store the particle properties at two different times [**25**]. The majority of the results presented in this thesis were obtained using the **moldyPSI** MD program written by Dr. Peter Derlet from the Paul Scherrer Institute in Switzerland [**26**], which by default employs the Gear predictor-corrector algorithm discussed below. However, in chapter 5 we use a different code called **LAMMPS**, developed by Steve Plimpton and others at Sandia National Laboratories in

California, which is optimised for large-scale parallel computing and uses this velocity-Verlet integration scheme (see [**48**] and [**49**] for more details).

Another class of methods often used to integrate equations of motion are known as predictor-corrector algorithms. Rahman [**38**] used a predictor-corrector algorithm in his studies of Ar. However, for MD the most often used and relevant form of this class of integration method is that attributed to Gear, which is presented below.

Gear first described the integration method that bears his name in a 1966 Argonne National Laboratory report [**50**], although it was presented more formally in two journal publications of 1967 and 1969 [**51**, **52**], and later in a book [**53**]. The method consists of three distinct steps:
1. Prediction: The positions, velocities, and higher derivatives at a time t are used to predict the same quantities at a time $t + \Delta t$ via Taylor expansions. For example, for a third-order Gear iterator, as in **moldyPSI** [**26**], the predictor equations have the form:

$$\begin{aligned}
\mathbf{r}_0(t+\Delta t) &= \mathbf{r}_0(t) + \Delta t \mathbf{r}_1(t) + \frac{(\Delta t)^2}{2}\mathbf{r}_2(t) + \frac{(\Delta t)^3}{6}\mathbf{r}_3(t) \\
\mathbf{r}_1(t+\Delta t) &= \mathbf{r}_1(t) + \Delta t \mathbf{r}_2(t) + \frac{(\Delta t)^2}{2}\mathbf{r}_3(t) \\
\mathbf{r}_2(t+\Delta t) &= \mathbf{r}_2(t) + \Delta t \mathbf{r}_3(t) \\
\mathbf{r}_3(t+\Delta t) &= \mathbf{r}_3(t),
\end{aligned} \tag{2.5}$$

where

$$\mathbf{r}_n(t) = \frac{\mathrm{d}^n \mathbf{r}(t)}{\mathrm{d}t^n}.$$

Here $\mathbf{r}_0(t) \equiv \mathbf{r}(t)$, $\mathbf{r}_1(t) \equiv \mathbf{v}(t)$, etc.
2. Force evolution: The forces on each atom (due to its neighbours) are calculated for the predicted positions. These forces are derived from the gradient of a potential function V, which defines the potential energy of the

system of atoms based on their positions. In other words, for the force $\mathbf{F}_i$ acting on an atom i this is:

$$\mathbf{F}_i = -\nabla_{\mathbf{r}^i} V(\mathbf{r}^i, \ldots, \mathbf{r}^N), \tag{2.6}$$

for N atoms with position vectors $\mathbf{r}^i$ [**24**].

In the conventional MD case, one of a system with constant volume and energy - producing so-called microcanonical (NVE) ensemble averages [**28**] - these forces are used in Newton's second law to directly calculate the $t + \Delta t$ acceleration of each atom. However, in some atomic systems it may be desirable to relate the simulations to laboratory experiments performed under constant temperatures and/or pressures. In these circumstances the equations of motion relating forces on atoms to their accelerations will be different. In section 2.1.4 below we discuss the equations of motion for a system under controlled pressure devised by Parrinello and Rahman [**54**].
3. Correction: The new accelerations calculated in step 2 will generally be different from those predicted in step 1. The difference between the two is used to correct the predicted atomic positions and their higher derivatives. For the Gear [**53**] method the corrected value for the nth derivative of the atomic position of an atom i is given by:

$$\mathbf{r}_n^{\text{correc}}(t + \Delta t) = \mathbf{r}_n(t + \Delta t) + c_n \left[\frac{\mathbf{F}_i}{2m_i} - \mathbf{r}_2(t + \Delta t) \right], \tag{2.7}$$

where the part enclosed within square brackets is $\Delta\mathbf{a}$, the difference between the (corrected) acceleration of step 2 and the predicted acceleration of step 1. The c_n are the coefficients or 'magic numbers' [**25**] used to determine the 'strength' of the correction to each quantity, and are chosen to produce the maximum stability and accuracy of the algorithm.

The 'best' choices are discussed by Gear [**53**] and for the third-order case described above $c_n = \left[\frac{1}{6}, \frac{5}{6}, 1, \frac{1}{3}\right]$.

It is perhaps more accurate to refer to the method of Gear described here as the Nordsieck-Gear predictor-corrector because only the particle positions and several time derivatives, all evaluated at the same time, are stored [**24**]. This is the so-called Nordsieck method. Other methods, such as those attributed to Adams by Gear in [**51**], involve storing velocities and accelerations from previous time-steps as well.

The velocity-Verlet algorithm also resembles a predictor-corrector algorithm in the sense that it involves two stages with a force calculation in between. The first step is the determination of the $t + \Delta t$ particle positions, and then the velocities are updated using the results of the force evaluation. However, velocity-Verlet is less accurate than the Gear algorithm for small values of the time-step Δt [**24**, chapter 3] and in the simulations discussed in this thesis we have primarily used a relatively short MD time-step of one femtosecond (1×10^{-15}s). Also, it is not very convenient when the equations of motion involve both the first and second derivatives of the positions [**24**, Appendix E], which is the case for the Parrinello-Rahman equations discussed in section 2.1.4. Thus, while this pseudo-predictor-corrector was available in the **moldyPSI** program the research results presented in this thesis have always been obtained using the Gear integrator, except in chapter 5 where we use the implementation of the velocity-Verlet scheme in **LAMMPS**.

2.1.3 Neighbour lists

Whilst the integration method might be the engine of an MD program, the 'speed' of this engine is almost entirely dependent on the force calculation

step. It is by far the most time-consuming part in any MD simulation. In both simple pairwise potentials such as the Lennard-Jones, and the more advanced many-body potentials developed in the 1980s (see section 2.4), the 'brute-force' approach is to consider the interaction of each particle with every other particle in the system. For even modestly sized simulations this quickly becomes computationally very expensive, which was a particularly significant problem in the early days of MD when computing power was limited. This led to the development of a number of time-saving tricks for the force evolution in an attempt to reduce the computational cost, most of which are still in use today.

Alder and Wainwright [**30**–**32**] improved speed by having a variable time-step, which advanced according to the time required before the first collision between hard or elastic spheres. Thus they did not waste computation on iterations where no events took place. A more important development was made in Verlet's famous 1967 paper [**41**], which introduced what is now known as the 'Verlet neighbour list'. This involves, for each particle, storing a list of all the particles which lie within a pre-defined (say r_m) distance of that particle. In [**41**] this is done every nth integration step, and for the next $n-1$ steps only the particles in the list are considered when computing the force acting on a particular particle. Verlet suggested that this system cut the computing time required for his simulations by a factor of 10. However, it is reliant on choosing the interval between list-updates carefully; too short and computation time goes up; too long and some particle-pairs, not considered in the current list, may have become close enough to interact.

Fincham and Ralston in 1981 [**55**] and later Thompson in 1983 [**56**] suggested an important refinement to Verlet's scheme that addressed the

issue by allowing the updating to take place automatically as required. In [**56**] the method is described thus: every time a new neighbour list is built, a vector for each particle is initialised to zero. At every subsequent time-step this vector is incremented by the displacement of the particle to which it refers, and hence it stores the total distance moved by the particle since the last list update. The maximum displacement in these vectors provides a guide as to when the list should be updated. For example, if the sum of the two maximum magnitudes exceeds the difference between the list sphere radius r_m and the potential cut-off distance r_c then the list is rewritten [**24**] (in [**55**] a modified version of this is used where the list is updated if the maximum displacement exceeds half of the difference mentioned above).

The basic neighbour-list system works well for systems with relatively few particles, but as the size increases towards 1000 particles the list itself becomes too large to store easily [**24**]. In this case there is a more efficient way to keep track of the neighbours, called the cell index method or cell subdivision ([**57**, Quentrec and Brot, 1973], [**58**, Hockney *et al.*, 1974] and [**59**, Schofield, 1973]). The basic idea of the technique is to divide the simulation cell into a number of identical cubic sub-cells, whose dimension along a side is chosen so that it is greater than the cut-off radius for the potential describing the interaction between particles. At the start of each time-step each particle can be quickly assigned to one of these cells, so that when the force evaluation is performed it is only necessary to consider a particle's interactions with particles in the same sub-cell or in one of the 26 neighbouring sub-cells. In practice, because of symmetry and Newton's third law, it is only necessary to check 13 of the neighbours [**28**] for a given sub-cell, with the remaining interactions considered during the force

evaluation of the other 13 neighbours (although with modern computers the time speed-up associated with looping over 14 sub-cells instead of 27 is negligible).

To improve efficiency further, in MD simulations the above procedure has been refined using the method of linked lists to set-up the sub-cell structure [**60**, **61**]. Instead of storing a list of the particles in each sub-cell, the linked list method creates a non-sequential path through the particles [**28**] by *linking* all the particles of a given sub-cell to one-another. At each time step or iteration, the particles can be rapidly sorted into sub-cells. During this process two lists or arrays are created. The first contains a single entry for each sub-cell and points to the particle at the top of the linked list for that particular sub-cell. Allen and Tildesley [**24**, chapter 5] call this the 'head-of-chain' array or HEAD. The second list contains an entry for each particle in the simulation. The entry for each particle referred to in the HEAD list points to the next particle in the sub-cell, and the entries for these particles point to the next particles, and so on. The entry for the last particle in a sub-cell is given an unambiguous value, such as zero, indicating that all that particles for that cell have been considered. When the force evaluation is performed it is a simple process to find all the particles of a given sub-cell using this array of linked lists, starting from the top particle, with a termination value to indicate when to move to the linked list for the next sub-cell. The linked list system is particularly beneficial from a storage point-of-view, not only because storage requirements are reduced, but also because the amount of storage needed is fixed. Whereas the size of a list containing the particles of each sub-cell varies in length and is not known in advance, for linked lists the size of the two arrays used are fixed for the entire simulation [**28**].

2.1.4 Derivation of the Parrinello-Rahman equations of motion

As discussed in section 2.1.2 above, in some circumstances it is desirable to deviate from strict Newtonian time evolution of the NVE ensemble (*i.e.,* constant volume, energy, and number of particles) in a molecular simulation, particularly if we are seeking comparisons with laboratory experiments where the temperature and pressure may be controlled instead of the energy and volume. One such alternative is the canonical or NVT ensemble, in which the temperature is constant (rather than the energy). Nosé [**62**] and Hoover [**63**] described a technique whereby this could be achieved using a frictional term, whose evolution in time is controlled by the difference between the instantaneous kinetic energy and the average kinetic energy defined by the desired temperature via:

$$\dot{\xi} = \sum_{i=1}^{N} m_i \dot{\mathbf{r}}_i^2 - \frac{3Nk_BT}{2}, \tag{2.8}$$

where ξ is the friction coefficient, $\mathbf{r}_i$ is the usual position vector of particle i, k_B is Boltzmann's constant, m_i is the mass of the ith particle, with N the total number of particles in the system, and T is the desired temperature. A dot over a variable refers to the time derivative. The frictional coefficient then appears in an extra term in the equation of motion defining the acceleration of a particle [**63**].

Another alternative ensemble is the isoenthalpic-isobaric or NPH ensemble, in which the pressure is a constant, controlled quantity and enthalpy H is conserved [**25**]. Andersen [**64**] originally introduced a method for constant pressure MD whereby the system volume is an external variable or additional degree of freedom, which, coupled to the atomic coordinates, mimics the action of a piston on a real system [**24**]. Parrinello

and Rahman [**54**, **65**, **66**] developed this further by allowing the box shape to vary as well as the volume, whilst still maintaining a constant pressure. Such a scheme is useful in the study of solids where phase changes in the material may cause the unit cell to change its dimensions and angles [**24**], but also has relevance to the present studies where we are concerned with defects that are small in comparison to the bulk material, and in the far field a controlled pressure (*i.e.,* almost constant in the absence of external stress) is appropriate.

Almost a decade after Parrinello and Rahman (PR), Cleveland [**67**] and then Wentzcovitch [**68**] proposed an alternative Lagrangian to that given in [**54**], one that was invariant with respect to a modular transformation of the box shape. Wentzcovitch [**68**] explains that the non-invariance of the PR Lagrangian leads to a situation in which the choice of simulation cell may have a strong influence on the resulting dynamics, although it is pointed out that this may only be significant at zero Kelvin, or in simulations of phase-transitions. In the present work we have always used a regular box shape (*i.e.,* cubic), and so the equations of motion derived from the PR Lagrangian will behave uniformly in our case.

To derive the equations of motion for NPH ensemble of Parrinello and Rahman we begin with the Lagrangian for a system of N particles of mass m_i interacting under constant external pressure, p_{ext} [**65**]:

$$\mathcal{L} = \frac{1}{2}\sum_{i=1}^{N} m_i \dot{\mathbf{s}}_i^T \mathbf{G} \dot{\mathbf{s}}_i - \sum_{i=1}^{N}\sum_{j>i}^{N} \phi(r_{ij}) + \frac{1}{2} W \mathrm{Tr}[\dot{\mathbf{h}}^T \dot{\mathbf{h}}] - p_{\text{ext}}\Omega, \tag{2.9}$$

where, as before, a dot above a variable refers to differentiation with respect to time t. Here the system of particles has an arbitrary volume and

shape defined by the 3×3 matrix $\mathbf{h}$, whose columns are the three vectors $\{\mathbf{x}_1, \mathbf{x}_2, \mathbf{x}_3\}$ describing the sides of the simulation cell. These nine extra degrees of freedom, (instead of the one introduced by Andersen [**64**]) evolve in time together with the $3N$ degrees of freedom associated with the atomic positions.

In equation (2.9), $\mathbf{s}_i$ is a column vector describing the position of a particle i relative to the box vectors, via:

$$\mathbf{r}_i = \mathbf{h}\mathbf{s}_i = s_i^1\mathbf{x}_1 + s_i^2\mathbf{x}_2 + s_i^3\mathbf{x}_3, \tag{2.10}$$

where $\mathbf{r}_i$ is the real position of the particle and $\mathbf{s}_i = (s_i^1, s_i^2, s_i^3)^T$, where ^{T} means 'the transpose of' the given matrix or vector. Note that the components of $\mathbf{s}_i$ have values in the range [0,1]. $\mathbf{G} = \mathbf{h}^T\mathbf{h}$ is the metric tensor. Ω is the volume of the box given by the determinant of $\mathbf{h}$ (*i.e.,* $\det \mathbf{h}$).

W is the constant of proportionality determining how the system responds to the imbalance between the externally applied stress p_{ext} and the internally generated stress and has units of mass [**65**]. (Note that in the present research, we did not consider external stresses using the Parrinello-Rahman (PR) equations of motion.) In other words, the value of W simply determines how strongly or quickly the box-shape and volume changes in response to internally generated stress. Andersen [**64**] likened this quantity to the mass of an external piston acting on the system. A low value of W results in rapid, undesirable, and difficult-to-damp, box-size oscillations, while a large value produces a slow searching of volume-space, thus reducing computational efficiency. In the limiting case of an infinite W the system evolves as if controlled by the normal Newtonian equations of motion [**24**]. In **moldyPSI** its value was set at between 1.5 and 2 times the

mass of a single atom, depending on the metal being simulated. Note that we observed that the choice of W had little or no effect on the particle trajectories, which was also noted by Andersen [**64**], and is only important when measuring dynamic averages.

In equation (2.9) the interatomic potential defining the interaction between particles is a simple pairwise function ϕ, whose value for a given pair (i, j) is defined according to their separation r_{ij}. Generally, the potential function will have a more complex form (see section 2.4) and we will discuss how a more appropriate form affects the resultant equations of motion at the end of this derivation.

To derive equations of motion from the above Lagrangian (2.9) we apply the *principle of least action* (also known as Hamilton's principle), which states that a system must move between two states at times t_1 and t_2 in such a way that the action S, defined by the integral:

$$S = \int_{t_1}^{t_2} \mathcal{L} \, \mathrm{d}t,$$

takes the least possible value [**69**]. This condition leads to the requirement that each degree of freedom of the system must satisfy the equation:

$$\frac{\mathrm{d}}{\mathrm{d}t}\left(\frac{\partial \mathcal{L}}{\partial \dot{q}_i}\right) - \frac{\partial \mathcal{L}}{\partial q_i} = 0, \tag{2.11}$$

where in this case $q_i(t)$ is one of the $3N{+}9$ degrees of freedom in $(\mathbf{s}_1, \ldots, \mathbf{s}_N, \mathbf{h})$. The set of differential equations produced from the above are known as Lagrange's equations. Note that these can also be derived in a slightly different way using D'Alembert's principle (see *Classical Mechanics* by Goldstein *et al.*, [**70**, chapter 1]).

Substituting (2.9) into (2.11) for a particle position $\mathbf{s}_i$ we have, changing

subscripts as necessary:

$$\frac{\mathrm{d}}{\mathrm{d}t}\left\{\frac{\partial}{\partial\dot{\mathbf{s}}_i}\left(\frac{1}{2}\sum_{j=1}^{N}m_j\dot{\mathbf{s}}_j^T\mathbf{G}\dot{\mathbf{s}}_j\right)\right\}+\frac{\partial}{\partial\mathbf{s}_i}\left(\sum_{j=1}^{N}\sum_{k>j}^{N}\phi(r_{jk})\right)=0. \tag{2.12}$$

Considering the first term on the left-hand side, we see that the only non-zero term occurs when $j=i$, giving:

$$m_i\frac{\mathrm{d}}{\mathrm{d}t}\left\{\frac{\partial}{\partial\dot{\mathbf{s}}_i}\left(\frac{1}{2}\dot{\mathbf{s}}_i^T\mathbf{G}\dot{\mathbf{s}}_i\right)\right\},$$

In Appendix C.1 we derive the required partial derivative and substituting the result (equation (C.1)) into the above expression gives:

$$m_i\frac{\mathrm{d}}{\mathrm{d}t}\left(\mathbf{G}\dot{\mathbf{s}}_i\right)=m_i\big(\dot{\mathbf{G}}\dot{\mathbf{s}}_i+\mathbf{G}\ddot{\mathbf{s}}_i\big), \tag{2.13}$$

via the product rule for differentiation.

For the second term on the left-hand side of (2.12) we have

$$\frac{\partial}{\partial\mathbf{s}_i}\left(\sum_{j=1}^{N}\sum_{k>j}^{N}\phi(r_{jk})\right)=\sum_{j=1}^{N}\sum_{k>j}^{N}\frac{\partial}{\partial\mathbf{s}_i}\phi(r_{jk})=\sum_{j=1}^{N}\sum_{k>j}^{N}\phi'(r_{jk})\frac{\partial r_{jk}}{\partial\mathbf{s}_i}. \tag{2.14}$$

r_{ij} is the length or magnitude of the vector $\mathbf{r}_{ij}$, and the square of this distance can be expressed as:

$$r_{ij}^2=\|\mathbf{r}_{ij}\|^2=(\mathbf{s}_i-\mathbf{s}_j)^T\mathbf{G}(\mathbf{s}_i-\mathbf{s}_j). \tag{2.15}$$

Using this we can find the derivative of r_{jk} with respect to $\mathbf{s}_i$ (see Appendix C.2):

$$\frac{\partial r_{jk}}{\partial\mathbf{s}_i}=\frac{1}{r_{jk}}(\delta_{ij}-\delta_{ik})\mathbf{G}(\mathbf{s}_j-\mathbf{s}_k), \tag{2.16}$$

where δ_{ij} is the Kronecker-Delta function whose value is one if $i=j$ and

zero otherwise. Substituting into (2.14) we have

$$\begin{aligned}
&\sum_j \sum_{k>j} \frac{\phi'(r_{jk})}{r_{jk}}(\delta_{ij} - \delta_{ik})\mathbf{G}(\mathbf{s}_j - \mathbf{s}_k) \\
&\quad = \sum_{k>i} \frac{\phi'(r_{ik})}{r_{ik}}\mathbf{G}(\mathbf{s}_i - \mathbf{s}_k) - \sum_{i>j} \frac{\phi'(r_{ji})}{r_{ji}}\mathbf{G}(\mathbf{s}_j - \mathbf{s}_i) && \text{(for } j = i \text{ and } k = i, \text{ respectively)} \\
&\quad = \sum_{j>i} \frac{\phi'(r_{ij})}{r_{ij}}\mathbf{G}(\mathbf{s}_i - \mathbf{s}_j) + \sum_{i>j} \frac{\phi'(r_{ij})}{r_{ij}}\mathbf{G}(\mathbf{s}_i - \mathbf{s}_j) && \text{(using } r_{ij} = r_{ji} \text{ and replacing } k \text{ with } j) \\
&\quad = \sum_{j\neq i} \frac{\phi'(r_{ij})}{r_{ij}}\mathbf{G}(\mathbf{s}_i - \mathbf{s}_j).
\end{aligned}$$

Using the above result, together with (2.13), in (2.12) gives, for a particle position $\mathbf{s}_i$,

$$m_i\big(\dot{\mathbf{G}}\dot{\mathbf{s}}_i + \mathbf{G}\ddot{\mathbf{s}}_i\big) + \sum_{j\neq i}^{N} \frac{\phi'(r_{ij})}{r_{ij}}\mathbf{G}(\mathbf{s}_i - \mathbf{s}_j) = 0,$$

which can be rearranged to give the equation of motion for an atom i:

$$\ddot{\mathbf{s}}_i = -\sum_{j\neq i}^{N} \frac{\phi'(r_{ij})}{m_i r_{ij}}(\mathbf{s}_i - \mathbf{s}_j) - \mathbf{G}^{-1}\dot{\mathbf{G}}\dot{\mathbf{s}}_i, \tag{2.17}$$

which is equivalent to equation (2.9) in [**65**]. If the box matrix is constant then the second term on the right in the above equation is zero and we recover the Newtonian equation of motion.

An equation of motion for the second derivative (with respect to t) of the box matrix (*i.e.,* $\ddot{\mathbf{h}}$) is derived using similar arguments (see Appendix

C.3). From equation (C.14) we obtain:

$$W\ddot{\mathbf{h}} = \sum_{i=1}^{N} m_i \mathbf{h}\dot{\mathbf{s}}_i\dot{\mathbf{s}}_i^T - \sum_{i=1}^{N}\sum_{j>i}^{N} \frac{\phi'(r_{ij})}{r_{ij}}\mathbf{h}(\mathbf{s}_i-\mathbf{s}_j)(\mathbf{s}_i-\mathbf{s}_j)^T - p_{\text{ext}}\Omega\left(\mathbf{h}^T\right)^{-1}, \quad (2.18)$$

which can be expressed in terms of real particle vectors (*i.e.,* $\mathbf{r}_i, \dot{\mathbf{r}}_i$, *etc.*) as

$$W\ddot{\mathbf{h}} = \left(\frac{1}{\Omega}\sum_{i=1}^{N} m_i\dot{\mathbf{r}}_i\dot{\mathbf{r}}_i^T - \frac{1}{\Omega}\sum_{i=1}^{N}\sum_{j>i}^{N}\frac{\phi'(r_{ij})}{r_{ij}}(\mathbf{r}_i-\mathbf{r}_j)(\mathbf{r}_i-\mathbf{r}_j)^T - p_{\text{ext}}\right)\boldsymbol{\sigma}, \quad (2.19)$$

where $\boldsymbol{\sigma} = \Omega(\mathbf{h}^T)^{-1}$ contains information about the size and orientation of the MD cell [**65**]. In this equation on the right-hand side we see that, for the internal pressure of the system, we have the sum of the particle kinetic energies (positive pressure) minus a term produced from the force between atoms multiplied by the square of their separation (equivalent to force × area), which will generally be a compressive or negative pressure as a result of attraction between atoms. In the predictor-corrector algorithm, as it is implemented in the **moldyPSI** MD program [**26**], the corrected box coordinates are calculated first, using the above equation, before the particle positions are updated using these new box variables via equation (2.17).

It is also possible to extend the above formalism to the case of a general stress applied through a stress tensor **S**. In this case the Lagrangian of equation (2.9) receives an extra term associated with this new tensor, which then leads to an additional term in the equation for the second time-derivative of **h**. The derivation of this extended model can be found in [**65**]. **moldyPSI**, which contains an implementation of the PR equation of motion, includes the ability to define a general external stress tensor.

In practice the difference between the system evolution in non-Newtonian dynamics, such as those produced by the equations of

Parrinello and Rahman above, and true Newtonian dynamics may be extremely small. However, in some cases it is more convenient to use alternative ensembles. For example, during the relaxation of non-cubic boxes the Parrinello-Rahman (PR) equations can become very useful. Also in circumstances where a system contains large artificial compressions before relaxations, such as after the insertion of dislocation loops (chapter 3), allowing the volume to change (expand) is preferable to a large increase in pressure. This is particularly relevant if we are seeking minimum energy system configurations.

2.2 Conjugate gradient energy-minimisation

Conjugate gradient energy-minimisation is similar to the Molecular Statics (MS) method discussed previously in that they are both ways of finding minimum energy configurations for a system of interacting particles. The key difference between the two methods is that whereas MS, as defined in this thesis, essentially evolves the equations of motion in time with occasional artificial adjustments, the conjugate gradient (CG) method is a way of actively seeking the minimum configuration. However, since the CG method does not involve the full time evolution of a system, it could also be defined as 'molecular statics'. In this thesis we distinguish it from the MS described previously because of the different minimisation scheme it uses.

The MS method, as implemented in **moldyPSI**, is essentially a steepest descent method. The system is evolved successively to local minima following the local potential energy gradient specified by the particle interactions. Once a local minimum is reached the system sets off again in a new direction (by removing existing atomic velocities in MS) towards another minimum, but this may not be in the direction of the global

minimum. Whilst this method works adequately for small systems of particles, for larger systems it is inefficient because a lot of time may be spent going in the 'wrong' direction with respect to the global minimum required. CG is a technique whereby the global minimum can be obtained in fewer steps by following a path that is as 'straight' as possible.

The method itself was first developed in the 1950s by Hestenes and Stiefel [**71**, **72**] as a way to solve linear equations [**73**]. Algorithms were later developed (for example the Fletcher-Reeves [**74**] or the Polak-Ribière [**75**]) to apply the method to a generalised function. In the case of the atomic CG simulations performed in our research we have an interatomic potential function defined on the N position vector triplets, one for each atom (plus the 9 box dimensions in the Parrinello-Rahman case). The algorithm used in the present work, which uses a basic form that is common to both Fletcher-Reeves and Polak-Ribière, is summarised below.

At any point during a simulation, the CG method, rather than following the exact new gradient direction (as in steepest descent), moves the system in a direction that is constructed to be the conjugate of the old gradient direction, and, where possible, all other previous directions [**76**]. The CG method applied by us, which is implemented as part of the CG-minimisation routines of **moldyPSI**, uses a CG direction which is the current maximum CG of all the atoms in the system. The CGs on the atoms contain weighted contributions (by total force) from all previous gradients considered. The particular definition of the weighting (γ), which adds the contribution from all previous atom CGs to the current force on atoms to produce the new CG, is that defined by the Fletcher-Reeves algorithm [**74**]. The algorithm proceeds by 'drawing' a line in multi-dimensional space from the current atomic configuration in the new

CG direction. The length of this line is an important adjustable parameter as it defines the maximum distance that the system can jump from its current position to find a new minimum. If, in a simulation, the global minimum is expected to be close to the initial configuration then it is appropriate to set the maximum CG line length to be small. However, if the minimum is unknown or is predicted to be far from the initial position then the search length should be large in order to ensure sufficient searching of the energy landscape.

The CG line defines a subset of possible new configurations that the system can move to, and the system is translated to the minimum-energy configuration of this subset. This so-called line minimisation is achieved in **moldyPSI** using sub-routines described in *Numerical Recipes, FORTRAN example book* [**77**, chapter 10]. The first of these, **mnbrak**, defines a smaller subset of the line, which contains the minimum. **golden** is then used to define the exact minimum, subject to convergence criteria, of this 'bracketed' subset. In the present work, convergence was achieved if both the energy change for a new minimum configuration (compared to the previous minimum), and the maximum force on any atom, were sufficiently small. The energy convergence criteria was typically of the order of 1×10^{-4} eV or lower, while force convergence was attained if the maximum force on any atom was less than around 0.1 eV/Å.

In this thesis, the CG method has been used successfully to locate the minimum energy structure of defects. However, we have noted in our simulations that in some cases, the CG method gets 'stuck' in a local minimum and is unable to escape, no matter how the convergence and searching criteria are changed. In this case MS (steepest-descent) has been utilised to find a configuration that is significantly lower in energy than

that suggested by CG. On the other hand, combining CG with MS has proven to be a useful tool because CG relaxation can be used initially to get close to the minimum configuration in a short computation time-span, and then MS relaxation can be applied to fine-tune the configuration to the absolute minimum.

2.3 The nudged elastic band method

In investigations of atomic defect structures, it is often of interest to identify the lowest energy pathway between one stable configuration of atoms and the next. For example, in the current research we are interested in the transition pathway between two equilibrium lattice sites for a straight screw dislocation. The method employed in this work to identify these 'minimum energy paths' (MEPs) is known as the Nudged Elastic Band (NEB) method. It was first devised in the 1990s by Jónsson and Mills [**78**, **79**], and later extended by Henkelman and Jónsson [**80**].

The technique begins with two relaxed (energy-minimised) configurations of a system of atoms. These are the initial and final states between which the MEP is sought. The method proceeds by defining a set of image configurations between these fixed end-points (*i.e.,* their atomic positions do not change during the calculation). In this research we have typically found that 17 images (19 configurations in total) is the most appropriate number of images (or replicas [**78**]). The simplest way of defining the initial image positions is to 'draw' a linear path between the end-points in multi-dimensional space and spacing the images equally along this path. This means that each atom's position varies along a straight line from the position it occupies in the initial state to its position in the final state, with the interval between positions in the images evenly distributed

along the line.

The image configurations form the 'elastic band' and they are connected to one another by 'springs' with a constant stiffness (spring constant) of k. The total potential energy of the system, to be minimised, is then defined by the objective function

$$S(\mathbf{R}_1, \ldots, \mathbf{R}_N) = \sum_{i=1}^{N} V(\mathbf{R}_i) + \sum_{i=1}^{N+1} \frac{k}{2}(\mathbf{R}_i - \mathbf{R}_{i-1})^2, \tag{2.20}$$

where $\mathbf{R}_i, \ldots, \mathbf{R}_N$ are the positions of the N image configurations. $V(\mathbf{R}_i)$ is the potential function defining the energy of a given configuration [**78**].

In this basic formalism, which Jónsson and Mills refer to as the plain elastic band method [**78**], the force on each image is defined as

$$\mathbf{F}_i = -\nabla V(\mathbf{R}_i) + \mathbf{F}_i^s, \tag{2.21}$$

where $\mathbf{F}_i^s$ is the spring force on image i given by:

$$\mathbf{F}_i^s = k[(\mathbf{R}_{i+1} - \mathbf{R}_i) - (\mathbf{R}_i - \mathbf{R}_{i-1})], \tag{2.22}$$

for a constant spring stiffness k. However, Mills and Jónsson noted that using this expression for the force on a image often resulted in the true MEP being missed [**78**]. Firstly, the component of the spring force $\mathbf{F}^s$ perpendicular to the image path tended to pull images off the MEP causing corner-cutting (missing the top of the energy barrier). In addition, the components of the 'true force' [**78**] $\nabla V(\mathbf{R}_i)$ parallel to the path can cause the images to slide down the barrier.

To solve these problems Jónsson and Mills [**78**] proposed a new force description where the perpendicular spring force component and the

parallel part of the true force are projected out (*i.e.,* omitted). The force on an image became:

$$\mathbf{F}_i = \mathbf{F}^s_{i\|} - \nabla V(\mathbf{R}_i)_\perp. \tag{2.23}$$

The unit vector tangent to the path at image i, $\hat{\boldsymbol{\tau}}_i$, is used to find [**10**, **78**]

$$\mathbf{F}^s_{i\|} = (\mathbf{F}^s_i \hat{\boldsymbol{\tau}}_i)\hat{\boldsymbol{\tau}}_i, \qquad \text{and}$$
$$\nabla V(\mathbf{R}_i)_\perp = \nabla V(\mathbf{R}_i) - (\nabla V(\mathbf{R}_i)\hat{\boldsymbol{\tau}}_i)\hat{\boldsymbol{\tau}}_i \qquad .$$

This projection of the perpendicular ∇V and parallel spring force is what Jónsson and Mills refer to as 'nudging', and it has the effect of decoupling the dynamics of the path from the discrete image distribution, therefore enabling correct convergence of the system to the MEP [**78**].

Calculation of the unit tangent can be performed in a number of ways, and Henkelman and Jónsson [**80**] discuss the pros and cons of each method. In the research presented in this thesis we found that changing the formula for $\hat{\boldsymbol{\tau}}_i$ did not usually produce any change in the MEP found. However, in contrast to the observations of Jónsson and Mills, we did find that the choice of the spring constant k was important in determining the accuracy of the MEP calculated. This was particularly noticeable using a modified NEB method in chapter 6, where atoms and interatomic potentials were replaced by strings and string interaction laws.

2.4 Interatomic potentials

All of the computational methods discussed above rely upon the realism of the interatomic potentials they use to define the interaction between the atoms. How realistic the dynamics of an MD simulation are, how reliably MS or CG predict the correct minimum energy configuration, or how

appropriate a minimum energy path (MEP) found by an NEB is, are all determined by the suitability of a given potential for the atomic system considered. The use of a potential is both an advantage and a limitation of these kinds of atomistic simulations. Compared to techniques such as kinetic Monte-Carlo simulations, where much of the dynamics of atoms and defects must be known in advance to produce rates and probabilities for different events, simulations that use potentials are more fundamental because they require no prior knowledge other than the way one atom behaves relative to another. However, evaluating forces and moving atoms in this way is relatively expensive computationally. Potentials can also never hope to fully match the accuracy of techniques such as density functional theory (DFT) where electronic interactions are also considered. On the other hand, interatomic potentials require much less time to evaluate and so out-perform such computationally intensive techniques in terms of efficiency and also the dynamic time-scales reachable. The design of interatomic potentials is therefore largely a delicate balance between a desire to have accurate representations of interatomic forces, but also acceptable computational demands.

Previously, we have mentioned the Lennard-Jones potential (see equation (2.1)), which is one of the original and most widely used potentials. It is a type of pairwise, or two-body, potential, which are limited in that they can only realistically model rare gases, where there are no free electrons to consider and the particle interactions are limited to those caused by weak van der Waals forces [**25**]. More interesting materials, such as metals and semiconductors, cannot be effectively modelled by pairwise interactions because they are unable to reproduce the correct energies and structures of a sufficiently broad range of phenomena to make

simulations practical.

The above shortcoming led to the development of so-called many-body potentials for metals. This process began in the 1980s and continues to the present day. The most popular group of potentials in this category are based on the concept of expressing one part of the configurational energy of a particle (*i.e.,* the total energy resulting from the sum over all possible neighbour interactions) as a *functional* of an intermediate sum of pair terms [**81**]. For this reason interatomic potentials derived in this way are often referred to as being of a 'pair-functional' form [**81**, **82**]. The potential in this case has the following analytical form [**25**]:

$$V = \frac{1}{2} \sum_{\substack{i,j=1 \\ (j \neq i)}}^{N} \phi(r_{ij}) + \sum_{i=1}^{N} U(n_i), \tag{2.24}$$

where ϕ is the remaining two-body (pair-potential) part, and U is a function of the sum n_i of a pairwise function describing the local environment about particle i [**81**]:

$$n_i = \sum_{\substack{j=1 \\ (j \neq i)}}^{N} \rho(r_{ij}). \tag{2.25}$$

U describes how the part of V associated with particle i depends on the local environment, which is described by a single physical parameter. Many-body potentials described in this way have similar computational requirements to simple pair-potentials, but provide a much better description of the complex environments in metals (and other materials) [**81**].

The pair-functional approach can be justified in two ways. They both

lead to the same mathematical expression for the interatomic potential (2.24), but differ in which physical parameter is associated with the local environment about each atom. In the *tight-binding* formalism the local electron valence bandwidth is the parameter considered, whilst in the *embedded-atom* analysis particles are influenced by a local background electron density. A detailed description of these two derivations can be found in the review of Carlsson [**81**], as well as in [**83**] and [**84**], for the two different methods respectively.

Several different (but at the same time similar) potentials have the form defined in (2.24). These include:

- The Finnis-Sinclair potentials. Originally defined by Finnis and Sinclair in 1984 [**83**], these potentials are second-moment approximations (SMAs), and have a many-body, or bonding, term equal to the sum over all atoms of the square-root of a site density, which itself is the sum over neighbours of a cohesive (attractive) potential. The potential described by Finnis and Sinclair differs slightly from the other well-known SMA-potential described later by Rosato *et al.* [**85**]. Finnis and Sinclair use a fitting function with a polynomial form, whereas Rosato *et al.* [**85**] use one with an exponential functional form. Many modern potentials are based on the original version by Finnis and Sinclair (see for example [**86**]).

- The Embedded Atom Method (EAM). So-named because it views each atom as embedded in a host lattice consisting of all other atoms [**87**]. Devised by Daw and Baskes in the early 1980s [**84**, **87**], and still popular today.

- The Glue Model of Ercolessi *et al.* [**88**], which uses a

density-dependent many-body term to mimic the 'gluing' or cohesion caused by conduction electrons in metals.

- The Effective-Medium theory adapted for iron by Jacobsen *et al.* [**89**]. This does not quite fit into the pair-functional scheme, and strictly speaking it is most applicable to gas systems, but it is similar to EAM in that it considers atoms embedded in a homogeneous electron gas. However, it goes much further and fits many more parameters to the local density functions.

These schemes differ primarily in the way that they construct the various parts which make up the expressions given in (2.24) and (2.25). This often leads to completely different parameterizations of the same material. The fitting of physical characteristics to the necessary functional forms is in fact where most time is spent in the building of new potentials [**25**].

Whilst the pair-functional potentials, and the simpler pairwise potentials, discussed above are the most widely used in MD, they are not the only solution to the problem of accurately describing the interaction of particles in simulations. There are cluster potentials and functionals, where the pairwise terms are joined by higher order interactions. Such functions are dependent on three atoms simultaneously and so must be summed over the subscripts i, j, k [**81**]. There is also some work on deriving potentials that also include angular forces, *i.e.,* forces which depend on the orientation of atoms with respect to one another. For example, the potentials developed by Lee *et al.*, for Fe [**90**] and then the other bcc transition metals [**91**], explicitly incorporate angular contributions in the formulation of the background electron density part of the Modified Embedded Atom Method (MEAM) (see [**92**, **93**]).

There has also been an effort over the last couple of decades to develop

potentials using quantum-mechanical (tight-binding) techniques. This was first suggested by Ducastelle and Cyrot-Lackmann in 1970 [**94**], and has been developed further by several groups, including Pettifor *et al.* (see for example [**95**–**98**]), and Moriarty [**99**]. These potentials have proved highly successful in predicting the equilibrium configurations and energies of systems, but it has proved difficult and computationally expensive to apply them to dynamical problems, although Streitz *et al.* [**100**] (solidification) and Wu *et al.* [**101**] (plastic flow) have recently had success in simulating dynamic processes in Ta. Further details of these and the various other options for potentials can be found in the extensive review of Carlsson [**81**], and also in the recent book of Finnis [**102**].

However, these other types of potentials, particularly as far as bcc transition metals are concerned, have, thus far, been unable to reproduce the same combination of accuracy and computational efficiency as pair functional potentials because of the uncertainty and complexity surrounding the required fitting parameters and procedures. In the future it may be possible to derive *tight-binding* potentials that are almost as efficient as pair potentials (and more accurate). In the meantime pair-functional potentials are an acceptable compromise, and, as a result, most of the effort since the inception of many-body potentials in the 1980s has been spent on refining the handful of related, but subtly different, pair-functional potentials in order to produce more realistic descriptions of the materials under investigation. In what follows we will briefly mention some of the relevant potentials that have been constructed for MD studies of bcc transition metals (particularly Fe), and discuss the primary potentials used in the present work.

In 1993, Cleri and Rosato [**103**] derived tight-binding potentials for

face-centred cubic (fcc) and hexagonal close-packed (hcp) transition metals and their alloys using the second moment approximation. The potentials were able to reproduce the experimentally observed thermal behaviour of the pure metals. However, they state in the paper that the scheme used to create the potentials did not work for bcc transition metals.

In 1997 Ackland *et al.* [**86**], produced a new Finnis-Sinclair potential for Fe by choosing coefficients that fitted the lattice parameter, cohesive energy, unrelaxed vacancy formation energy, and elastic constants for α-Fe at 0K [**82**]. It was constructed with the same format as a previously derived Cu potential [**104**], so that the two could be used to study the Fe-Cu alloy. Subsequently, simulations were performed with the combined potential, which is often referred to as the Ackland-Bacon potential, and the influence that Cu had on the lattice parameter of Fe agreed well with experiment.

In a later paper of 2003 by Mendelev *et al.* [**82**] it is pointed out that the use of cohesive energy as one of the fitted parameters in [**86**] can cause errors in the description of the interatomic forces. Mendelev *et al.* [**82**] improved the Fe potential of Ackland *et al.* [**86**] by also fitting first-principles atomic forces, which produced a proper pairwise part at small atomic separations. This potential for crystalline Fe is now known simply as the Mendelev potential. In [**82**] there is also a description of an Fe potential that was constructed by fitting diffraction data, leading to a potential that offers a good description of the liquid state of Fe.

The discussion above demonstrates that there has been much time and effort spent in recent times on the development of potentials for Fe. However, what is also obvious is that these potentials, which are based on the many-body formalisations originally developed for non-magnetic metals, do not include the effect of magnetism [**105**]. The importance of magnetism

in the bcc α-phase of Fe was first suggested by Hasegawa and Pettifor in 1983 [**106**]. Therefore, after recent computer experiments, which showed that magnetism did indeed have an important role to play in the interatomic forces of Fe (see for example [**107**], [**108**], and [**109**]), a new potential for Fe was proposed - one that included the effect of magnetism.

This 'magnetic' interatomic potential of Fe has been developed by Dudarev and Derlet [**105**, **110**]. It is an EAM-type potential, with magnetism included in the fit of the embedding part, which is derived using a combination of the Stoner and Ginzburg-Landau models. In this relatively short-ranged many-body potential the pairwise density radial function $f(r)$ (the embedding part) and the pairwise repulsive function $V(r)$ are made up of a summation of cubic knot functions. For example, $f(r)$ has the form:

$$f(r) = \sum_{n=1}^{N^f} f_n (r_n^f - r)^3 \Theta(r_n^f - r), \tag{2.26}$$

where the f_n and r_n^f are the fitted knot coefficients and points, respectively. These functions have been fitted to various material properties including the bulk cohesive energy, lattice constant, elastic stiffness constant of different phases, the un-relaxed vacancy formation energy, and the relaxed formation energies of the three high-symmetry self-interstitial atom configurations (see [**105**] for more detail). Even though the potential is short-ranged compared to others, such as the popular Mendelev potential [**82**], it is still capable of accurately reproducing many of the fundamental properties of bcc Fe (it is not designed to model the γ fcc phase or the phase-transition).

More recently Derlet *et al.* [**111**] have used similar fitting methods to derive interatomic potential parameters for five of the non-magnetic bcc transition metals (V, Nb, Ta, Mo, and W). The parameters for the

interatomic interaction between atoms in W described by Derlet *et al.* [**111**] were used in the simulations discussed in chapters 3 and 4.

As discussed in the introduction, there is a need to develop potentials that are capable of representing the interaction between systems of particles containing more than one atomic species. The Fe-Cu potential of Ackland and Bacon [**86**], mentioned previously, is one of a number of Fe-Cu potentials. There is also the pairwise potential of Osetsky *et al.* [**112**, **113**], and the EAM-type potential of Ludwig *et al.* [**114**], which is fitted to several experimentally measured properties, including the heat-of-solution of Cu in Fe, and the binding energies of Cu atoms and vacancies in an Fe lattice [**114**]. A review and critical evaluation of the available Fe-Cu potentials was recently published by Caro *et al.* [**115**], and the reader is referred here for more information.

In [**115**], Caro *et al.* also present a new Fe-Cu potential, which includes concentration dependent interactions. This method, which proved very successful for Fe-Cu, was also applied to a potential for Fe-Cr [**116**, **117**]. This marked the beginning of renewed interest in Fe-Cr potentials, which was brought about, in part, by a desire in the fusion-community to design more advanced steels for reactor components, of which Fe and Cr will be the major constituents. Other recent Fe-Cr potentials include those of Malerba *et al.* [**118**] and Wallenius *et al.* [**119**]. Shim, Lee, and Wirth [**120**] reviewed these two sets of potentials in their 2006 paper, and discussed their limitations. They then constructed two new potentials, fitted to the extremes of binding energies between the Cr additions and Fe interstitial atoms. One was fitted to the case of positive (attractive) binding, whilst the other was fitted to the negative (repulsive) case. Various other parameters were fitted in both cases. Cascade simulations

again indicated that Cr influence was minimal in terms of defect numbers for either potential, although the percentage of mixed Fe-Cr dumbbells was increased for the 'positive' potential.

In this thesis we limit ourselves to studying only single atom systems, focussing mainly on Fe using the potentials of Mendelev *et al.* [**82**] and Dudarev and Derlet [**105**, **110**], although we do consider the other bcc metals (particularly W) using the potentials described in [**111**]. This was a decision made, in part, due to a lack of confidence in the accuracy of multi-component potentials, but primarily by a desire to fully understand the structure and behaviour of defects in pure materials, before considering more complex systems. With the improvements currently being made in Fe-Cr potentials, it should, in the future, be possible to extend the observations made in this thesis to this and other important binary alloys.

Part I

IRRADIATION INDUCED DEFECTS

3. THE STRUCTURE AND STABILITY OF VACANCY DEFECTS IN FE AND W

The recent observations of dynamic time-dependent fluctuating behaviour of mesoscopic radiation defects in bcc metals by Arakawa *et al.* [**121**, **122**], and Yao and Hernández-Mayoral *et al.* [**123**, **124**] have highlighted the need to develop adequate quantitative models for the structural stability of defects in the *mesoscopic* limit where defects are accessible to direct *in-situ* electron microscope imaging. This chapter investigates the stability, as a function of size, of various types of vacancy cluster structures, and offers explanations for the low yields of such defects in irradiation experiments of Fe and W.

The work presented in this chapter has been published in [**125**][1], [**126**][2], and [**127**][3].

3.1 Introduction

As mentioned in chapter 1, ferritic-martensitic bcc (body-centred cubic) iron-based steels and bcc tungsten and its alloys are among the main candidate materials for structural and plasma facing components of both planned experimental fusion devices such as ITER [**3**] and future deuterium-tritium fusion power plants [**8**]. During the lifetime of components Fe and W will be subject to a significant flux of neutrons, resulting in radiation damage due to knock-on cascades. This is the process in which incoming (irradiating) particles, such as neutrons, impact on the

[1] Permission to reproduce granted by Fraunhofer IRB Verlag, © 2006.
[2] © 2008 IOP Publishing Ltd. Permission to reproduce granted.
[3] © 2009 M.R. Gilbert.

atoms of a lattice, causing them to be displaced. These primary knock-on atoms (PKAs) proceed to displace other atoms, which then in turn collide with other atoms, and so on, resulting in a cascade of displacements. In the ITER experimental reactor, these cascades will typically lead to between 3 and 10 displacements per atom (dpa) during the operational life time of first wall components, with this value rising to 100-150 dpa in a commercial reactor [**6**]. In turn, these collision cascades lead to the production of point interstitial and vacancy defects that later form defect clusters, either in the core of the cascade itself, or as a result of subsequent migration and interaction [**128**, **129**]. This irradiation-induced mechanism is likely to be the main source of vacancy clusters and voids in fusion components, although it is also possible that they may be produced in structural materials as the result of stress/strain loading (see for example the work of Shabrov and Needleman [**130**]).

The accumulation of this irradiation damage can lead to a loss of material integrity, either directly as a result of localised build-up or indirectly due to the reduced ability of screw and edge dislocations to move un-impeded through a material in response to high stresses and temperatures (see chapter 5). In other words, the presence of irradiation-induced defects could be highly detrimental to the working lifetime of structural components in a fusion reactor. Therefore, there is an urgent need to understand the evolution of defects produced in bcc metals, such as Fe and W, as a result of neutron irradiation. However, such an understanding first requires knowledge of the structure and relative stability of the different types of interstitial and vacancy defects formed. In particular, the work presented in this chapter investigates the electron microscopy observation of unexpected stability of planar vacancy loops in

ion-irradiated bcc metals, as well as the corresponding low-yield of visible (in electron microscope images) loop defects in collision cascade events compared to other metals such as face-centred cubic (fcc) copper (see, for example, the work of Yao *et al.* [**123**]).

There is a significant amount of experimental work on the damage produced by heavy-ion bombardment of Fe and extensive reviews have been presented by English and Jenkins [**131**], Jenkins, Kirk and Phythian [**132**], and most recently by Jenkins, Kirk and Nicol [**133**, **134**]. For W, experimental information is less extensive but Häussermann [**135**], and Jäger and Wilkens [**136**], have investigated defects formed by irradiating this metal.

The work on defects formed by heavy-ion bombardment of Fe by Jenkins *et al.* [**133**, **134**, **137**], has recently been extended to *in-situ* electron microscope observations of time-dependent fluctuating dynamics of radiation defects in thin foils (see [**121**–**124**]). Meanwhile, Horiki *et al.* [**138**, **139**] have performed experiments explicitly with neutron irradiation. In [**123**], Yao *et al.* observed the formation of vacancy loops in heavy-ion irradiated foils of Fe and FeCr-alloy. In the work of this thesis, we specifically concentrate on the investigation of vacancy and interstitial defects in the mesoscopic limit, where a defect may contain up to several hundred individual self-interstitial atoms or vacancies and be a few nanometres in diameter, since these defects are observed in electron microscope examinations of irradiated foils [**133**]. At the end of this chapter we discuss the recent experiments of Yao *et al.* [**123**] and suggest where our results are supported by their observations.

Alongside the experimental work there have been several computational investigations of irradiation damage. In 1985, Molecular Dynamics (MD)

simulations of model fcc and bcc metals by Matthai and Bacon [**140**] were the first to demonstrate that vacancy defects could form in the thermal spikes associated with irradiation cascades, provided the concentration of vacancies was sufficiently high. The 1996 review of Diaz de la Rubia [**141**] summarises the results from this period. More than a decade after these first simulations, Soneda and Diaz de la Rubia [**142**] made a significant step in the understanding of evolution of cascades in Fe through the combined use of MD and kinetic Monte-Carlo (kMC) simulations to study the production of defects and their stability in bcc Fe, both during and after neutron-irradiation.

In particular, Soneda and Diaz de la Rubia [**142**] calculated diffusion coefficients for single vacancies and 1, 2, and 3-atom clusters of interstitials using MD (clusters of vacancies and larger groups of interstitials were considered immobile, which is not correct - as demonstrated by the work in chapter 4 of this thesis), and then fed these results into kMC simulations to study the cascade evolution of a system of such defects. They observed that single vacancies migrated significantly slower than self-interstitial atom defects. This meant that in the kMC simulations the interstitials formed clusters quickly and then began to recombine with the slower moving vacancies or migrated away from the centre of the cascade. Only when the self-interstitial atom defects became rare did the vacancies start to agglomerate into clusters [**142**]. Additionally, Soneda and Diaz de la Rubia [**142**] concluded that the $\mathbf{b} = a/2[111]$ planar self-interstitial loops were the most stable interstitial cluster configuration in Fe. They noted that spherical voids had the highest binding energy per vacancy, and therefore the lowest formation energy, of all the vacancy cluster configurations. Similar findings were reported by Beeler [**143**].

The graph originally presented here cannot be made
freely available via ORA because of copyright.
The graph was sourced from Ref. [**142**]

Fig. 3.1: Evolution of defect distribution during annealing at 600K using kMC. (reproduced from [**142**])

Figure 11 of [**142**], which is reproduced here as Figure 3.1, demonstrates the time-delay for vacancy-cluster formation. The graph shows the time evolution of defects during a kMC simulation at 600K on a $100 \times 100 \times 100$ nm^3 cube of bcc Fe ($\approx 10^8$ atoms) with a $17 \times 17 \times 17$ nm^3 initial configuration at the centre generated by a MD cascade simulation [**142**].

The graph illustrates how the number of single interstitials quickly falls as the number in clusters increases. The high mobility of the interstitials causes their number in all defect types to fall to zero after about 10^{-7} s, due to recombination and migration. This is then followed by an increase in the vacancy clusters together with the continued fall (some were lost with the interstitials) of the single vacancy numbers. Eventually the vacancies are also lost from the system, and all the defects have disappeared after about 10 seconds of simulation. Note here that there is no equilibrium

concentration of defects (*i.e.,* one that does not disappear at long times) because Soneda and Diaz de la Rubia [**142**] deleted defects from the system as they reached the boundaries.

At the same time, in the simulations of voids and vacancy clusters Soneda and Diaz de la Rubia [**142**] did not observe the collapse of a group of individual vacancies into a vacancy dislocation loop, and in the kMC simulations no evidence was found for the formation of large vacancy clusters. This was in agreement with previous studies, such as those of Bacon *et al.* [**144**] and Stoller [**145**]. However, an observation of an individual $\langle 100 \rangle$ vacancy loop forming directly in a cascade was reported in 2001 by Soneda, Ishino, and Diaz de la Rubia [**146**]. In a single displacement-cascade MD simulation in α-Fe, they observed the formation of a vacancy sphere, which then relaxed to a planar loop with a $\langle 100 \rangle$ Burgers vector. This happened in only one out of a hundred simulations, each of which were started from a 50KeV PKA, indicating that this is an event with low probability [**146**]. More recently Calder *et al.* [**147**] have simulated the formation of $\langle 100 \rangle$ vacancy loops in α-Fe and showed that the yield of defects increases with both the mass and energy of the PKA due to the heightened energy density in the cascade region.

Later, in 2003, Puigvi, Osetsky, and Serra [**148**] performed atomistic simulations of mesoscopic defects in bcc Fe. They analyzed the $\mathbf{b} = a/2\langle 111 \rangle$ interstitial loops and the so-called closed vacancy loops. This work followed earlier research by Osetsky *et al.* [**149**] on the structure and stability of vacancy and interstitial clusters in bcc Fe and fcc Cu. As in [**149**], they performed their MD calculations first using a long range pairwise potential, and then using the many-body potential (MBP) of Ackland *et al.* [**86**]. Figure 3.2 shows their formation energy results from

The graph originally presented here cannot be made
freely available via ORA because of copyright.
The graph was sourced from Ref. [**148**]

Fig. 3.2: Formation energies of vacancy (E_{vac}) and Self-Interstitial atom (SIA) (E_{SIA}) clusters simulated with a MBP. (reproduced exactly from [**148**])

the simulations performed using the MBP. Here, the formation energy is defined as the difference between the (relaxed) energy of the defect in a perfect lattice, and the energy of a perfect lattice containing the same number of atoms but no defect - see the end of this section for a mathematical explanation.

The theoretical curve shown in Figure 3.2 was derived, by the authors, via a consideration of the energy of a hexagonal dislocation loop, following a method described in Hirth and Lothe [**150**]. Notice that the two sets of simulation results seem to follow the theoretical curve quite closely, although they do diverge from one another as the cluster radius increases (see chapter 4 for further discussion of this). We consider this graph further in the next chapter (section 4.2) where we compare the results from our interstitial- and vacancy-loop formation-energy simulations.

More recently, in 2006, Kulikov, Malerba, and Hou [**151**] reported

calculations of vacancy cluster formation and binding energies for Fe-Cu alloys. They also considered the energies of Cu clusters, and those of clusters composed of a mixture of Cu atoms and vacancies. The formation energy curves they produced for vacancy clusters were similar to those for pure Fe. However, they also found that the Cu atoms tended to coat an inner cluster of vacancies. These results, they suggest, are consistent with experimental observations [**151**].

The above literature review demonstrates that a significant volume of simulation work has been performed to develop understanding of irradiation damage in Fe. However, there is still a need to relate firmly simulations with experiment, and in particular to explain why some defect types are seen while others are not. Conversely, there has been no significant advances in the understanding of defects produced in irradiated W, from either experiment or simulation, and so the need for work on this material is obvious. By performing identical simulations on both Fe and W we hope to infer behaviour in W based on the evidence in Fe.

Definition of the formation energy of defects

The formation energy E_{D}^{f} of a defect configuration is defined as the difference between the minimum energy evaluated for a simulation cell containing the defect, and the energy of a perfect lattice containing the same number of atoms but no defect. In other words, if a perfect lattice contains n atoms and we remove (or add) x atoms to create a defect, then the energy to which this is compared is that of a perfect lattice of $n - x$ (or $n + x$) atoms. Mathematically we have:

$$E_{\mathrm{D}}^{f} = E_{\mathrm{L+D}}^{r}(n) - E_{\mathrm{p}}^{r}(n), \tag{3.1}$$

where $E^r_{\mathrm{L+D}}(n)$ is the energy of a lattice L of n atoms containing the defect D and $E^r_{\mathrm{p}}(n)$ is the energy of a perfect lattice of n atoms. For the case of a Bravais lattice (*i.e.,* a lattice in which unit cells make up an infinitely repeating 3D crystal [**97**]) $E^r_{\mathrm{p}}(n)$ is equal to nE^r_{atom}, which is n times the energy of a single atom in a lattice (the cohesive energy). Here the minimum energy values are defined as the energy of the system at zero Kelvin [**126**]. In the simulations carried out here, the cohesive energy of Fe for the Dudarev-Derlet (D-D) [**105**] magnetic potential is -4.316 eV per atom, whilst for the Fe potential of Mendelev *et al.* [**82**] it is -4.122 eV per atom. For W, the cohesive energy per atom is -8.90 eV, as defined by the potential of Derlet *et al.* [**111**]. Throughout this chapter we imply the defect formation energy whenever we refer to the energy of a defect.

3.2 Vacancy defects in bcc Fe

The recent experiments of Yao *et al.* [**123**] have confirmed the previous observations that vacancy loops form in Fe during the collapse of the cascades produced by irradiation, whilst there is anecdotal evidence from the older work of Häussermann [**135**] that similar phenomena are also observed in W. In the following sections, we evaluate the formation energies of the mesoscopic circular $\mathbf{b} = (a/2)\langle 111\rangle$ and $\mathbf{b} = a\langle 100\rangle$ vacancy loops that are observed in ion-irradiation experiments. As was noted in 1967 by Johnson [**152**] for nickel, there is an issue as to the stability of vacancy dislocation loops relative to other types of vacancy cluster. To investigate this for Fe and W, we compare the energy of these closed (collapsed) vacancy dislocation loop with the energies of spherical voids and open loops (planar voids) containing the same number of single vacancy defects. For completeness we also consider the energies of equivalent interstitial

dislocation loops.

The formation energies are calculated by using MS simulations to relax lattices with periodic boundary conditions (PBCs). As discussed in chapter 2, MS is the energy minimisation form of molecular dynamics and involves forcing the kinetic energy of the system to decrease, thereby causing the atoms to 'relax' to a 'frozen' zero-temperature configuration. Each simulation was performed under constant pressure conditions using the Parrinello-Rahman (PR) [**54**] equations of motion (see section 2.1.4). However, a slight modification to this formulation was made, whereby the system has an orthorhombic geometry that allows the lattice to expand and contract in each of the three coordinate directions but not in other directions. In the case of the $\langle 111 \rangle$ defects this meant the $[1\bar{1}0], [11\bar{2}],$ and $[111]$ coordinate axis directions, while for the $\langle 100 \rangle$ loop the box was allowed to expand in the normal Cartesian directions (see Appendix A for more details of the crystallography). The result of this process was a simulation cell that could change its volume, perhaps in order to accommodate extra atoms, but would always remain cubic. Such a set-up is equivalent to time evolution using the equations of motion of Andersen [**64**], from which the PR equations are derived.

3.2.1 $\frac{1}{2}\langle 111 \rangle$ *Vacancy loops at 0K*

Constructing the initial configurations of vacancy dislocation loops for atomistic simulations is known to present a non-trivial problem when using short-ranged interatomic potentials, as we have in the present studies. The only practical solution found so far was the method employed by Puigvi *et al.* [**148**] (see section 3.1), which involved switching between a long-range and a short-range interatomic potential. In our case, to construct open

vacancy loops, circular discs of atoms of a given radius were removed from three consecutive (111) ABC planes for $\frac{1}{2}\langle 111\rangle$ loops and two consecutive (001) AB planes for $\langle 001\rangle$ loops (see Appendix A for more details).

One might suppose that such open loops (or planar voids) would transform, upon relaxing, into the ring-like structure of the closed loop seen experimentally [**123**, **135**]. However, the short-ranged nature of the interatomic potentials used here prevented this from happening, because the opposing surfaces of the *open* loop did not 'feel' each other. To overcome this problem and construct a *closed* vacancy loop, planes of atoms *outside* the loop radius (*i.e.,* in the bulk) were appropriately *added* to the initial bcc lattice at the mid-way points between the (111) or (001) planes. When these configurations were relaxed, the extra planes in the bulk expanded to a perfect lattice configuration, and a prismatic closed vacancy dislocation loop was created. This procedure did not require the sub-relaxations and sequential applications of long- and short-range interatomic potentials as described in [**148**], but did produce the desired closed vacancy dislocation loop. Figure 3.3 demonstrates how the two different kinds of vacancy loop were created.

A spherical void was created by removing a sphere of atoms of a given radius. Like planar voids, they are not easily observed experimentally due to a lack of the strong elastic strain fields needed for the formation of images in conventional diffraction electron microscopy. We did not consider the possibility of faceting in the voids as this would only have a small effect on the energy of defects. Finally, interstitial loops were created using the opposite or 'negative' of the procedure used to produce closed vacancy loops, *i.e.,* an extra layer of atoms were inserted as a disc of the required radius.

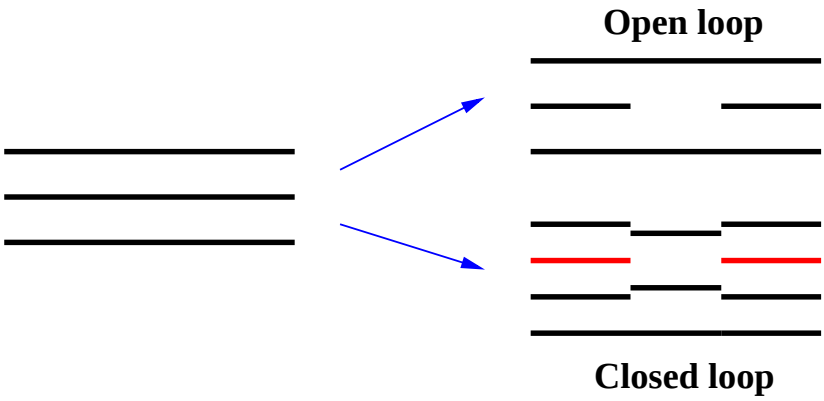


Fig. 3.3: Loop construction methods: Open loops created by removing a disc of atoms from a perfect lattice; Closed loops created by inserting atoms (the red layer) outside of the disc radius. The Burgers vector is the vertical direction in these diagrams.

For calculations of the $\frac{1}{2}\langle 111\rangle$ loop and spherical void energies with the Dudarev-Derlet [**105**] potential for Fe we used an approximately cubic base lattice consisting of 48,000 atoms. In validation simulations to confirm that this lattice size was sufficient we investigated the formation energy of defects in a range of cubic cell-sizes, with the number of atoms ranging up to 400000. The MS relaxations showed that there was less than a 1% difference in the defect energies for simulation cells containing more than around 30,000 atoms up to the maximum size considered.

Figure 3.4 shows the results of this validation exercise for the largest $\frac{1}{2}\langle 111\rangle$ defects considered in Fe. For the loop defects, this corresponded to a defect containing 121 vacancies or Self-Interstitial atoms (SIAs), which is the number of point defects associated with a loop centred on a lattice site with a diameter of about 2.7 nm, and for the spherical voids the maximum cluster considered had 137 vacancies. The graph in Figure 3.4 shows that the formation energy of the defects is only affected for very small lattice sizes, and even then it is only the closed vacancy and interstitial loops, with

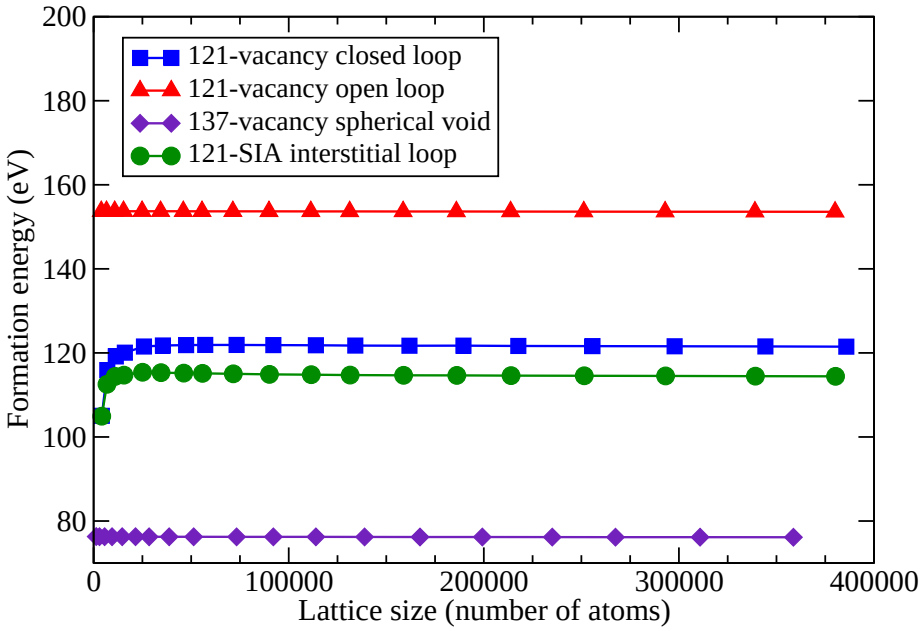


Fig. 3.4: Formation energy of 121-vacancy or -SIA loops and 137-vacancy voids as a function of the number of atoms in the periodic simulation cell.

their large elastic strain fields, that show any noticeable change.

These simulations also imply that image forces associated with the boundary conditions cancel out once the lattice is sufficiently large (compared to the size of the loop). The periodic boundary conditions (PBCs) used in the simulations essentially create an infinitely repeating sequence of cubes, each containing a single defect. This means that the defect 'sees' images of itself through the PBCs in all directions and therefore experiences a force that is similar to the one that would be produced by close proximity to a free surface, for example in a thin foil. However, in our case, the loop experiences equal and opposite forces in each coordinate direction. As long as the elastic fields of a defect and its images do not interact significantly, these forces should cancel each other out. The validation simulations demonstrate that this happens in our simulations, using a 48,000-atom lattice.

A lattice containing around 30,000 atoms is roughly $7 \times 7 \times 7$ nm^3 in size, which means that a loop defect is around 7 nm away from itself in the [111] direction (the only defects for which image forces are significant are the closed vacancy and interstitial loops with their relatively long-range elastic fields, but these primarily extend in the [111] direction). This shows that our simulations apply to systems where the defect density is relatively low (*i.e.,* the defects do not generally come into close contact with each other), and also in which surfaces do not play a significant role.

For the D-D potential, Figure 3.5 shows the defect energy as a function of defect size, measured in terms of the number of vacancies/interstitials, for all open and closed $\frac{1}{2}\langle 111\rangle$ vacancy loops, spherical voids and $\frac{1}{2}\langle 111\rangle$ interstitial loops. Here the lines represent continuous interpolations between the discrete data points found using atomistic simulations. More specifically, in this graph, and in the other formation energy versus size graphs presented in this chapter (unless otherwise stated), we have fitted the data points for each curve to a polynomial of degree four (which was found to produce the *best* fits) using the regression fitting functions of the **Grace** graph-plotting program [**153**]. We do not attribute any significance to the form of these fits; they are merely a visual guide to the trends in the data.

The graph in Figure 3.5 shows that spherical voids represent the lowest energy configuration for a cluster of vacancies of any size. This agrees with the findings of Soneda and Diaz de la Rubia [**142**], and Beeler [**143**]. We see that there is an intersection between the formation energy curves for the open and closed vacancy loops. This intersection can also be seen if the loop energies are plotted as a function of defect diameter, as shown in Figure 3.6 (displaying spherical voids on such a graph is meaningless as

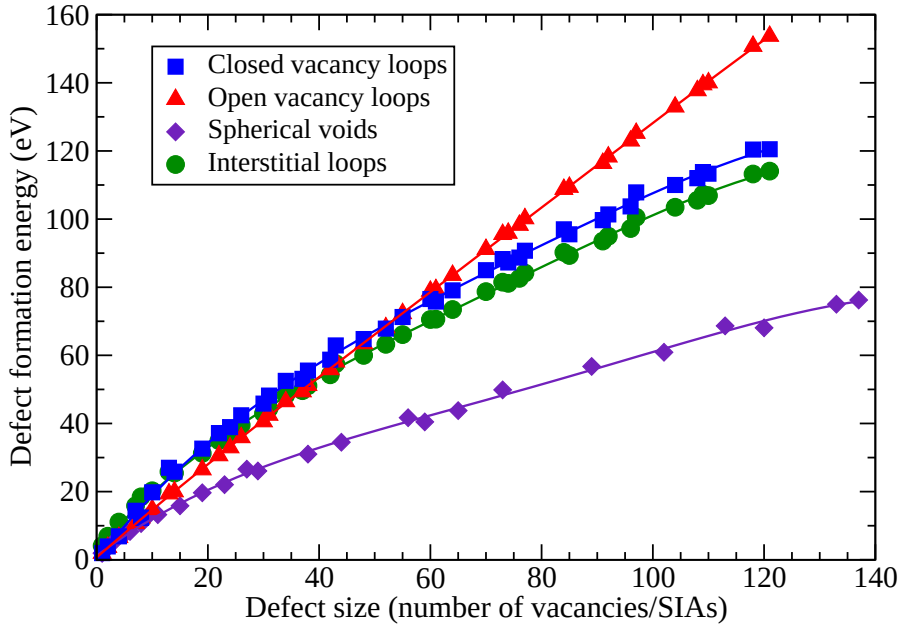


Fig. 3.5: Variation in formation energy of spherical voids and various $\frac{1}{2}\langle 111\rangle$ loop defects in Fe under the Dudarev-Derlet [**105**] magnetic potential. Plotted as a function of defect size (number of SIAs/vacancies). The lines represent continuous interpolations between the discrete data points found using atomistic simulations.

they have a completely different shape). To calculate the diameter d of a loop we have made use of the following approximate formula

$$d = 2\sqrt{\frac{A_{atom}N}{\pi}}, \tag{3.2}$$

where N is the number of vacancies or SIAs in the loop. It approximates the total area occupied by a circular loop in the (111) plane as the sum of the areas of the vacancy (or interstitial) sites that make up the loop. A_{atom} is the area occupied by each lattice site in the (111) plane. From Appendix A.1, we calculate A_{atom} as 4.744 Å^2, where 1 Å$= 1 \times 10^{-10}$ m.

The cross-over from positive to negative differences between the energies of an open and a closed loop occurs near the 17.7 Å loop diameter, or a

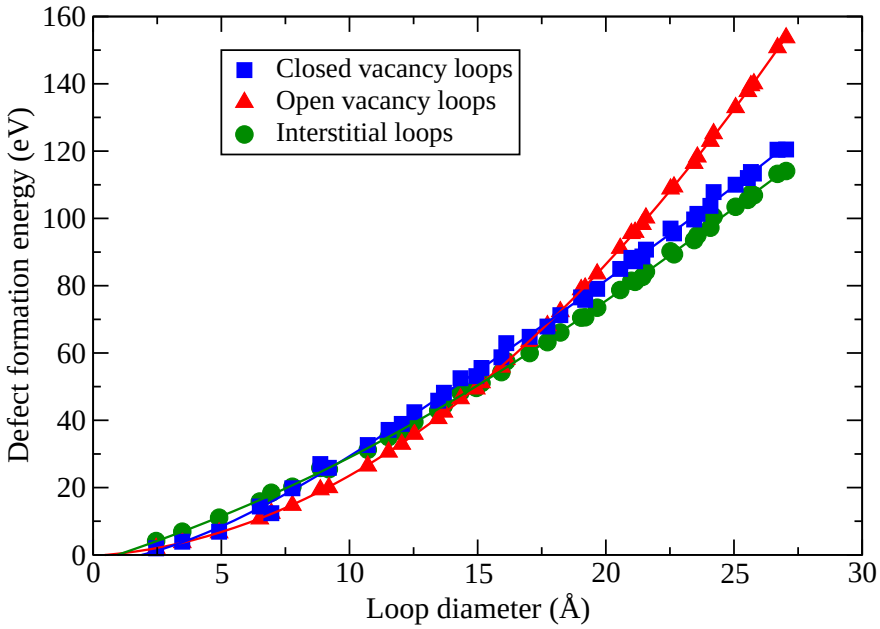


Fig. 3.6: Variation in formation energy of various $\frac{1}{2}\langle 111\rangle$ loop defects in Fe under the Dudarev-Derlet [**105**] magnetic potential. Plotted as a function of loop diameter.

52-vacancy defect, where the closed loop structure becomes energetically more favourable. Below this size, an open vacancy loop configuration has lower formation energy. To see this more clearly, in Figure 3.7, we plot the difference between the formation energies for an open and a closed loop as a function of the loop diameter. For diameters below 5 Å, it is effectively impossible to form a closed vacancy loop, as an attempt to form it in a simulation immediately results in the loop opening-up, even at 0K. For loop diameters between 5 Å and 17.7 Å a closed loop is inherently metastable with respect to relaxation into an open loop configuration. This uncertainty was one of the reasons for the complete investigation of energies versus size presented here. When relaxing closed loops with diameters less than around 7 Å we noticed that some actually opened up during the MS simulation.

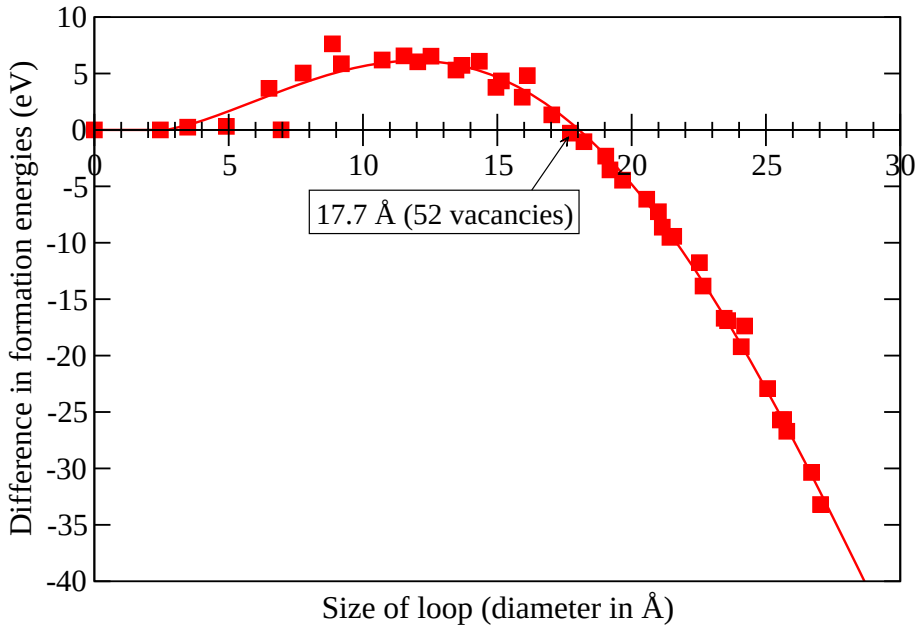


Fig. 3.7: Difference between formation energies of closed and open $\frac{1}{2}\langle 111\rangle$ vacancy loops in Fe as a function of diameter (D-D potential).

3.2.2 Transformation at finite temperature

We have confirmed that at finite temperature T a closed vacancy loop of sub-critical size (diameter less than ∼17.7 Å) readily transforms into an open vacancy loop, and then into a spherical void, using finite temperature MD simulations. After inserting and relaxing a 26-vacancy closed $\frac{1}{2}\langle 111\rangle$ loop in a perfect bcc Fe lattice of 15360 atoms (about 200 nm^3 in volume, which was sufficient for this size of loop) we performed a series of MD simulations at various 100K temperature intervals. In each run, the temperature was maintained by scaling the velocities, as required, every few time-steps. The scaling factor is determined using the following equipartition formula relating the instantaneous total kinetic energy $K(t)$

of a system of N particles to the instantaneous system temperature

$$K(t) = \frac{3}{2} N k_B T(t), \tag{3.3}$$

where k_B is Boltzmann's constant [**25**]. $K(t)$ is defined as

$$K(t) = \sum_{i=1}^{N} m_i \mathbf{v}_i^2, \tag{3.4}$$

where $\mathbf{v}_i$ and m_i are, respectively, the velocity and mass of particle i. A new temperature T^* is applied by scaling all velocities by $\sqrt{T^*/T}$, where T is the original temperature of the system.

The system was integrated in time at each temperature for 1 ns, and then 'quenched' to 0K using a MS run. The formation energy of the current defect (or defects) was then calculated. Note that the temperature was 'ramped-up' to the higher temperatures in increments of 100K, with a brief (a few picoseconds) equilibration at each stage before increasing the temperature again. This avoided the violent response (*i.e.,* defect obliteration) that would have been produced if the temperature was suddenly increased by a large amount. Figure 3.8 shows the results from these simulations. The graph also shows the results for a sequence of temperature runs performed on a 26-vacancy open $\frac{1}{2}\langle 111 \rangle$ loop.

In Figure 3.8 we see that the defect-energy changes with temperature. In both sets of simulations the initial energy is that of the relaxed defect at 0K, which is 42.5 eV for the 26-vacancy closed loop and 35.9 eV for the equivalent open loop (as shown in Figure 3.5). As the temperature increases, both defects begin to transform into spherical voids, which is reflected in the graph by a decrease in the defect-energy. At around 1000K the energy reaches a minimum of about 25 eV, which agrees well with the

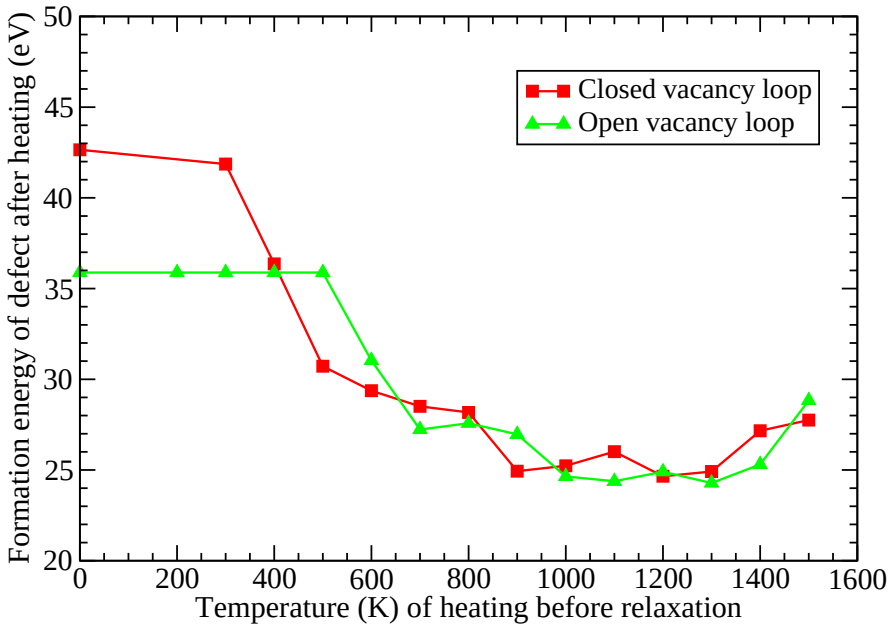
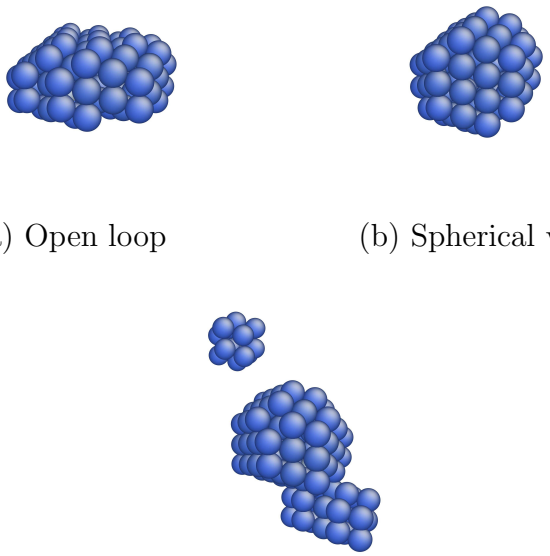


Fig. 3.8: Heating of 26-vacancy closed and open loops: Final energy of remaining defect(s) after 1 ns heating at each temperature. Change in energy indicates a transformation in the defect structure.

formation energy results for spherical voids shown in Figure 3.5. Figure 3.9 shows the different structural stages that the defects go through during these simulations.

In Figure 3.9a we have the initial 26-vacancy open loop configuration of the second set of simulations. This configuration was attained in the closed loop simulation during the heating at 400K. Figure 3.9b represents the final spherical void configuration that both runs attained at 1000K, while Figure 3.9c shows the beginning of the 'evaporation' of the defect at 1500K. Here the simulations were stopped because the temperature was high enough to cause single vacancies to break-off from the void, which led to the slight increase in defect energy seen in Figure 3.8. Note that, whilst the transformations only began in the $T = 400 - 500$K range during these 1 ns simulations, the transformation would also be expected to occur at lower



(a) Open loop (b) Spherical void

(c) 'Evaporating'

Fig. 3.9: The temperature-driven configurational changes of a cluster of 26 vacancies in Fe, originally arranged as either a closed or open loop. Only atoms around the vacancy defects are shown. Bulk atoms are invisible. At 400K the closed loop becomes 'open'. The spherical void is formed by 1000K, while the evaporation begins at 1500K.

temperatures, albeit on much longer timescales. This fact also justifies simulating at temperatures above the $\alpha - \gamma$ phase transition for Fe (around 1200K). The potential of Dudarev and Derlet [**105**] does not reproduce this transition (it is not designed to model the fcc phase) and therefore maintains the bcc structure up to higher temperatures. Hence it is possible to simulate at higher temperatures and reduce the time taken for transformations to occur, even though they would still happen at lower temperatures.

A remaining question from these simulations is; by what mechanism did the transformations take place? It is clear that a sub-critical closed vacancy loop can easily become an open loop - atoms simply have to move apart

slightly to create the space - but it is less clear how a spherical void is formed from this configuration. However, on a few occasions we have observed single vacancies that had moved (diffused) from their original location on the loop's surface to an alternative position. This indicates that the conversion into a spherical void occurs *via* the diffusion of single vacancies across the internal surfaces of the open loop. Since it is reasonable to expect this to happen at lower temperatures, but with reduced frequency, on the timescales associated with real experiments (typically seconds or longer), sub-critical closed loops would readily transform into open loops and then into voids, even at low temperatures, and certainly at room temperature.

On the other hand, the closed vacancy loops of super-critical size (diameter greater than ~ 17.7 Å), which could be created during cascade collapse in regions of high vacancy density (perhaps as a result of cascade overlap [**123**]), can also eventually transform into voids, but the mechanism of transformation is now entirely different. We repeated the finite temperature simulations, this time for a 61-vacancy super-critical closed loop and discovered that no change in the structure or energy of the loops occurred on the 1 ns timescale below 1200 K. However, at higher temperatures we began to see the evaporation of single vacancies from the main defect. This is the same phenomenon we observed above for the minimum-energy spherical voids in the simulations of sub-critical loops. Figure 3.10 shows the formation energies as a function of temperatures for the super-critical closed loop.

It therefore appears that these metastable loops shrink *via* the evaporation of individual vacancies. These free vacancies are then left to diffuse in the material and then to perhaps coalesce, forming stable voids,

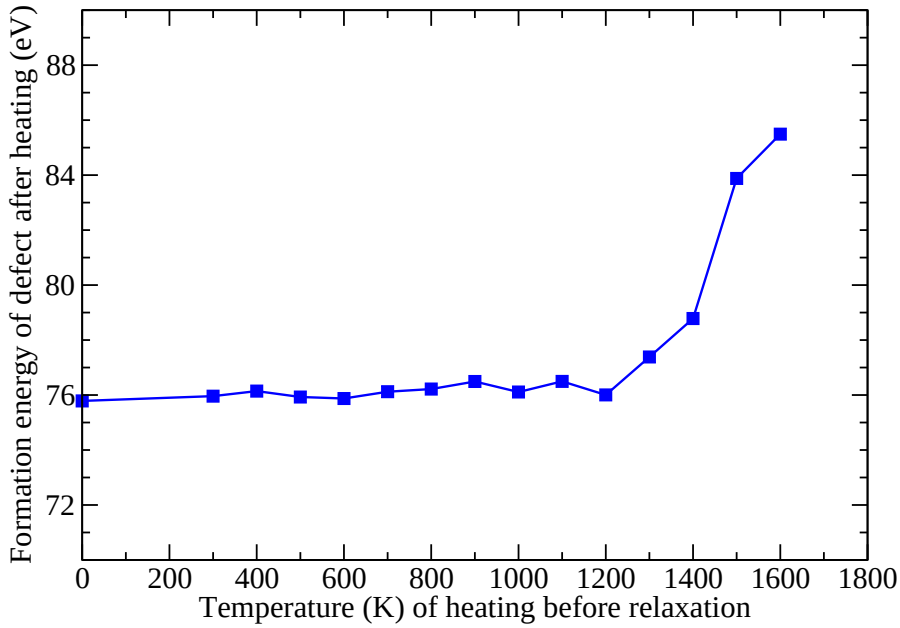


Fig. 3.10: 61-vacancy closed dislocation loop heating: variation in formation energy as a function of heating temperature before relaxation. The formation energy, and hence the defect, remained stable almost up to the melting temperature.

which then grow further by the agglomeration of vacancies. Once the loop has shrunk to a size in the sub-critical size region it would quickly transform into a void via the mechanism described previously, and could then grow by absorbing any surrounding vacancy-cluster debris that may have originally evaporated from it. It seems unlikely that super-critical loops can transform directly into spherical voids, even at high temperatures, because the transformation pathway is not straightforward. At elevated temperatures the evaporation of vacancies would occur readily and would most likely be favoured over and above more complex processes.

3.2.3 Origin of the energy differences

Before considering why there is subtle interplay between the energies, and therefore stability, of these different kinds of vacancy-cluster defect, it is important to check that the observed effect is not an artefact of the particular interatomic potential used. Recently, Björkas and Nordlund [**154**] simulated recoil collision cascades in Fe using the D-D and Mendelev [**82**] potentials and found that the Frenkel pair production was roughly the same under both, even though they are derived from different fitting parameters. This suggests that the Mendelev potential would produce a similar set of curves as those found for the D-D potential.

We have tested this hypothesis by repeating the same molecular relaxations on $\frac{1}{2}\langle 111\rangle$ defects (as well as on spherical voids) using the potential of Mendelev *et al.* [**82**]. The results are shown in Figure 3.11. The pattern is essentially the same as that seen in results from the D-D potential, although the sub-critical region for collapsed vacancy loops is now smaller, with the intersection of the collapsed and open vacancy loops curves happening in the $20 \rightarrow 30$ vacancies ($\sim 10.5 \rightarrow 13.5$ Å diameter) region. The main reason for this appears to be the extended range of the Mendelev potential (5.3 Å versus 4.1 Å for the D-D potential [**105**]), which causes the opposing surfaces of an open loop or planar void to influence each other. This increases the relative energy of open loops when compared to their equivalent collapsed loops, leading to an earlier onset of stability cross-over.

Additionally, Osetsky *et al.* [**155**] noted that small (less than 60 vacancies in size) perfect vacancy dislocation loops were unstable under the many-body potentials of Ackland *et al.* [**86**, **104**], suggesting that our findings would also be repeated in a complete study of other Fe potentials.

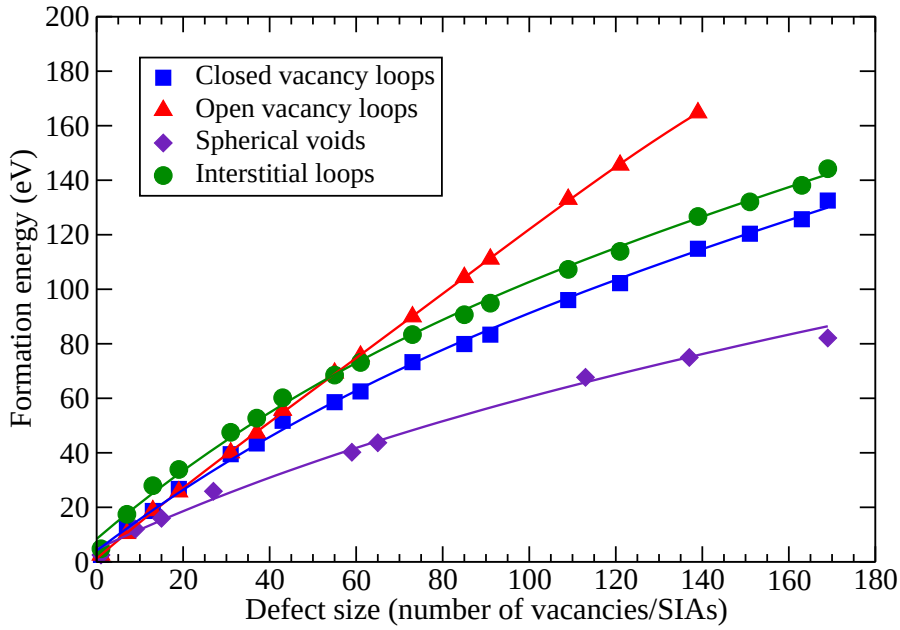


Fig. 3.11: Variation in formation energy, as predicted by the Mendelev [**82**] potential, of spherical voids and various $\frac{1}{2}\langle 111\rangle$ loop defects in Fe. Plotted as a function of defect size.

This, together with Figure 3.11 demonstrates that our observations are not artefacts of a particular interatomic potential, and so there must be another explanation for the fundamental difference between the energies of voids, closed and open vacancy loops.

The formation energy of a void containing N vacancies to a very good approximation [**126**] equals its internal surface energy

$$E_{void} = 4\pi \left(\frac{3N\Omega_0}{4\pi}\right)^{2/3} \overline{W}, \tag{3.5}$$

where $\overline{W}$ is the average (over the low-energy orientations of surface facets) surface energy, which according to calculations by Van Zwol *et al.* [**156**] is of the order of 1.7 Jm^{-2} for the D-D potential. $\Omega_0 = a^3/2 = 11.77$ Å^3 is the formation volume of a vacancy in Fe (see Appendix A), where $a = 2.8664$ Å

is the lattice constant for the D-D potential [**105**]. For example, the formation energy of a 102-vacancy void estimated using equation (3.5) is 58.0 eV, using 1 eV = $1.60217646 \times 10^{-19}$J and converting to the correct distance units. This is in good agreement with our simulations where the energy of a 102-vacancy void was found to be 60.9 eV using the D-D potential.

Similarly, the formation energy of an open $\frac{1}{2}\langle 111\rangle$ loop is given by the sum of energies of the two free surfaces plus a contribution from the perimeter:

$$E_{open} = 2\frac{a^2}{\sqrt{3}}NW_{111} + E_{perimeter}, \tag{3.6}$$

where $a^2/\sqrt{3}$ is the surface area corresponding to a single vacancy (see Appendix A.1), and $W_{111} = 2$ Jm^{-2} is the surface energy for the (111) surface termination from [**156**]. The first term in equation (3.6) gives the formation energy $E_{open} = 123.5$ eV for a $N = 104$-vacancy loop compared with 132.9 eV found in our D-D potential simulations. The second term in (3.6), describing the contribution to the formation energy from the perimeter of the loop, is relatively small, and, in the case of a $\frac{1}{2}\langle 111\rangle$ loop, the energy per unit length of the perimeter of the loop (*i.e.,* energy difference between theoretical surface energies and total energy from simulation), averaged over all the loops simulated, is 0.125 eVÅ^{-1}.

The formation energy of a closed dislocation loop is given by the sum of the energy stored in the elastic field loop and the core energy of the dislocation forming the perimeter of the loop [**157**]. Dudarev, Bullough, and Derlet [**158**] derive an approximate expression for the formation energy of a dislocation loop based on the *anisotropic* elasticity approximation, which must be used for iron since the material is strongly elastically anisotropic,

even at low temperatures. From [**158**], the energy of a closed loop is

$$E_{closed} \approx 2\pi R^* \left[\frac{K\mathbf{b}^2}{4\pi} \ln\left(\frac{4R^*}{e\delta}\right) + F_\delta + F_c \right], \tag{3.7}$$

where for the case of a $\frac{1}{2}\langle 111\rangle$ loop the pre-logarithmic $K\mathbf{b}^2/4\pi \approx 0.39$ eVÅ^{-1}, $F_\delta \approx 0.35$ eVÅ^{-1} is the zero-temperature core-traction energy, and $F_c \approx 0.47$ eVÅ^{-1} is the zero-temperature anharmonic core energy. Dudarev *et al.* [**158**] assume a hexagonal shape for the loop when calculating the value of K, but in the above formula R^* is the effective radius of an equivalent circular loop. δ is the characteristic cut-off radius for the dislocation core, which was estimated in [**158**] to be 4 Å. For a 104-vacancy loop, equation (3.7) gives a formation energy of $E_{closed} = 109.1$ eV compared with a value of 110 eV found from simulation (D-D potential), which is a very good agreement.

The accuracy of our data compared to the theoretical values can be seen more clearly in a graphical format. Figure 3.12 reproduces the vacancy-cluster formation energies for $\frac{1}{2}\langle 111\rangle$ from Figure 3.5. The graph also plots the theoretical curves (as dashed lines) for the three cluster types, as prescribed by equations (3.5), (3.6), and (3.7). We can see that there is excellent agreement in the case of closed vacancy loops, and the spherical void data points are also very close to the theoretical curve. The theoretical curve for the open vacancy loops is systematically below the simulation data, reflecting the fact that the perimeter contribution in equation (3.6) has been omitted, although there is excellent agreement in the shape of the curves. In fact, if we add the average 0.125 eVÅ^{-1} perimeter energy to the theoretical curve then it sits perfectly on the simulation data and crosses the theoretical curve for closed loops at approximately the same cross-over point seen in the simulation data.

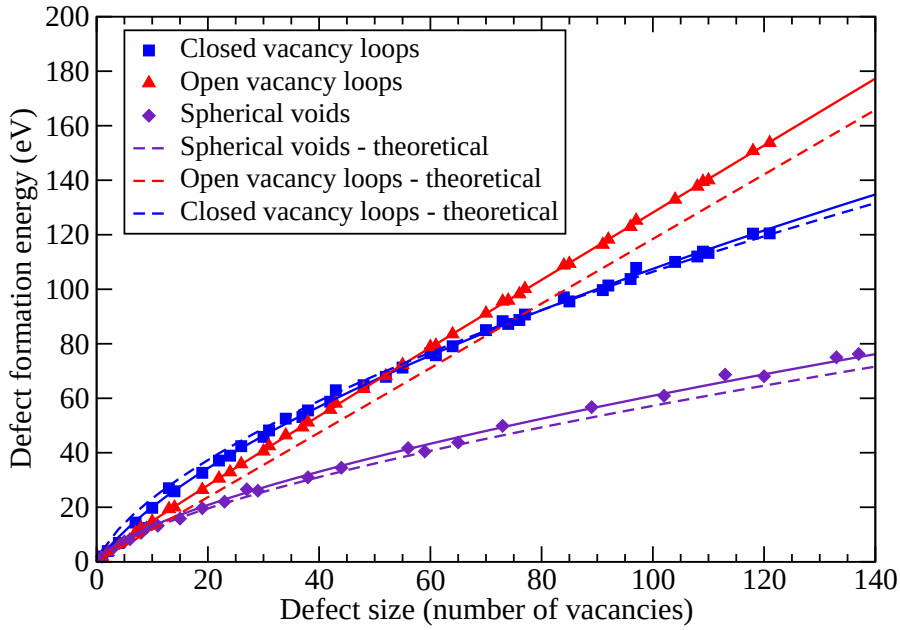


Fig. 3.12: Theoretical curves for the formation energy of $\frac{1}{2}\langle 111\rangle$ loops and spherical voids in Fe. Also shown are the simulation data from Figure 3.5, as well as improved fits (see text) to the data (solid lines).

Also shown in Figure 3.12, are improved fits (solid lines) to the simulation data. Rather than the 4th degree polynomial fits used elsewhere in this chapter (e.g. in Figure 3.5), in Figure 3.12 functions based on the theoretical equations have been used. Specifically, the functions used are:

$$\begin{aligned} E_{closed} &= A\sqrt{N}(\ln(\sqrt{N}) + B), \text{ since } R^* \propto \sqrt{N}, \\ E_{open} &= P\sqrt{N} + QN, \\ E_{void} &= CN^{\frac{2}{3}}, \qquad \text{and} \\ E_{interstitial} &= D\sqrt{N}(\ln(\sqrt{N}) + G), \end{aligned} \tag{3.8}$$

where the form of the function for $E_{interstitial}$, which is not shown in Figure 3.12, was selected based on the assumption of similarity to closed vacancy loops, as illustrated by the strain analysis in section 4.2.

A, B, P, Q, C, D, and G are all constants determined by fitting to the data (using **Grace** [**153**] and **GNUPLOT** [**159**]). For E_{closed}, $A = 3.82081$ and $B = 0.510356$; $P = 0.973519$ and $Q = 1.18403$ for open loops; for spherical voids $C = 2.82613$; and the interstitial loop parameters are $D = 3.3072$ and $G = 0.727151$.

Note that here we can now consider the accuracy of our earlier approximation for the average surface energy in a spherical vacancy void. In equation (3.5), we considered $\overline{W}$ to be the average surface energy over the low-energy orientations, calculated to be 1.7 Jm^{-2} by Van Zwol *et al.* [**156**], without determining whether this was a reasonable approximation, especially given the small size of the defects considered. The fitting constant C in equations (3.8) can be used to determine $\overline{W}$ explicitly from our simulations via:

$$\overline{W} = \frac{C}{4\pi}\left(\frac{3\Omega_0}{4\pi}\right)^{-2/3}. \tag{3.9}$$

Using this equation we find $\overline{W} = 1.81$ Jm^{-2}, which is in reasonable agreement with the value used previously, and so the approximation used was quite valid.

These new fits to the simulation data now allow us to calculate the vacancy (and SIA) binding energy as a continuous function of cluster size. From [**142**], the binding energy of a cluster is defined as:

$$E^b_\alpha = E^f_\alpha(N-1) + E^f_\alpha(1) - E^f_\alpha(N), \tag{3.10}$$

where α is either V (vacancy) or I (interstitial), and $E^f(N)$ is the formation energy of a defect of size N. Equations (3.8) have been used here to calculate the binding energies for the three $\frac{1}{2}\langle 111\rangle$ loop types in Fe

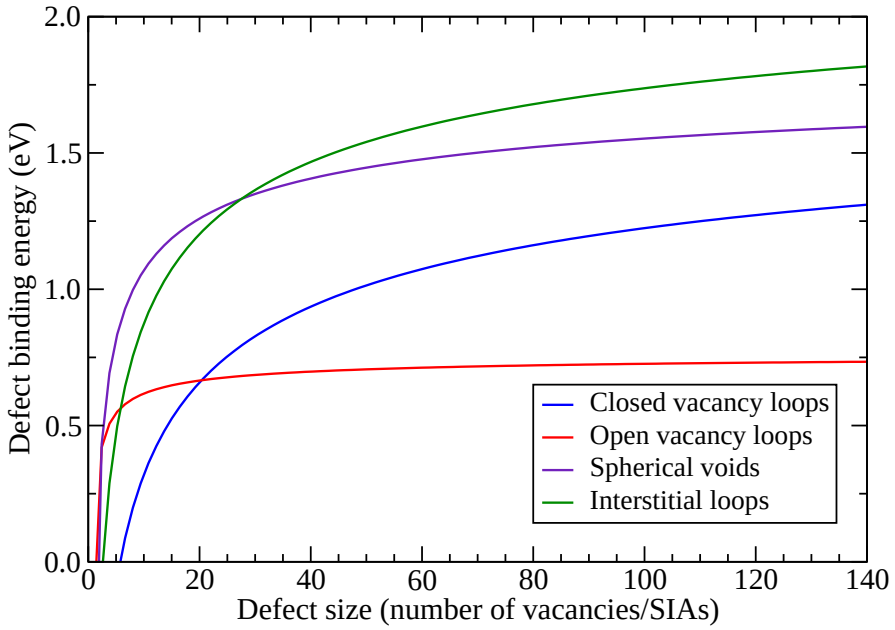


Fig. 3.13: The binding energy of $\frac{1}{2}\langle 111\rangle$ loop defects and spherical voids as a function of size. Calculated using equations (3.8) and (3.10).

(under the D-D potential), as well as for spherical voids. Figure 3.13 shows these results. The binding energies shown in the graph are in good agreement with the previous results of Puigvi *et al.* [**148**] and Soneda and Diaz De La Rubia [**142**].

Note that here we have assumed that the binding energy is a continuous smooth function of cluster size. In reality, for a circular loop or spherical void of size N there does not necessarily exist an equivalent circular or spherical defect of size $N-1$. For example, a vacancy or interstitial loop containing 19 point defects is regular and approximately circular. However, the next circular defect size (assuming that an atom sits at the centre of the circle) contains only 13 vacancies or interstitials. This can be seen clearly in Figure 6.2, by comparing the number of atoms (strings) contained within the U_3 and U_2 circles (see chapter 6 for more details). Thus a 'loop' containing 18 vacancies or interstitials is likely to be an energetically

unfavourable configuration. This would mean that the binding energy, as defined by equation (3.10), of a $N = 19$ loop would actually be higher than the values given by the three loop-curves in Figure 3.13. Therefore, the real variation in binding energy with N would show significantly more scatter than that suggested by the smooth curves. At the same time, the graph does present the general trend in the binding energy for a given defect types, and demonstrates the lower binding energy of vacancy clusters compared to interstitial loops, which means that they would be less stable at higher temperatures [**142**].

Finally in this section, from the theoretical equations we can now understand the fundamental differences between the energies of the different vacancy loop types. Considering equations (3.7) and (3.8), we see that the diameter of a closed loop is proportional to the square root of the number of vacancies N, and in the mesoscopic limit $E_{closed} \sim \sqrt{N}\ln(\sqrt{N})$. Conversely $E_{open} \sim N$ in equations (3.6) and (3.8), and hence for relatively small N the formation energy of an open loop is lower than the formation energy of a closed loop.

3.2.4 $\langle 001 \rangle$ *Vacancy loops*

We have repeated the analysis of formation energies for the $\langle 001 \rangle$ loops. We have only considered the D-D potential for Fe, since the comparison discussed previously indicates that the Mendelev potential produces similar results. Results are summarised in Figure 3.14, where data for spherical voids are included for comparison. The lattice sizes used range from 85,000 to 120,000 atoms. As in the $\frac{1}{2}\langle 111 \rangle$ loop case, the energies of the $\langle 001 \rangle$ vacancy loops are significantly higher than those of similarly sized spherical voids. However, the cross-over point between the energies of the open and

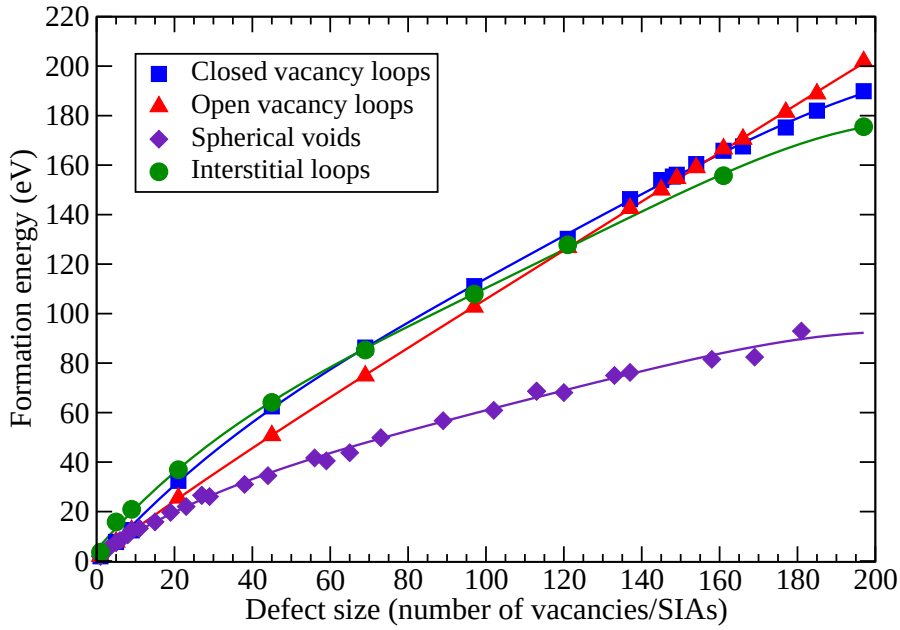


Fig. 3.14: Variation in formation energy of ⟨001⟩ mesoscopic vacancy and interstitial dislocation loops, and spherical voids in Fe plotted as a function of the number of individual defects forming the loop or a void (D-D potential).

closed loops is higher than for the $\frac{1}{2}\langle 111\rangle$ case. For loops containing fewer than about 150 vacancies (approximately 28 Å in diameter) the open loop configuration is more stable than the closed one. This cross-over is easier to see, as before, by plotting the difference between the energy of the two vacancy-loop types as a function of loop diameter - see Figure 3.15.

Again, the formation energy of an open ⟨100⟩ loop is the sum of energies of the two free surfaces

$$E_{open} = 2\frac{a^2}{2}NW_{100} + E_{perimeter}, \tag{3.11}$$

where $a^2/2$ is the surface area corresponding to a single vacancy (see Appendix A), and $W_{100} = 1.8$ Jm^{-2} is the surface energy for the (100) surface calculated for the D-D potential in [**156**]. The first term in

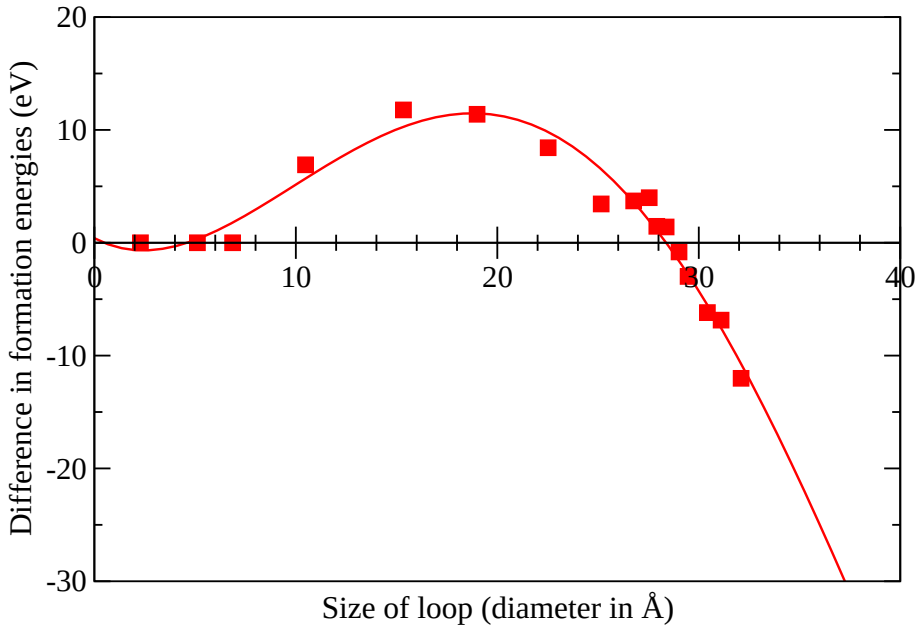


Fig. 3.15: Difference between formation energies of closed and open ⟨001⟩ vacancy loops in Fe as a function of diameter (D-D potential). The switch from positive to negative difference occurs at around the 28 Å diameter loop-size.

equation (3.11) gives $E_{open} = 89.5$ eV for a $N = 97$ vacancy loop compared with 102.7 eV found in simulations. This shows that in the case of a ⟨001⟩ vacancy loop the contribution of the perimeter term is larger than in the $\frac{1}{2}\langle 111\rangle$ open vacancy loop case, and the average energy per unit perimeter length across all simulations is in this case 0.190 eVÅ^{-1}.

The formation energy of a closed dislocation loop is given by equation (3.7), where $\mathbf{b} = (0, 0, a)$ and the anisotropic elasticity factors are $K\mathbf{b}^2/4\pi \approx 0.465$ eVÅ^{-1}, $F_\delta \approx 0.39$ eVÅ^{-1}, and $F_c \approx 0.5$ eVÅ^{-1} [**158**], and R^* is the effective radius of the loop. By substituting these values into equation (3.7) for a 97-vacancy loop ($R^* = 11.3$ Å) we find the *elastic* formation energy of the loop $E_{closed} = 114$ eV compared with 111.1 eV found in atomistic simulations, which is excellent agreement.

The reason for the difference observed in the critical size between $\frac{1}{2}\langle 111\rangle$

and $\langle 001 \rangle$ closed vacancy loops can, in part, be understood through a direct comparison between the two different orientations. The graph shown in Figure 3.16 compares the two sets of vacancy loop energies. Note that we have extended the original $\frac{1}{2}\langle 111 \rangle$ results to larger sizes (some of which do not appear on the graph) to confirm the trends represented by the extrapolated lines, although this seemed to be the case when comparing results with theoretical curves. For small defect sizes, the $\langle 001 \rangle$ closed loops are slightly more stable than their $\frac{1}{2}\langle 111 \rangle$ equivalents. The reverse is true for defects containing more than about 50 vacancies. However, the difference between the two curves does not become significant until the defect size approaches 150 vacancies ($\sim$ 30 Å diameter for $\frac{1}{2}\langle 111 \rangle$, and $\sim$ 28 Å diameter for $\langle 001 \rangle$ loops), and so this alone does not explain the large difference in the critical size for closed loops.

However, Figure 3.16 indicates that the formation energies of open loops for the two different orientations diverge significantly at fairly modest defect sizes. Density functional calculations by Spencer *et al.* [**160**] and MD simulations performed using the magnetic potential by Van Zwol *et al.* [**156**] have demonstrated that the (100) surface energy is significantly lower than the energy of the (111) surface. This trend is reproduced in our simulations, where surface energies give the leading contribution to the energy of open loops. This fact is responsible for the significantly lower energy of the $\langle 001 \rangle$ open loops, which in turn is the factor determining the greater cross-over size for the $\langle 001 \rangle$ open/closed loop structures.

One consequence suggested by these simulations is that the $\langle 001 \rangle$ collapsed loops are likely to form even less frequently during cascade collapse than their $\frac{1}{2}\langle 111 \rangle$ counterparts. This is due to the preference of loops in this orientation to become planar voids up to a much larger size.

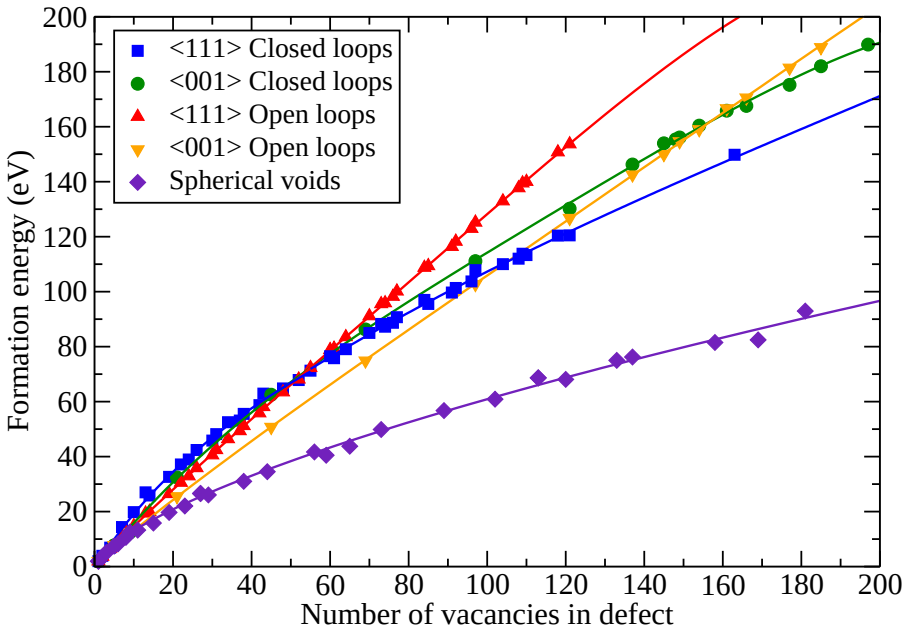


Fig. 3.16: Comparison of formation energies for mesoscopic vacancy loops with different Burgers vectors in Fe, as predicted by the D-D magnetic potential for Fe.

Furthermore, it may also be the case that the lower energy, and therefore higher stability, of $\langle 001 \rangle$ planar voids when compared to the $\frac{1}{2}\langle 111 \rangle$ orientation might actually lead to open $\langle 001 \rangle$ vacancy loop configurations being more frequent in irradiation-induced cascades. However, the much lower probability of *collapsed* $\langle 001 \rangle$ loops forming in cascades would manifest itself experimentally as a preference for the $\frac{1}{2}\langle 111 \rangle$ orientation. We note that the $\langle 001 \rangle$ *open* loops (planar voids) are invisible in an electron microscope and probably absent at equilibrium due to the ease with which they transform into the lowest energy spherical void configuration.

This matter has been recently studied by Dudarev *et al.* [**158**]. They investigated the change in elastic properties of bcc Fe as it approaches the $\alpha \rightarrow \gamma$ phase-transition. A full anisotropic model shows that a soft elastic mode develops in bcc Fe at elevated temperatures, which eventually brings

about the structural changes associated with the phase transition. They found that $\langle 001 \rangle$ dislocation loops become more favourable than $\frac{1}{2}\langle 111 \rangle$ loops at temperatures above ~ 500°C. This has recently been confirmed in irradiation experiments by Yao *et al.* (extensions to the work in [**123**, **124**]), where they find only $\langle 001 \rangle$ loops at irradiation temperatures above 500°C, whereas below 300°C, $\frac{1}{2}\langle 111 \rangle$ loops dominate.

3.2.5 Rectangular vacancy-dislocation loops

One final question to be considered here is what effect the shape of the dislocation 'loop' might have on the conclusions. In recent MD simulations of cascades in Fe, Calder *et al.* [**147**] observed the formation of rectangular $\langle 001 \rangle$ closed vacancy loops. This suggests that rectangular $\langle 001 \rangle$ clusters of vacancies are more energetically favourable than those with a more circular structure, a prediction confirmed by the recent work of Dudarev *et al.* [**158**]. To investigate whether this might affect our conclusions we have performed a series of MS relaxations using the D-D Fe potential on selected rectangular closed vacancy loops with varying size and shape for both $\frac{1}{2}\langle 111 \rangle$ and $\langle 001 \rangle$ Burgers-vector orientations. Figure 3.17a displays the results for $\frac{1}{2}\langle 111 \rangle$ loops. For comparison, the circular loop results of Figure 3.5 are also shown. The label indicates the dimensions of the loop for the rectangular vacancy defects. The first dimension is the length of the defect in the $[1\bar{1}0]$ direction in multiples of $a/\sqrt{2}$, which is the distance between the $(1\bar{1}0)$ planes in the $([1\bar{1}0], [11\bar{2}], [111])$ coordinate system. The second dimension is the length in the $[11\bar{2}]$ direction, this time in multiples of $a/\sqrt{6}$, for the same reason.

Figure 3.17a shows that rectangular $\frac{1}{2}\langle 111 \rangle$ vacancy loops are generally higher in energy than circular closed loops of an equivalent size. Indeed the

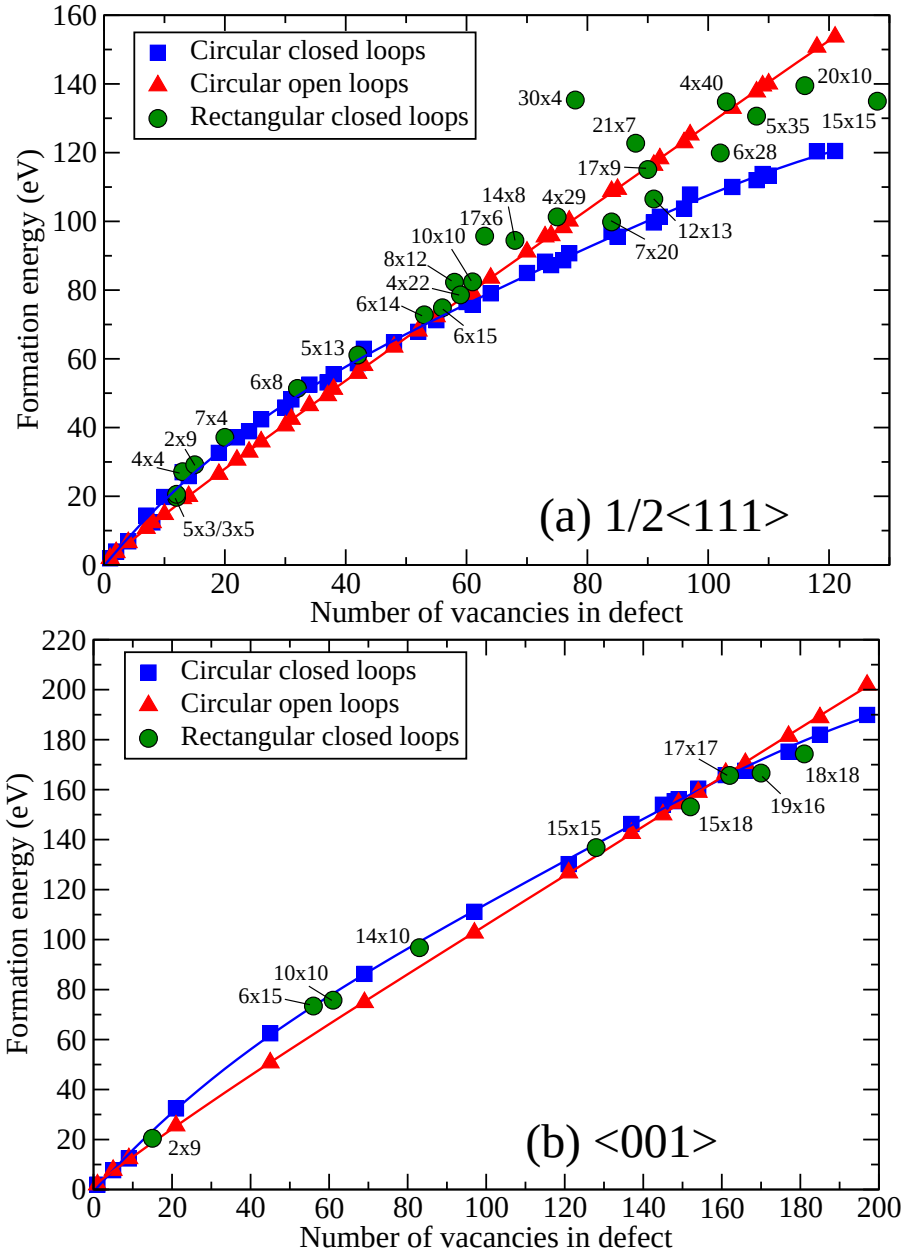


Fig. 3.17: Comparison of formation energies of (a) $\frac{1}{2}\langle 111\rangle$ and (b) $\langle 001\rangle$ vacancy loops of different shape in Fe (D-D potential).

results seem to indicate that the energy of circular and rectangular loops of equivalent size seems to diverge with increasing size because some of the larger (more than ~ 80 vacancies) rectangular $\frac{1}{2}\langle 111\rangle$ vacancy loops are significantly higher in energy than their circular counter-parts. Of course, one explanation for this is that there is interaction between opposing edges of the loops when they become long and narrow (*i.e.,* when one dimension is much greater than the other), which leads to an increased energy. At the same time, the vacancy loops with a more square profile are predominantly lower than those with pronounced elongation, but they are all still higher than the circular loops.

One question that should be considered for rectangular loops is whether their energy would be lower if they were able to rotate. In these simulations we relax ('freeze') the loops relatively quickly. This does not allow for rotation of the loop on its habit plane. It is known from simulation (see for example Osetsky *et al.* [**161**] and chapter 4 of the present work) that *interstitial* loops rotate easily between their preferred {111} and {110} habit planes, but this cannot happen in MS relaxations because there is a slight energy barrier to overcome (requiring thermal fluctuation). However, in the finite-temperature simulations of *vacancy* loops presented in chapter 4 we did not observe rotation, even at the highest temperatures. This demonstrates that there are no alternative habit planes for $\frac{1}{2}\langle 111\rangle$ vacancy loops, so it is unlikely that the formation energy of rectangular loops would be reduced by rotation. However, this matter should be explored thoroughly via further simulation.

If we now inspect Figure 3.17b, which shows the results for the $\langle 001\rangle$ rectangular vacancy loops, a different picture emerges. In this case the rectangular-loop dimensions are the lengths in multiples of $a/2$ in the [100]

and [010] directions, respectively. The rectangular ⟨001⟩ loops are mostly of lower energy than their circular counterparts. This demonstrates that they should become viable (*i.e.,* stable compared to open loops) at a lower defect size than circular loops, and so rectangular ⟨001⟩ vacancy loops should form in preference to circular ones. There is also evidence to suggest that, as expected, the energies of rectangular and circular ⟨001⟩ loops diverge with increasing size, with rectangular loops becoming even more energetically favourable. Although our results are not conclusive (we would need to investigate larger loop sizes), they do agree with the general trend seen in experimental observations of much larger defects, which indicate that ⟨001⟩ edge dislocation loops (either vacancy or interstitial) formed under irradiation are rectilinear in shape. For example, Masters [**162**], and Little and Eyre [**163**, **164**] both observed the formation of large, rectangular interstitial-type dislocation loops in irradiated Fe with sides parallel to ⟨100⟩ directions and pure edge in character.

3.3 Vacancy defects in bcc W at 0K

The formation energy analysis performed for vacancy-defect clusters in Fe is extended to consider defects with both $\frac{1}{2}\langle 111\rangle$ and ⟨001⟩ Burgers vectors in W. The recent potential of Derlet *et al.* [**111**] is used in all of the following MS simulations. As was the case for Fe, spherical voids and interstitial loops are also considered. ⟨001⟩ loop-energies are also calculated for completeness, despite the experimental observations of Häussermann [**135**] and Jäger and Wilkens [**136**], which show that $\frac{1}{2}\langle 111\rangle$ loops occur exclusively during irradiation, giving no evidence for loops with other Burgers vectors. Figure 3.19 summarises our key results for $\frac{1}{2}\langle 111\rangle$ loops, while Figure 3.20 gives the results for ⟨001⟩ defects.

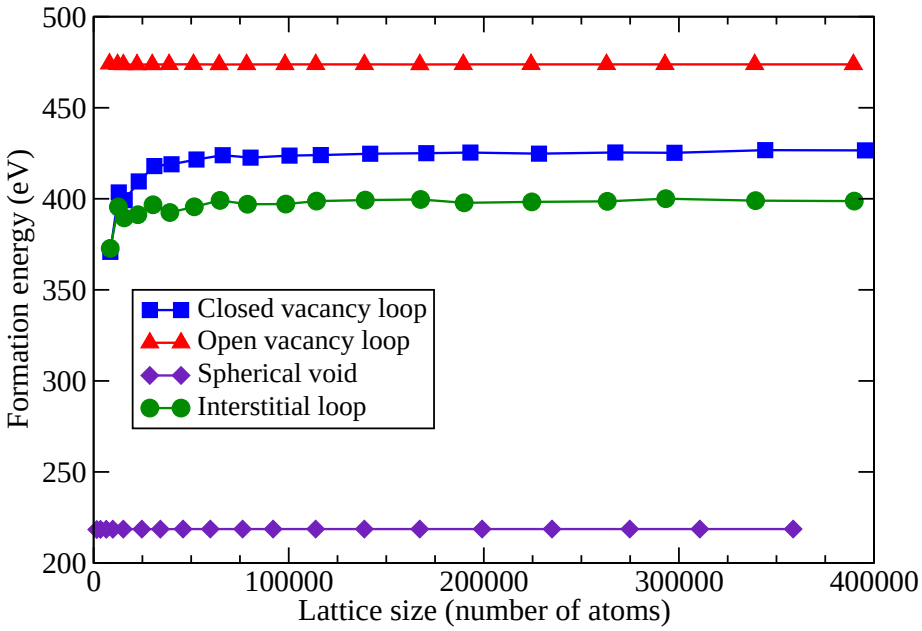


Fig. 3.18: Formation energy of 211-vacancy or -SIA loops and 259-vacancy voids as a function of the number of W atoms in the periodic simulation cell.

For the $\frac{1}{2}\langle 111\rangle$ calculations we used a base lattice containing around 146,000 atoms, which was validated for the largest defect sizes (211 vacancies/SIAs for loop, 259 vacancies for voids) in a sequence of simulations using a range of lattice sizes. Preliminary investigations indicated that the intersection of the formation energies for the two types of vacancy loop in W was going to be at a higher defect size than that found in Fe, and hence both a larger maximum defect size and base lattice was required. Figure 3.18 displays the results of this validation, confirming that the chosen lattice size was more than sufficient. For $\langle 001\rangle$ loops in W a lattice containing 128,000 atoms was used.

Figure 3.19(a) shows the variation in the energy of closed $(a/2)\langle 111\rangle$ vacancy-loops, interstitial loops, open vacancy loops, and spherical voids plotted as a function of defect size given by the number of vacancies or self-interstitials. As was the case with Fe, the open loops are more

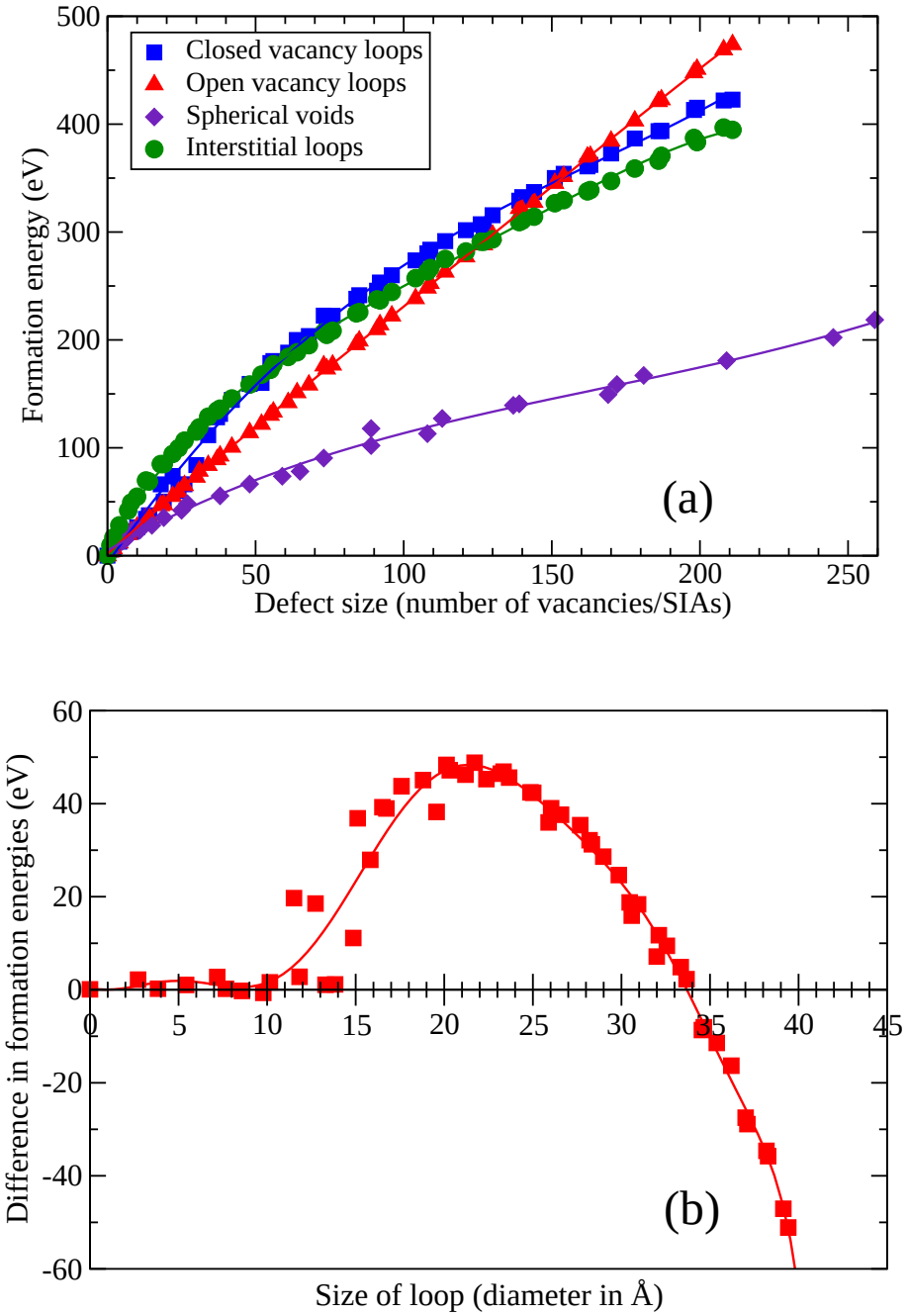


Fig. 3.19: (a)$\frac{1}{2}\langle 111\rangle$ defect energies in W as a function of size; (b)Variation of difference between closed and open $\frac{1}{2}\langle 111\rangle$ vacancy loop energies in W as a function of diameter (closed minus open).

energetically favourable than their closed vacancy-loop equivalents for small defects. There is a critical size above which the reverse becomes true. Figure 3.19(b) shows how the difference in the formation energy of closed and open $\frac{1}{2}\langle 111\rangle$ vacancy loops varies as a function of the diameter of a loop. The critical size, above which the closed loops are energetically more stable than the open ones, is about 34 Å, corresponding approximately to a 157-vacancy defect. This is considerably larger than in Fe (18 Å, ~ 50 vacancies). For $\langle 001\rangle$ loops, Figure 3.20, indicates that a cross-over in stability also occurs for open and closed vacancy loops in this case. However, the exchange occurs at defect sizes of around 260 vacancies, corresponding to diameters of 41 Å, which is a significant size. This may be one of the reasons why $\langle 001\rangle$ (closed) vacancy dislocation loops have not been observed experimentally in W.

Similarly to the case of Fe, the spherical voids are the most stable configuration for a vacancy cluster of any size or type in W. The difference in energy between these voids and the equivalently sized (in terms of the number of vacancies) planar defects is somewhat larger in W compared to Fe, which could mean that vacancy loops of *any kind* in W, being highly metastable, transform more readily into spherical voids through surface vacancy diffusion and/or vacancy evaporation. However, as we discuss later in this chapter, the migration energy for a single vacancy in W is much higher than in Fe (1.78 eV [**165**] in W compared to 0.67 eV in Fe [**108**]), and so the transformation from loop to void, which requires vacancy migration, may in fact take longer and require higher temperatures in W.

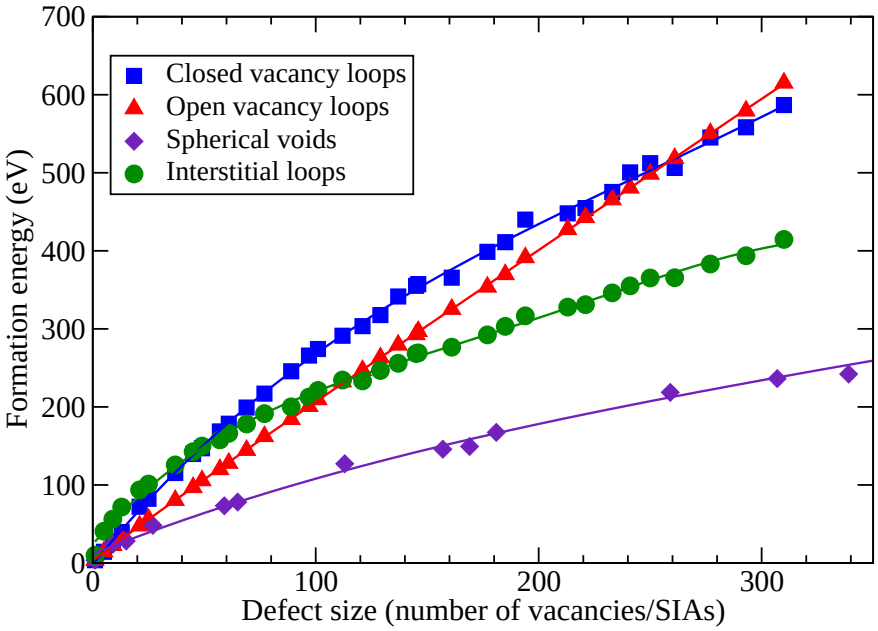


Fig. 3.20: Formation energy as a function of defect size of ⟨001⟩ loop defects in W

3.4 Comparison with experiment

It is important to appreciate the difference between the length-scales of our simulations and experimental observations. Whilst a mesoscopic loop might be considered as small in experiments, such a defect contains several hundred vacancies or self-interstitial atoms and is very large in the context of an MD/MS simulation.

When comparing the results of the simulations performed to what has been seen in transmission electron investigations of irradiated samples, one must keep in mind that in the few nm defect size range, only the long range strain fields associated with prismatic dislocation loops (*i.e.,* closed vacancy loops) can be resolved [**123**, **135**]. Spherical voids do not carry a large strain field, and so, with the exception of very large cavities containing several hundred vacancies, such voids, if present at equilibrium, are difficult to see experimentally in transmission electron microscope (TEM)

images [**133**]. Thus the prediction that, at loop diameters less than a critical value, it is the open loops, transforming into spherical voids, that are the most energetically favourable configurations may be relatively difficult to verify by means of electron microscope observations.

Recently, Yao *et al.* [**123**] improved the technique for imaging small voids and confirmed the presence of numerous small voids in Fe and FeCr alloy foils irradiated with energetic ions. When the image resolution in their experiments was particularly good, a 'sea' of tiny unidentified defects were observed at a much higher density than the larger dislocation loops (typically greater than 2 nm in size). An example of one such experimental image is shown in Figure 3.21, which is reproduced from a published paper [**127**] combining the results of our simulations with the experiments of Yao *et al.* [**123**]. The figure shows a weak-beam image (taken under somewhat unusual diffraction conditions) of a small region of Fe containing 8% Cr foil irradiated with 150 keV Fe^+ ions at 300°C to a dose of 10^{18} ions m^{-2}. Defects appear as white dots, some of which are interstitial loops, but some of which may be small voids. This provides some evidence to support our view that small voids are the predominant defect produced in annealed cascades. Only under specific circumstances can long-lived metastable (closed) vacancy dislocation loops be formed [**127**].

Further evidence for the predominance of tiny voids has been seen in the neutron irradiation experiments of Horiki *et al.* [**138**, **139**], where an observed reduction in interstitial clusters, under certain experimental conditions, was thought to be due to the production of a large number of small, and in their case invisible, vacancy clusters or voids.

It is important to discuss here the issue concerning the regions of a material to which the simulation results presented in this chapter

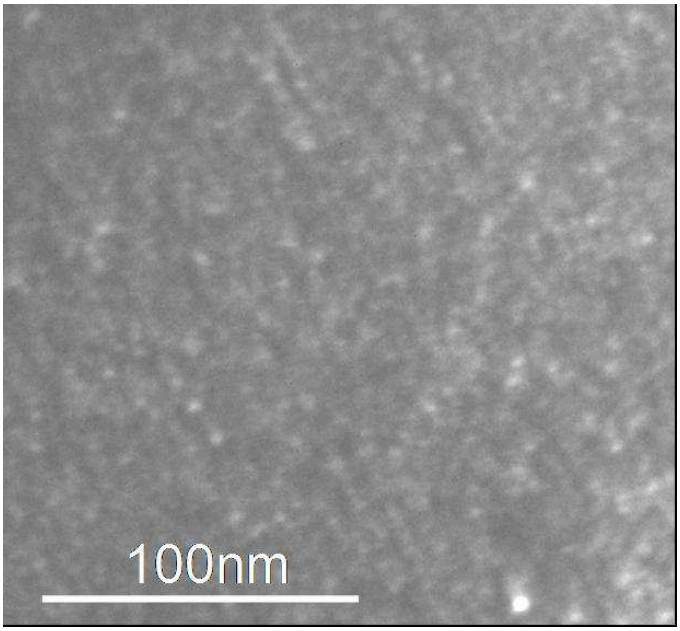


Fig. 3.21: Weak-beam dark field contrast image of Fe8%Cr irradiated with Fe^+ ions at 300 ^{o}C - see main text and [**127**] for more details. The scale indicator shows that the defects seen are very small.

correspond. As discussed in section 3.2.1, the validation simulations indicate that our results are most appropriate to defects in the bulk of irradiated materials. In particular, they are not directly applicable to the region close to the surface of the thin-foils (typically $\sim$ 10 nm thick [**123**]) used in the above experiments, where in-plane dislocation loops are strongly attracted to the surface leading to a so-called *depleted zone*. However they can be compared to the deeper damage regions of some experiments, where surface effects are not significant. Also, if a dislocation loop (spherical and planar voids have no elastic fields and so are unaffected by surfaces in general) lies perpendicular to the surface its elastic field would not interact with the surface and in these circumstances our simulations would apply to the loop regardless of its distance to a boundary.

In other experiments, Eldrup *et al.* [**166**, **167**] have been able to detect

small (typically less than 1 nm in diameter) void defects produced in Fe (and Cu) using Positron Annihilation Spectroscopy (PAS). This technique is based on the concept of positrons, which can be injected into a material, becoming trapped in vacancy defects due to their reduced atomic, and hence electron, density compared to the bulk. When the positron finally annihilates with an electron, the spectrum of the emitted gamma ray gives information about the defect that trapped the positron. Alternatively, the lifetime of the trapped positron (*i.e.,* the time between trapping and annihilation), which varies according to the trapping defect, can also be measured. This is the method employed by Eldrup *et al.* [**166**, **167**]. In Fe, the small voids they detect are produced in large numbers ($\sim 10^{24}$ m^{-1} [**167**]) at relatively low doses, which is further evidence for the preferential formation of small voids over vacancy dislocation loops of the same size. Thus, in the majority of irradiation conditions, and certainly in neutron irradiation, most of the vacancy defects produced in cascade collapse events in Fe are voids, with an occasional super-critical vacancy loop. Only under heavy-ion irradiation where the cascades are smaller but have a higher vacancy density, or at very high doses where there is significant cascade overlap, does the yield of vacancy dislocation loops become more significant [**123**].

In summary, for Fe, our results offer a likely explanation for the low closed vacancy loop yield observed using electron microscopy in irradiation-induced cascade experiments (typically of the order of 1% or lower in self-ion irradiation experiments, and certainly much lower than in similar experiments on fcc metals [**132**]). To produce a long-lived closed vacancy loop, the number of vacancies in a cascade (or group of cascades) must be sufficiently high (*i.e.,* the local vacancy density must be high) so

that on collapse a super-critical (more than around 30-50 vacancies in size) loop is formed. In most cascade regions the local vacancy density is too low to produce a stable loop, since any closed loop forming in the sub-critical size range will be metastable, and will transform rapidly to an open loop structure and finally to a small spherical cavity.

For W, the situation is different. In the experiments of Häussermann [**135**], where W (and Mo) was irradiated using energetic gold ions, the $\frac{1}{2}\langle 111\rangle$ vacancy loops were found to have an average diameter of between 27 and 46 Å, depending on the sample used in experiments. Thus vacancy loops with diameters less than the critical size of 34 Å were observed, in contradiction with our simulation results.

A reason for the discrepancy may lie in the strongly non-equilibrium nature of the defects generated by irradiation in W. The time taken for a particular cascade event to reach equilibrium can be estimated by considering the timescale of migration of the vacancies produced during the cascade expansion phase. During collapse, which leads to the formation of voids and other defects, these vacancies migrate across the volume of the cascade, and therefore their motion is the rate determining factor for reaching equilibrium [**126**]. The characteristic equilibration time τ is estimated via:

$$\tau \approx \frac{L_{\text{cascade}}^2}{D_v}, \tag{3.12}$$

where L_{cascade} is the size of a cascade, typically of the order of 0.5×10^2 Å, and D_v is the diffusion coefficient for a single vacancy at temperature T, given by the Arrhenius equation:

$$D \approx d^2 \nu_0 \exp\left[-\frac{E_a}{k_B T}\right]. \tag{3.13}$$

Here the attempt frequency ν_0 can be approximated as the Debye frequency ω_D divided by 2π. ω_D is calculated from the Debye temperature T_D via

$$\omega_D = \frac{k_B T_D}{\hbar}. \tag{3.14}$$

For Fe, $T_D = 420$K and for W it is 310K [**168**], giving Debye frequencies of 8.75×10^{12} s^{-1} and 6.46×10^{12} s^{-1}, respectively. d is the jump distance, which for a bcc lattice is $\frac{\sqrt{3}}{2}a$. The activation energy E_a for vacancy migration used in these calculations was 0.67 eV for Fe [**108**] and 1.78 eV for W [**165**]. Assuming that $T = 300$K ($\sim$ room temperature) we find that for Fe this leads to a characteristic time of around 8 seconds, whereas for W the result is of the order of 4×10^{20} s, which is equivalent to more than 10^{13} years!

The above estimate explains why in irradiation experiments of W the size range of the observed vacancy loops includes diameters below the critical size predicted by our simulations. Whereas in Fe it is realistic to expect the experimental observations to be of equilibrium configurations, it is virtually impossible for this to be the case in experiments on W because the system is not able to reach equilibrium over normal timescales at room temperature. Thus the configurations observed in experiments on W at room temperature do not represent the minimum energy configurations required for direct comparison with the simulation results presented here.

The characteristic time for Fe obtained from our estimate above is a little longer than the timescale for the formation and evolution of vacancy dislocation loops observed in the recent irradiation experiments by Yao *et al.* [**123**], which was of the order of 0.1 s. kMC simulations of cascade evolution in Fe by Hudson *et al.* [**169**] have also indicated that the single-vacancy concentration falls to zero on this 0.1 s timescale at

$T = 500$K as a result of diffusion, followed by clustering or recombination with self-interstitial atoms.

3.5 Concluding remarks

In this chapter we have investigated the 0K stability of vacancy dislocation loops and considered a comparison of their structure with interstitial defects of the same size. Analysis of the formation energy of vacancy clusters confirmed that spherical voids are the most energetically favourable configuration for a cluster of any given number of vacancies. Hence the vacancy loop structures seen experimentally represent metastable configurations, which, given enough time and sufficient thermal activation, should evolve into the void structure. Additionally, the stability investigation also suggests that there is a critical size below which these (closed) vacancy dislocation loops become even more energetically unfavourable. In this region the open loop (planar void) structure is more stable, although this has a tendency to transform into a spherical void at modest temperatures via the diffusion of single vacancies across its surface, which we have demonstrated using finite-temperature MD simulations.

For Fe, our results are in good agreement with recent experimental observations by Yao *et al.* [**123**], where the smallest loops observed in Fe were no smaller than around 2 nm or 20 Å in diameter. For the case of W, experiments [**135**] indicate the presence of vacancy loops below the stability threshold found in the simulations. This observation seems to be explained by realising that in W, due to its extremely low vacancy diffusion coefficient, the cascade evolution cannot proceed to equilibrium conditions on the typical experimental time scale.

Conversely, the experimental observations of void defects, which our

results confirm are the most favourable, are somewhat inconclusive. However, techniques have improved recently and there is now some evidence for a large number of defects in a void 'sea'. The finite temperature simulations described in the next chapter show that the observable dislocation loop defects are mobile whilst the voids are not. Therefore, while experiments concentrate on defects which are relatively easy to see there is a significant omission of the majority of vacancy defects, namely the voids, which, with their long residence times, will surely have the greatest impact on material integrity and hence component lifetime in irradiation environments. In the future it will be important to develop the understanding of the behaviour and accumulation of these voids by applying the latest techniques in molecular simulation at various length scales and levels of accuracy.

Parallel to this, recently developed experimental methods should be employed to validate the simulation results. For example, atom-probe tomography, where atoms are 'evaporated' from the surface of a material as ions using an electric field and then received by a position sensitive detector, is now able to describe the spacial distribution of atoms at resolutions of less than 0.5 nm [**170**]. This is a level of accuracy that should make it possible to detect individual void-defects in the 1 nm size range, and in conjunction with simulation this offers the future possibility of finding ways to reduce void build-up in the first place.

4. THERMALLY ACTIVATED MOBILITY OF VACANCY AND INTERSTITIAL LOOPS IN FE AND W

The latest experimental observations of the defects produced during irradiation of bcc metals such as Fe have shown that both interstitial and vacancy dislocation loops are mobile [**121**–**124**]. In this chapter we calculate the relative mobility of equivalently-sized interstitial and vacancy dislocation loops using finite temperature Molecular Dynamic (MD) simulations.
Some of the work presented in this chapter has been published in [**125**–**127**] (for details of copyright, see page 56).

4.1 Introduction

In the previous chapter we have seen how the relative stability of vacancy defects of different type varies as a function of their size. The observations made there offered an explanation for the relatively low yield of vacancy dislocation loops in bcc metals such as Fe and W (when compared to other materials such as fcc Cu [**123**]).

However, the formation of defects under irradiation conditions is only part of the story. In structural components of fusion reactors an understanding of the evolution of irradiation-induced defects after formation is also of utmost importance. In chapter 3, we partially addressed this issue when considering how sub-critical vacancy dislocation

loops transform at the elevated temperatures that might be expected in a fusion environment. Conversely, it was seen that super-critical vacancy dislocation loops are comparatively stable at finite temperature, at least on MD timescales, and so they may remain in a system for extended periods. If this is the case then the thermally activated mobility of these dislocation loops becomes important.

One of the key questions surrounding the motion (or diffusion) of vacancy dislocation loops concerns the comparison with interstitial dislocation loops. It is well known that interstitial loops are highly mobile and that nearby surfaces act as strong sinks for them [**137**]. In irradiation experiments this often leads to an absence of interstitial defects during post-irradiation observations (see, for example, Yao *et al.* [**123**]), even though MD simulations, such as those by Calder and Bacon [**171**], have demonstrated that interstitial clusters can form directly in irradiation induced cascades. At the same time, vacancy dislocation loops are seen more readily in experiments, although they have also been seen to move towards surfaces in bcc metals. For example, Jäger and Wilkens [**136**] observed the loss of $\frac{1}{2}\langle 111\rangle$ vacancy dislocation loops from gold-ion-irradiated W, while the recent thin-foil experiments of Yao *et al.* [**123**] suggest that a proportion of the observed mobile loops in irradiated Fe were vacancy in nature [**127**]. On the other hand, new electron microscope observations by Arakawa *et al.* [**122**] give the impression that the interstitial loops have much higher thermally activated mobility than vacancy loops.

If vacancy loops are mobile, then what is the reason for their greater residence time in irradiated materials, especially in the presence of nearby surfaces? Osetsky *et al.* [**155**] performed MD investigations of vacancy loop

mobility in Fe, which suggested that vacancy loops move by thermal activation in the direction of their Burgers vector. The mobility is less than that seen for interstitial loops, but it is higher than that of single vacancies. In an earlier work, Soneda and Diaz de la Rubia [**142**] demonstrated (using MD simulations) that single vacancies in Fe migrated more slowly than single interstitials, although they treated clusters as being immobile in the subsequent kMC simulations performed. Similar simulations in Cu by Osetsky *et al.* [**155**] indicate that the same vacancy loops do not move in this fcc metal.

Later, Osetsky *et al.* [**172**] interpreted the simulations in Fe by fitting the mobility parameters to the Arrhenius law. For a self-interstitial atom (SIA) cluster of size N the equation describing the diffusion coefficient has, according to the Arrhenius law, the form

$$D_N = D_N^0 \exp\left(-\frac{E_N^m}{k_B T}\right), \tag{4.1}$$

where D_N^0 is the pre-exponential factor, k_B is Boltzmann's constant ($= 8.617343 \times 10^{-5}$ eVK^{-1}), E_N^m is the migration energy of the cluster, and T is the temperature [**172**]. This law was widely discussed for, and applied to, the thermally activated defect movement in solids in the 1950s and 60s (see for example the work of Vineyard [**36**] and Landauer and Swanson [**173**]). However, in another paper, Osetsky *et al.* [**149**] had cast doubt on whether the motion of glissile clusters and dislocation loops (either SIA or vacancy) was a conventional diffusion process. Indeed, in our research, presented in this chapter, we show that such an Arrhenius law, does not approximate the temperature dependence of the rate of Brownian motion (diffusion) of mesoscopic loops in pure metals at elevated temperatures.

More recent simulations of bcc vanadium by Zepeda-Ruiz *et al.* [**174**] have shown that the diffusion coefficient for $\frac{1}{2}\langle 111\rangle$ interstitial dislocation loops varies *linearly* as a function of absolute temperature (particularly at high temperature) in a way that does not fit the Arrhenius law. They found that the weakly temperature-dependent activation barrier for loop motion is so small that at modest temperatures, just above room temperature, the loops essentially perform free particle diffusion, which leads to diffusivity varying linearly with temperature T [**174**]. In their studies of Fe, Osetsky *et al.* [**172**] also found that the activation energy varied weakly with temperature, but still fitted their results to an Arrhenius law. Zepeda-Ruiz *et al.* [**174**] suggest that this may have been due to the reduced temperature range considered in the studies, which prevented the full temperature-dependence of the diffusivity from being observed.

There are several other examples of interstitial cluster migration in Fe, including the work of Soneda and Diaz De La Rubia [**142**], Marian *et al.* [**175**], Wirth *et al.* [**176**], and Terentyev *et al.* [**177**]. In all cases they fit the calculated diffusion coefficients to an Arrhenius law, without considering the possibility of non-Arrhenius behaviour.

Clearly, there is some debate about the true nature of the thermally-activated mobility of, in particular, interstitial clusters. However, in the work presented in this chapter we are primarily concerned with the direct (quantitative) comparison of interstitial and vacancy loops in Fe and W.

As discussed previously, both experiments and simulations seem to indicate that vacancy dislocation loops have different mobility (diffusivity) rates to interstitial loops. There is, however, a clear need to quantitatively measure this difference. In this chapter we calculate and compare, as a

function of temperature, the diffusion coefficients of equivalently-sized interstitial and vacancy dislocation loops in both Fe and W using long timescale MD simulations. In particular we demonstrate that the thermal diffusion of a loop in a pure bcc metal is a non-Arrhenius function of temperature. Additionally, we also present our early investigations into the coherent motion of $\frac{1}{2}\langle 111\rangle$ interstitial dislocation loops in Fe, which are an attempt to reproduce and explain the current experiments of Yao *et al.* [**178**], where they observe loops lining-up and diffusing together as a prelude to coalescence.

4.2 Structural comparison of loops

Since interstitial and vacancy dislocation loops have different thermally-activated mobilities, it is worth comparing their structures to highlight the similarities and differences. In chapter 3, Figure 3.5 shows that except at very small defect sizes (less than 10 vacancies/interstitials), under the Dudarev-Derlet (D-D) [**105**] potential in Fe, $\frac{1}{2}\langle 111\rangle$ interstitial loops are of lower energy than equivalently sized closed vacancy loops. This is repeated for $\langle 001\rangle$ loops in Fe (Figure 3.14) and for all Burgers vectors in W (Figures 3.19(a) and 3.20).

Since the difference between energies of closed vacancy loops and interstitial loops is related to the length of the perimeters of the loops, these observations suggest that, in the limit of large defect size, the core energy of the curved dislocation forming the perimeter of a vacancy loop is greater than that of an interstitial loop of the same size. The difference between the interstitial and closed vacancy loop curves in all the graphs of Figures 3.5, 3.14, 3.19, and 3.20 increases slightly with defect size. This is consistent with the concept of the energy per unit perimeter length being

greater for vacancy loops.

Puigvi *et al.* [**148**] observed this divergence in atomic simulations of defects in Fe, and found that the relative energies of interstitial and vacancy loops are sensitive to the choice of interatomic potential. Using the long-range pair potential of Osetsky *et al.* [**179**] they found the same relationship for $\frac{1}{2}\langle 111\rangle$ loops in Fe as presented in our work, but, with the Ackland *et al.* [**86**] many-body potential, the reverse situation was observed, namely that vacancy loops were of lower energy than their interstitial counterparts (see Figure 3.2 on page 62, which shows the fig. 2b graph from [**148**]). We observed a similar phenomenon in our simulations. Under the Mendelev [**82**] potential for Fe, we see that the $\frac{1}{2}\langle 111\rangle$ interstitial loops are higher in energy than equivalent collapsed vacancy loops (see Figure 3.11), which is opposite to the results under D-D.

Both interstitial and closed vacancy loops are related to an edge dislocation; one with the extra half-plane inside the loop (interstitial), and one with it on the outside (*closed* vacancy loop). This results in the relaxed configurations of equivalently sized interstitial and vacancy loops being difficult to distinguish from one another. For example, consider the pictures shown in Figure 4.1. Pictures (a) and (b) in the figure show two different views of a large (in MD terms), super-critical 199-vacancy $\frac{1}{2}\langle 111\rangle$ closed loop in W. (a) is a side view, looking in the (111) plane of the defect (*i.e.,* looking in a direction perpendicular to the $\frac{1}{2}\langle 111\rangle$ Burgers vector), whilst (b) is a view along the defect's [111] axis (parallel to the Burgers vector). Pictures (c) and (d) show the same views of an equivalent 199-SIA $\frac{1}{2}\langle 111\rangle$ loop. As in Figure 3.9 (page 75), atoms are only shown if they have been significantly displaced (and therefore have a higher energy than bulk atoms) by the presence of the defect. Thus atoms surrounding and within

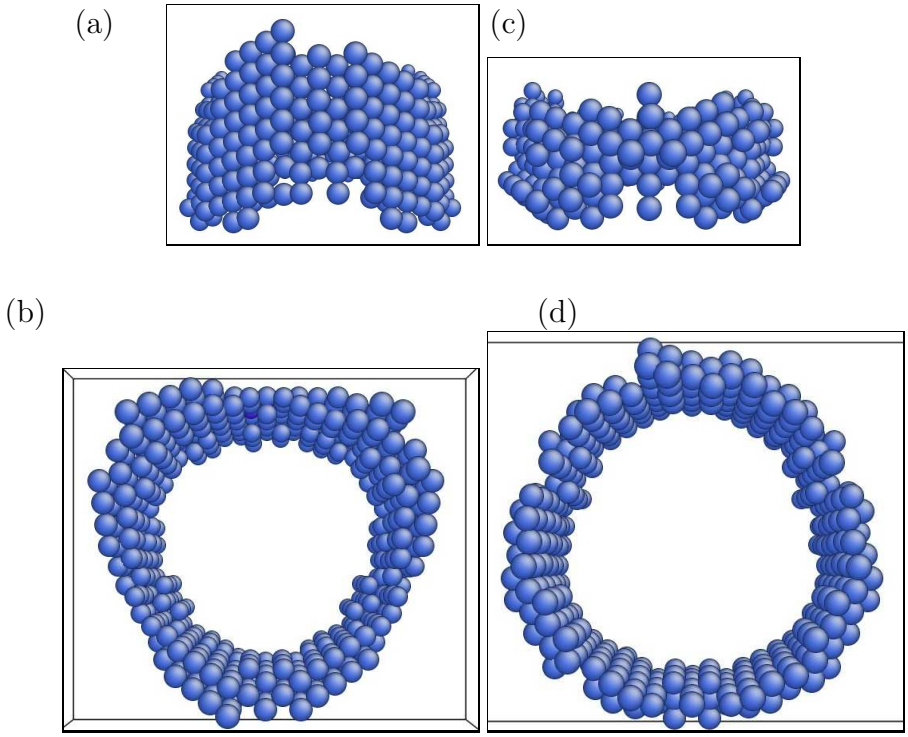


Fig. 4.1: Relaxed structures of various $\frac{1}{2}\langle 111\rangle$ mesoscopic dislocation loops in W: (a) 199-vacancy closed loop - view in the (111) plane; (b) as (a) but looking down the [111] axis of the defect; (c) 199-atom interstitial loop (in-plane view); (d) as (c) but axial view.

the loop perimeter are visible, with all other atoms considered as being part of the invisible bulk. The atoms in the middle of both loop types are invisible (see Figures 4.1b and 4.1d) because they have relaxed into a near-perfect bcc lattice configuration. In these idealised representations it is clear that the two different structures are quite similar.

Clearly, it is not possible to observe the differences between the interstitial and vacancy dislocation-loop structures, which must exist, by direct viewing of their constituent atoms. However, by analyzing the strains in directions parallel to the Burgers vector of a loop we can gain some insight. In the $([1\bar{1}0], [11\bar{2}], [111])$ coordinate system (see Appendix A.1) the atoms can be grouped according to which [111] atomic string they belong

to. For $\frac{1}{2}\langle 111\rangle$ loops we can then calculate the strain in the [111] direction between each pair of adjacent atoms of a particular string, using the equation:

$$\varepsilon_n^{[111]} = \frac{\delta\ell}{\ell_0} = \frac{\left(x_n^{[111]} - x_{n-1}^{[111]} - \frac{\sqrt{3}}{2}a\right)}{\frac{\sqrt{3}}{2}a}, \tag{4.2}$$

where $\varepsilon_n^{[111]}$ is the strain associated with atom n in the [111] direction relative to the $n-1$ atom neighbouring (below) it. $\delta\ell$ is the extension, which is the difference between the current separation of the atoms in [111], $(x_n - x_{n-1})$, and their original separation in a perfect lattice ℓ_0. As shown in Appendix A.1, for the [111] direction this is $\sqrt{3}/2$ times the lattice parameter a. In a perfect lattice these strains are all close to zero, but if the string passes through a defect then we can expect some of the strain values to be either negative (compressive) or positive (tensile). Note that here we do not consider the lateral relaxation of atoms (*i.e.,* displacement perpendicular to the [111] direction), which is very small compared to the relaxation along the [111] direction.

In Figure 4.2 the 'maximum strain magnitudes' for each string have been calculated for the 199 interstitial and super-critical vacancy $\frac{1}{2}\langle 111\rangle$ loops in W shown in Figure 4.1. In the graph the maximum strains are plotted as a function of the corresponding string's radial distance from the centre of the loop. To aid visualisation (*i.e.,* to relate the variation in strain to the loop shapes) we have plotted the strings lying in the positive $(1\bar{1}0)$ half-plane, relative to the loop centre, on the right of the graph, and those in the negative half-plane to the left. Thus, there are 199 internal and perimeter points for each data-set, corresponding to the 199 vacancies or interstitials used to create each loop. Of these, roughly 50% have a $[1\bar{1}0]$ coordinate greater than the loop centre and are therefore plotted on the

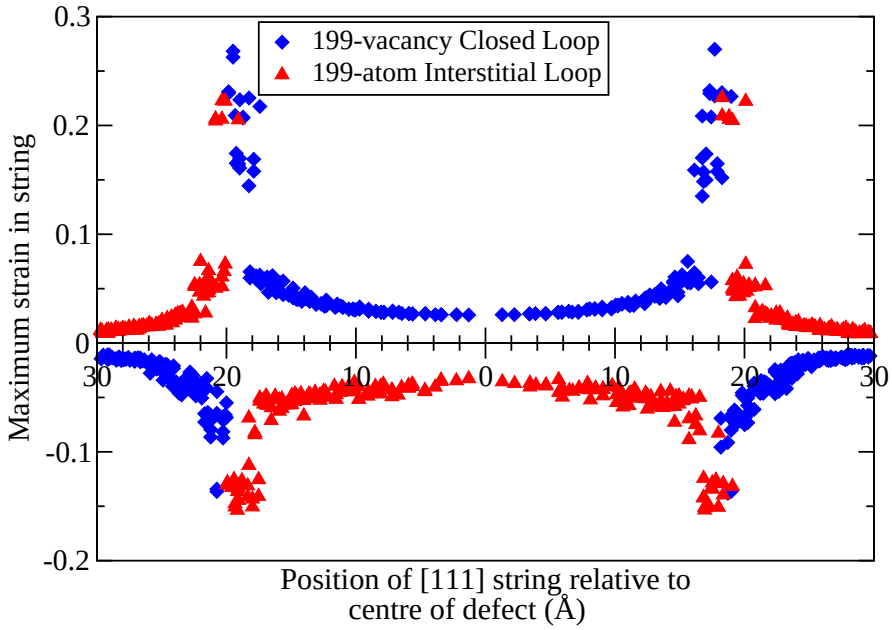


Fig. 4.2: Variation of maximum strain through $\frac{1}{2}\langle 111\rangle$ closed vacancy and interstitial loops in W.

right of the chart, with the other 50% having a negative $[1\bar{1}0]$ coordinate relative to the centre on the left. In addition to these strings that intersect the loops, we have also extended the radius of interest out to 30 Å (each loop has a radius of around 19 Å) to include [111] strings outside the loop. Thus, 482 [111] strings are plotted for each loop.

At both ends of the graph in Figure 4.2 the strains are essentially zero, and these correspond to strings on the outside of the loops that are so far from the defects that they experience little or no distortion. As the strings get closer to the edges of the loops the strains they experience become greater, reaching a maximum (either positive or negative) at the approximate position of the loop-edges at around 19 Å in these 38 Å diameter loops. As we move through the interior of the loops the strains fall away from their maximums at the edges and are near zero again at the centres, before increasing again towards the other edge.

We note that the strains in the defect centres are not as close to zero as those on the outside, far from the loop. This is due to the combined perimeter effect from all directions (as opposed to just one direction for strings exterior to the defect) which leads to some strain (less than 5%), even at the centre of the loop. Only in very large loops do the centres experience no strain, although, in our simulations, this condition was not reached even in a 463-vacancy closed $\frac{1}{2}\langle 111\rangle$ loop in Fe (5.3 nm diameter). The maximum tensile strain at the loop edges is roughly 10% greater than the associated compressive strains. For the closed vacancy loop (blue diamonds) the strains become rapidly more negative (compressive) as the strings get closer to the loop edge from the outside. The strains reach a maximum compression of almost 15% before switching to tensile strains (positive strains) of the order of 25% at the loop edge, which are associated with the absence of atoms. The tensile strains fall to nearly zero within 2 Å of the edge.

In the case of the interstitial loop (red triangles) there are extra atoms inside the loop, which causes the mirror image of the strain patterns seen for the vacancy loop. This time the compressions increase to 15% from inside the loop (which again persist at a less than 5% level to the centre of the loop), which then switches to the 25% tensile strain on the outside of the loop, which drops to less than 3% within about 2 Å. So there is some asymmetry between the structure of interstitial and vacancy dislocation loops, originating from the opposite way that the 'edge-dislocation-like' perimeter is orientated relative to the loop centre. In an interstitial loop the extra atoms are internal, whereas in a vacancy loop they are external. Using the usual $\vdash$ notation for an edge dislocation (where the horizontal line represents the position of the extra half-plane of atoms) an interstitial

loops appears quite different to a vacancy loop in cross-section:



This difference in 'sign' of the loop perimeters is the reason for the asymmetry between the two sets of data shown in Figure 4.2.

However, there is still a degree of structural similarity between interstitial and vacancy loops, which suggests that, assuming the interaction between [111] atomic strings is similar in both cases, the thermal migration of equivalently-sized stable interstitial and vacancy loops might be expected to be quite similar. In what follows, we investigate this issue by calculating the respective diffusion coefficients using long-time finite-temperature MD simulations.

4.3 Finite-temperature MD simulations

In designing the required simulations for defect diffusion at finite-temperature the first decision made concerned the size of the defects to investigate. For interstitial dislocation loops in bcc metals, it has been well established by simulation (see, for example, Zepeda-Ruiz *et al.* [**174**] and Terentyev *et al.* [**177**]) that for defects containing more than four or five interstitials [**177**] the motion is 1-dimensional and parallel to the Burgers vector of the loop. Dudarev [**180**] also identified this transition for interstitial clusters containing more than three SIAs.
Zepeda-Ruiz *et al.* [**174**] found that the size-dependence of diffusivity was simply described by a pre-factor with a power law scaling. Experimental observations, such as those by Arakawa *et al.* [**122**] and Yao *et al.* [**123**], confirm that this 1D motion occurs in the large defects seen under the

electron-microscope, and also that mobile vacancy loops undergo a similar 1D diffusion process. Therefore, in the first instance, we suggest that, for a comparison, it is only necessary to perform a detailed temperature versus 1D diffusivity analysis for one size of interstitial and vacancy defect.

The only size constraint for interstitial loops is that they should contain more than approximately five SIAs, with 10 SIAs certainly being sufficient. However, for vacancy loops, there is a further consideration to be made when choosing a defect-size to simulate. To obtain sufficient statistics to measure diffusivity, the simulations at each temperature must be performed over relatively long timescales. As was seen in the previous chapter, sub-critical vacancy prismatic loops are unstable with respect to the transformation into a vacancy platelet at modest temperatures (see Figure 3.8). Therefore, it would not be possible to obtain sufficient statistics to measure the diffusivity of such a sub-critical loop. However, we can use a finite temperature simulation of a sub-critical loop to illustrate how the loop suddenly opens up into a planar void, and also to show the striking difference in mobilities of the two kinds of vacancy defect. The graph in Figure 4.3 plots the position of a $\frac{1}{2}\langle 111\rangle$ sub-critical closed vacancy loop containing 26 vacancies during a MD simulation at 400K in Fe (D-D potential). In particular, it shows variation in the defect's centre-of-mass (COM) in the [111] direction at 1 ps intervals over the course of a 1 ns simulation.

In Figure 4.3 the loop moves around 4 Å (equivalent to the whole loop moving in the [111] direction by just under two Burgers-vector distances) during the first 200 ps of simulation time. However, at about $t = 200$ ps, the behaviour of the defect suddenly changes. Its COM remains almost fixed for the remaining 800 ps of simulation time, with the only variation

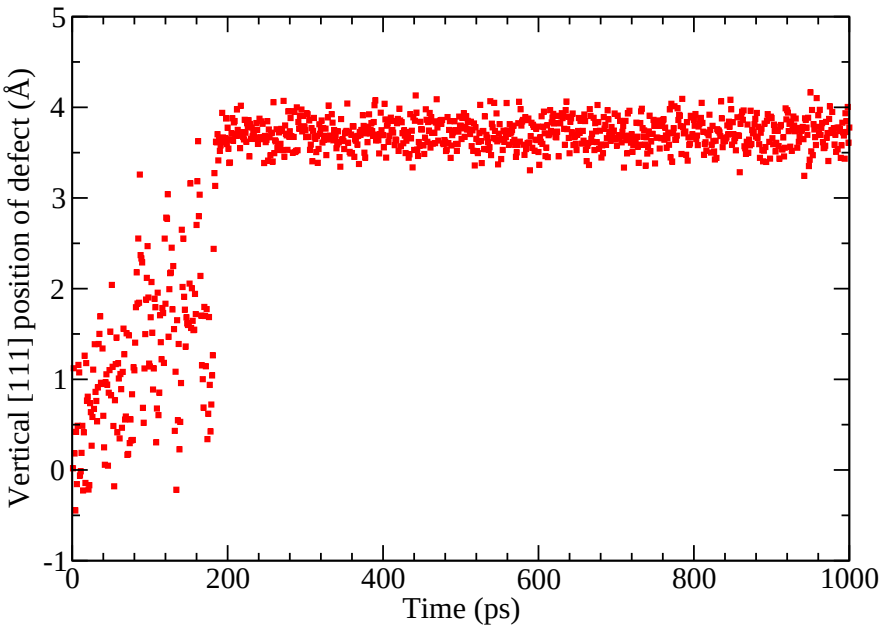


Fig. 4.3: Motion of a sub-critical $\frac{1}{2}\langle 111\rangle$ closed vacancy loop (26-vacancy) at 400K in Fe. The graph shows how the centre-of-mass (COM) of the defect varied in time.

due to thermal fluctuations. Examination of the defect during the simulation indicates that the defect has abruptly transformed into a planar void at $t = 200$ ps. As this simulation demonstrates, such a void defect is immobile, and so the diffusion observed in the initial part of the simulation stops once the transformation has taken place.

These simulation results demonstrate why a sub-critical vacancy loop cannot be used for a diffusion analysis. We therefore use closed vacancy loops in the super-critical size range, together with equivalently sized interstitial loops. The results presented below are from simulations of 61-vacancy/interstitial $\frac{1}{2}\langle 111\rangle$ loops (19.2 Å diameter) in Fe and 187-vacancy/interstitial loops (37.1 Å) with the same Burgers vector in W. For both Fe and W, the $\frac{1}{2}\langle 111\rangle$ loops were inserted into the same periodic lattices of 48,000 and 146,000 atoms, respectively, used in the formation

energy studies described in the previous chapter. In Fe, we have also considered the diffusivity of a super-critical ⟨001⟩ vacancy loop containing 185 vacancies (31.1 Å diameter), along with the equivalently sized interstitial loop.

For loops in both Fe and W, the simulations were performed by first relaxing a given defect to 0K using MS, and then the system was heated and equilibrated to 100K for 5 ps using MD. This was followed by 5 ps at 200K, then 5 ps at 300K, and so on, up to 800K. The eight 'at temperature' MD restart files generated by this process were used as the input configurations for longer simulations of 2 ns, the results of which have been used to calculate diffusivities (for the ⟨001⟩ loops in Fe we only considered four temperatures - 100, 400, 600, and 800K). Note that the temperature control required for these simulations was accomplished via the method described in the previous chapter (section 3.2.2), *i.e.,* using equations (3.3) and (3.4), although temperature rescaling was performed less often in the current simulations. For all the simulations in Fe we have used the D-D potential [**105**], while for W we used the potential described by Derlet *et al.* in [**111**].

During the main MD simulations the position of a defect was computed every 0.1 ps (corresponding to once every 100, 1 fs time-steps). The position or COM of a defect at a given moment was defined as the average position of all the interstitials or vacancies forming the loop. In practice, this was calculated by averaging the positions of atoms with higher energy than those in the bulk (due to the proximity of extra or missing atoms for SIA or vacancy loops, respectively), subject to the constraint that a significant number of other high-energy atoms were nearby (bonded-to) each included atom. The precise filtering parameters used in a particular

simulation varied according to the temperature, but it was confirmed by visual inspection of the included atoms that they were nearly all located in and around the defect. Occasionally, other atoms, not part of the defect, were included in the COM calculation, perhaps as a result of local compressions or tensions caused by thermal vibrations. However, since the overwhelming majority of atoms were part of the defect, these 'rogue' inclusions did not have any significant effect on the COM.

4.3.1 Simulation results

Figure 4.4 shows the 1D motion trajectories for the 61-vacancy $\frac{1}{2}\langle 111\rangle$ loop in Fe at each of the temperatures considered. In particular, the graph shows how the $z = [111]$-coordinate of the defect's COM varied in time in each simulation. The two graphs in Figure 4.5 demonstrate that the motion of vacancy dislocation loops is indeed 1D. Figure 4.5(a) shows how the loop's position varied in the $[1\bar{1}0]$ direction in the 400K simulation in Fe, which is the x-coordinate in the $([1\bar{1}0], [11\bar{2}], [111])$ system (see Appendix A.1). Figure 4.5(b) displays the variation in the remaining direction - the $y = [11\bar{2}]$ direction. In these two graphs we see that there is no change in the loop's position in directions perpendicular to the [111] axis, except for minor thermal fluctuations that cause the COM to vary randomly in time. When comparing the scales of axes in Figure 4.5 with those in Figure 4.4, it is clear that these fluctuations have a much smaller magnitude than the displacements associated with the 1D diffusion in z. Inspection of the trajectories for the motion of the interstitial loops confirmed that they too perform only 1D diffusion parallel to the Burgers vector, as was found in previous simulations, such as those by Terentyev *et al.* [**177**] and Zepeda-Ruiz *et al.* [**174**].

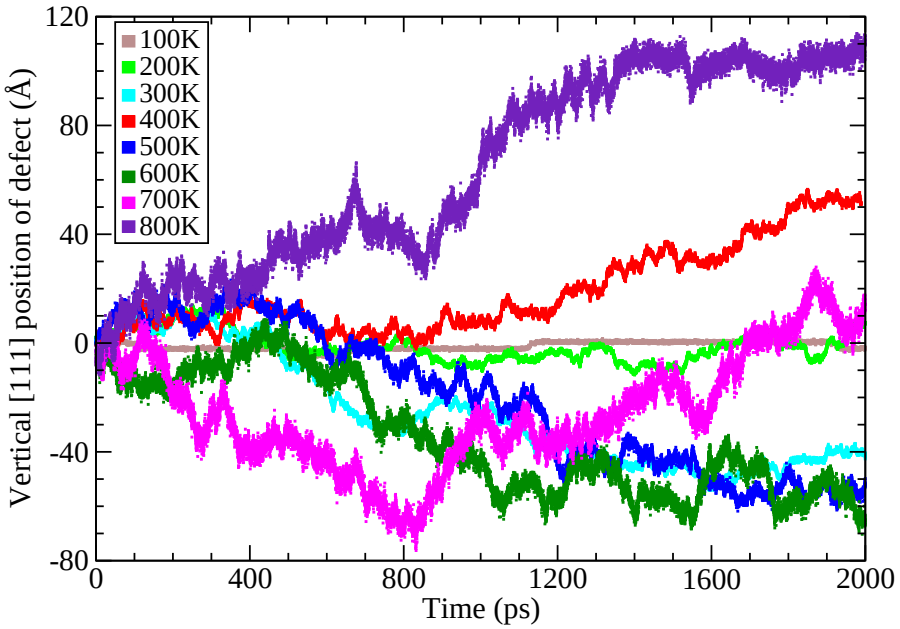


Fig. 4.4: 1D motion in the $z = [111]$ direction of a 61-vacancy closed $\frac{1}{2}\langle 111\rangle$ loop in Fe during finite temperature MD simulations. Defect position was computed every 0.1 ps for each temperature.

On inspection of Figure 4.4, it is apparent that the simulation conditions are unbiased and do not introduce any unbalanced stresses on the defect. This can be understood by observing that there is no particular bias towards either the positive or negative [111] directions. Whilst the simulation set-up was always designed to avoid external forces, by having PBCs which cause stresses to be cancelled-out in all directions regardless of the defect's position in the lattice, it is reassuring to see this validated by the results.

The trajectories for the 187-SIA/vacancy $\frac{1}{2}\langle 111\rangle$ loops in W, and for the $\langle 001\rangle$ loops containing 185-SIA/vacancy in Fe, are on a slightly reduced scale compared to those of the smaller 61-vacancy loops shown in Figure 4.4. This is primarily because of their much larger size (*i.e.,* many more SIA/vacancy point defects must move for the loop to be translated by

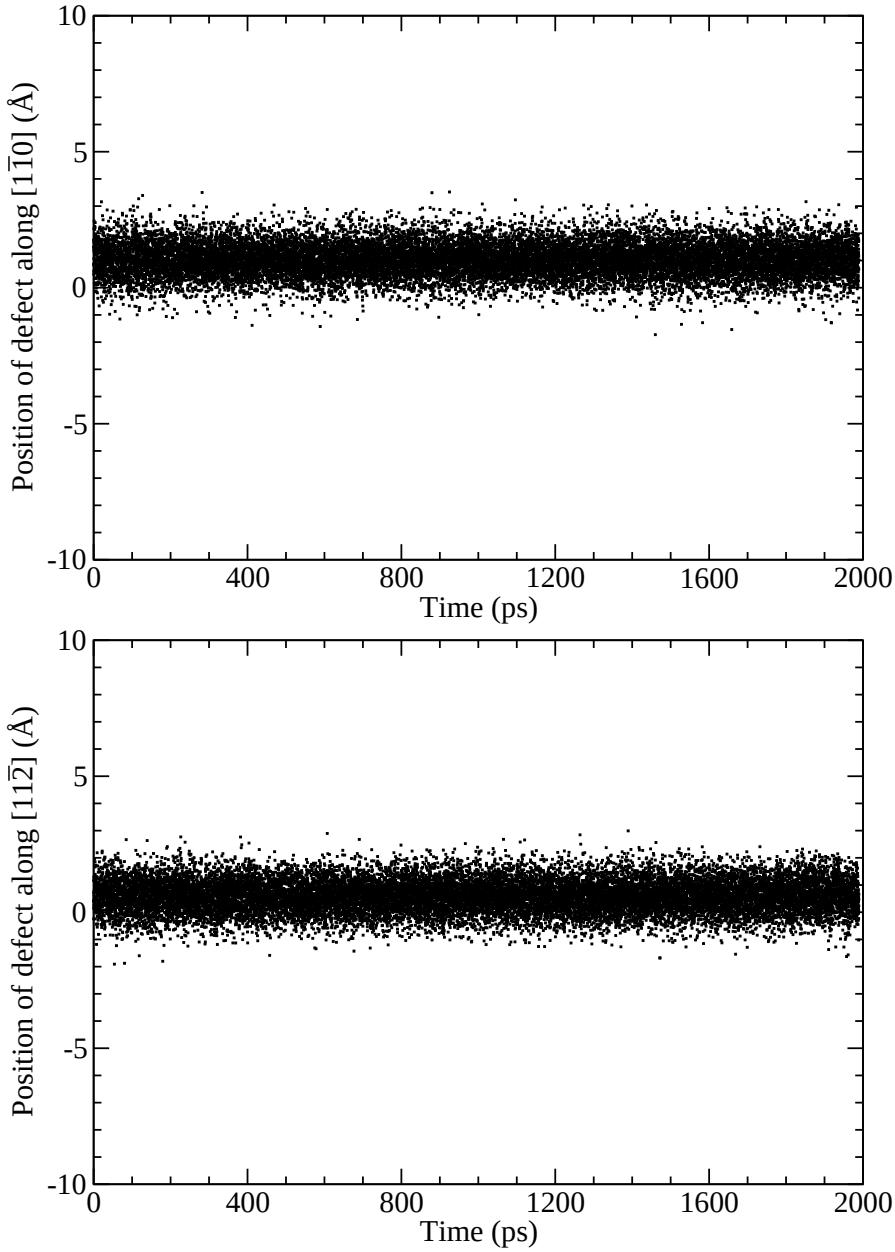


Fig. 4.5: Variation in the (a) $x = [1\bar{1}0]$ and (b) $y = [11\bar{2}]$ positions of the 61-vacancy loop in Fe during a 400K MD simulation.

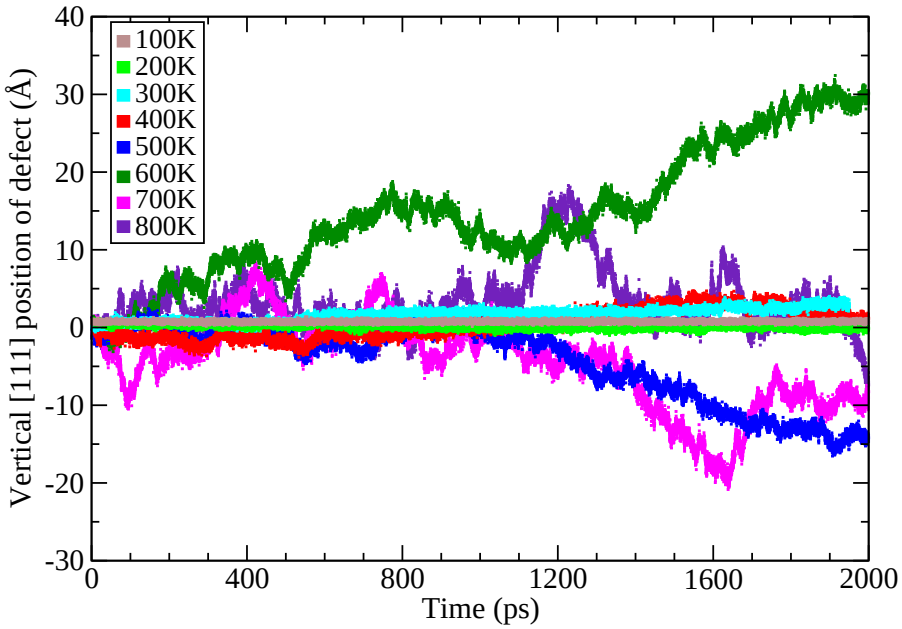


Fig. 4.6: Variation in the $z = [111]$ position of the 187-SIAs $\frac{1}{2}\langle 111\rangle$ loops in W during simulations at finite temperature.

any significant amount). As an illustration of this, consider the results for the 187-SIA interstitial loops in W shown in Figure 4.6. At the lower temperatures, this reduced motion may mean that longer simulations are needed to calculate the diffusion parameters more accurately.

On first inspection of the trajectories shown in Figure 4.4 it is difficult to distinguish much difference in the magnitudes of motion between some of the temperatures. Certainly at 100K and 200K the rate of motion is lower than at higher temperatures, and at 800K the defect appears to have moved much further than even at 700K. However, in between these two extremes the motion appears quite similar, and it is not obvious how the diffusivities vary between the different simulations; for this we need to analyze the data more carefully. Even more intriguingly, comparison of the results for a $\frac{1}{2}\langle 111\rangle$ vacancy loop in Fe with the trajectories obtained for the equivalent interstitial loop, which are shown in Figure 4.7, seem to indicate that the

two types of loops have similar mobilities. For completeness, we also display, in Figure 4.8, the squares of the defect position presented for the 61-vacancy loop (Figure 4.4). This is particularly significant for the calculation of the diffusion coefficient in the diffusion equation (4.3), because it is the differences between the values in the graph of Figure 4.8 that will determine the values of this coefficient at each temperature.

4.4 Calculation of the diffusion coefficient

To obtain the coefficient or constant of diffusion D for the dislocation-loop trajectories we start from its classical definition. In one dimension (*i.e.,* $z = [111]$ or $[001]$ in the present simulations) D is defined via the well-known Einstein relation [**181**, **182**]

$$D = \lim_{t\to\infty} \frac{\langle R^2 \rangle}{2t}, \tag{4.3}$$

where $\langle R^2(t) \rangle$ is the time-averaged (mean) square displacement of the centre of the loop from its initial position. In other words, for the present results we have

$$D = \lim_{t\to\infty} \frac{\langle [z(t) - z(0)]^2 \rangle}{2t}. \tag{4.4}$$

The above equation is subject to the condition that $z(t) - z(0)$ is random and therefore has zero mean, *i.e.,*

$$\langle z(t) - z(0) \rangle = 0. \tag{4.5}$$

This implies that, on average, the defect does not drift away from its initial position $z(0)$ [**183**]. In finite time MD simulations this condition is not normally met, and instead the defect tends to drift away from its initial

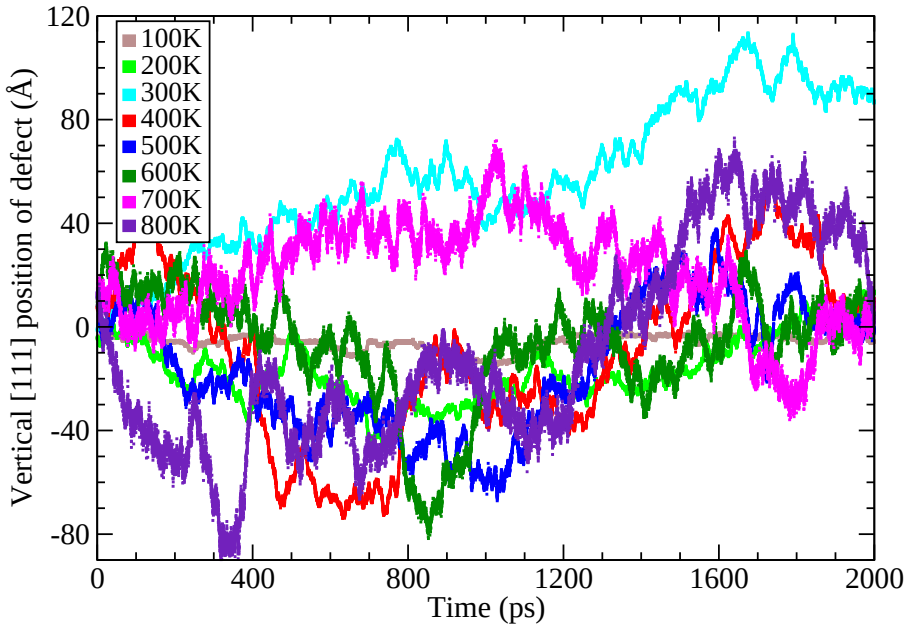


Fig. 4.7: 1D motion in the [111] direction of a 61-atom interstitial $\frac{1}{2}\langle 111\rangle$ loop in Fe during finite temperature MD simulations.

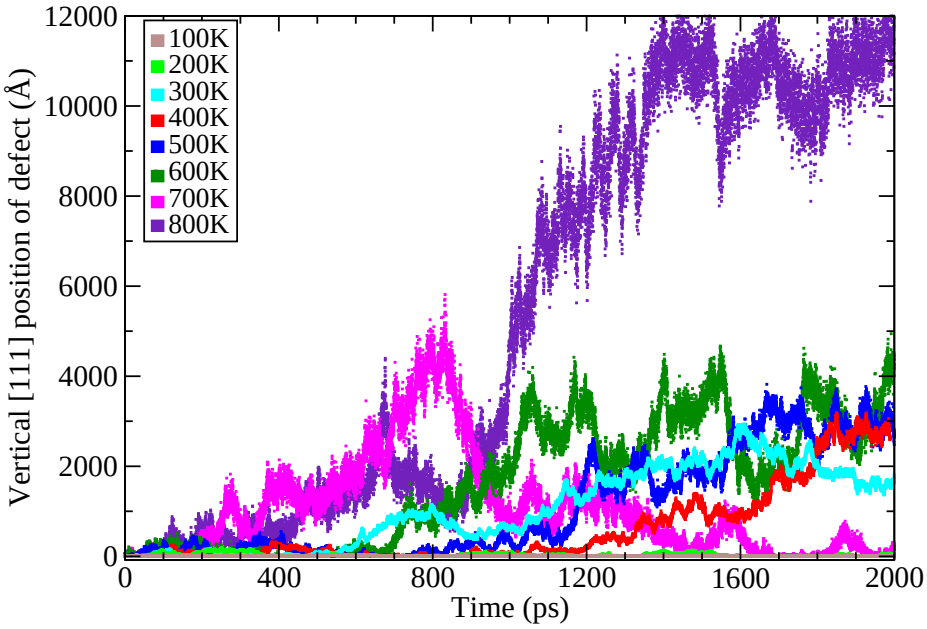


Fig. 4.8: Variation in the [111] squared displacement of the 61-vacancy loops in Fe during simulations at finite temperature.

position [**111**]. To eliminate the systematic drift from our results, which would lead to an error in the calculation of D, we have applied the correction method described by Derlet, Nguyen-Manh, and Dudarev [**111**].

For a finite time simulation of length τ a drift term is subtracted from $z(t)$ to give the corrected loop position $\tilde{z}(t)$ via

$$\tilde{z}(t) = z(t) - t\frac{\sum_{i,t_i<\tau} z_i}{\sum_i^\tau t_i}, \tag{4.6}$$

where the summations run over all discrete positions of the defect trajectory. The mean displacement is then:

$$\begin{aligned}
\langle \tilde{z}(t) - \tilde{z}(0) \rangle &= \left\langle z(t) - t\frac{\sum_{i,t_i<\tau} z_i}{\sum_i^\tau t_i} - z(0) \right\rangle \\
&= \frac{1}{\sum_i^\tau t_i} \sum_{i,t_i<\tau} \left(z(t) - t\frac{\sum_{i,t_i<\tau} z_i}{\sum_i^\tau t_i} - z(0) \right) \\
&= \frac{\sum_{i,t_i<\tau} z_i}{\sum_i^\tau t_i} - \frac{\sum_i^\tau t_i \sum_{i,t_i<\tau} z_i}{\left[\sum_i^\tau t_i\right]^2} - \frac{\sum_{i,t_i<\tau} z(0)}{\sum_i^\tau t_i} \\
&= -\frac{\sum_{i,t_i<\tau} z(0)}{\sum_i^\tau t_i},
\end{aligned}$$

which achieves $\langle \tilde{R}(t) \rangle = 0$ if we define $z(0)$ to be the origin of the system of coordinates defining the position of the defect (*i.e.,* $z(0) = 0$) [**111**].

In [**111**], Derlet *et al.* found that a drift correction of the type described above reduces the statistical uncertainty in D and improves numerical convergence. In [**111**] it is also suggested that the correction does not alter the calculated values of the diffusion coefficient. Recently, however, it has been discovered that the correction for drift results in an underestimation of D by a factor of three. The origin of this additional adjustment factor is described in Appendix E. Note that this adjustment does not qualitatively alter any of the results or conclusions presented in the remainder of this

chapter.

With the drift correction given in equation (4.6) and the adjustment factor derived in Appendix E the diffusion coefficient D for a given defect trajectory is approximated as:

$$D \approx 3\frac{\tilde{z}^2(\tau)}{2\tau}, \tag{4.7}$$

where $\tilde{z}(\tau)$ is the displacement of the loop at the end of the simulation ($t = \tau$).

In an ideal situation simulations would be repeated many times to obtain an averaged D over multiple single-defect trajectories. However, this is not practical because of the significant computational requirements of simply performing a single simulation at each temperature. Following a method similar to that of Guinan *et al.* [**184**], we can obtain good statistical accuracy by splitting the data from a single, long simulation into smaller time-intervals, and then producing an average D over all intervals. For the results presented here, the diffusion coefficients are the averages of coefficients calculated from subsets (in time) of the whole data. The size of the samples ranged from a minimum of at least 100 positions (10 ps) (see below) up to a maximum of 2000 positions (out of a possible 20,000 in each trajectory), or 200 ps of time. The maximum size was partially arbitrary, but was also chosen by considering the need to reduce the statistical error, which is proportional to the inverse of the number of intervals of a given length (*i.e.,* there are fewer possible intervals as the sample size increases so the error increases) [**172**, **177**]. For a given interval size n of positions, all possible samples of this size were considered, and the diffusion coefficients averaged to produce D_n, the average diffusion coefficient for intervals of size n. The final D was then the average over all D_n.

The minimum sample size n_{min} was chosen primarily to satisfy the criteria derived from the relation between the diffusion coefficient and the friction coefficient for Brownian motion, as discussed by Dudarev [**183**], which follows the theory presented by Chandrasekhar [**185**, eq. 175]. In [**183**], it was determined that the minimum sample size should be at least 10 ps. However, as was found by Terentyev *et al.* [**177**], the values obtained for the diffusion coefficient are strongly dependent on size when the interval size is small, and that the value of D_n decreases for increasing n. This dependence on n eventually becomes weaker, and the values of D_n essentially level-out [**177**]. The value of n_{min} was therefore chosen to only consider values of D_n from the region where its value was more stable.

For the relatively small, 61 vacancy/SIA $\frac{1}{2}\langle 111\rangle$ loops in Fe it was acceptable to use $n_{min} = 10$ ps for all simulations, because the variation in D as n_{min} increased was only very slight (less than a factor of 1.5). However, for the $\frac{1}{2}\langle 111\rangle$ loops in W, containing 187 point defects, the dependence was stronger. Experimentation showed that a minimum interval size of 50 ps (500 positions) reduced deviation of D_n (about D) to a minimal level. For the 185 vacancy/SIA $\langle 001\rangle$ loops in Fe, we also found that a minimum sample size of 50 ps (instead of 10 ps) reduced the standard deviation of the calculated Ds by an order of magnitude.

4.4.1 Diffusion results

Applying the statistical analysis described above resulted in the variation of D for $\frac{1}{2}\langle 111\rangle$ loops, in units of $\mathrm{m^2 s^{-1}}$ with temperature in Kelvin, shown in Figure 4.9 for Fe and Figure 4.10 for W. In both graphs the coefficients are scaled by a factor of 10^{-10}. Note the large difference in the scale of the two graphs. This difference in scale is primarily due the fact that in W much

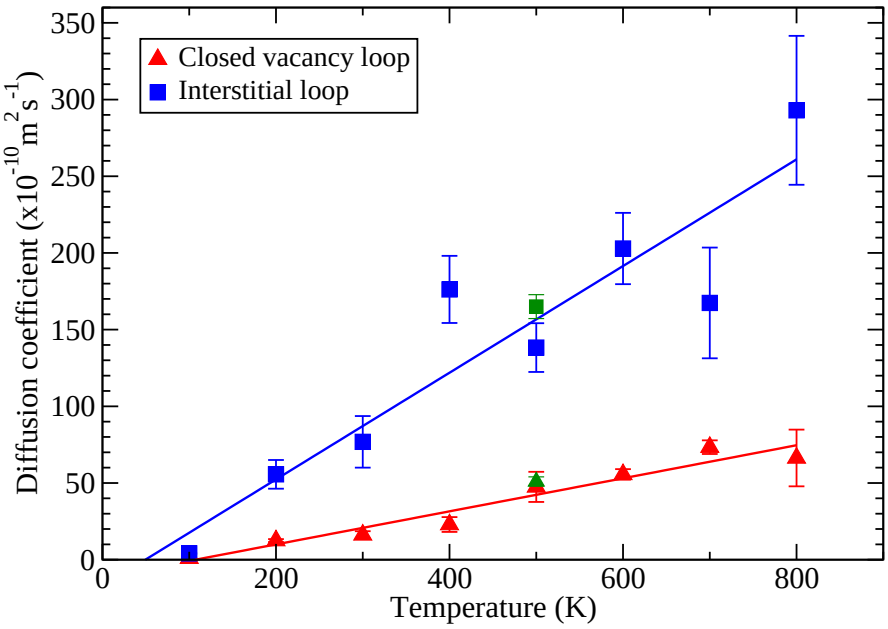


Fig. 4.9: Plot of calculated diffusion coefficients as a function of temperature for 19.2 Å diameter (61 vacancies/self-interstitials) $\frac{1}{2}\langle 111\rangle$ loops in Fe. The fitted curve for each set of data has a linear $D = CT$ form, as suggested by Zepeda-Ruiz *et al.* [**174**]. The green points for each set of data at 500K represents the result for an extended simulation of 20 ns (compared to the 2 ns of the primary results).

larger loops have been simulated (necessary in order to meet the super-critical vacancy loop criteria). In both graphs, and in other diffusivity graphs in this chapter, the error bars indicate the standard error (one standard deviation) in the D_n values about D at each temperature. Additionally, in Figure 4.10 for W there are two extra temperature points for each loop type, at 1000 and 1200K. The reason for these high-temperature points is discussed later.

Before discussing the results shown in Figures 4.9 and 4.10, it is worth considering their validity. In particular, it could be argued that the 2 ns timescale of these simulations is insufficient to unambiguously determine diffusion coefficients, even using the statistical analysis described

previously. To check if increasing the simulation time has any significant effect on the calculated diffusion coefficients we have performed extended, 20 ns, simulations on the two $\frac{1}{2}\langle 111\rangle$ defects in Fe at 500K. The simulations were identical to those described above, except that they were extended by an order of magnitude in time. Performing the same diffusion calculations on the resulting trajectories produced a diffusion coefficient of 16.5×10^{-9} for the 61-SIA loop and 5.1×10^{-9} $\mathrm{m^2 s^{-1}}$ for the 61-vacancy loop in Fe, with standard errors of 7.8×10^{-10} and 3.0×10^{-10}, respectively. The green points in Figure 4.9 show how these 'extended-time' results compare to our earlier results at the shorter timescales. The comparison reveals that, for the vacancy loops at least, these 'long' results fall within the error bars of the 'short' results, and vice-versa.

As the graph in Figure 4.9 indicates there is more scatter in the results for interstitial loops, although the linear fit-line shown in the figure is still clearly the trend in the data. The scatter may be partially related to the lack of statistics, but could also be due to the rotation that the interstitial loops undergo during motion. The rotations are caused by neighbouring self-interstitial-atoms (SIAs) forming the perimeter of the loop sliding relative to each other in the [111] direction. We note that this does not happen in the case of vacancies, which meant that the vacancy loops remained planar during our simulations, and no rotation was ever observed.

The rotation we observe for interstitial loops is between the favoured {111} and {110} habit planes, which has been noted by others (for example, Osetsky *et al.* [**161**]), and results in it being more difficult to precisely define the COM of the defect. We speculate that this is the source of the variation. Thus, while the value of D obtained from the longer simulation of an interstitial $\frac{1}{2}\langle 111\rangle$ loop in Fe does not agree exactly with

the value obtained after 2 ns, it does agree well with the general trend in the data, suggesting that our conclusions would not be altered by extending all the simulations. Of course, to be sure of this, we would need to extend the simulation time for all defects at all temperatures. However, our additional simulations do give some validation to the D values obtained.

For Fe, there is an obvious linear dependence on temperature in both vacancy and interstitial loops, as illustrated by the linear fit lines shown in Figure 4.9, which is in agreement with the findings of Zepeda-Ruiz *et al.* [**174**] for bcc V. Therefore, it would not be appropriate to consider an Arrhenius fit to this data. The diffusion coefficient of both types of dislocation loop are monotonically increasing functions of the absolute temperature. In [**111**], Derlet *et al.* interpreted this linear temperature dependence for the migration of crowdions (single interstitial defects). Dudarev [**186**] extended this method to dislocation loops by following the work of Hiratani and Zbib [**187**]. Considering a Langevin equation for the motion of the COM of the loop, and considering the fluctuation-dissipation theorem [**111**, **182**, **183**], it was found that the diffusion coefficient of the loop should vary linearly as a function of T, and also that it should vary inverse proportionally to the perimeter of the loop. This size dependence has also been noted by Osetsky *et al.* [**172**] and Zepeda-Ruiz *et al.* [**174**]. Zepeda-Ruiz *et al.* [**174**] suggest that the size dependence could be absorbed into a power law pre-factor in an equation for D with a linear T dependence.

The pattern of results shown in Figure 4.10 for W is different. There is no obvious linear dependence on temperature, and an exponential function is the most appropriate fit to the data. Thus, the curves fitted using **GNUPLOT** [**159**] shown in the graph of Figure 4.10 have an exponential

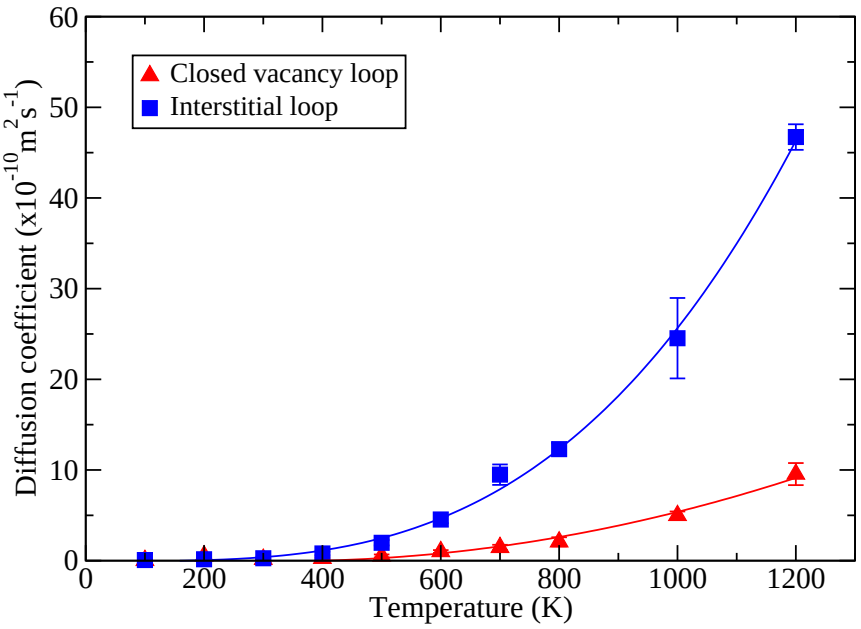


Fig. 4.10: Plot of calculated diffusion coefficients as a function of temperature for 37.1 Å diameter (187 vacancies/self-interstitials) $\frac{1}{2}\langle 111\rangle$ loops in W. The fitted curve for each set of data has a exponential form.

form. Note that while Figure 4.10, and indeed most other graphs in this thesis, was produced using the **GRACE** plotting program, which also has the ability to fit curves, **GNUPLOT** has been used in some cases to perform the fitting because its command-line interface is better suited to defining specific functional forms for curves. Of course, the fitting algorithms used by the two packages give identical results (if properly applied).

When analyzing the results shown in Figure 4.10, and in particular, when comparing them to the results in Fe, we were initially surprised by the non-linearity. For this reason, two further finite temperature simulations at 1000 and 1200K were performed for each $\frac{1}{2}\langle 111\rangle$ loop-type in W. It was hoped that the diffusion coefficients at these higher temperatures would demonstrate a clear linear dependence on temperature. The

simulation duration and set-up were the same as before, as were the calculations used to find D from each trajectory. However, as Figure 4.10 shows, while there may be some evidence for a more linear behaviour at these high temperatures for both loop types, it is still not absolutely certain. Specifically, the extra points still adhere closely to an exponential dependence of D on temperature.

This difference in behaviour compared to Fe may be partially related to the large size of the defects considered in W. Osetsky *et al.* [**172**] observed such a change in behaviour for very large interstitial loops in Fe. They also observed the reduced mobility in fcc Cu, but this was due to the dislocation lines forming the perimeter of the loop splitting into partials; an effect that cannot occur in bcc crystals [**172**]. Osetsky *et al.* suggest that the mechanism causing the severe reduction in mobility (or even complete immobility) for large loops in Fe may be related to entropy effects, whereby the probability of correlated motion of all the SIAs contained in a cluster decreases at large cluster size [**172**]. However, as discussed by Terentyev *et al.* [**177**], there is currently insufficient evidence from dynamic studies of large SIA clusters to be able to reliably define the intersection between the relatively large 1D motion seen in smaller clusters (such as shown in our results for Fe), and the dramatically reduced motion in larger clusters. The difference in behaviour between our two sets of $\frac{1}{2}\langle 111\rangle$ loop results, both interstitial and vacancy, merely adds to the anecdotal evidence for an additional class of behaviour in loop-mobility.

The main point to take from our results is that in both metals the interstitial $\frac{1}{2}\langle 111\rangle$ loops migrate faster than the equivalent vacancy loops, but also that the relative magnitudes of diffusion coefficients are not very different. For the small loops in Fe the value of D is about four times

greater for the interstitial loop than for the vacancy loop at room temperature, while for W the difference is even smaller at low temperature, but does seem to increase with temperature. However, even at high temperature in W the difference in diffusivities between the vacancy and interstitial loops is only around one order of magnitude (or less). From these results it is clear that while $\frac{1}{2}\langle 111\rangle$ interstitial loops do move more rapidly than vacancy loops in Fe and W, the vacancy loops still migrate on similar timescales. We expect the power law scaling of diffusivity with defect size for interstitial clusters observed by others (for example, Zepeda-Ruiz *et al.* [**174**] and Osetsky *et al.* [**172**]) to also be repeated for vacancy clusters. Thus, it is reasonable to expect the observations for a single size of vacancy and interstitial loop to apply to larger sizes of defect, but not smaller ones because the vacancy loops become sub-critical. However, further simulations are required to confirm this, particularly because of the possibility of a different mobility mechanism for larger loops [**172**, **177**].

Before discussing $\langle 001\rangle$ loops in Fe it is worth considering the more traditional graphical representation of diffusivities for the $\frac{1}{2}\langle 111\rangle$ loop results, namely the logarithm of the diffusion coefficient against $1/k_BT$, where k_B is Boltzmann's constant. Using this type of graph is most appropriate if it is believed that behaviour is represented by an Arrhenius law of the type given in equation (4.1) on page 107. Figures 4.11 and 4.12 show graphs of this type for the Fe and W $\frac{1}{2}\langle 111\rangle$ loop diffusivities, respectively.

For Fe, both sets of data in Figure 4.11 appear to fall on the straight line expected for a classical Arrhenius relation. However, in this kind of logarithmic plot it is difficult to truly determine the behaviour at high

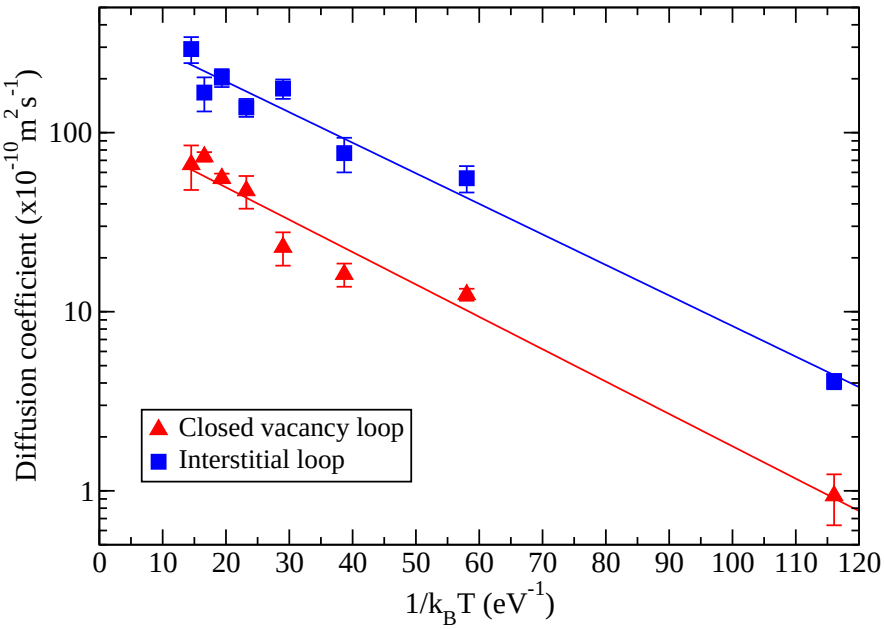


Fig. 4.11: Logarithmic plot of diffusion coefficients as a function of $1/k_BT$ for 19.2 Å diameter (61 vacancies/self-interstitials) $\frac{1}{2}\langle 111\rangle$ loops in Fe.

temperature, corresponding to low values of $1/k_BT$. Zepeda-Ruiz *et al.* [**174**] noted that the divergence from the Arrhenius behaviour was most pronounced at high temperature. Whilst we see some evidence for this in our results, it is likely that simulations at temperatures above 800K would be needed to see the effect more clearly.

On the other hand, even if the data appears to fit an Arrhenius law, this does not mean that it should be applied. According to the original formulation of the equation for thermally activated rate processes (see for example Vineyard [**36**] and Landauer and Swanson [**173**]) the Arrhenius relation given by equation (4.1) should only be applied to events that take place on a fairly infrequent basis. In the equation, this corresponds to a situation when the exponential part is much less than one, *i.e.*,

$$\exp(-E_N^m/k_BT) \ll 1,$$

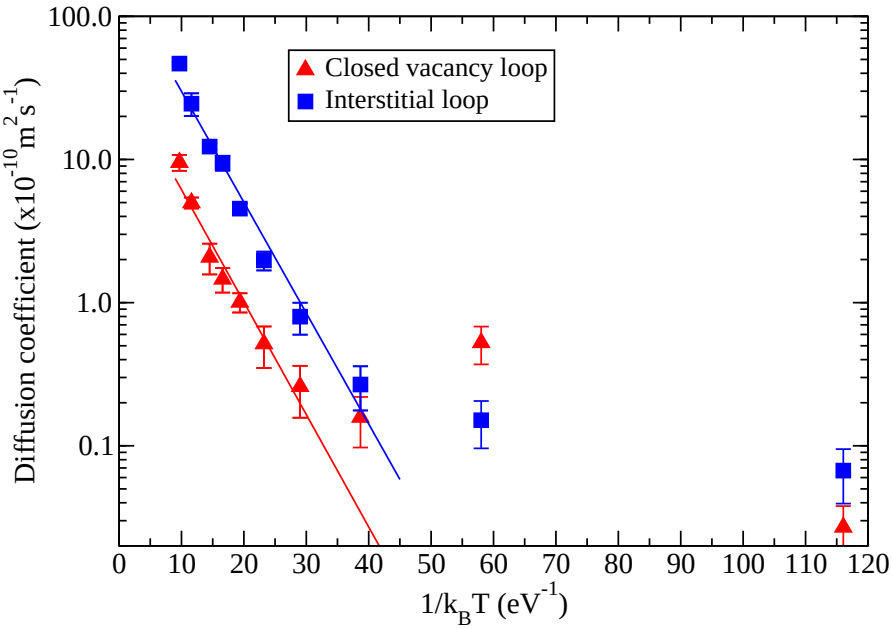


Fig. 4.12: Logarithmic plot of diffusion coefficients as a function of $1/k_BT$ for 37.1 Å diameter (187 vacancies/self-interstitials) $\frac{1}{2}\langle 111\rangle$ loops in W.

which means that the value of E_N^m/k_BT should be relatively large. Below we assess whether this is the case for the current simulations.

In Figure 4.11, the straight-line fits to the data for Fe represent equations of the form given by (4.1). The functions, fitted using **Grace** [**153**], have a migration energy E_{61}^m for both interstitial and vacancy loops of around 0.04 eV, with pre-exponential factors of 4.2×10^{-8} m^{2}s^{-1} and 1.1×10^{-8} m^{2}s^{-1}, respectively. Whilst at low temperatures this means that the exponential part is relatively small (~ 0.01 at 100K) and so an Arrhenius law is justifiable, for higher temperatures it becomes larger, and by 800 K it is close to 0.6. Under such circumstances there is divergence from pure Arrhenius behaviour and we are justified in our original analysis.

However, this does not explain why straight-lines fit the diffusion results for Fe when plotted both linearly (Figure 4.9) and in an Arrhenius form (4.11). The 0.04 eV migration energy obtained if an Arrhenius law is

assumed, which agrees well with the ≈ 0.025 eV migration energy found by Osetsky *et al.* [**172**] in MD simulations of SIA cluster migration in Fe, is relatively low, and so the associated energy barrier (to migration) would be equally small. At even modest finite temperature this barrier is completely 'masked' or swamped by thermal fluctuations, and hence the motion (diffusion) appears to be free (of barriers) resulting in the linear response to temperature shown in Figure 4.9. On the other hand, the energy barrier, even if only slight, is always there and so we can observe a straight-line behaviour on an Arrhenius, log-D versus $1/k_BT$, plot. This observation illustrates one of the difficulties associated in distinguishing between different types of behaviour in finite-temperature MD simulations, namely that the thermal fluctuations can hide what it really happening. The issue is also discussed in chapter 5, where we observe a change in the velocity response of screw dislocations at finite temperature and stress.

For W, the behaviour, at first sight, appears more appropriate to an Arrhenius law. In Figure 4.10 an exponential function was required to adequately fit the data, and now, in Figure 4.12, we obtain excellent straight-line fits, corresponding to an exponential function (equation (4.1)) for the logarithm of diffusivity versus $1/k_BT$. At low temperatures, where the large 187-vacancy/SIA loops show almost no mobility on the 2 ns simulation timescale (see, for example, Figure 4.6), the statistics for the calculated diffusion coefficients D are poor, and so there are sufficient grounds for omitting them from consideration when performing the fitting. For the fits shown in Figure 4.12, we have neglected the data points at 100 and 200K for both loop types, with the 300K result for closed vacancy loops also omitted (the 200K result for a vacancy loop in W is particularly spurious - visualization of the structure suggests that it may have somehow

become a planar void). However, if these low-T results are included, there is only a slight change in the activation energy parameters presented below, even though the fit itself becomes very poor.

The fitted functions for W give $E^m_{187} = 0.178$ eV for the 187-SIA loops and 0.180 eV for the vacancy loops (with pre-factors of 17.8×10^{-9} and 3.8×10^{-9} m^{2}s^{-1}, respectively). Note that, as was the case with the results for Fe, the migration energies of the two loop-types are very similar (hence the parallel lines in Figures 4.12 and 4.11). Since the migration of both $\frac{1}{2}\langle 111\rangle$ SIA loops and $\frac{1}{2}\langle 111\rangle$ vacancy loops occurs via the translation of the individual $\frac{1}{2}\langle 111\rangle$ SIA crowdions that make up their perimeters, it is not surprising that the migration (activation) energies are similar (in fact they would be the same were it not for statistical variation).

The factor of four difference between the migration energies of the W loops compared to the loops in Fe, which can not be wholly explained by a difference between the migration energies of SIA crowdions in the two metals (because it would not be so extreme), might be another manifestation of the observation of others [**172**, **177**], discussed earlier, that there is a different and reduced diffusive-motion occurring in MD simulations of larger loops. However, in the present work, we suggest that the higher migration energy simply means that the onset of a linear response of D to temperature (non-Arrhenius) would only occur at higher temperatures because greater thermal fluctuations are required to swamp the migration energy barrier (which, if present, is fixed). However, as we noted, it was not possible to confirm this conclusively even by performing simulations at temperatures as high as 1200K.

Finally, in Figure 4.13 we display the diffusivity results for the simulations of $\langle 001\rangle$ loops in Fe. The mobility is even lower than for the

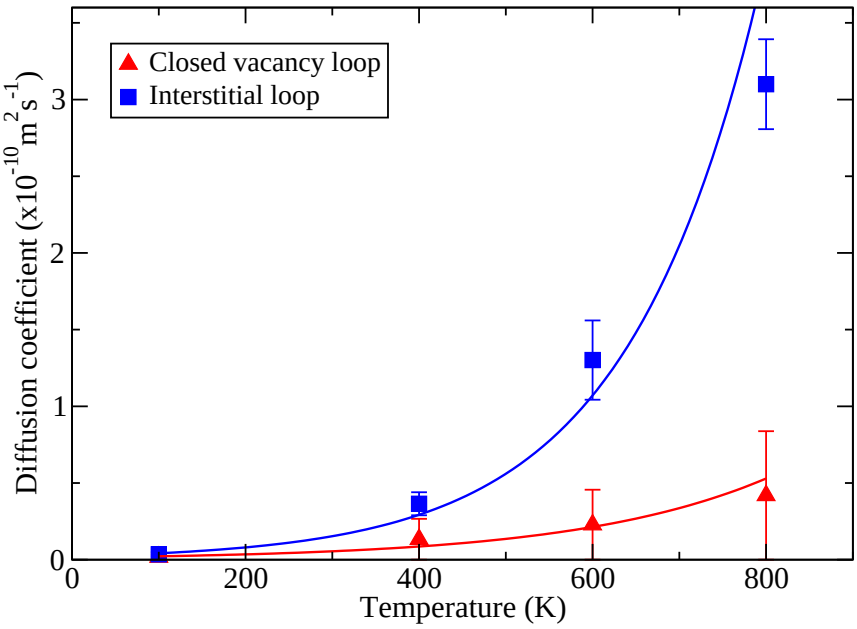


Fig. 4.13: Plot of calculated diffusion coefficients as a function of temperature for 31.1 Å diameter (185 vacancies/self-interstitials) ⟨001⟩ loops in Fe. The fitted curve for each set of data has an exponential form.

large loops considered in W, which are an order of magnitude larger, and at the lower temperatures there is almost no appreciable diffusion on these nanosecond MD timescales. We attribute this low mobility (or even immobility) to the fact that the [001] direction is not a favoured migration path for single SIAs or vacancies. For $\frac{1}{2}\langle 111\rangle$ loops these point defects have low energy barriers associated with motion in the [111] closed-packed direction, which allows for coherent group-motion and hence translation of whole loops. In the ⟨001⟩ case coherent motion parallel to the [001] Burgers vector of all the point defects making up a loop is more difficult. This means that such loops, if not actually immobile, have very low diffusivities, that may not be measurable in MD. In fact, we suggest that further study is required in order to determine if these ⟨001⟩ loops do actually move by diffusing parallel to the Burgers vector in a conventional way, although the

present studies do suggest that the motion is 1D. On the other hand, as for the $\frac{1}{2}\langle 111\rangle$ loop results, our simulations do suggest that $\langle 001\rangle$ vacancy loops are mobile on similar timescales to their interstitial equivalents, albeit at a systematically lower rate.

4.5 Comparison with recent experiments

In some of the recent *in situ* experiments of Yao *et al.* [**123**, **127**] it was possible to perform dynamic observations. The motion of individual loops was observed in both pure Fe and FeCr alloy, although the motion was most pronounced in pure Fe because of the relative absence of solute atoms. The motion consisted of sudden, discrete hops over distances of several nanometres or more, and occurred both during irradiation and afterwards under observation in the electron microscope, at both room temperature ($\sim$ 300K) and 300°C ($\sim$ 570K) (see Gilbert *et al.* [**127**] for more experimental details).

Figure 4.14 shows an example of a loop in pure Fe that moved in 1D over the course of three image frames under the electron microscope beam at 300°C. The direction of motion is parallel to the $\frac{1}{2}\langle 111\rangle$ Burgers vector of the defect and the frames are approximately 34 ms apart. The loop is seen to move between the first and second frames. Yao *et al.* [**123**] have observed this kind of motion in multiple experiments, indicating that many of the loops formed under irradiation are mobile. Their experiments also suggest that it is highly likely that some of the mobile loops are vacancy in nature.

The graph shown in Figure 4.15, displays the results of an analysis, performed by Yao *et al.* [**123**], of the observed 1D motion for a single $\frac{1}{2}\langle 111\rangle$ loop defect in pure Fe. The frequency and amplitude of jumps of this individual loop were measured by examining successive video frames of

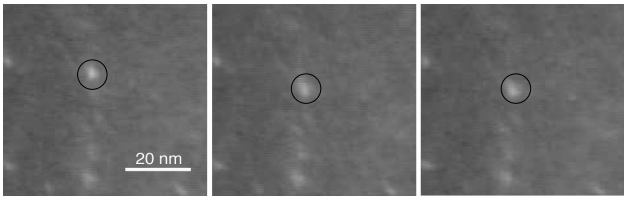


Fig. 4.14: Frames of video recording dynamic observations of ultra-high-purity Fe irradiated using 150 keV Fe^+ at 570K. The loop is seen to 'hop' between the first and second frames. Reproduced from [**127**].

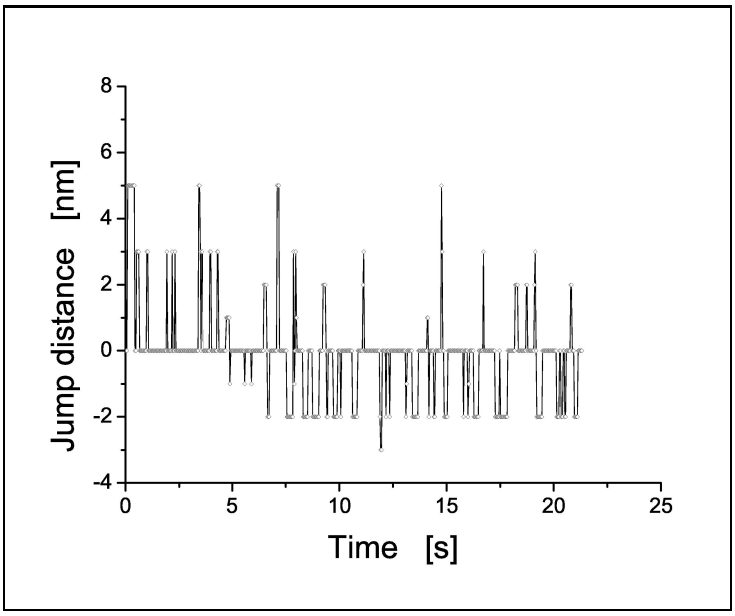


Fig. 4.15: 1D hopping of a $\frac{1}{2}\langle 111\rangle$ loop in ultra-high-purity Fe under the electron beam at 300°C after irradiation. Reproduced from [**127**].

in situ observation after irradiation. In the figure the loop seems to occupy several discrete positions and performs jumps of several nanometres between them, although it spends a large proportion of its time in the 'zero' position. This 'majority-residence' location may be caused by a particularly deep energy minimum produced by local defects or impurities (even in 'pure' Fe there are still impurities) [**127**].

Comparison of the graph in Figure 4.15 with the trajectories obtained from MD simulations (for example, as shown in Figure 4.4) demonstrates

that the motion seen in experiments is much more discrete than the motion observed in atomistic simulations. More significantly, the experimental observations extend over much longer timescales. It is probable that the behaviour shown in Figure 4.15 corresponds to the loop moving between pinning sites in the lattice, perhaps caused by impurities and solute atoms. In between these sites the motion is so rapid that it cannot be resolved on the 34 ms frame-interval timescale of the recordings made by Yao *et al.* [**123**]. Additionally, the loop motion seen in experiments, while still thermally assisted, is unlikely to be purely diffusive. The presence of solutes, other defects, surfaces, *etc.*, will produce significant stresses, and so the hops between pinning sites should more accurately described as stress-induced, thermally-assisted glide.

Even though the simulations are more representative of purely diffusive motion, as a rough estimate, we can work out the approximate velocity of dislocation loops based on the MD results. Consider the trajectory for the 61-vacancy $\frac{1}{2}\langle 111\rangle$ loop in Fe at 300K shown in Figure 4.4. Over the course of the 2 ns simulation it has moved approximately 4 nm from its original position, which equates to a velocity of 2 ms^{-1}. Of course this estimate corresponds to a loop that is much smaller and hence more mobile than those seen in experiments. However, it is likely that even for very large loops the distances moved in a second would be of the order of several centimetres. Thus, it is reasonable to expect the motion or 'hops' between pinning sites to appear as instantaneous events in experiments [**127**].

4.5.1 Migration of vacancy loops to surfaces

As discussed in the introduction to this chapter, it is well known from experiment that interstitial loops are strongly attracted to surfaces. This

partially explains why they are often absent or rare in post-irradiation observations. However, if this is the case for interstitial loops, what is the situation for vacancy loops? There is no reason why they too should not move towards nearby surfaces.

We confirmed this by performing an additional MD simulation on the 61-vacancy super-critical $\frac{1}{2}\langle 111\rangle$ loop in Fe at 500K. This time the periodic boundary conditions, which we have employed in all the other simulations were removed in the [111] direction. This resulted in a free boundary condition, which mimics the situation produced by surfaces in a real material. The relaxed defect was initially at the centre of the box (in the [111]-sense), and so the 'surfaces' above and below it were approximately 50 Å away. The defect was tracked at 500K in the same way as before.

Figure 4.16 compares the trajectory produced during this simulation with the previous trajectory obtained in the absence of the free surfaces. To start with, the two trajectories are broadly similar, indicating that the loop does not immediately feel the image forces produced by the surfaces (the striking agreement results from the fact that both simulations were begun from the same MD restart file). However, after around 70 ps, when the defect has moved approximately 15 Å in the positive [111] direction, the trajectories begin to diverge. Within just a few picoseconds the loop in the new simulation reaches the upper surface of the simulation box and it is no longer possible to resolve its position. This simulation reveals that at 500K the $\frac{1}{2}\langle 111\rangle$ vacancy dislocation loops are attracted to nearby surfaces when as close as 50 Å.

We note that, in contrast with the diffusion simulations presented earlier in this chapter, the motion observed in the presence of free-surfaces is strongly influenced by the stress induced by the surfaces. In this sense it

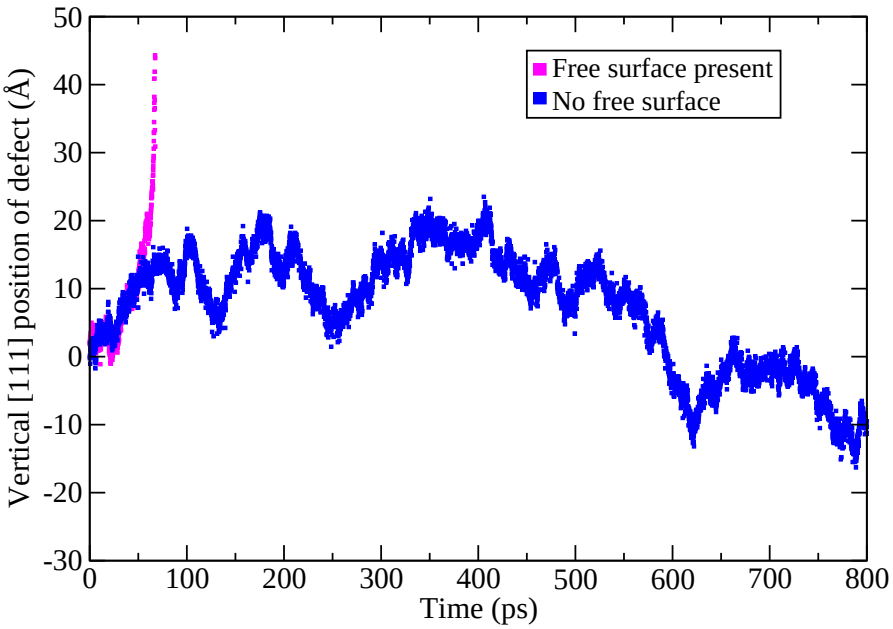


Fig. 4.16: Comparison between diffusion of a 61-vacancy $\frac{1}{2}\langle 111\rangle$ loop in Fe at 500K with periodic boundary conditions and no free surfaces, and with free surfaces above and below the defect (approximately 50 Å away).

may be more representative of the experimentally observed 'hops' discussed in the previous section.

4.6 Coherent motion of interstitial loops

As an extension to their earlier work [**123**], Yao, Jenkins, and Kirk have recently performed further experiments to investigate the formation and evolution of dislocation loops in Fe. In particular, they have been looking for evidence to confirm the recently developed theory of Dudarev *et al.* [**158**] concerning an explanation for the apparent change from the low temperature observation of irradiation damage where $\frac{1}{2}\langle 111\rangle$ loops dominate, to the high temperature case, where $\langle 001\rangle$ loops are more common. In [**158**], Dudarev *et al.* explain that this change in behaviour at

high temperature is brought about by the change in the elastic properties of Fe, which occur as the temperature of the $\alpha \rightarrow \gamma$ phase transition at 912°C is approached.

In some of the new *in situ* experiments, Yao, Jenkins, and Kirk [**178**] have made video recordings of defect evolution in which they observe the coherent motion of interstitial $\frac{1}{2}\langle 111\rangle$ loops. Specifically, they note situations in which several loops (most often three) line up along a single direction, perpendicular to their common Burgers vector. These loops then continue to move along their [111] glide prisms, but now the group of loops move coherently rather than independently as they did before. In the irradiation experiments, this coherent motion is often seen as a prequel to the groups of loops coalescing to form single, larger loops as a result of the migration of single SIA and small SIA-clusters towards the dislocation loops. Osetsky, Serra, and Priego [**188**] have previously investigated the interaction between interstitial loops in Fe, and found a strong attraction between non-overlapping (*i.e.,* they cannot merge by gliding solely in the [111] direction) loops with the same Burgers vector. There seems to be an opportunity to extend their studies, with a particular emphasis on relating the simulations to experimental observations.

We have begun a series of MD simulations for $\frac{1}{2}\langle 111\rangle$ interstitial loops situated in close proximity. Initially, we have considered a triplet of 19-SIA (10.7 Å diameter) loops lined up along a $[1\bar{1}0]$ direction (*i.e.,* they all have the same $[11\bar{2}]$ position) in an Fe lattice, but with a random position in the [111] diffusion/Burgers vector direction. As before, the simulation cell has periodic boundary conditions in all directions (we do not want surfaces to affect the motion). However, this meant that we had to be more careful about placing the defects. Equally spacing the three loops along the

$[1\bar{1}0]$-axis of the simulation cell means that each loop sees two other identical loops at equal but opposite separation distances. In trial simulations of such a configuration no coherent motion was observed because an outer loop (first) could not position itself favourably relative to a middle (second) loop, without being pushed from this position by the other outer loop (third), which was also trying to align itself with the middle loop. In other words, an outer loop could not align itself favourably with both the centre loop and the other outer loop, which was exactly the same distance away through the periodic boundary, because then the other outer loop would not itself be aligned favourably compared to the middle loop. This resulted in the loops never becoming fully trapped by each other and the trajectories always remained incoherent.

The solution to this problem was to have a 'skin' region in the $[1\bar{1}0]$ direction, at either edge of the lattice, which acted as a buffer zone, reducing the interaction forces between the outer loops and making them much less than the forces between the outer loops and the middle loop. Such a configuration is shown in Figure 4.17. The simulation cell in this case is a $30 \times 20 \times 160$ simulation cell (in the $[1\bar{1}0] \times [11\bar{2} \times [111]]$ coordinate system - see Appendix A.1) of 576,000 Fe atoms (plus the 57 extra atoms to create the interstitial loops). In Figure 4.17a the three 19-SIA loops are seen lined up along $[1\bar{1}0]$ in the plane perpendicular to their [111] Burgers vector, whilst in Figure 4.17b the random initial position in z=[111] of the same three loops is shown. The skin region in this setup was 20 Å wide in the $[1\bar{1}0]$ direction, leaving just over 80 Å for the placement of the three loops. They were placed evenly in this core region, giving a distance between adjacent loop centres of about 2.7 nm, which is much less than the 6.7 nm gap between loops one and three through the periodic boundary

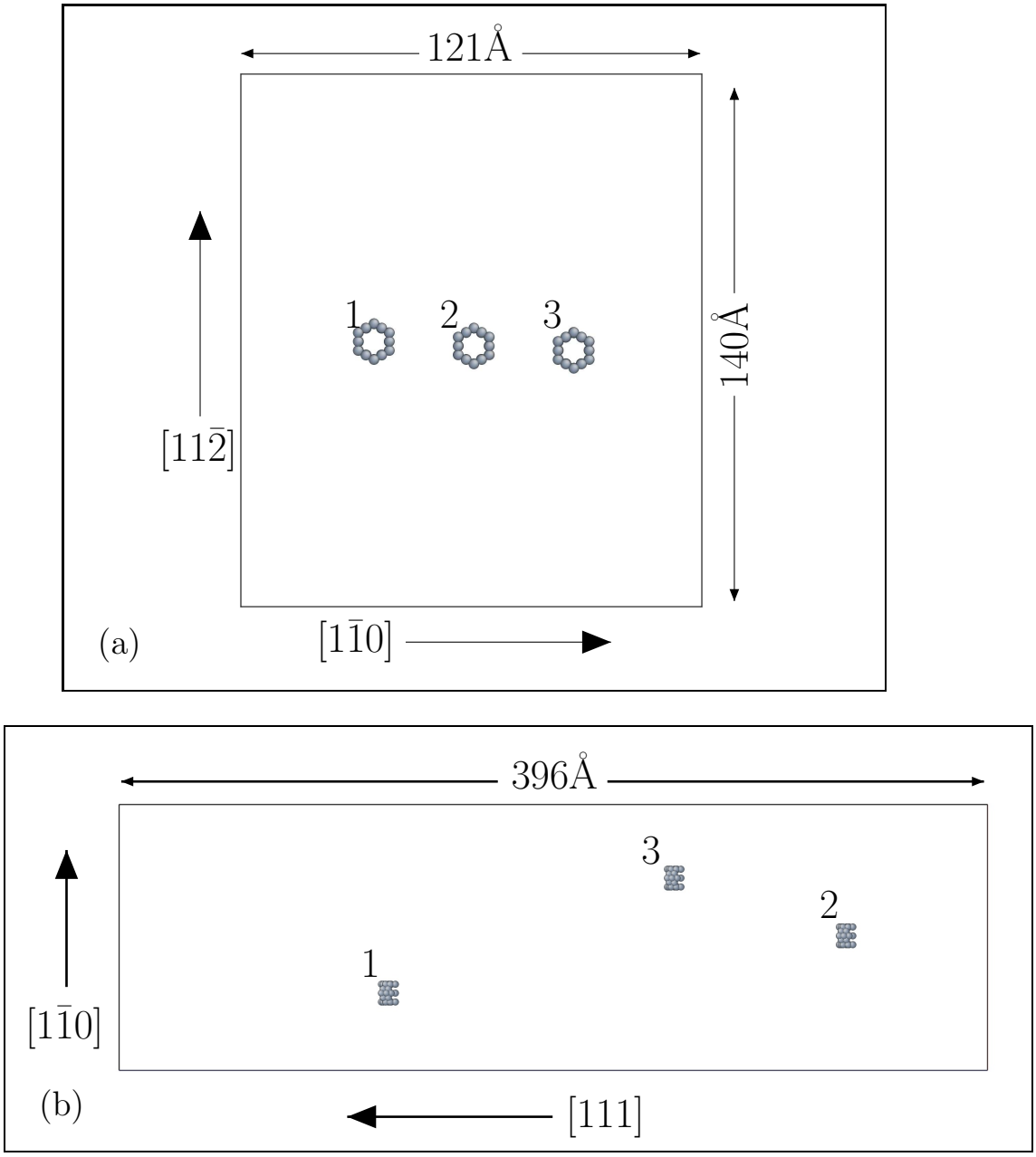


Fig. 4.17: Initial positions of three 19-SIA interstitial $\frac{1}{2}\langle 111\rangle$ loops in Fe. The view in the (111) plane in picture (a) shows them lined up along $[1\bar{1}0]$, while the view looking along $[11\bar{2}]$ shown in (b) illustrates their random displacement in [111].

(*i.e.,* 4 nm skin plus 1.35 nm to the centre of each loop).

After relaxing this configuration the system was heated up to 500K in 100K, 5 ps increments in the same way as for the single loop simulations. The 500K simulation was then continued for several nanoseconds, with the positions of the three defects recorded every 1 ps. The 1D trajectory of the three 19-SIA interstitial loops during the simulation is shown in Figure 4.18. We confirmed that the only motion performed by all three defects was in the [111]-direction, as shown in the graph, and that they remained fixed relative to the other coordinate directions. Note that in Figure 4.18, defects two and three move through the periodic boundary at ± 200 Å during the course of the simulation. Thus the trajectories, which show sudden jumps from one side of the simulation box to the other, differ from those seen earlier in this chapter where motion through a periodic boundary was 'folded-out' to produce a continuous 'real' displacement from the initial position.

In Figure 4.18 the three loops are initially separate and as the simulation progresses they begin diffusing independently. However, after about 0.5 ns loops two and three, which were initially quite close together, occupy the same vertical [111] position. They begin to move together, and continue in this way until loop one also joins them after almost 3 ns of simulation. We continued the simulation for a further 3.5 ns to confirm that the three loops stay 'attached' to one another in the mobility sense. Figure 4.19 shows the relative positions of the three loops at the end of the simulation. In the close-up picture 4.19(a) it appears as though the three loops have lined-up in a particular orientation. The coherent motion observed in this simulation agrees well with the previous results of Osetsky, Serra, and Priego [**188**].

The orientation is close to one of the preferred habit planes for $\frac{1}{2}\langle 111\rangle$

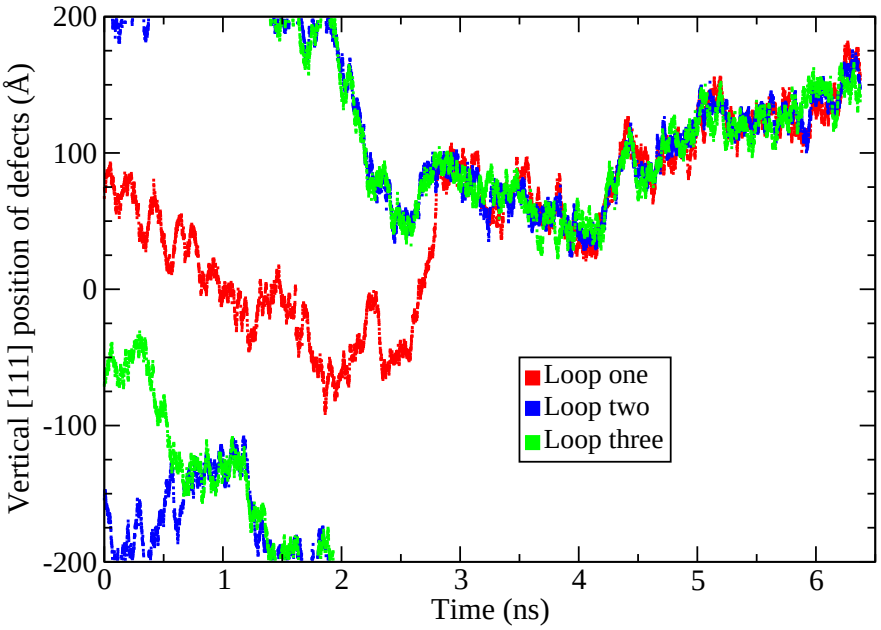


Fig. 4.18: Trajectories of three 19-SIA $\frac{1}{2}\langle 111\rangle$ loops in Fe at 500K, all contained within the same simulation cell.

interstitial loops, *i.e.,* the loops are all sitting on the same habit plane as each other. It is well known from previous MD simulations (see, for example, the work of Osetsky *et al.* [**161**]), and also from experiment (for example Masters [**162**]), that the habit plane of $\frac{1}{2}\langle 111\rangle$ SIA clusters in Fe varies from {111} to {110} during motion in the direction of the Burgers vector because individual interstitials jump in opposite directions in the [111] direction [**161**]. Indeed, we observed this 'backwards-and-forwards' rotation about the COM during the finite-temperature simulations of single interstitial loops discussed previously in this chapter (no rotation was observed for vacancy loops). In the configuration shown in Figure 4.19(a) the habit plane of the three loops is close to (101). The fact that all three loops lie in the same habit plane is a further demonstration of coherence. In [**188**], Osetsky *et al.* do not specifically mention the orientation of complexes of loops with the same Burgers vector (but they do consider the

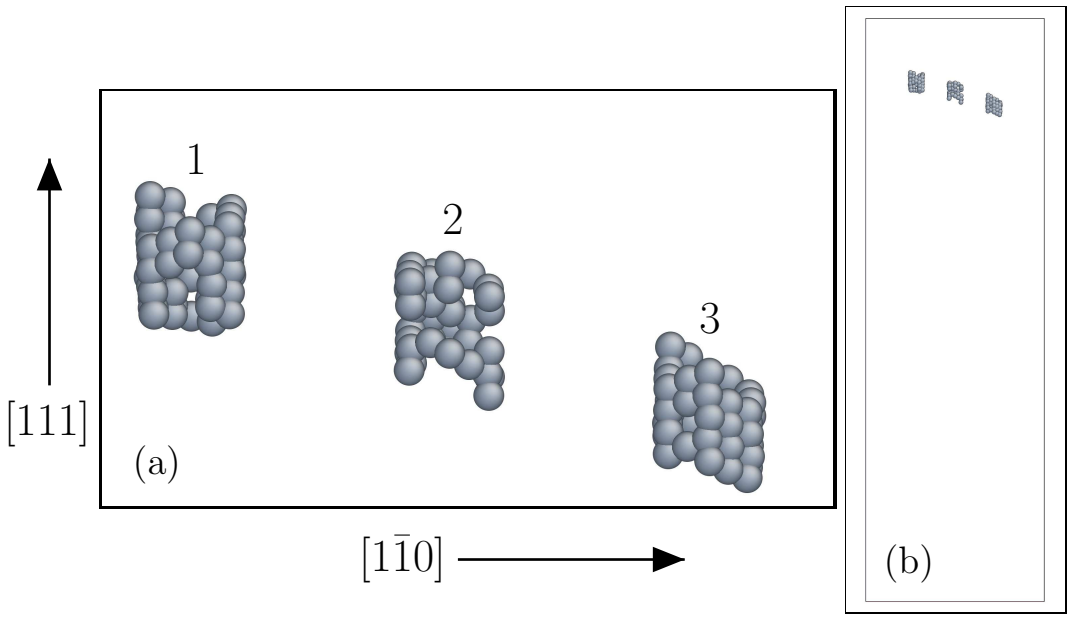


Fig. 4.19: Final positions of three 19-SIA loops after 6.5 ns of simulation time at 500K. (a) shows a close-up of the relative orientation of the three loops, while (b) displays their positions in full simulation box. Note that in this (relatively) high temperature simulation, the defects appear extended in the [111] direction because the strain fields cause additional atoms to have energies significantly above the average.

merging of loops with different Burgers vectors), although we expect that this was the case.

Although our studies in this area are still at a preliminary stage, we can compare the relative diffusivities of loops moving together to values of D obtained from loops moving singly. Using the same analysis technique described before (see section 4.4) we have calculated the diffusivities of the three 19-SIA loops, but have only considered the part of the trajectory (as shown in Figure 4.18) where all loops moved coherently, *i.e.,* for $t >\sim 3$ ns. We have also performed a second simulation of three 19-SIA loops with the same setup as before, except that the initial [111] position of the defects was different. In this second simulation, the loops 'came-together' much

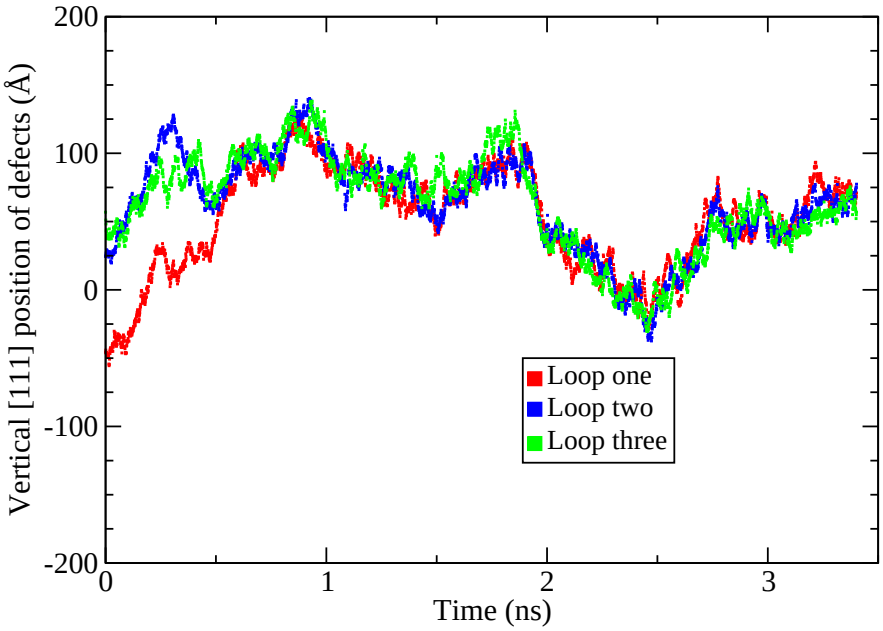


Fig. 4.20: A second simulation of three 19-SIA interstitial loops migrating coherently at 500K.

quicker, after only 0.5 ns, and we continued the simulation for a further 3 ns. The trajectories from this second simulation are shown in Figure 4.20. Analysing both sets of results produces six different values of D (three from each simulation), with an average value of 25.2×10^{-9} m^{2}s^{-1}, and the average standard deviation was 3.9×10^{-9}, which encompasses all of the D values obtained.

Simulations of single 19-SIA loops at 500K in Fe produce a value for the diffusion coefficient of around 33×10^{-9} m^{2}s^{-1}, which suggests around a 20 to 25% reduction in the diffusivity of the loops when they form complexes. Meanwhile simulations of two 19-SIA loops moving coherently produce a calculated diffusion coefficient that is approximately equal to that obtained for a triplet of loops. This may indicate that, at least at the 2.7 nm separation distance simulated so far, the reduction in the diffusion coefficient is solely due to the interaction between adjacent loops and is not

the result of the increased number of SIAs. If the latter were true then we would have observed a noticeable difference in the diffusivities of a doublet containing 38-SIAs in total compared to the 57-SIA triplet. Of course, further simulations covering a wider range of loop-complex configurations is needed to confirm these preliminary observations.

4.7 Concluding remarks and further work

In this chapter we have performed constant temperature simulations of dislocation loops to demonstrate that $\frac{1}{2}\langle 111\rangle$ vacancy loops diffuse on similar timescales as $\frac{1}{2}\langle 111\rangle$ interstitial loops in both Fe and W. However, our simulations confirm the observations from experiments and other simulations, that the motion of vacancy loops is systematically slower than that of interstitial loops. Additional simulations in Fe suggest that this situation is also repeated for $\langle 001\rangle$ loops, although the motion of both interstitial and vacancy loops of this type appears much reduced. Simulations have also demonstrated that vacancy loops can be lost to nearby surfaces just as readily as interstitial loops, by performing stress-induced, thermally assisted glide. Thus, defect statistics derived from electron microscope investigations of irradiated materials will at best give lower estimates of defect populations when defects (interstitials *and* vacancies) can exit the system via thermal migration towards free surfaces.

To improve and clarify our conclusions for the mobility of isolated loop defects it would be beneficial to repeat the finite temperature simulations for alternative sizes of loop. In particular, it would be interesting to explore the possibility of another type of behaviour in very large loops, for which there is currently only anecdotal evidence (see, for example, Osetsky *et al.* [**172**]). This would be computationally expensive and could

only be achieved by performing simulations on a range of defect sizes at a range of temperatures, so that a transition size and/or transition temperature might be identified. Additional simulations are also necessary for a more complete comparison between the results in Fe and W. The current results are for very different loop sizes, and it would be beneficial to perform diffusion simulations in Fe on the same 187 SIA/vacancy loops considered in W.

We have also presented the preliminary results from our investigations into the experimentally observed coherent motion of interstitial loops in Fe at finite temperature. We observe a strong attraction between loops of the same Burgers vector and find that the motion of loop complexes is reduced compared to the motion of isolated loops. In the future this work will be extended by considering alternative sizes of interacting loops, both smaller and larger. We will also investigate the effect of the separation distance between interacting loops, particularly with reference to the 'strength' of interaction and the effect on mobility of the resulting complex.
Osetsky *et al.* [**188**] saw that small loops were able to climb due to the interaction with a larger loop nearby and therefore be absorbed by it, but only if they were sufficiently close. For larger separations the climb process did not occur. In such circumstances it would be interesting and valuable to investigate the mobility of complexes. As suggested by Osetsky *et al.* [**188**], it may be that at some point the complexes become immobile, either due to the interaction of several large loops, or by the interaction of smaller loops over large distances. In this case the implications for defect accumulation in irradiated materials may be severe. Increased accumulation may cause severe radiation induced hardening leading to brittleness, especially if the defects impede the motion of screw and edge dislocations, which move in

response to applied stress (see chapter 5).

Part II

SCREW DISLOCATIONS: THE CARRIERS OF PLASTIC DEFORMATION

5. MOLECULAR DYNAMICS SIMULATIONS OF SCREW-DISLOCATION MOTION IN FE

In fusion components, the radiation induced embrittlement and hardening of bcc metals such as Fe, is a significant problem. It is well known that screw dislocations are the rate-limiting carriers of plastic deformation in bcc metals [**22**, **189**], and therefore the impedance of their motion is a significant factor determining the mechanical properties of fusion materials. In this chapter we develop mobility laws for the motion of screw dislocations through pure bcc Fe under applied stress at finite temperatures using large-scale MD simulations. Accurate mobility laws are needed for input into dislocation dynamics simulations where, together with descriptions of defect interactions, they can be used to model the behaviour of systems of dislocations in a realistic representation of irradiated materials.

5.1 Introduction

Screw dislocations have been the subject of much study, both experimentally and computationally, ever since they were first distinguished from edge dislocations and other defects in the 1930s, by Burgers [**190**] and others. In 1960, P.B. Hirsch [**189**] was the first to introduce the idea that the temperature-dependent plastic behaviour of bcc materials was associated with the mobility of $\frac{1}{2}\langle 111\rangle$ screw dislocations at low temperatures, which was later confirmed by experiment (see discussion

in [**191**]). In particular, the motion of many dislocations normal to their Burgers vectors under applied stress results in *slip*, which is the most common manifestation of plastic deformation [**22**]. Further information on the properties, particularly under equilibrium, of screw dislocations can be found in the excellent book by Hirth and Lothe [**150**], whilst a review of early studies into the thermodynamics and kinetics of their motion (or slip) can be found in the publication of Kocks *et al.* [**192**].

In the next chapter, we will consider, in detail, modelling of the core structure of screw dislocation by interatomic potentials, which may have implications for the validity of the simulation results presented below, but in this chapter we focus on perfecting the large-scale MD simulation of screw dislocations in pure bcc materials. However, we note that, in a recent study, Vitek [**193**] found that the equilibrium core structure may not play a significant role in the response of screw dislocations to stress.

Screw dislocations have, as a result of their non-planar structure, low mobility compared to other defects, such as edge dislocations, and require significant stresses before they move at all. It is for this reason that their motion is one of the characteristic mechanisms behind plastic deformation. It is now widely accepted that low-stress limit of screw dislocation motion is determined by the thermally-activated formation of kink pairs ('double-kinks'). This mechanism was first suggested in connection with metals (specifically fcc Cu) by Seeger in the mid-1950s (see Seeger [**194**]), and later applied to bcc metals (Fe) by Basinski and Christian in 1960 [**195**] to explain experimental results. Since then the theory has been expanded and quantified by Seeger and Šesták [**196**], Seeger [**197**], and Hirth and Lothe [**150**]. Meanwhile, experimental studies (for example, see the work of Brunner and Diehl [**198**] on bcc Fe), have confirmed the validity

of the kink-pair model for the flow stress in high-purity bcc metals [**199**].

In a review published in 2002 by Moriarty *et al.* [**200**] the current state of research in the atomic simulation of screw dislocations is discussed, with particular focus on bcc metals. Specifically, they mention the need to resolve the disagreement in the literature between simulation and experiment. In simulations only kinks on {110} planes are ever considered because, for example, Xu and Moriarty [**201**] show that the other planes, such as {112}, have large kink formation energies and heights. Conversely, Hollang *et al.* [**202**] found from experiments that screw dislocation motion in ultra-high-purity bcc Mo takes place via kink formation on {112} planes at all temperatures and stresses. However, both Brunner and Diehl [**198**, **203**, **204**] and Seeger [**205**] discuss experimental results that indicate different temperature regimes where the preferred slip plane can be either {110} or {112}. In another 2002 review Seeger [**199**] indicates that slip on {110} planes has been observed in several bcc metals at low temperatures, whereas at high temperatures {112} planes dominate.

Also in [**200**], Moriarty *et al.* discuss the motion of screw dislocations under high stress in the so-called phonon drag regime [**206**, **207**], and pointed out that, as of 2002, this remained the primary mechanism explored in MD using small, confined lattice volumes (see, for example, Chang *et al.* [**208**]). The velocities produced in this regime are the most readily measurable on MD timescales, although the observed behaviour may not be strictly representative of screw dislocations during plastic deformation. The motion seen at these high stresses is usually linearly dependent on stress [**200**], and the gradient of this linear-response decreases with increasing temperature as a result of friction. In the work presented below, we also explore a linear velocity-stress regime at high stresses in a

relatively large simulation cell, as well as a definite kink-pair thermal activation regime at low stress, and what (in our case) caused the transition between the two.

Recently, there have been advances in both techniques and computational power, which have allowed for the simulation of screw dislocation in bcc metals at lower stresses. Marian *et al.* [**209**] were the first to fully investigate the smooth motion of dislocations through the formation and propagation of atomic-sized kinks using dynamic simulations on Fe with the EAM potential of Ackland *et al.* [**86**]. They also explored the motion of screw dislocations under very high stress conditions, which is characteristic of conditions experienced by materials under shock [**209**]. Similarly, Domain and Monnet [**210**] simulated screw dislocation motion in Fe using the Mendelev [**82**] interatomic potential. They investigate the response of $\langle 111 \rangle$ screw dislocations subjected to pure shear strain, which leads to a build-up of stress, and observed that the dislocation glides (slips) and remains in a (110) plane. They also found that the motion occurred exclusively through the nucleation and propagation of double-kinks.

In [**210**], the main physical quantity measured by Domain and Monnet is the critical stress at which the dislocation begins to move at each temperature, although they also make estimates of the activation energies for the nucleation of kinks. The critical stresses appear to differ significantly from experimental results, but Domain and Monnet explain this in terms of differences between the experimental and simulation set-up. It is also suggested that the MD results are in good agreement with experimental observations and thus provide the first reported validation of the double-kink formation theory for dislocation motion [**210**].

Chaussidon *et al.* [**211**] also presented results from screw dislocation

studies using the potential of Mendelev *et al.* [**82**]. In particular, they discussed the differences between results produced using this potential, which favours the correct non-degenerate core structure (see next chapter) [**210**–**212**], and one that does not by Simonelli *et al.* [**213**]. In their research, the non-degenerate core caused the dislocation motion to stabilise on a {110} glide (slip) plane, which is in agreement with some experiments [**214**, **215**]. At the same time, it was observed that the degenerate core favoured by the Simonelli potential produced a tendency to follow {112} average glide planes. Conversely, the simulations of Marian *et al.* [**209**] were performed using the potential of Ackland *et al.* [**86**], which is known to produce a degenerate screw core, but they found a preference for a {110} glide plane.

Additionally in the work of Chaussidon *et al.* [**211**], there is a very good investigation and discussion of the various influences that the simulation boundary conditions have on the motion of the dislocation. They impose periodic boundaries along the length of the dislocation line, as is usual, but have free or pseudo-free surfaces in the other two directions. In particular, they suggest that having a periodic boundary in the direction of motion or glide (in their case in the x-direction) causes the line to favour the {112} slip planes, whilst having a free surface in that direction stabilises the glide on a {110} plane. Chaussidon *et al.* suggest that the image forces produced by the free surface in the direction of motion are only slight, but it may be sufficient to stabilise slip on a {110} plane. While such a slip plane does agree with the experimental evidence cited in [**211**] (namely, Spitzig and Keh [**214**] and Kuramoto *et al.* [**215**]), more recent studies on bcc Fe by Brunner and Diehl [**198**, **203**, **204**] suggest that kinks can form on either {112} or {110} planes, depending on the temperature regime. This concept

was also discussed in the review by Seeger [**199**]. We will revisit the findings of Chaussidon *et al.* [**211**] later in this chapter, when we discuss the favoured glide plane in our simulations.

An unfortunate consequence of having a free boundary in x is that Chaussidon *et al.* [**211**] are only able to measure the dislocation motion for a very short time, namely 100 ps, during which time the dislocation moves over just 25 Peierls valleys. Thus, it is questionable as to whether the measured velocities for each applied stress and temperature in [**211**] are representative of the situation over longer timescales, particularly since, as we find in our simulations, it takes time for the motion to reach a 'steady-state' velocity corresponding to a smooth stress-field throughout the atomic lattice (see section 5.3).

What is clear from the above review of the literature, is that the techniques used to model screw dislocations in bcc metals are still in their infancy. Only with the recent advances in computational power and efficiency is this problem, which is perhaps the most challenging for MD simulations, becoming open to detailed atomistic studies. The aim of the research presented in this chapter is to produce mobility functions, which are a function of both temperature and stress, for the velocity of motion of $\frac{1}{2}\langle 111\rangle$ screw dislocations in pure bcc Fe. Of particular interest is the lower stress regime, where the rate of motion is clearly defined by the thermally-activated production of kinks, since this is the most relevant for real conditions like those predicted for the temperatures and loading in a fusion reactor. Such a task required large-scale, massively parallel MD simulations, which are described below.

In the simulations presented we have used the Mendelev [**82**] potential for Fe because, as mentioned before, it produces the correct non-degenerate

core structure. In addition, it has been found by others (e.g. Chaussidon *et al.* [**211**]) to be the most appropriate potential, of those currently available, for screw dislocation calculations in Fe.

In what follows we use the term 'glide (or slip) plane' to refer to the plane on which the dislocation is moving. The 'glide direction' or direction of motion is the direction in which the dislocation moves (*i.e.,* perpendicular to the Burgers vector for a screw dislocation). The direction of shear is always parallel to the Burgers vector for a screw dislocation and is therefore perpendicular to glide direction. Only in the case of a pure edge dislocation do the glide and shear directions coincide on the glide plane.

5.2 Simulation set-up and computational requirements

In a given simulation it is important that the motion of a screw dislocation can be tracked for significant timescales, so that the velocity can be reliably measured. This means that the simulation set-up must be carefully designed in order to minimise the influence of several possible external factors that could alter the results. In the present work we considered three different criteria in designing the simulations.

First, we needed to make the physical length of the $\frac{1}{2}\langle 111\rangle$ screw dislocation line sufficiently long enough, so as to produce realistic motion. Very short screw dislocations are known to move via a mechanism other than the production of double-kinks. In particular, they have a tendency to jump from one Peierls valley (*i.e.,* equilibrium core position) to the next in one step as a whole, rather than continuously through kinks [**209**]. Recent work by Ventelon *et al.* [**216**] suggests that single kinks in Fe, using the Mendelev potential, have widths of the order of $20b$ in the [111] direction at 0K, where b is the magnitude of the $\frac{1}{2}\langle 111\rangle$ Burgers vector. However, the

calculations described in [**216**] were performed on single, isolated kinks, rather than on kinks as a part of a double-kink complex.

Terentyev and Malerba [**217**] found using molecular statics (0K) on the Mendelev potential that the energy of a double-kink increases with total length (*i.e.,* distance between kinks). This increase was only seen to occur at small double-kink lengths, and Terentyev and Malerba observed that the energy saturated at double-kink lengths of the order of $20b$. The difference between the findings of Terentyev and Malerba [**217**] and Ventelon *et al.* [**216**] may be partially caused by the kinks interacting with each other, leading to an overall reduction in length along the dislocation line.

However, the total double-kink energy obtained by Terentyev and Malerba is higher at 0.75 eV than that calculated by Ventelon *et al.*. Following the methods described in [**216**], we reproduced the results of Ventelon *et al.* and obtained the same total energy (energy of left-kink plus energy of right-kink) of 0.67 eV that was given therein. In fact, like Ventelon *et al.*, we obtained a value of 0.67 eV in a large number of alternative lattice arrangements and sizes, and as a consequence we believe that the results of Terentyev and Malerba are somewhat spurious. Since the 0.67 eV result is more reliable we have used the kink lengths obtained by Ventelon *et al.* [**216**] as the lower limit of our dislocation length. The $20b$ kink width found in [**216**] gave us minimum length of $40b$.

Additionally, we wanted to minimise the occurrence of more than one kink pair simultaneously, so as to avoid cross-kinks. Under such circumstances there is a chance that the screw dislocation could become pinned and significant computational time would be wasted waiting for the pinning [**209**] to be overcome. Following the arguments provided by

Marian *et al.* [**209**], we required that the kink mean-free-path $\lambda(L)$ be at least as large as the dislocation length L. $\lambda(L)$ is defined as

$$\lambda = \sqrt{\frac{v_k}{J_K}}, \tag{5.1}$$

where v_k is the kink velocity and J_k is the kink-pair nucleation rate. At the highest stresses, kink migration is limited by viscous drag [**208**] and is proportional to σ/T, where σ is the stress. On the other hand, at lower stresses,

$$J_K \propto \exp(-E_a(\sigma)/k_B T), \tag{5.2}$$

where $E_a(\sigma)$ is the activation energy for kink production at a given stress. Order of magnitude estimates at the highest stresses and lowest temperatures we expected to consider in the simulations suggested that a dislocation length of $80b$ (~ 198 Å for the Mendelev potential) was a suitable choice to minimise the occurrence of multiple kinks, whilst still allowing for a reasonable nucleation rate. Of course, we also had periodic boundary conditions in the $y = [111]$ close-packed direction, which is also the direction of shear or deformation under stressed conditions in our simulations, making the actual dislocation length effectively infinite.

In the other two coordinate directions (of $\langle 110 \rangle$ and $\langle 112 \rangle$ type, respectively) we have a periodic boundary in the glide direction x (direction of motion) and free surfaces in the other direction z. As described later in this section, a σ_{yz} shear stress will be applied at the top and bottom (in z) of the cell to induce motion in the screw dislocation. We chose the size of the lattice in z (*i.e.,* its height) in order to minimise/mitigate the effects of image forces due to the free surfaces. However, computational limitations prevented us from having a box that was 'infinitely' large in z, and so, even

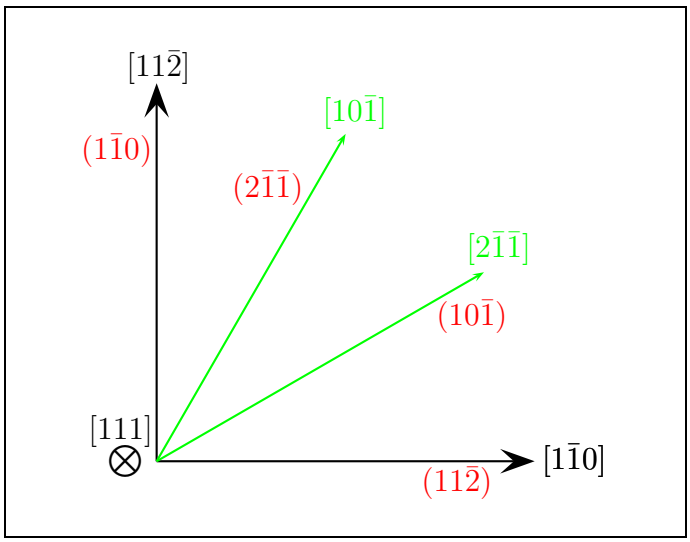


Fig. 5.1: Example secondary glide planes (red) and associated motion directions (green) of the $([1\bar{1}0],[11\bar{2}],[111])$ coordinate system. The primary glide direction is either $[1\bar{1}0]$ or $[11\bar{2}]$. In the figure the $y = [111]$ Burgers vector direction is pointing out of the page. For the $(11\bar{2})$ glide plane the secondary glide plane shown is $(10\bar{1})$, while for the $(1\bar{1}0)$ primary glide plane the $(2\bar{1}\bar{1})$ is the secondary shown.

with the height of almost 600 Å used in the simulations presented here, there are still some residual image forces. These forces could lead to the dislocation drifting from the horizontal primary glide plane yz, and instead moving to one of the alternative (secondary) glide planes. In such a scenario the dislocation would quickly approach the surface and be destroyed, thereby reducing the simulation time available from which to measure the velocity. It would also be more difficult to extract a reliable velocity from the resultant 2D motion.

To determine which glide plane was the most stable in our set-up, we performed test simulations of the alternative orientations, *i.e.,* where the primary glide (slip) plane is either of type {110} or type {112} (corresponding to ⟨112⟩- or ⟨110⟩-type glide (motion) directions, respectively). These indicated that a {110} glide plane was not stable in

our case, as the dislocation moved off the primary glide plane onto one of the secondary glide planes (see Figure 5.1, for illustration of what these are for the $([1\bar{1}0],[11\bar{2}],[111])$ coordinate system) almost as soon as the stress was applied. Thus, in the present simulations we have used a $x = [\bar{1}10]$ glide direction on a $(11\bar{2})$ glide plane, with $z = [11\bar{2}]$, which has the added benefit of allowing us to distinguish between the twinning and anti-twinning directions of slip (see later). Figure 5.3 (page 169) shows the simulation set-up and gives the direction of the coordinate axes.

When applying the stress we did this in the twinning (as opposed to anti-twinning) sense of shear on the $(11\bar{2})$ plane. This was determined by considering the crystallography, but we also checked that applying shear in the opposite, anti-twinning sense did not produce results. In particular, we found that shearing in the anti-twinning sense (applying stress in the negative [111] direction to the upper half-plane of the simulation cell shown in Figure 5.3 and the opposite for the lower half-plane) did not lead to stabilisation of the motion on the $(11\bar{2})$ plane, but instead the dislocation moved on one of the secondary glide planes. Only by applying stress in the (positive) twinning sense of shear on the $(11\bar{2})$ plane (as shown in Figure 5.3) were we able to perform simulations with a stabilised primary glide plane. Note that there is no twinning/anti-twinning sense to be considered when shearing on a {110}-type glide plane (in our case $(\bar{1}10)$).

The {112} preferred glide plane of our simulations disagrees with the findings of Domain and Monnet [**210**] where there were free surfaces in the glide direction, and also disagrees with the appropriate free surface simulations of Chaussidon *et al.* [**211**]. In our case the presence of periodic boundary conditions (necessary in order to have long simulation times) stabilises the $(11\bar{2})$ glide plane, as was observed by Chaussidon *et al.* [**211**]

when they altered the boundary conditions in their simulations. This does seem counter-intuitive, since movement in ⟨112⟩-type direction on a {110}-type plane makes more sense crystallographically due to it having the shortest distance between adjacent Peierls valleys (see next chapter), but experimentalists have found evidence for both glide planes [**198**, **203**, **204**], with {110} glide (slip) planes favoured at low temperature, while the [111]{112} slip systems become activated at higher temperatures [**199**].

With striking similarity to experiment (see [**198**, **203**, **204**]), we note that Chaussidon *et al.* [**211**] found that increasing the temperature (and stress) of a simulation can lead to the rotation of the glide plane towards {112} from {110}. This may, at least partially, explain the preferred glide plane observed in the present simulations, but further study is required to investigate this.

The final design parameter, namely the dimension in the periodic glide direction x, was chosen such that the heat generated by the dislocation was dissipated within one passage through the box. This was necessary to avoid the need for temperature control during the simulations because we did not want to affect the results by applying artificial thermostats. Therefore, it was important that the glide path did not heat up too much during the simulation, since otherwise it would not be possible to specify unambiguously the temperature to which the measured velocity applied.

Suitable MD test simulations allowed us to produce temperature decay curves for various increases in temperature ΔT. For example, the graph in Figure 5.2 shows how the temperature in a heated region dissipated in time. These curves represent the temperature decay in a simulation cell equilibrated for 20 ps at 200, 300, 400, and 500K (giving ΔT values of 100, 200, 300, and 400K, respectively), which was then coupled to a skin region

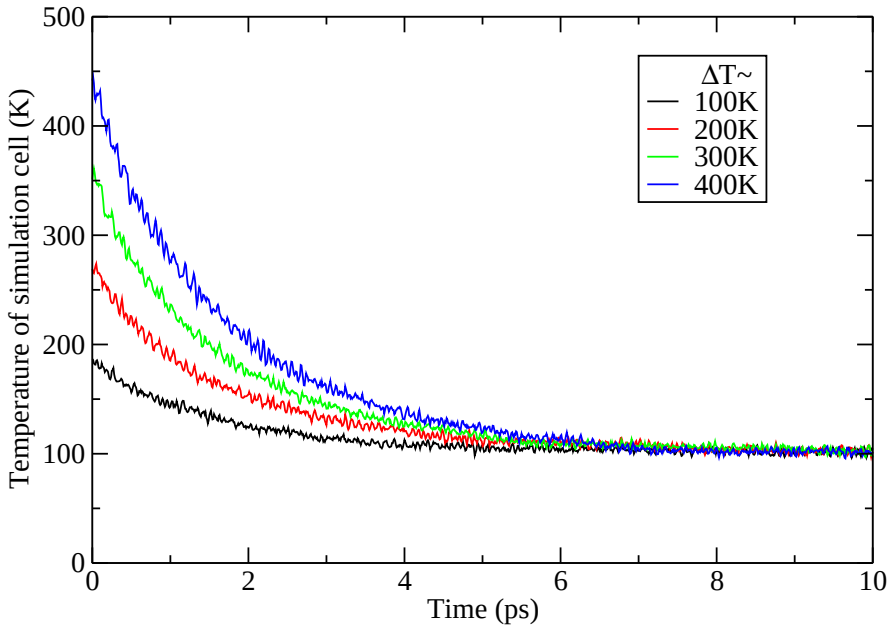


Fig. 5.2: Temperature dissipation in a Fe lattice equilibrated to 100K. The ΔT increases in temperature mimic the effect of the localised heating caused by the passage of a screw dislocation.

of atoms whose temperature was controlled at 100K. This skin region mimicked the effect of a much larger bulk lattice at 100K. The system was evolved under these conditions for several tens of picoseconds (only 10 ps are shown in Figure 5.2) and the temperature of the whole system falls gradually towards 100K. Notice that the simulations do not start exactly from their original temperatures (for example 500K) because the temperature calculation includes all atoms in the system, even those in the skin region whose temperature is 100K.

By fitting these curves to an inverse exponential law of the form

$$T = T^{\infty} + \Delta T \exp(-Bt),$$

we found an average decay exponent factor B of around 0.5 ps^{-1}. This

suggests that after a ΔT of 2000K the lattice would require around 10 ps to return to within approximately 10K of the initial temperature. With *overestimated* dislocation velocities in the range 1500 to 2000 ms^{-1}, a box width (glide-path length) of at least 200 Å would be required to ensure that this (extreme) level of heating had dissipated sufficiently. In the event we selected a cell containing 60 unit cells in the $[\bar{1}10]$ direction of motion, giving a total width of 242.3 Å. During all of the subsequent simulations we noted that the temperature change during a run was always less than 10% of the start temperature.

Taking into account all of the above factors, we performed the subsequent applied stress simulations using a large lattice with dimensions of $243 \times 198 \times 587$ Å^3 containing approximately 2.4 million Fe atoms ($60 \times 80 \times 84$ unit cells in a $([\bar{1}10], [111], [11\bar{2}])$ coordinate system - see Appendix A.1, but note the change from $[1\bar{1}0]$ to $[\bar{1}10]$ required to maintain the right-handedness of the axes). Figure 5.3 shows the overall simulation setup used.

To allow for periodic boundaries in the motion direction a screw dislocation dipole (*i.e.,* two screw dislocations) was inserted into a box with twice the intended final height z given above. The screw dislocations were displaced relative to each other in the direction perpendicular to the glide plane (in this case $z = [11\bar{2}]$) by half the height of this larger, $60 \times 80 \times 168$, cell. Each was inserted using the isotropic elasticity solution (see equation (6.1), page 199, with u_z replaced by u_y), but in opposing 'screw' directions (*i.e.,* each had the negative displacements of the other). Half of this large box was removed to leave a single dislocation in a lattice of the required size and orientation (see Figure 5.3).

After static relaxation, the simulation cell was heated at the required

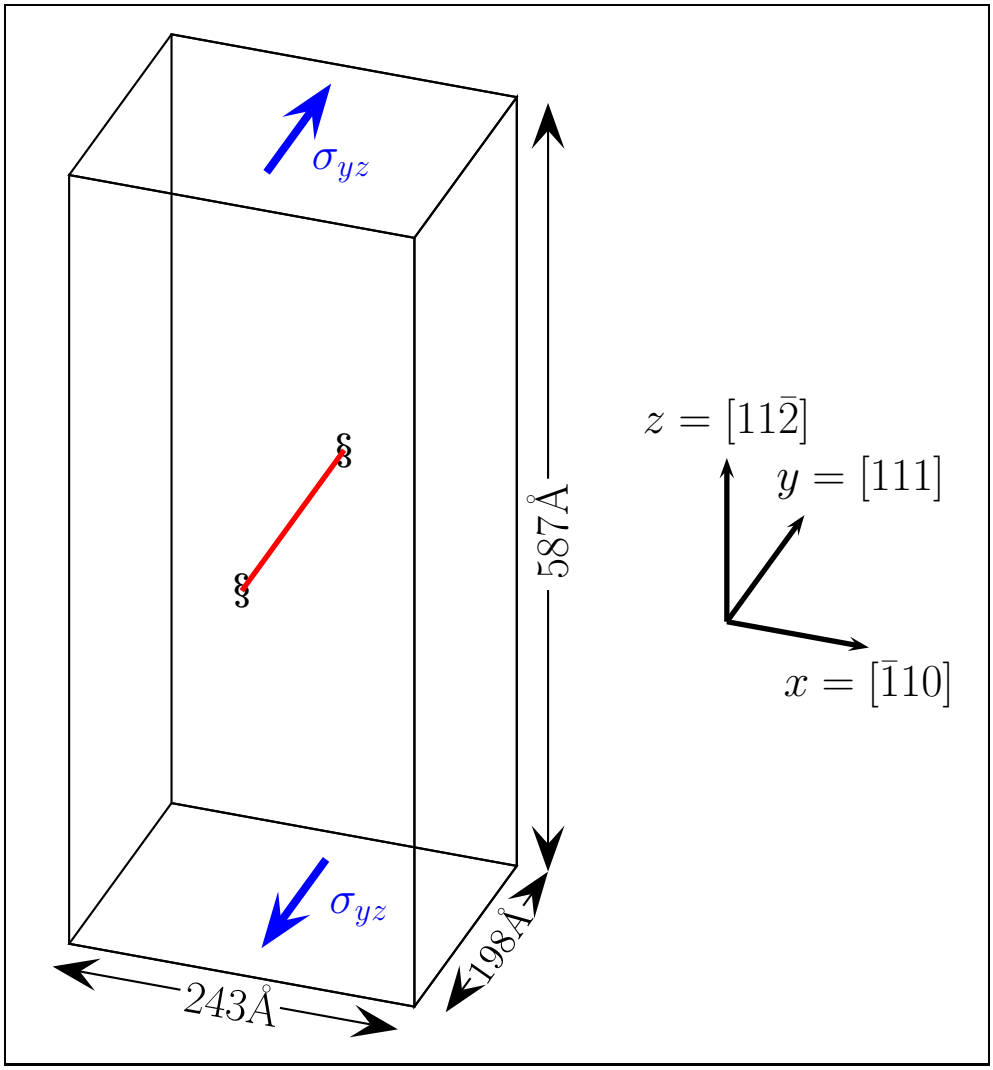


Fig. 5.3: The simulation set-up used to measure the velocity response of a $\frac{1}{2}\langle 111\rangle$ screw dislocation to applied stress at finite temperature.

temperature (either 100, 200, 300, or 500K in the present simulations) for 20 ps. After allowing the pressure oscillations (caused by the temperature increase) to relax, temperature control was switched off and the desired stress was applied to force the dislocation to glide. Note that both the top and bottom surfaces (in the z sense) have free boundary conditions applied to them (technically *modified* free boundary conditions [**211**] - see below), and so it does not matter that the insertion of the screws leads to a mismatch between the displacements at opposite sides of the box (if periodic boundaries were required in this direction we could not have created the box in this way). On the other hand, the screw solution (6.1) produces different displacements in the positive x direction ($[\bar{1}10]$) compared to those in the negative direction. We would like periodic boundaries in this direction (so that we can have long simulations) and fortunately the mismatch between displacements is exactly one Burgers vector ($\sqrt{3}a/2$), which means that the atomic rows still line up across the boundary and there is no misalignment in the lattice.

As is done commonly in these types of simulation, such as in those by Marian *et al.* [**209**] and Chaussidon *et al.* [**211**], the stress-controlling boundary conditions were applied by superimposing constant and opposite forces in the $y = [111]$ direction to atoms in thin slabs near the 'free' surfaces at the top and bottom (in the z sense) of the simulation cell. This produced σ_{yz} shear components as shown in the simulation set-up summary in Figure 5.3. In our simulations each slab contained around 50,000 atoms and the force added to an atom was calculated by dividing the total force required at each surface (stress $\times$ surface area) by the total number of atoms in each skin region. Note that since the simulation cell has periodic boundaries in both the x and y directions the material is effectively infinite

in the glide plane. This means that the applied shear components $\pm\sigma_{yz}$, which would cause a finite cell to rotate about the x-axis, do not produce rotation of the box in this case because the $\pm x$-surfaces and $\pm y$-surfaces are attached to each other. Only in the z-direction do we have free surfaces.

The applied stresses considered ranged from 100 MPa to more than 1.3 GPa, with the actual range varying depending on the temperature (see below). Note that the atoms in each slab were forced to move only in 2D, and had their z ($[11\bar{2}]$) direction velocities and forces zeroed out after each time-step. Chaussidon *et al.* [**211**] refer to this as *2D-dynamics* and find that the favoured glide plane can be altered (from {110} to {112}) compared to dynamics in which the atoms of the slabs are free to move in all directions.

Each simulation was performed using the **LAMMPS** [**48**, **49**] MD code on a massively parallel computer cluster. The large number of atoms involved in the calculations, together with the need to evolve the sample on statistically-meaningful timescales of several hundred picoseconds (or even several nanoseconds at the lower temperatures and stresses), meant that, even on almost 500 processors of the System X computing facility at Virginia Tech University (some of the simulations were also performed on the Thunder parallel computer based at the Lawrence Livermore National Laboratory), a simulation for a single temperature-stress pair could take more than 24 hours to obtain. As the number of velocity data points shown in Figure 5.6 demonstrates, the computational effort required to perform this detailed study was significant.

5.3 Results

For each simulation at a given temperature and fixed applied stress the position of the screw dislocation was measured every 1 ps using a method equivalent to that described in chapter 4 (page 118) for diffusing dislocation loops. We confirmed in all simulations that there was no appreciable drift or anomalous slip away from the primary glide plane (other than that which occurred during the temperature equilibrations), so the motion was 1-dimensional in each case. Figure 5.4 shows the first 500 ps of the trajectories from the 300K simulations at a range of applied stresses. Note that we only consider the trajectories associated with the applied stress simulations (the equilibration simulations are not included). In contrast with the diffusion trajectories seen in the previous chapter we see that motion is mono-directional due to the presence of the applied stress field. As expected, the pattern is that the magnitude of motion (displacement) increases with applied stress. This pattern was also reproduced at the other simulation temperatures (100, 200, and 500K).

However, we found that, at all temperatures, there was an upper limit to the applied stress achievable in the simulations. For example, in Figure 5.4, we have included the trajectory at 1150 MPa, even though it is clearly anomalous. What has happened in this case is that the screw dislocation has initiated a thin plate of sheared crystal, known as a twin [**209**]. The shearing occurred almost as soon as the dislocation started to move, and afterwards the motion of the screw dislocation was replaced by the rapid propagation of the twin-plates through the lattice until they occupied the entire glide plane. This is why, in the 1150 MPa trajectory of Figure 5.4, the motion of the 'dislocation' (in this case the twin) plateaus.

This twinning behaviour at very high stresses was observed previously

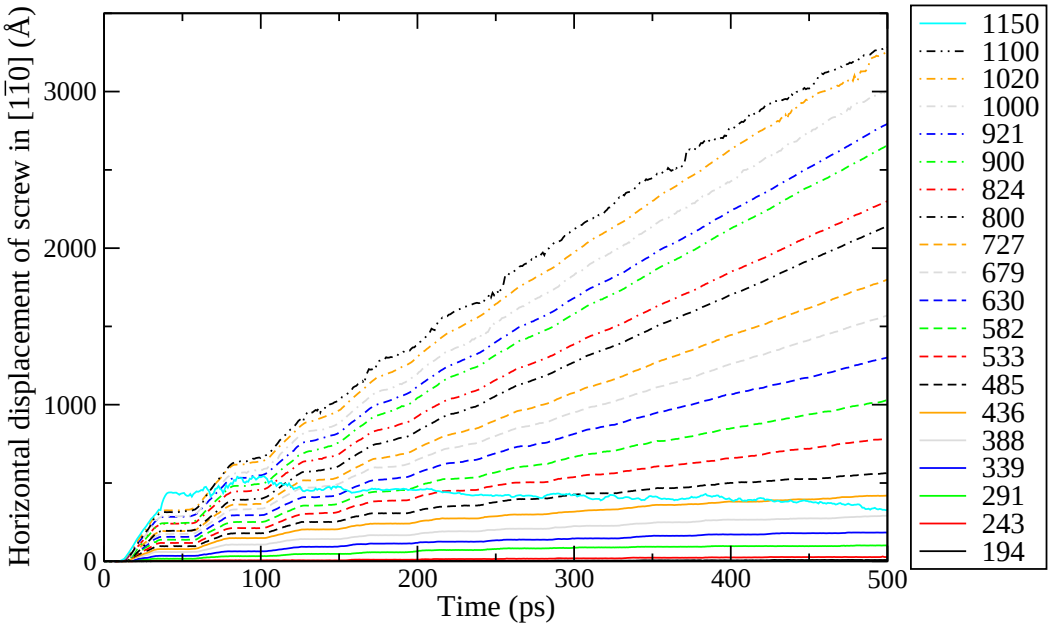


Fig. 5.4: Motion of the dislocation at 300K in pure Fe under the influence of a range of applied stress σ_A values. The applied stresses are given in MPa.

in MD simulations of Fe by Marian *et al.* [**209**]. It is consistent with the idea that screw dislocations are preferential sites for twin nucleation (*i.e.*, the stress required for twinning from a screw is much lower than in a perfect lattice [**209**]), and that at such high stresses screw dislocations are unable to move fast enough to relieve the strain in the lattice. At this point, twin nucleation becomes the primary plastic response to deformation [**209**]. In the present simulations the transition to twinning nucleation from 'normal' dislocation motion occurred at a different stress depending on the temperature. At 500K, the maximum applied stress σ_A we were able to simulate was just over 800 MPa. As stated above, this rose to 1.1 GPa at 300K, was higher again for 200K at 1.2 GPa, while at 100K we were able to perform successful simulations up to 1.5 GPa.

As well as an upper limit to the applied stress, there was also a lower limit, which was defined by determining whether the motion at a given low

stress was sufficient to enable reliable computation of a velocity on the 0.5 to 2 ns simulation timescale. Clearly, the lowest achievable applied stresses should be at the higher temperatures, and at 500K a simulation was performed satisfactorily at $\sigma_A = 100$ MPa. At 100K, on the other hand, it was difficult to go much below 750 MPa, and even though 650 MPa was considered at this temperature, it is not clear if the calculated velocity is statistically reliable.

Each trajectory has been used to define the velocity of motion for the screw dislocation at the particular temperature and applied stress. However, we did not simply measure the gradient of the 'straight-lines' shown in Figure 5.4. We observed that at the start of each simulation there was a period of time during which the motion of the dislocation was erratic. This was caused by the fluctuations in the stress field generated by the shear components at the surfaces of the box.

At the start of the simulation, the superimposed force components produce shear-waves that start at the surfaces (in z) and propagate through the material towards the dislocation. Since it takes time for the shear-wave to reach the dislocation we observe a period of around 10 ps at the start of each simulation where the dislocation does not move. To move from either surface to the centre of the box (where the dislocation is) the shear wave must travel approximately 300 Å $= 3 \times 10^{-8}$ m, and the velocity of shear waves in Fe is around 3000 ms^{-1} at room temperature [**218**]. This means that the shear wave from the surfaces requires 10 ps to reach the dislocation, which is in surprisingly good agreement with our 'lag-time' before the onset of motion, given that the Mendelev potential is only an approximate representation of Fe.

When these shear-waves first hit the dislocation they cause a sudden

burst in motion as seen in Figure 5.4, which is then followed by a period of reduced motion, or even immobility, as the waves are reflected back towards the surfaces. In addition, the screw dislocation itself also produces shear-waves, which under normal ('real') circumstances would relieve some of the applied stress. However, these waves, along with those produced by the surfaces, sweep backwards and forwards through the box until eventually they have overlapped sufficiently to produce a homogeneous and constant stress profile. Only then does the motion of the dislocation become smoother. One consequence of this effect is that the actual stress experienced by the dislocation during its steady-state velocity regime is not exactly equal to the applied stress at the surfaces. We do not expect the discrepancy to be great, but to be unambiguous our mobility laws are presented in terms of (normalised) applied stress. Note also that 'stress' is a macroscopic quantity that is somewhat difficult to relate completely to the simulations at the atomistic level. In other words, stress is ill-defined in MD simulations, but applying external forces in the way described in this study is the best that atomistic modellers can do at present.

In the current work we neglected the erratic velocities seen before the transition to smooth behaviour, and only measured the velocity in the steady-state regime. In each simulation we made sure that it was run for long enough for the velocity to become as close to constant as possible. In some instances this required simulation lengths of 2 ns. Figure 5.5 demonstrates how the steady-state velocity was measured, in this case for $\sigma_A = 800$ MPa at 300K. The gradient of the linear fit gives a dislocation velocity of 4.34 Åps^{-1}, which is equivalent to 434 ms^{-1}.

The graph shown in Figure 5.6 displays the calculated velocities as a function of applied stress at each of the 4 temperatures considered. At 100,

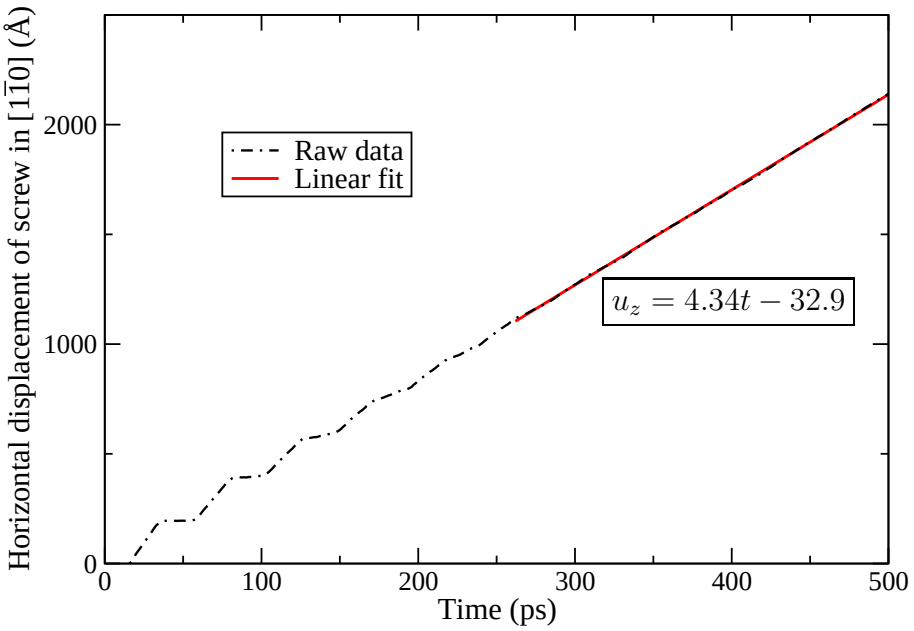


Fig. 5.5: Example of the procedure used to measure the velocity from each simulation trajectory. The velocity is measured as the gradient of the straight-line fit to the steady-state motion. The simulation conditions in this case were 300K under applied stress of 800 MPa.

200, and 300K there are clearly two types of behaviour. At low stress, the velocity increases exponentially with stress, while at higher applied stresses this is replaced by a linear response. At 500K there is more scatter in the data, particularly at the higher stresses, but it is still clear that there is a small exponential regime at low stress.

The first type, at lower stresses, corresponds to a regime in which the so-called kink-pair thermal activation mechanism [**150**, **194**] is clearly observable. The picture in Figure 5.7 shows an example snapshot of the screw dislocation moving through the box in this regime. The simulation in this case took place at 300K under an applied stress of 300 MPa. The figure shows the screw dislocation with a single double-kink propagating along its length. Note that atoms are shown in this picture if they have

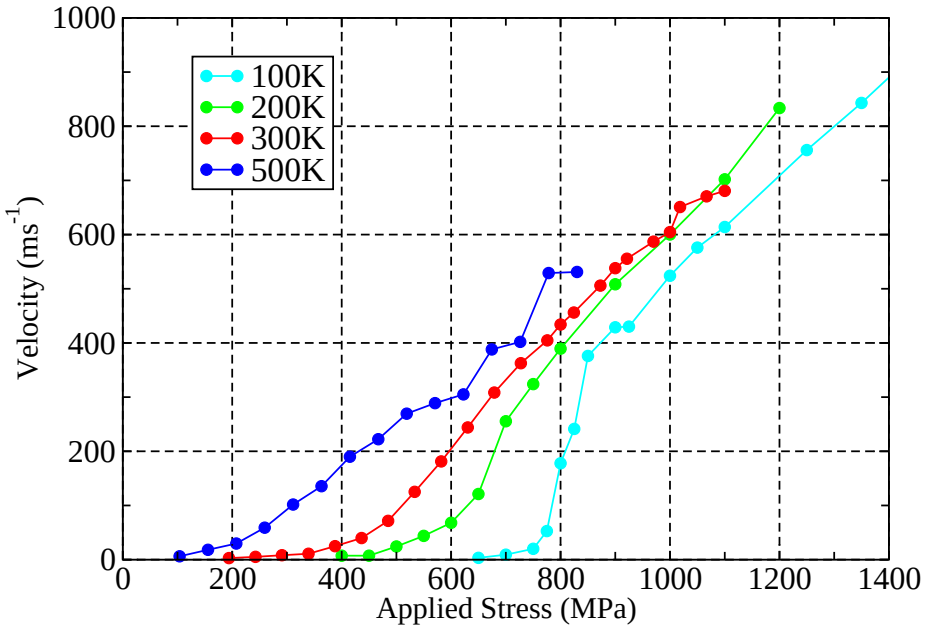


Fig. 5.6: The variation of the measured dislocation velocity at each simulation temperature as a function of the applied stress σ_A.

high energy (0.15 eV above the average) and also high coordination number (relative to the energy filter).

At a given applied external stress there is an energy barrier preventing the screw dislocation from gliding freely through the lattice. In the absence of stress this barrier is at its maximum height, and then at 0K is known as the Peierls energy barrier. We discuss further this particular version of the energy barrier (at 0K and zero stress) in chapter 6 when we consider how its shape is influenced by the choice of the potential function used in atomistic simulations. The only way the dislocation can overcome the energy barrier at a given stress is via the formation of double-kinks, which is a thermally activated process and therefore requires finite temperature. As the finite temperature increases (for a given stress), the thermal fluctuations increase and the formation of double-kinks becomes more frequent. This is why in Figure 5.6, the measured velocities increase with temperature, a fact that

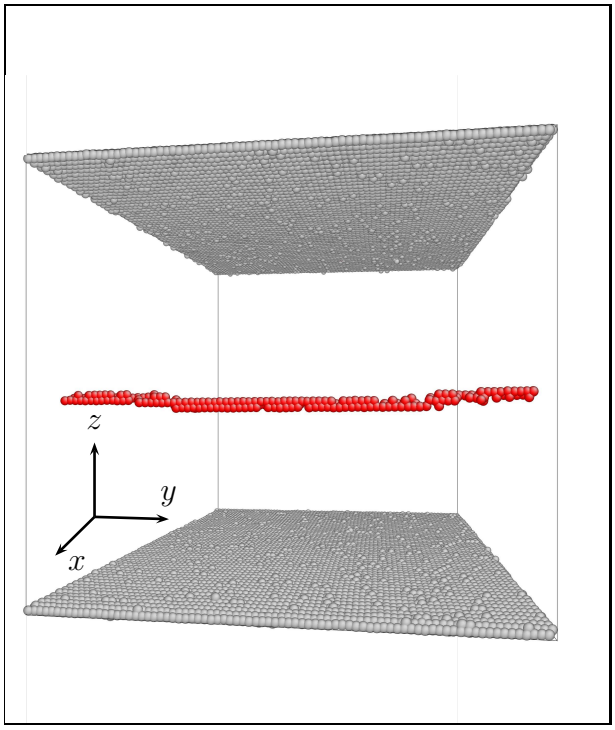


Fig. 5.7: Example simulation snapshot (not to scale in z) of the kinked screw dislocation (red atoms) at 300K with an applied stress of 300 MPa. Surface atoms are also shown (grey).

remains true even when the behaviour appears to change at higher stresses.

As the applied stress σ_A is increased the height of the energy barrier for motion in one particular direction (the direction of the applied stress) is reduced. This makes it easier to form kinks in that direction (of motion) and so the thermal activation occurs more frequently at finite temperature. In our results this is manifested as the measured velocities increasing with σ_A at all temperatures. Note that the finite temperatures have almost no effect on the energy barrier, so that at a given applied stress the energy barrier is essentially the same for all the temperatures considered in the present study.

Recently, Rodney and Proville [**219**] have investigated the change in the energy barrier (which they call the Peierls potential) as a function of applied stress. They found, via atomistic simulations on fcc Al, that the potential landscape for (Lomer) dislocation motion was strongly dependent on the applied stress. Whilst they do not consider finite temperatures in their simulations, their results validate our findings. Even in simulations of screw dislocations in bcc Fe using the same potential as we have used in the present simulations, Rodney and Proville [**219**] noticed a reduction in the energy barrier. Similar findings for bcc crystals were reported earlier by Ngan and Wen [**220**], where they found a reduction in the activation barrier (and activation energy) for kink formation. However, Ngan and Wen did not consider the consequences associated with reducing the barrier (through σ_A) and then applying finite temperature, which is the situation in the present research.

In the absence of thermal fluctuations (*i.e.,* at 0K) there is no way for thermal activation to occur. Under such circumstances the dislocation can only be moved by increasing the applied stress to the point at which the

(Peierls) energy barrier is reduced to zero. This value of σ_A, which produces dislocation motion at 0K, is defined as the Peierls stress σ_p, and was found by Chaussidon *et al.* [**211**] to be 1200 MPa for the Mendelev [**82**] potential. At, and above, σ_p the dislocation no-longer moves via the thermally-activated formation of double-kinks, but instead can glide 'freely' through the lattice as a whole. In simulation, this would be observed as the dislocation moving through the lattice as a straight line with little or no 'kinking'. However, in the present simulations we cannot be in this 'free-motion' regime because, except for a few of the highest stress simulations at 100K and 200K, the values of σ_A are all below the stress necessary to remove the energy barrier to motion (*i.e.,* $\sim$ 1200 MPa). [Although it is not possible to be sure about the exact value of σ_A that would reduce the migration barrier to zero because of the previously discussed (see page 175) difficulties in relating the applied external forces to macroscopic applied stresses, so it is not certain which (if any) of the σ_A values reduce the energy barrier to zero.]

This poses an interesting question: if the barrier to migration is still non-zero, why is it that at a certain transition stress σ_d the behaviour seems to change from the classical exponential velocity versus σ_A response associated with a thermally-activated process, to a linear velocity-σ_A response, which is characteristic of barrier-free motion? The answer is that in fact the thermal activation is still occurring, but, as we also observed in our diffusion simulations of dislocation loops in chapter 4 (see page 136), the thermal fluctuations in the molecular dynamics are effectively masking or hiding the (very) low energy barrier. In chapter 4 the zero-stress energy barrier was low, and so we observed this effect even in the absence of stress, but for the present simulations the energy barrier is significant at low stress,

and so the velocity profile obeys the expected exponential (Arrhenius) response. Only at and above σ_d does the barrier become low enough for its influence to be hidden by the thermal fluctuations at finite temperature.

In essence, above a certain transition stress σ_d, which is always less than σ_p, the energy barrier is reduced to such an extent that the thermal fluctuations associated with a given finite temperature completely overwhelm it. Under these circumstances the formation of double-kinks (in one direction only) becomes so easy that we lose all notion of an 'attempt frequency', and kinks are always being formed on the (relatively) short dislocation in the direction of glide, with no discernible waiting time in between 'activations'. The transition stress σ_d at each simulation temperature marks the first applied stress at which the 'baseline' or average of the thermal fluctuations is greater than the energy barrier at that stress. In other words, while the energy barrier at a given stress is fixed, the effective potential-energy landscape seen by the double-kinks is statistically reduced to zero by the finite temperature fluctuations. Since thermal fluctuations increase with temperature, in our simulations it is no surprise that we observe a decrease, with increasing temperature, in the stress σ_d at which the linear velocity-stress regime begins, with the highest, in the 100K simulations, at around 800 MPa (more precise values for σ_d are given in table 5.1 in the next section).

Above σ_d, as the applied stress is increased further, it seems that the rate of kink-formation remains fairly constant for this finite length dislocation, and the linear velocity-stress response we observe indicates that the motion is being limited by frictional forces, either on the dislocation itself, or on the double-kinks that must propagate along the dislocation for forward motion to take place. At around $\sigma_A = 1200$ MPa, when the energy

barrier was finally reduced to zero, this motion would be replaced by one where the dislocation moves through the lattice as a straight line, rather than via the formation and propagation of double-kinks. Since this 'true' free-motion would also be limited by friction or phonon-drag the velocity would continue to increase linearly with temperature. Therefore, as was suggested in chapter 4, it may be difficult to determine the transition to barrier-free motion in simulations of the kind presented here. It may be possible to determine the 'switch-over' by carefully examining how the screw dislocation moves, but in the present simulations we did not observe a third type of motion because we were not able to apply sufficiently high applied stresses (as discussed earlier, the finite size of the box caused the screw to twin above a given σ_A for each temperature).

Another possible explanation is either, that the induced stress in the simulation cell is much higher than σ_A so that the barrier does actually become zero in the simulations, or that the value of $\sigma_p = 1200$ MPa found in [**211**] is too high. Both of these options can be discounted by realising that the onset of the linear velocity-stress response varies with temperature (see the values of σ_d in table 5.1), implying that there is still some kind of thermally-activated process taking place, and so an energy barrier is still present.

At this point it is worth emphasizing that the large variation in transition stress observed in the simulation results does not imply large variations in the elastic properties of the material. The large decrease (with increasing temperature) is simply the result of the thermal fluctuations overwhelming the falling (with stress) energy barrier earlier at higher temperatures [**221**].

In Figure 5.6 the linear regime at higher stresses is clearly apparent at

100, 200, and 300K. While there is more scatter in the 500K results at very high stresses (compared to the transition stress), the response is approximately linear, particularly just above the transition stress at about 300 MPa. As stated above, the linear response of velocity to an applied stress (or force) indicates that the motion is limited by a frictional process, even though thermally-activated kink-formation is still taking place. At very high stresses (well above σ_p) it is well known that the primary impedance to motion is the speed at which phonons can escape (radiate) from the dislocation core [**150**, **222**, **223**]. Our results cannot fall into this category because the applied stress is still below the Peierls stress, and, as has been suggested elsewhere [**200**, **208**], it may only be possible to study phonon drag if a dislocation is confined in a small volume. In our case, the linear regime seems to be partially explained as being a limitation of the molecular dynamics method.

In the next section we fit appropriate mobility laws to these velocity versus stress results, with particular emphasis on the clearly distinguishable exponential regime at the lower stress, which is the closest match to experimental conditions, and hence the most relevant for dislocation dynamics simulations.

5.4 Mobility laws

For the low stress regime, where classical thermally-activated kink-nucleation is dominating the motion and is thus the rate determining mechanism, Hirth and Lothe [**150**] suggest that the dislocation velocity is a negative exponential function of the double-kink formation energy divided by k_BT, where k_B is Boltzmann's constant, with a pre-factor proportional to σ/T (see [**150**, eq.15-17]). Kocks, Argon, and Ashby [**192**], who

discussed the thermodynamics and kinetics of general dislocations, developed equations that include an explicit stress dependence for the thermal activation. Following equations 43a of [**192**] and 15.17 of [**150**] we consider the following expression for the velocity of a screw dislocation in the low stress regime:

$$v(\sigma_N, T) = \frac{A\sigma_N}{k_B T} \exp\left(-\frac{H(\sigma_N)}{k_B T}\right), \tag{5.3}$$

where A is a fitting parameter with units of $\mathrm{ms}^{-1}\mathrm{eV}$. Here, since we desire a single law that is applicable at all temperatures, we have introduced the new variable σ_N for the normalised stress σ_A/σ_d, where σ_A is the applied stress. As discussed in the previous section, the value of the transition stress σ_d varies significantly with temperature (see table 5.1), and so it would be very difficult to fit a single law to all the results without using normalised stresses. We acknowledge that the presence of σ_d may be an artefact of the statistical nature of the MD simulations, but since it is present and clearly temperature dependent we feel justified in including it in our mobility law. What the normalisation does is effectively remove the part of the temperature dependence associated with the transition stress and leaves us only with the thermally activated part. Table 5.1 shows the values of σ_d used at each of the simulated temperatures.

The transition stresses were chosen by considering the highest applied stress of the observable thermally activated regime at each temperature. As a rough approximation, σ_d was then given a value equal to 1 MPa above this maximum. To obtain greater accuracy for σ_d we would need to perform many more simulations near to the transition between the two regimes, which has not been possible at this time. Note that the applied stress values are not distributed evenly in the 300 and 500K simulation sets

because of an error in the original force calculations required to produce the stresses at these two temperatures for the **LAMMPS** MD code. This meant that the actual applied stresses were slightly different to the intended ones, and this explains why the transition stresses in these cases are not necessarily close to hundred or fifty MPa intervals.

As mentioned in the previous section, we associate the $\sigma_d(T)$ transition stress with the point at which the applied stress has reduced the energy barrier to the extent that the finite-temperature thermal-fluctuations completely swamp it. Above this stress the thermal activation process (of double-kink formation) is hidden and the equation presented above cannot be applied.

$H(\sigma_N)$ in equation (5.3) is the stress-dependent free energy of activation (or activation free enthalpy) [**192**, pg.114]. Here we employ a generic functional form for H suggested by Kocks *et al.* [**192**]. This functional form was also recently utilised by Rodney and Proville [**219**, **224**], where they use the zero temperature Peierls stress as the normalising factor (in [**224**]), but then discuss why this might change under the action of applied stress [**219**], as it does in the present simulations. From Kocks *et al.* [**192**, eq.43w] we have:

$$H(\sigma_N) = H_0 \left(1 - \sigma_N^p\right)^q , \tag{5.4}$$

where H_0 is the zero stress activation energy [**192**]. For the case of the MD simulations described in this study the only sensible value to use for H_0 is that of the formation energy of a double-kink E_{DK}^f. In experiments the effective activation energy does not necessarily equal E_{DK}^f because the deformation process is more complex than that described by simulation and it is not possible to ascribe the measured activation energy to one specific

phenomenon.

Recently, Ventelon *et al.* [**216**] found, by simulating single kinks, that the sum of the formation energies of the two kinks forming a double kink was 0.67 eV for the Fe potential of Mendelev *et al.* [**82**] used in the present simulations. For this potential it has not been possible to measure definitively the total formation energy for a fully-formed double kink, which may or not be exactly equal to 0.67 eV (it could be slightly lower, but is certainly not greater). As mentioned earlier, applying the techniques of Ventelon *et al.* [**216**] we replicated the calculations and confirmed that this value of 0.67 eV is correct. Thus it is a suitable approximation to use $H_0 = 0.67 \text{ eV} \approx E^f_{DK}$.

The adjustable parameters, p and q, were introduced by Kocks *et al.* [**192**, page 141] to describe better the behaviour of a glide process that is particularly sensitive to thermal activation, which we can see is true in our low stress regime by observing the variation in σ_d; q describes the behaviour at applied stresses close to the maximum (in our case σ_d), while p describes the response at very low stresses ($\sigma_A \simeq 0$) [**192**].

Using **GNUPLOT** [**159**], we fitted all of the velocity-stress data points in the low stress regime to a single instance of equation (5.3) and found the following values for the three parameters

$$\begin{aligned} A &= 3.61 \text{ ms}^{-1}\text{eV}, \\ p &= 0.16, \text{ and} \\ q &= 0.94. \end{aligned} \tag{5.5}$$

The four graphs (one for each simulation temperature) shown in Figure 5.9 (page 190), demonstrate the quality of fit that this single function obtains for the MD simulation results below the transition stresses. Note that the

Tab. 5.1: Values of the transition stress, σ_d and linear-regime parameters at each simulation temperature. Also shown are the friction coefficients $\mathcal{B}$, defined by equation (5.7).

T (K)	100	200	300	500
σ_d (MPa)	851	701	534	313
C (ms^{-1})	797.83	785.14	532.70	259.05
D (ms^{-1})	-419.23	-515.92	-378.72	-166.60
$\mathcal{B}$ ($\times 10^{-4}$ Pa·s)	2.64	2.21	2.48	2.99

quality of fit is good at the three lowest temperatures (particularly at 200 and 300K) because there are a sufficient number of points in the low-stress regime at each temperature. In the 500K series there are only four points in the exponential regime because the onset of the linear regime occurs at a relatively low applied stress. This meant that it was difficult to obtain a good fit for the 500K data. If it is possible to perform more simulations in the future, then having extra points here, as well as performing simulations at 400K, would be beneficial.

Table 5.1 shows how σ_d decreases or 'softens' with increasing temperature. Marian *et al.* [**209**] also observed a change in 'transition stress'. They observed a transition with increasing stress to 'rough' motion where the dislocation produced significant debris in its wake, and noticed that the transition stress fell with increasing temperature, although they did not explore the phenomenon at the same level of quantitative detail presented here. Additionally, Marian *et al.* [**209**] performed their simulations with the potential of Ackland *et al.* [**86**], rather than the Mendelev potential we have used. On the other hand, Chaussidon *et al.* [**211**] do use this potential and also found that a transition to a 'rough multiple kink-pair regime' occurred at different stresses with a

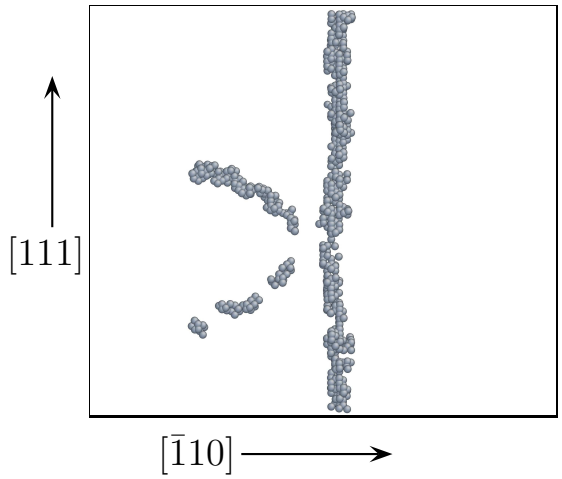


Fig. 5.8: Simulation snapshot for a screw dislocation moving at 300K under an applied stress of 800 MPa. Debris is clearly visible in the wake of the screw dislocation.

strong temperature dependence.

In the present work we do not observe the formation of multiple cross-kinks (kinks forming on different planes) at higher stresses because the simulations were designed to prevent this (although it may have still occurred occasionally). Thus, strictly speaking, the transitions observed by Marian *et al.* [**209**] and Chaussidon *et al.* [**211**] are not the same as those discussed here. However, in some of the simulations above the transition stress for a given temperature it was noted that debris production did occur, as was found by Marian *et al.* [**209**]. For example consider Figure 5.8, which shows a snapshot of the simulation at 300K and 800 MPa. In the picture there is significant debris in the wake of the screw dislocation, which we speculate could be part of a dislocation loop (the rest of the loop may not show up under the filtering conditions used to track the dislocation).

Above the transition stress σ_d it is less important to obtain a single

mobility function to cover all stresses because the validity of the simulations on this (short) dislocation is called into question by the statistical nature of the MD simulations, and also experimentalists and dislocation modellers are unlikely to be concerned with the behaviour of screw dislocations at such extremes of stress and velocity. For this reason we have fitted a separate simple linear function of the form

$$v(\sigma_N) = C\sigma_N + D \tag{5.6}$$

to the high stress regime at each simulation temperature, where C and D are constants with units of ms^{-1}. To be consistent with the low-stress fit we have used the same normalised applied stresses in these fits. The values of the fitted constants (also fitted using **GNUPLOT** [**159**]) at each temperature are shown in Table 5.1 and the fit-lines are shown against the calculated data points at each temperature in Figure 5.9.

Since the linear velocity-stress response is friction-limited, the most interesting quantity derivable from these fitted values is the viscous drag [**150**] or friction coefficient $\mathcal{B}$. Using the expression for $\mathcal{B}$ given by Hirth and Lothe [**150**, eq. 7-75 and 7-76], which is applicable up to half of the transverse-sound-wave velocity and is therefore suitable in our case, we can approximate $\mathcal{B}$ as

$$\mathcal{B} = \frac{b\sigma_d}{C}, \tag{5.7}$$

where, as before, $b = \sqrt{3}a/2 = 2.47$ Å is the magnitude of the $\frac{1}{2}\langle 111\rangle$ Burgers vector, and C is the fitting constant from equation (5.6). The last row in Table 5.1 displays the calculated values of the coefficient $\mathcal{B}$ obtained from the above equation at each temperature. We see that there is a weak temperature dependence, although the coefficient does generally increase

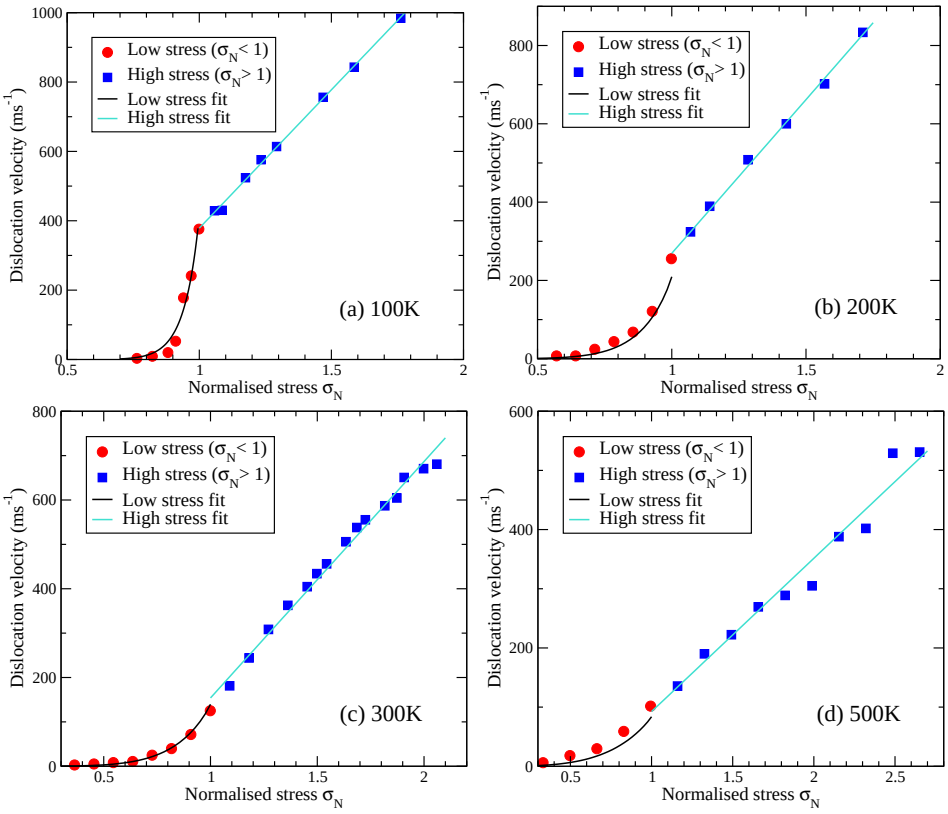


Fig. 5.9: Realisation of the fitted functions at (a) 100K, (b) 200K, (c), 300K, and (d) 500K. The original data are shown together with the fits to each regime.

with temperature (particularly if we consider the result at 100K to be anomalous).

On the other hand, since the temperature dependence is very weak, it is further demonstration of the fact that we are not strictly into a regime that is fully consistent with the phonon viscosity mechanism, where the dependence of $\mathcal{B}$ on temperature is known to be significant [**150**, **223**]. At the same time, as mentioned previously, the fact that we observe a clear linear relationship between velocity and applied stress demonstrates that the motion is being controlled by a frictional process to some extent, which is hiding the underlying thermally-activated process.

5.5 Summary and future work

We have performed large-scale finite-temperature MD simulations of screw dislocation glide under applied stress in bcc Fe. Using the set of 3D data points (T, σ_N, v) we have obtained a single mobility law for the motion of screw dislocations in the thermally-activated kink-pair nucleation regime at moderate to high stresses. This law, together with similar descriptions of the motion of edge dislocations (which are easier to simulate atomistically), will be instrumental in allowing macroscopic-scale plasticity simulations using dislocation dynamics of α-phase (bcc) Fe, which are urgently required to estimate the temperature-dependence of high-strength steels and other Fe alloys in structural applications, such as those in fusion experimental reactors.

A temperature-dependent transition to a linear velocity-stress regime has also been observed, with the (viscous) drag coefficient showing a weak dependence on temperature. This linear regime corresponds to the situation where, above a transition stress, the thermal fluctuations

completely overwhelm the energy barriers that impede the formation of double-kinks, and the kinks form so frequently that the motion of the dislocation as a whole appears 'free'. At this point the main restriction on motion is produced by friction between the dislocation (and the kinks) and its (their) surrounding environment.

There are two main areas in which the present studies could be extended. First, it would be highly desirable to investigate the temperature and stress dependence of dislocation velocity in more steel-like materials. In many steels being considered for fusion applications, Cr is the primary alloying element. There is currently a significant effort to produce effective interatomic potentials for the FeCr-alloy. In particular, Caro *et al.* have extended their work on FeCu [**115**] to FeCr [**116**, **117**]. Whilst it remains to be proven if these multi-species potentials are as effective at describing the behaviour of materials as the single atom potentials, progress is certainly being made. If simulations are possible for FeCr, then this should prove to be the more interesting of the two cases, not least because it should allow us, by comparison with the pure Fe results, to understand how the motion of screw dislocations is affected by the presence of Cr solute atoms. Further still, there is also the question of carbon, both in Fe and FeCr, since it seems that the major disagreements between simulation and experiment are primarily driven by the presence of carbon.

The second area where we hope to extend these studies concerns the very low or no stress behaviour of dislocations. We are currently working on long finite temperature simulations of screw dislocations in the absence of stress. However, in such circumstances, it is unlikely that the single or few kink-pair nucleation regimes observed at high stress is realistic. In particular, as was discussed by Hirth and Lothe [**150**] it is likely that a

screw dislocation at finite temperature has a certain 'equilibrium' concentration of kinks. Under these equilibrium conditions a dislocation may, from time-to-time, perform random jumps from one Peierls valley to the next, leading to a diffusive process. It is difficult to see how such situations can be simulated without using extremely long (in MD terms) screw dislocations, leading to obvious computational limitations.

Finally, we note that the simulations described above, as well as the proposed extensions, are entirely based on the assumption that the interatomic potentials are able to accurately model the behaviour of a moving screw dislocation. Whilst the Mendelev [**82**] potential is known to reproduce the correct non-degenerate core structure [**210**–**212**], it is not clear if it is able to effectively model the translation of the dislocation through the lattice. In the next chapter, we will investigate the fundamental origin of the difference between different core structures, and present findings that suggest that getting the correct core structure is only part of the story.

6. MULTI-STRING FRENKEL-KONTOROVA MODEL FOR $\frac{1}{2}\langle 111\rangle$ SCREW DISLOCATIONS

The accuracy with which atomistic simulations reproduce the *real* behaviour of screw dislocations in bcc crystals is primarily controlled by the potential describing the interaction between atoms. One of the long-standing issues in this respect concerns the prediction of the correct core structure. Recent Density Functional Theory (DFT) calculations have shown that the non-degenerate and symmetric core is favoured for $\frac{1}{2}\langle 111\rangle$ screw dislocations in all bcc transition metals [**212**, **225**–**228**]. In this chapter we formulate a multi-string Frenkel-Kontorova (MSFK) model for screw dislocations with a $\mathbf{b} = \frac{a}{2}[111]$ Burgers vector in bcc iron. Subsequently, we investigate the occurrence of degenerate and non-degenerate dislocation core structures as functionals of the law of interaction between the [111] strings of atoms forming the crystal.

By comparing interaction laws derived from DFT calculations and from interatomic potentials, we show that the *shape* of the function defining the interaction between strings determines whether the lowest energy screw-core configuration is degenerate or not. We also analyze the relationship between the inter-string interaction law, and the shape and the height of the Peierls barrier defining the energy required to move a screw dislocation from one equilibrium position to the next. We find that predicting the correct core structure does not guarantee accurate modelling

of screw-dislocation translation.

The work presented in this chapter will be published as Gilbert and Dudarev [**229**, © 2010 United Kingdom Atomic Energy Authority], and has already been extended to the work described in Chiesa *et al.* [**230**].

6.1 Introduction

In the previous chapter, we investigated the mobility of screw dislocations in bcc Fe under applied stress at finite temperature. The velocities measured in our simulations, as well as those measured by experiment, are much lower than those of other defects, in particular edge dislocations. This results from the non-planar core structure of screw dislocations, which is a direct consequence of the three-fold symmetry of $\langle 111 \rangle$ directions in a bcc lattice [**191**].

There has been significant debate about the exact nature of the screw dislocation core in bcc metals and how this might influence the response under stress. Noting a similarity with the case of fcc metals, Hirsch [**189**] suggested that the non-planar core would split on the {112} planes. Later, Mitchell *et al.* [**231**] discussed, in relation to work hardening in Nb, the splitting on both {112} and {110} planes under stress. After Sleeswyk [**232**] found, using isotropic elasticity theory, that splitting on {112} was unstable, Kroupa and Vitek [**233**, **234**] investigated the possible symmetry-broken configurations of the $\frac{1}{2}[111]$ dislocation core from its splitting on the {110} planes. Hirsch and Sun [**235**] confirmed the finding of Sleeswyk [**232**], this time using anisotropic elasticity effects, which is particularly important for the case of Fe.

More recently, interatomic potentials predicting both a {110}-split core (degenerate) structure and the compact non-split (non-degenerate)

structure have been used to investigate their impact on energies and the stress/strain-response [**193**]. Vitek [**193**] found, for two potentials predicting the opposing cores in Mo, that the behaviour of screws in a strained crystal did not seem to be significantly affected. However, Chaussidon *et al.* [**211**] observed that, for Fe, a potential predicting a split core (by Simonelli *et al.* [**213**]) most often leads to a {112} glide plane under stress, whilst for the non-split core predicted by the Mendelev [**82**] potential a {110} glide plane was favoured in most cases where the glide plane was bounded by free surfaces in the direction of motion. This suggests that a different response to external stress can occur depending on whether the core structure does or does not undergo the symmetry-breaking associated with the spontaneous displacement of atoms in the core region in either the [111] or the $[\bar{1}\bar{1}\bar{1}]$ direction [**236**] (this is an alternative explanation of a split screw core - see for example [**231**, **232**]).

The above observation comes from the idea that motion (both magnitude and type) could change according to the favoured glide-plane, and so the stress response may be altered. However, the situation was further confused by the discovery in [**211**] that the favoured glide plane can also be influenced by the boundary conditions of a simulation. Chaussidon *et al.* [**211**] found that, even with the symmetric-core favouring potential of Mendelev *et al.* [**82**], the {112} glide plane can be activated when the glide plane is infinite (*i.e.,* when there are periodic boundary conditions in the direction of motion). This was the case with the MD simulations presented in chapter 5, where we used the potential of Mendelev *et al.* [**82**].

In the [111] projection of the bcc lattice the non-degenerate core structure appears as sixfold, whereas the degenerate (split) core configurations are threefold [**193**, **237**]. Harry and Bacon [**238**] extended

the treatment to a case, very significant for applications, where a screw dislocation interacts with a precipitate. They found that the interaction of a screw dislocation with a precipitate is subtly influenced by the way in which the core spreads asymmetrically around the centre of the dislocation.

Simulations performed using various semi-empirical many-body interatomic potentials for Fe in most cases predicted the degenerate, symmetry-broken, threefold core structure as the lowest energy configuration [**86**, **105**, **110**, **111**, **213**, **239**, **240**]. There are notable exceptions to this rule, with some interatomic potentials [**82**, **193**] predicting non-degenerate screw dislocation core configurations [**210**–**212**]. More significantly, recent DFT simulations [**212**, **225**–**228**] show that in all the bcc transition metals, the core of $\frac{1}{2}[111]$ screw dislocations is symmetric and non-degenerate. The non-degenerate dislocation core structures are also predicted by tight-binding model simulations [**98**, **241**, **242**], which suggests that either long-range interatomic interactions (resulting from high-order quantum electron hopping pathways) or the directional bonding effects might be responsible for the non-degenerate structure of the $\frac{1}{2}[111]$ screw dislocation core.

In alternative investigations, Duesbery and Vitek [**243**] noted that the structure of the core of a screw dislocation in a bcc metal is intimately related to the [111] cross-section of the $\{110\}$ γ-surface (generalised stacking fault energies surface). In this chapter, we extend the notion of the γ-surface to the case of one-dimensional [111] atomic strings, which then allows a screw dislocation to be considered as a particular solution of the multi-string Frenkel-Kontorova (MSFK) model [**180**]. This model, in which a crystal is described by a set of one-dimensional atomic [111] strings, was originally developed by Dudarev [**180**, **183**] for studies of self-interstitial

⟨111⟩ crowdion defects, nano-scale prismatic dislocation loops, and edge dislocations. Initially we shall consider the strings to be *non-deformable*, as was the case in the work of Takeuchi [**244**] discussed below. Eventually the strings will be fully deformable, as in the work of Dudarev [**180**, **183**], which will allow for a study of kink formation.

In 1970, Suzuki [**245**] had proposed a similar model, in which a screw dislocation was represented by a set of *rigid* [111] atomic strings, and where interactions between atoms were modelled by pairwise interatomic potentials. This model was investigated further by Takeuchi [**244**] who considered various analytical inter-string interaction laws (see later for explanation), and studied the resulting structures of the dislocation core. In this chapter, we use a similar model to that of Takeuchi [**244**], although we do not assume in advance that the range of interaction is restricted to first nearest-neighbour [111] strings. Very recently, *ab-initio* parameterizations of the Suzuki-Takeuchi inter-string interaction law, taken in the form of a sum of two harmonic functions, have provided new insights into the problem of solute softening and hardening of bcc alloys (see Medvedeva *et al.* [**246**], and Chen *et al.* [**247**]). The *ab-initio*-parameterized *single*-string Frenkel-Kontorova model has also been used by Fitzgerald and Nguyen-Manh [**248**, **249**] to successfully explain the difference between thermally-activated mobilities of crowdion defects in the bcc transition metals of groups VB and VIB (of the periodic table).

The motivation for performing the study of screw dislocations described in this chapter comes from the need to understand how the inter-string interaction laws are related to *ab-initio*-derived semi-empirical interatomic potentials. In particular, we have sought to discover why it is that only one [**82**] of the widely-used many-body interatomic potential developed for

α-Fe appears capable of describing the core structure of the $\frac{1}{2}[111]$ dislocation in reasonable agreement with density functional calculations. Do the long-range interatomic interactions of DFT and tight-binding calculations play a part in stabilizing the non-degenerate structure of the screw dislocation core? We also investigate whether the range of interatomic interactions relevant to a screw dislocation can be estimated directly from density functional calculations. Finally, is the notion of a pairwise, as opposed to a more complex many-body, *inter-string* interaction law assumed in other studies (for example, [**246**, **247**]) consistent with density functional calculations?

In contrast to earlier studies [**244**], here we do not specify the functional form of the inter-string interaction law, and instead derive it directly from DFT data. We find that a fairly simple criterion can be applied to the selection of many-body semi-empirical interatomic potentials, which guarantees that the core structure of the $\frac{1}{2}[111]$ dislocation is non-degenerate, in agreement with density functional calculations. Finally, we discuss our progress in relating the choice of the inter-string interaction law to the Peierls energy barrier for a $\frac{1}{2}[111]$ screw dislocation, and the implications for atomistic modelling using the currently available interatomic potentials.

6.2 The multi-string Frenkel-Kontorova model

The field of atomic displacements for a perfect screw dislocation in a bcc lattice with a $\frac{1}{2}[111]$ Burgers vector is reasonably well approximated in most bcc transition metals, including Fe, by the following equation [**22**]:

$$u_z = \frac{b}{2\pi}\theta, \tag{6.1}$$

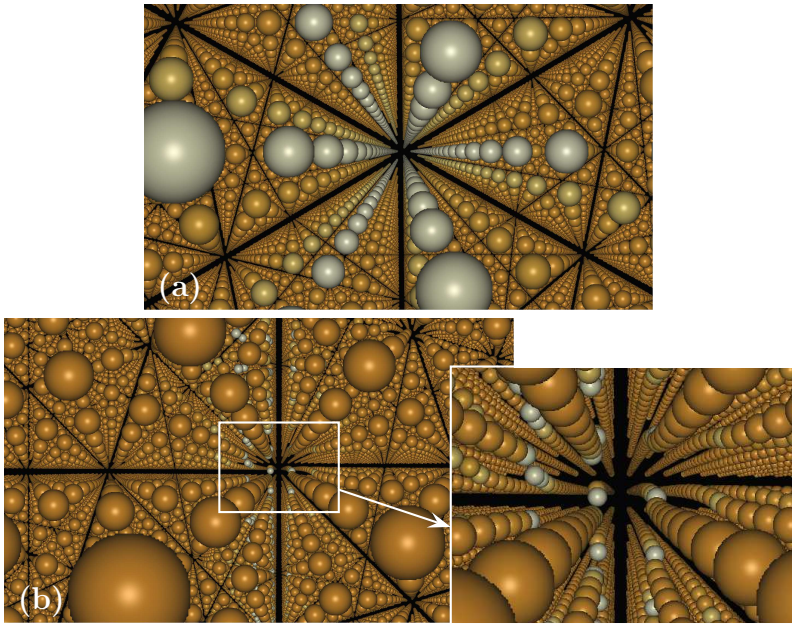


Fig. 6.1: Atomic scale structure of a $\mathbf{b} = (a/2)[111]$ screw dislocation in a bcc transition metal viewed in the [111] direction parallel to the dislocation line (a), and in the $[1\bar{1}0]$ direction normal to the dislocation line (b). The six atomic strings shown in lighter colour form the core of the dislocation. In (a) the positions of [111] strings in the (111) plane are unchanged compared to the perfect lattice, but in (b) the mismatch between atomic rows normal to the Burgers vector are clear [**250**].

where u_z is the displacement of each atom in the [111] direction relative to its position in a perfect lattice. Here $\mathbf{b}$ is the Burgers vector of the dislocation, with magnitude b, which is assumed to be parallel to the dislocation line, and θ is the angle the atom makes in the (111) plane about the line of the dislocation. This equation, and the atomic-scale image of a screw dislocation shown in Figure 6.1, indicates that the presence of a screw dislocation only influences the positions of atoms in the [111] direction. In the (111) plane, which is the plane normal to the dislocation line, the positions of atoms are essentially unchanged compared to their ideal bcc configuration (except for some relatively small in-plane

displacements of atoms close to the core, arising from elastic anisotropy effects [**212**, **251**]), making a perfect screw dislocation effectively invisible if it is viewed in the [111] direction. Equation (6.1) also shows that in a given [111] string of atoms (*i.e.,* a set of atoms with the same coordinates in the (111) plane) each atom is displaced parallel to the axis of the string by the same amount. Hence the structure of a perfect screw dislocation can be investigated by considering the [111] strings of atoms as single objects that have only one degree of freedom, namely their vertical displacement u (by which we mean u_z).

Since the strings do not change their position in the (111) plane (apart from the very small sideways displacements in the core of the dislocation [**212**]), the energy of such a system is a unique function of relative displacements of strings in the [111] direction, namely

$$E(u_1, u_2, \ldots, u_N) = \frac{1}{2} \sum_{i=1}^{N} \sum_{j \neq i} U_{ij}(z_i + u_i - z_j - u_j), \tag{6.2}$$

where i ranges over the total number of strings in the system N, z_i and z_j are the vertical positions of strings in an ideal bcc lattice, and summation over j includes strings that are the first, second, third, *etc.*, nearest-neighbour strings for string i. In previous studies [**244**, **246**, **247**] it was assumed that the sum (6.2) includes only the six nearest-neighbour strings, but, until now, the validity of this approximation was never verified.

Equation (6.2), which is a simplified version of the equation considered by Dudarev [**180**, eq. 1] for mobile interstitial defects, was derived by neglecting the kinetic energy and elastic deformation energy terms. It shows that the displacement field of a dislocation, including the core effects, is fully defined by a set of [111] displacements of strings $\{u_i\}$. Given a

complete inter-string interaction law $U_{ij}(\ldots)$, which is a set of functions representing interactions between the first (defined by U_1), second (U_2), *etc.*, nearest-neighbour strings, the determination of the equilibrium structure of the dislocation core requires minimizing the total energy (6.2) with respect to $u_1, u_2, \ldots, u_N$.

6.2.1 The inter-string interaction law

The inter-string interaction law is the key functional parameter of the model (6.2). In effect, the model is based on two fairly strong assumptions, one of them, that the energy of interaction between the strings can be approximated by a sum of inter-string pairwise terms, and the other, that the strength of the inter-string interaction rapidly decreases as a function of separation between the strings. Neither of these two assumptions are obvious. In two-dimensional string-like statistical mechanics problems, interactions between the strings are often long-range. Furthermore, interactions between atoms in a metal are many-body in character, and in principle there is no reason to expect that the assumed form of the inter-string interaction (6.2) is going to be in any way accurate.

To obtain functional forms for the interaction laws (U_1, U_2, *etc.*) we have performed calculations to measure the energy associated with the displacement of single string, double, and even triple-string complexes in an otherwise perfect bcc lattice. Differences in the resulting energy versus displacement curves illustrate the relative strengths of the inter-string interaction laws, while the curves themselves are used to produce the required functional forms (see below).

We start by verifying the validity of the expression (6.2) for the total energy using the results of DFT calculations performed by

Dudarev [**229**, **250**]. The DFT calculations involved using a relatively large (in DFT terms) supercell. One, or several, atomic strings were displaced ('pulled') in the [111] direction while the other strings remained frozen. The set of energy-change curves obtained in this way are then fitted to equation (6.2) without assuming any specific functional form for the inter-string interaction laws $U_1(...), U_2(...)$, *etc.* The accuracy of the model described by equation (6.2) is then verified by assessing how well the DFT curves satisfy the sum rules consistent with the assumed pairwise form of the total energy.

Figure 6.2 illustrates the definition of the set of inter-string potential laws $U_1(\ldots), U_2(\ldots)$, *etc.*, which make up $U_{ij}(\ldots)$. In an ideal bcc lattice each string has six first nearest-neighbour strings, of which three are displaced by $\mathbf{b}/3 = a/6[111]$ in the positive [111] direction, whereas the other three are displaced by $\mathbf{b}/3$ in the opposite $[\bar{1}\bar{1}\bar{1}]$ direction. Atoms in the six second nearest-neighbour strings, which define U_2, have the same coordinates in the [111] direction as the central string, and the six third nearest-neighbour strings are positioned directly behind the first nearest-neighbours, with their [111] displacements being opposite to those of the corresponding first nearest-neighbour strings.

Density functional calculations of energy pathways, associated with the translation of one or two strings through the surrounding lattice, were performed for ferromagnetic α-Fe using the VASP code [**252**] and the Perdew-Burke-Ernzerhof [**253**] generalised gradient approximation for electron exchange and correlation. Further details of these calculations are given in [**229**]. The 48-atom simulation cell was defined by the translation vectors of $4\sqrt{2}a$ in the $[1\bar{1}0]$ direction, $2\sqrt{6}a$ in the $[11\bar{2}]$ direction, and $\sqrt{3}a/2$ in the [111] direction, where $a = 2.82$ Å is the predicted equilibrium

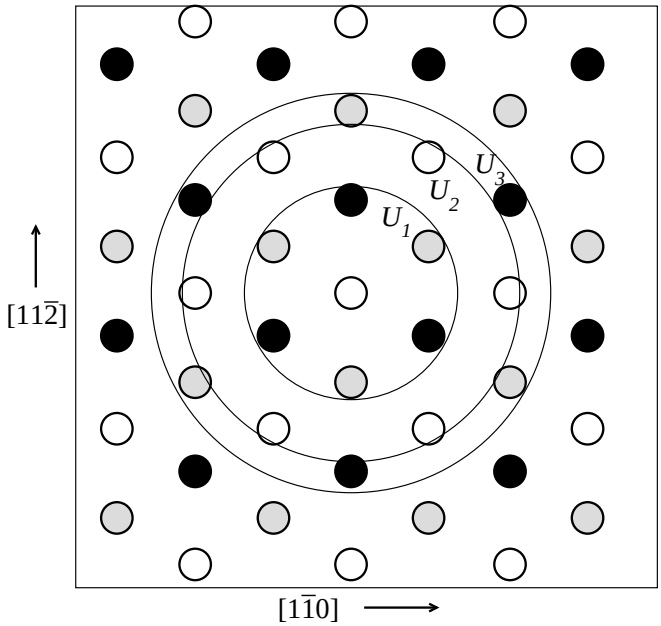


Fig. 6.2: bcc lattice viewed in the [111] direction. It forms a hexagonal two-dimensional lattice of atomic strings. The strings are displaced with respect to each other in the [111] direction (normal to the plane of the image), forming three subsets (or phases), where one of the atoms in the string subset shown in white is situated in the plane of the lattice. One atom of the grey string subset is situated $b/3$ above the plane of the image, whereas one atom of the black string subset is situated $b/3$ below the plane of the image, where b is the magnitude of the Burgers vector $\mathbf{b} = (a/2)[111]$. The circles indicate the 1st, 2nd, and the 3rd (for the components of the inter-string interaction law U_1, U_2, and U_3, respectively) nearest-neighbours of the central string.

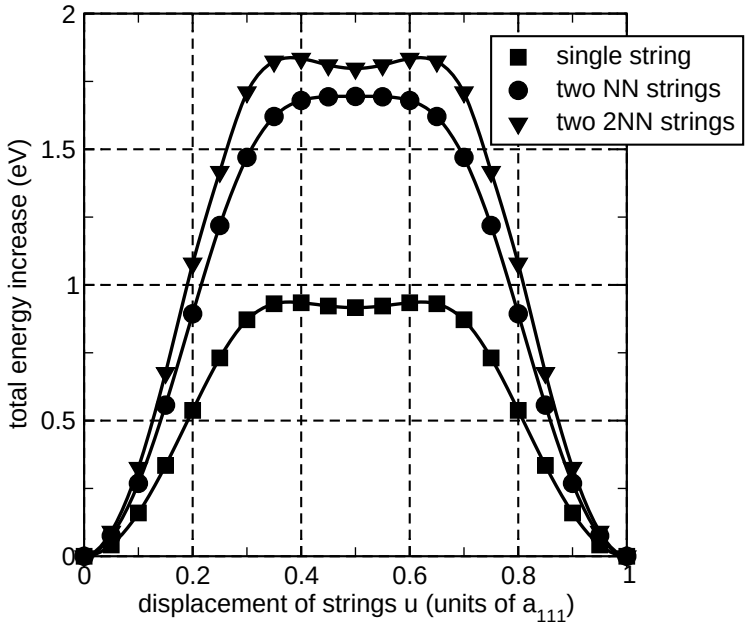


Fig. 6.3: Curves, evaluated using density functional calculations described in the text, showing how the total energy of the system (per Burgers vector distance) changes if (i) the central string shown in Figure 6.2 is translated through the lattice parallel to itself in the [111] direction, (ii) two nearest-neighbour strings are translated in the [111] direction, and (iii) the translation involves two second nearest-neighbour strings.

lattice constant.

Three independent sets of DFT calculations were produced, where a single string, a pair of two nearest-neighbour strings (NN), and a pair of two second nearest-neighbour strings (2NN) were translated ('pulled'), as rigid objects, through the lattice, with all other strings fixed. The resulting energy versus displacement curves are shown in Figure 6.3.

Using the expression for the energy of interacting strings defined by equation (6.2) we can express the energy variation associated with the three curves shown in Figure 6.3 in terms of a linear combination of the

nearest-neighbour string interaction laws U_1, U_2, and U_3 via

$$\begin{aligned}
\Delta E_1(u) &= 3[U_1(u-b/3)+U_1(u+b/3)] \\
&\quad + 6U_2(u) + 3[U_3(u-b/3)+U_3(u+b/3)] + \ldots, \\
\Delta E_{NN}(u) &= 5[U_1(u-b/3)+U_1(u+b/3)] \\
&\quad + 12U_2(u) + 6[U_3(u-b/3)+U_3(u+b/3)] + \ldots, \\
\Delta E_{2NN}(u) &= 6[U_1(u-b/3)+U_1(u+b/3)] \\
&\quad + 10U_2(u) + 6[U_3(u-b/3)+U_3(u+b/3)] + \ldots.
\end{aligned} \tag{6.3}$$

These equations (6.3) can be applied to test the dominance (or not) of the first nearest-neighbour interaction, U_1. If the assumption that the U_1 terms are dominant is correct then the three curves in Figure 6.3 would scale approximately as $3:5:6$. Indeed, dividing equations (6.3) by these ratios, as appropriate, we obtain

$$\begin{aligned}
\frac{1}{3}\Delta E_1(u) &= U_1(u-b/3)+U_1(u+b/3) \\
&\quad + 2U_2(u) + [U_3(u-b/3)+U_3(u+b/3)] + \ldots, \\
\frac{1}{5}\Delta E_{NN}(u) &= U_1(u-b/3)+U_1(u+b/3) \\
&\quad + \frac{12}{5}U_2(u) + \frac{6}{5}[U_3(u-b/3)+U_3(u+b/3)] + \ldots, \\
\frac{1}{6}\Delta E_{2NN}(u) &= U_1(u-b/3)+U_1(u+b/3) \\
&\quad + \frac{10}{6}U_2(u) + [U_3(u-b/3)+U_3(u+b/3)] + \ldots,
\end{aligned} \tag{6.4}$$

which demonstrates that, to a first approximation, the three quantities $\frac{1}{3}\Delta E_1, \frac{1}{5}\Delta E_{NN}$, and $\frac{1}{6}\Delta E_{2NN}$ are described by the same combinations of the first nearest-neighbour interaction law, namely $U_1(u+b/3)+U_1(u-b/3)$. Figure 6.4 shows the result of performing this same rescaling on the three curves of Figure 6.3. Over a significant range of variation of displacement u

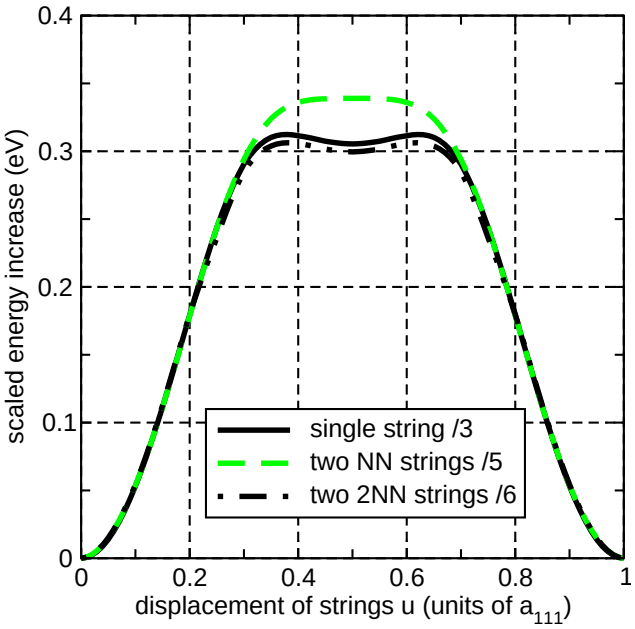


Fig. 6.4: These curves show data taken from Figure 6.3 and scaled by the factor of 1/3, 1/5, and 1/6, respectively. The fact that the re-scaled curves cannot be told apart over a large range of variation of displacement u suggests that the interactions between the strings that are further apart than the first nearest-neighbour distance are relatively weak.

these scaled DFT-derived curves shown in Figure 6.4 can be hardly distinguished from each other, which confirms that interaction between the first nearest-neighbour strings indeed dominates the inter-string Hamiltonian (6.2). It also demonstrates that the combined effect of the second and the third nearest-neighbour string interaction is small.

Numerical analysis of equations (6.4) shows that direct manipulation of the DFT data does not lead to a physically meaningful result for U_3. This stems from the fact that the third nearest-neighbour strings are located directly behind the first nearest-neighbour strings, and the relatively weak third nearest-neighbour interactions are likely masked by the many-body interaction effects from DFT calculations, which are not included in the model expression (6.2). Note, however, that U_3 (and U_2) can be extracted

from the semi-empirical many-body interatomic potentials considered in this work. This is due to the fact that their many-body terms are truncated between the first and second nearest-neighbour string interaction distance, and only the pairwise interactions extend beyond the first nearest-neighbour strings. We find that these are also negligible compared to U_1 (see later), which adds an extra validation to the interpretation of the DFT data discussed below.

To circumvent the difficulties in extracting the small U_2 and U_3 terms from the DFT data, we have employed a different strategy and have focused on the comparison between the effective (first) nearest-neighbour inter-string interaction laws U_1 derived directly from equations (6.4). This is done under the assumption that *all* the curves shown in Figure 6.4 are given by the sum of two terms $U_1(u - b/3) + U_1(u + b/3)$ and therefore yield slightly different versions of $U_1(d)$. Here we adopt the new variable d as the distance between (separation of) strings in the [111] direction, which is equivalent to $(z_i + u_i - z_j - u_j)$ in equation (6.2) (thus $d = u \pm b/3$ for U_1 and U_3, but $d \equiv u$ for U_2). Obtaining $U_1(d)$ from equations (6.4) requires the Fourier deconvolution process described below.

Introducing the phase variable $\phi = 2\pi u/b$, we re-write truncated versions of equations (6.4) (only the U_1 terms are included) in a general form

$$\Delta E(\phi) = U_1\left(\phi - \frac{2\pi}{3}\right) + U_1\left(\phi + \frac{2\pi}{3}\right). \tag{6.5}$$

The Fourier components of this sum of two terms are given by

$$\frac{1}{2\pi}\int_{-\pi}^{\pi} \exp(-in\phi)\Delta E(\phi)d\phi = 2(-1)^n \cos\left(\frac{\pi n}{3}\right) U_1^{(n)}, \tag{6.6}$$

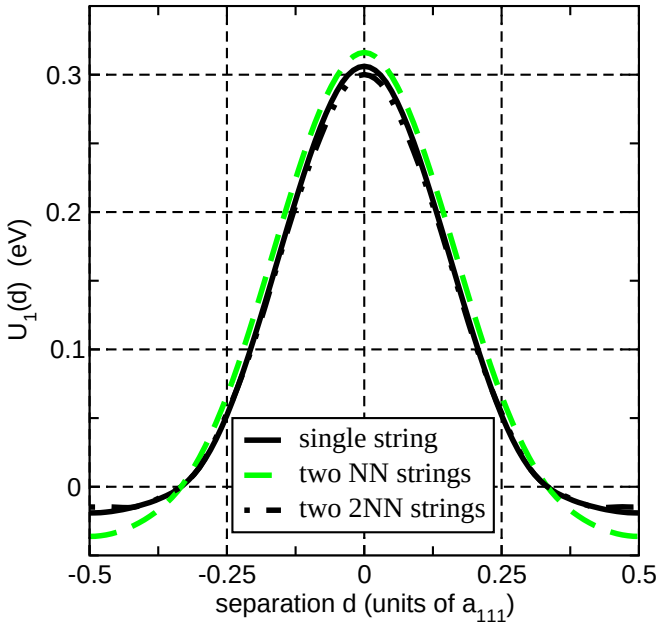


Fig. 6.5: The three effective nearest-neighbour inter-string interaction potentials $U_1(d)$ derived from the DFT data shown in Figure 6.4 using the Fourier deconvolution procedure described in the text.

where $U_1^{(n)}$ is the Fourier component of $U_1(d)$. Combining (6.5) and (6.6), we de-convolute the effective first nearest-neighbour inter-string interaction law as

$$U_1(d) = \sum_{n=-\infty}^{\infty} \exp\left(\frac{2\pi i n d}{b}\right) U_1^{(n)}, \tag{6.7}$$

where $U_1^{(n)}$ is found by numerically computing:

$$U_1^{(n)} = \frac{(-1)^n}{2b\cos(\pi n/3)} \int_{-b/2}^{b/2} \left[U_i\left(u+\frac{b}{3}\right) + U_i\left(u-\frac{b}{3}\right)\right] \exp\left(-\frac{2\pi i n u}{b}\right) \mathrm{d}u. \tag{6.8}$$

Note that the numerical integration was performed using Simpson's rule (see [**254**, pg. 872]).

The curves shown in Figure 6.5 represent the three realizations of the effective first nearest-neighbour string interaction law $U_1(d)$ de-convoluted

from the three curves shown in Figure 6.4. We see that the three forms of $U_1(d)$ do not differ significantly from each other, with any noticeable differences being associated with the 'tails' of the function at $d \approx \pm 0.5$. It is worth pointing out that the original DFT results shown in Figure 6.4 can be recovered from these U_1 curves by computing $U_1(u - 1/3) + U_1(u + 1/3)$. Graphically, this is equivalent to super-imposing two $U_1(d)$ curves on to each other and applying the $\pm 1/5$ periodicity, with one shifted by 1/3 ($b/3$) along the horizontal axis and the other shifted by -1/3 ($-b/3$). In subsequent sections (see 6.3 and 6.4) the dislocation core structures and the Peierls energy barriers produced by these three U_1 curves are analyzed to determine if the differences associated with the choice of the inter-string interaction law are significant.

6.2.2 Interaction laws derived from interatomic potentials

Figure 6.6 shows how $\Delta E_1(u)$ (equation (6.3)) varies according to MD calculations performed using two recent interatomic potentials for Fe. The potentials used in the calculations are those of Dudarev and Derlet [**105**, **110**], and of Mendelev *et al.* [**82**]. Also included for comparison are the 'single-string' DFT data from Figure 6.3. The MD data represent the change in total interaction energy (potential energy) evaluated using a given interatomic potential for a system of atoms with periodic boundary conditions. The total size of the simulation cell in the (111) plane was chosen to be sufficiently large enough to ensure that as a string is pulled through the lattice it does not interact with itself through the periodically repeated boundaries. In this particular case, the box had dimensions of 20×20 unit cells in the $[1\bar{1}0] \times [11\bar{2}]$ directions, where each unit cell contains 6 atoms (see Appendix A.1). In the [111] direction the cell

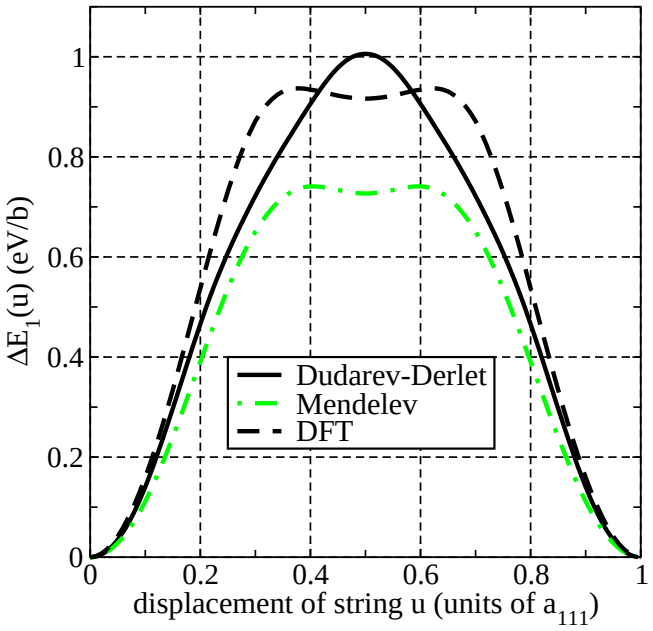


Fig. 6.6: Variation in system energy as a single [111] string moves through a stationary perfect lattice of Fe by one $\mathbf{b} = (a/2)[111]$ period. Results of calculations performed using the two interatomic potentials are shown together with the DFT data from Figure 6.3.

contains six atoms per string, giving 14,400 atoms in total. Calculations confirmed that the energy values scaled linearly with the number of atoms per string (*i.e.,* the number of Burgers vectors). We have also computed the curves for $\Delta E_{NN}(u)$ and $\Delta E_{2NN}(u)$ (see Figure 6.7).

Note that for a given configuration of atoms the energy was obtained from the 'zero-time' parameters of the MD simulation (*i.e.,* before any dynamics had taken place). Since each MD simulation had zero time-steps it was a quick and straightforward task to compute the energies for multiple string displacements. Each of the ΔE curves presented here for interatomic potentials contains 200 individual calculations.

Both of the semi-empirical potentials considered contain a short-range many-body contribution in the form of a non-linear function of the local

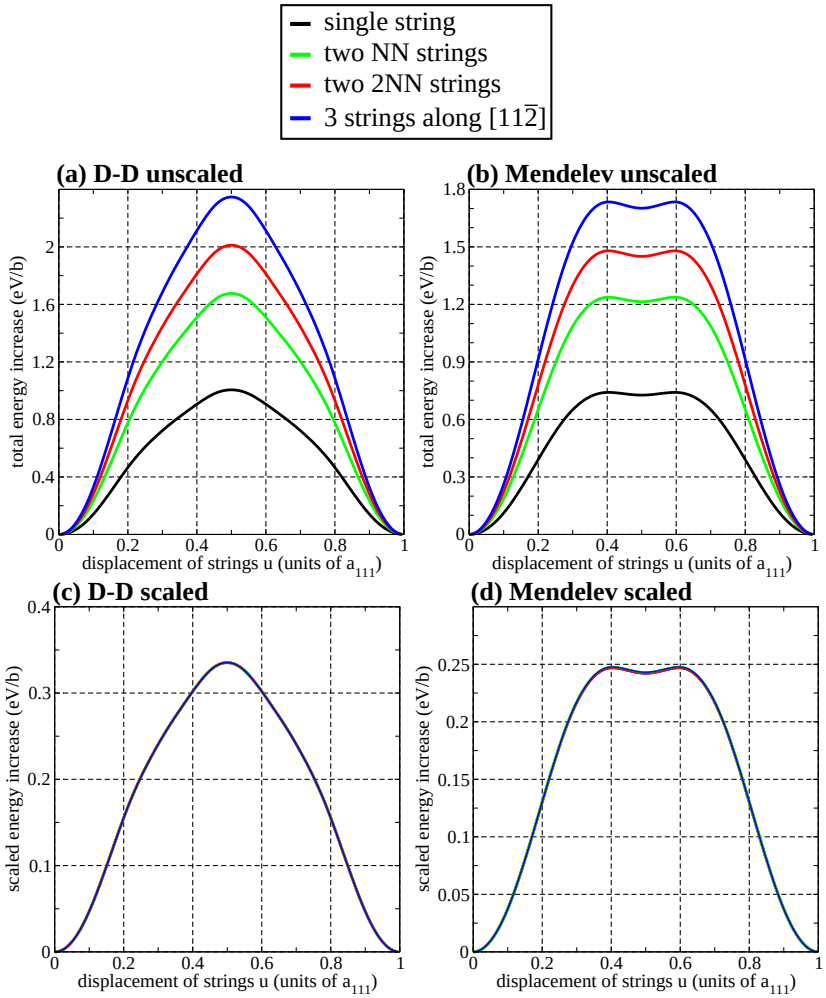


Fig. 6.7: Total energy increases resulting from the [111] displacement of single or groups of [111] strings in an otherwise perfect bcc Fe lattice. (a) and (c) show results from the D-D potential. (b) and (d) are for the M potential. (a) and (b) display the absolute energy change, while (c) and (d) show the scaled energy changes (see text). The scaling ratios are 3:5:6:7 for (single):(two NN):(two 2NN):(row), respectively. In (c) and (d) the four curves are indistinguishable, which demonstrates the dominance of U_1 over higher order terms.

electron density. In the Dudarev-Derlet (D-D) case this term is truncated between the second and the third nearest-neighbour atom distances, and so is zero at distances corresponding to inter-string interactions U_2 and U_3 (see Appendix D). The many-body contribution to the Mendelev (M) potential is at the maximum extent of its range close to the distance for U_2 (at the third nearest-neighbour atom), and so is negligible at this point. This means that both potentials behave in an essentially pairwise manner at distances associated with the higher order interactions, making these longer-range terms extractable from the simulated curves. However, to find U_3 exactly we need an additional set of data, namely the energy change associated with the translation of a row of three adjacent strings (in the $[11\bar{2}]$ direction), ΔE_{row}:

$$\begin{aligned}\Delta E_{row}(u) =& 7[U_1(u-b/3)+U_1(u+b/3)]+18U_2(u)\\ &+8[U_3(u-b/3)+U_3(u+b/3)]+\ldots.\end{aligned} \tag{6.9}$$

Figure 6.7a and 6.7b show all of the computed ΔE curves (four in each graph) for the D-D and M potentials, respectively. In Figures 6.7c and 6.7d, for D-D and M, respectively, we have also scaled the same curves by the appropriate U_1 ratios in equations (6.3) and (6.9) (namely 3:5:6:7). Thus the black curve for the single-string displacement in Figure 6.7b for Mendelev has been divided by 3 for the plot in Figure 6.7d. The green curve for the displacement of two nearest-neighbour strings in graph (b) is divided by 5 for graph (d), and so on. A similar process was performed to produce graph (c) from (a) for the D-D potential. In graphs (c) and (d) of Figure 6.7 we can see that the differences between the single-string curve and the other curves are so negligible that they cannot be resolved, and the curves appear to coincide. Even though this was always likely to be the case, due

to the (relatively) short-range nature of the potentials, it is still a further validation for the conclusion that U_2 and U_3 are small compared to U_1.

For the interatomic potentials, as mentioned earlier, we can now go one step further and explicitly compute these higher-order interaction laws. The convoluted forms of U_1 and U_3, as well as $U_2(d)$ (since $d \equiv u$ as far as U_2 is concerned), are found via:

$$\begin{aligned} U_1(u-b/3)+U_1(u+b/3) &= 2\Delta E_1(u)-\Delta E_{NN}(u), \\ U_2(d)\equiv U_2(u) &= 2\Delta E_1(u)-\Delta E_{2NN}(u), \\ U_3(u-b/3)+U_3(u+b/3) &= 3\Delta E_1(u)-\Delta E_{row}(u) \\ &\quad -2[U_1(u-b/3)+U_1(u+b/3)]. \end{aligned} \tag{6.10}$$

The $U_1(d)$ and $U_3(d)$ terms (U_2 requires no further manipulation) can now be de-convoluted using equations (6.5)-(6.7). Note that for the magnetic potential [**105**, **110**] the pairwise term is truncated just beyond the third nearest-neighbour-atom (NNA) distance, and hence from Table D.1 of the Appendix we see that for this case $U_3(d) \equiv 0$. The potential by Mendelev *et al.* [**82**] extends out to the fifth NNA, and thus U_3 does not vanish.

Figures 6.8 and 6.9 show the U_1 and U_2 string-string interaction laws, respectively, for the two interatomic potentials, while Figure 6.10 shows the U_3 curve evaluated for the M potential. Comparing the scales on each graph we see that the strength of U_2 for the M case is around two orders of magnitude smaller than that of U_1 (single-digit meV versus 100s of meV), while the U_2 for the D-D case is even smaller. Similarly, the magnitude of the U_3 term derived from the M potential is in the 100s of μeV range, which is another two orders of magnitude smaller than U_2. These results,

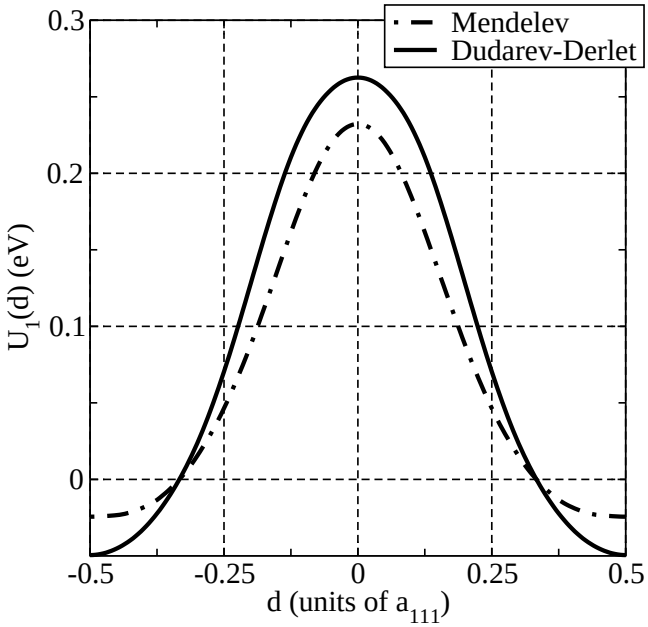


Fig. 6.8: The U_1 curves corresponding to the two interatomic potentials described in the text.

together with the similarity between the three scaled DFT curves in Figure 6.5 and the scaled interatomic potential curves in Figures 6.7c and 6.7d, show conclusively that the interactions with the second nearest-neighbours strings, and beyond, are very small compared to the strength of interaction with the six first nearest-neighbours strings (U_1).

6.3 The core structure of a screw dislocation

To answer the question as to whether longer range interactions play a part in determining the core structure of a screw dislocation, we have performed a series of conjugate gradient (CG) minimisations on systems of strings. The energy of such a system is determined by the inter-string interaction laws derived above. First, we confirmed that the minimum energy structure for a system of interacting strings with PBCs in the (111) plane was the

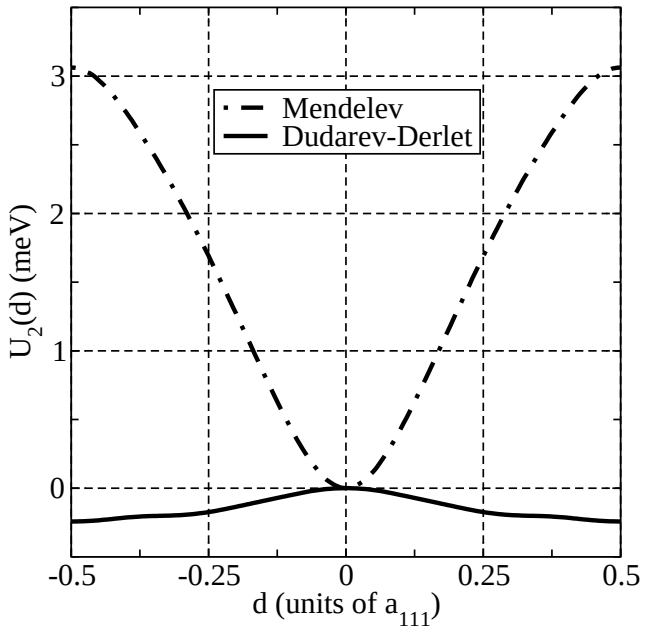


Fig. 6.9: The second nearest-neighbour inter-string interaction U_2 curves evaluated using the interatomic potentials. Note the difference in the absolute scale between the curves shown in this plot, and the U_1 curves shown in Figure 6.8.

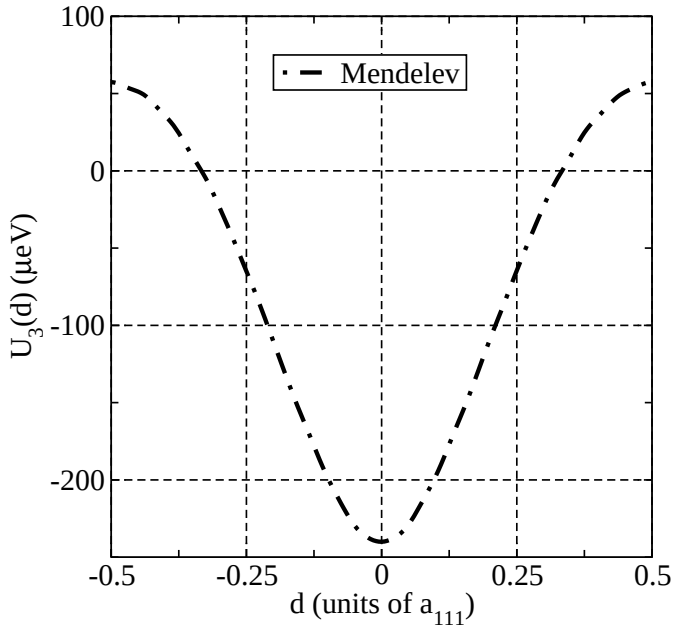


Fig. 6.10: The U_3 curve evaluated using the Mendelev *et al.* [**82**] many-body interatomic potential.

three-phase (see Figure 6.2) configuration of a perfect bcc lattice. Figure 6.11a depicts this configuration for a 40x40 lattice of strings (40 strings in the $[1\bar{1}0]$ direction by 40 strings in the $[11\bar{2}]$ direction) under the M potential-derived interaction laws. The perfect lattice configuration was reproduced both with and without the longer-range interactions (U_2 and U_3), and with all of the three U_1 DFT-derived inter-string interaction curves from Figure 6.5.

To investigate the minimum energy configurations associated with the screw dislocation structure, every string in a perfect lattice was initially given a displacement defined by the isotropic elasticity solution for a screw, as defined by equation (6.1). The core of the screw was centred in the middle of the same 40×40 two-dimensional simulation cell described above. The direction of the Burgers vector of the dislocation, and the exact position of its centre, was chosen in such a way that the 'sense of rotation' of the dislocation (*i.e.,* the direction of the Burgers vector) was the same as that of the three strings forming the core-triangle of the dislocation in the perfect lattice. This resulted in the so-called 'soft core' configuration (also known as the 'easy core') [**255**]. This is as opposed to the 'hard core' configuration, which corresponds to the case where the sense of rotation of the screw dislocation is opposite to that of the three strings forming the central triangle. The total energy of the system was minimised under the constraint that the displacements of strings contained in a two-string-thick border layer were *exactly* equal to the displacement field of a perfect screw dislocation in an infinite solid (6.1). The PBCs were only imposed in the z (*i.e.,* [111]) direction. The CG energy minimisation resulted in the lattice finding the local minimum for the screw dislocation core structure, consistent with the core structure produced from the original interatomic

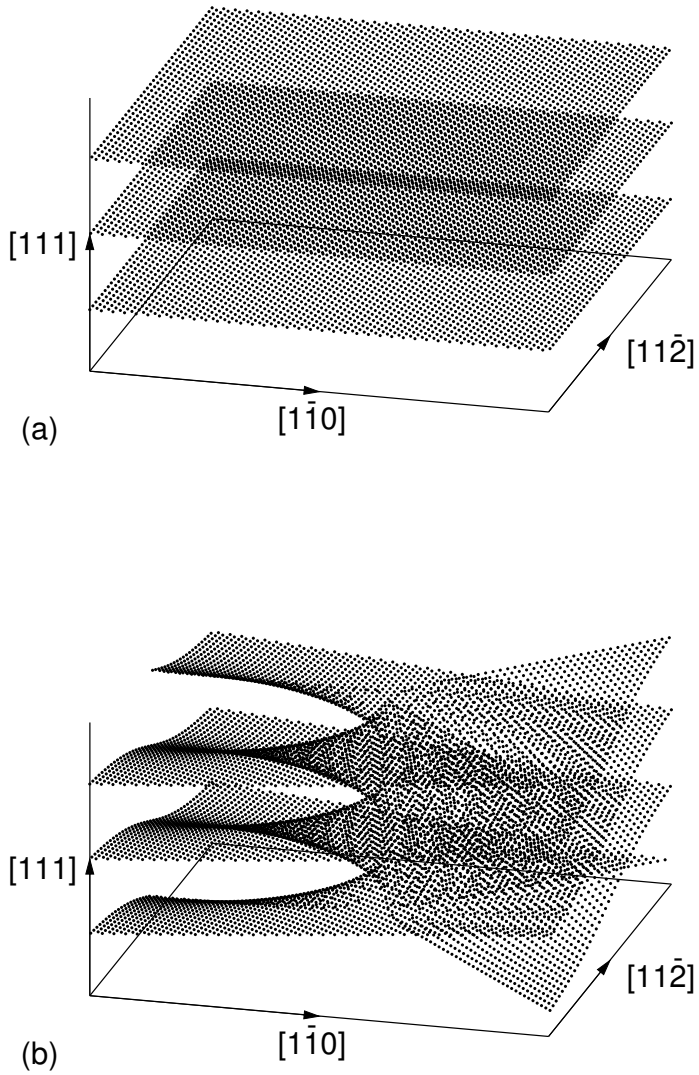


Fig. 6.11: The [111] string configurations for (a) the perfect bcc Fe lattice and (b) the symmetric non-degenerate core structure found for the inter-string interaction law derived from the M interatomic potential. Note that (b) is practically indistinguishable from the isotropic elasticity solution for a screw dislocation (equation (6.1)).

potential used to derive the chosen inter-string interaction laws. We also performed relaxations without constraining the border strings. This meant that the system contained free surfaces, but had no noticeable effect on the screw dislocation core structure.

Figure 6.11b shows the result for the inter-string interactions derived from the M interatomic potential. In comparison with Figure 6.11a, where the atomic planes are distinct, the screw dislocation structure causes the atomic planes to form continuous sheets of atoms. Both Domain and Monnet [**210**] and Chaussidon *et al.* [**211**] have shown that the M interatomic potential for Fe produces a symmetric non-degenerate core that is very similar to the isotropic elasticity solution. The configuration shown in Figure 6.11b does represent a screw dislocation with a non-degenerate core, which is demonstrated by the differential displacement map for the same system, shown in Figure 6.12a. This map, and others like it throughout the chapter, represents relative changes (compared to perfect bcc) in displacement between strings (or atoms) using the variation in the length and direction of arrows linking them (see the work of Vitek [**255**] for more details). The map in the figure shows the same compact symmetric core found in atomistic simulations performed using the original interatomic potential, as shown in Fig. 1b of [**210**] and Fig. 2a of [**211**].

Additionally, we have compared the [111] positions of strings in the relaxed configuration with the positions that the strings occupy according to the perfect isotropic solution for a screw core (as defined by equation (6.1)). Figure 6.13a shows the result from such an analysis as a function of string distance from the screw core, with the inter-string interactions in this case derived from the M potential. The deviation is very close to zero for the range shown in the graph, and also at larger distances.

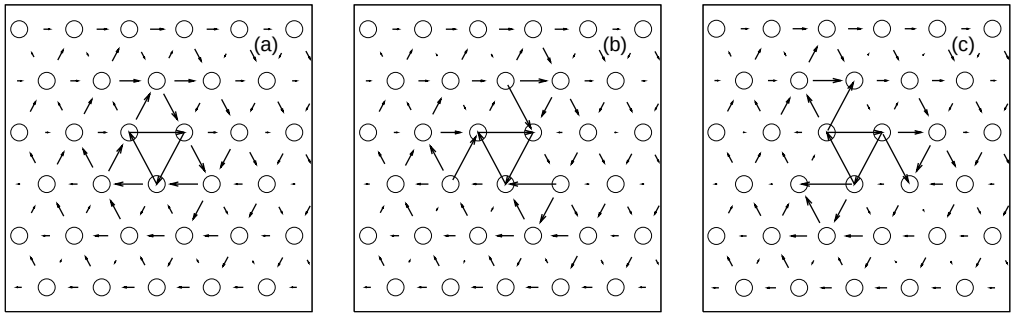


Fig. 6.12: Differential displacement maps of the screw dislocation cores produced by the inter-string potentials derived from the (a) M and (b,c) D-D interatomic potentials. $[1\bar{1}0]$ is the vertical direction, with $[11\bar{2}]$ horizontal. The energies of the two configurations shown in (b) and (c) are virtually identical.

This demonstrates that the core structure is very near to the isotropic elasticity solution.

Figure 6.13b shows results of the same analysis performed for the strings around the core of a screw dislocation relaxed using the inter-string interaction derived from the D-D magnetic potential. Atomistic simulations indicate that the D-D potential favours a degenerate symmetry-broken core structure, and this feature is well reproduced by the string model. In comparison with a symmetric core (Figure 6.13a), the differences for this symmetry-broken core are striking, with the three strings surrounding the core (represented by a single point on the graph) deviating from the symmetric solution by more than 0.2 Å. At the same time, the three strings in the next 'layer' from the core are displaced in the opposite direction by around 0.08 Å. In [**244**], Takeuchi also noted this opposing displacement behaviour for degenerate cores, and both the ratio and magnitude of change are in good agreement with our results. These deviations, however, are very short-range and die out rapidly in strings further away from the core. Beyond approximately 5 Å the differences have fallen to a random

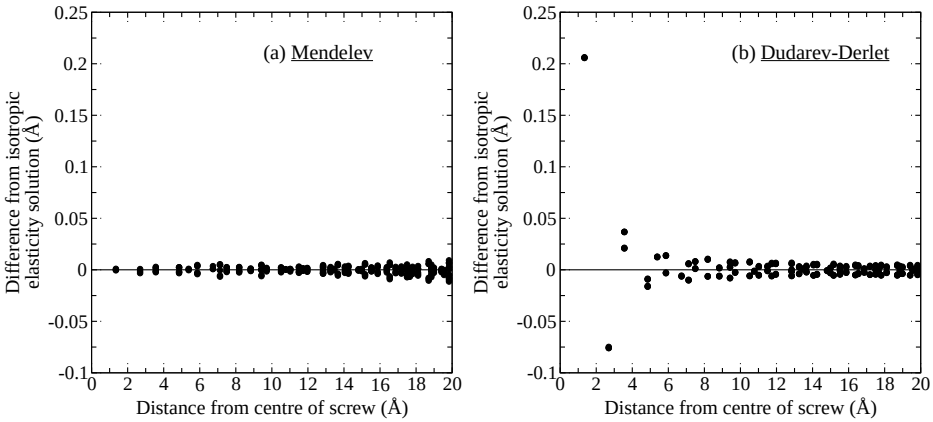


Fig. 6.13: The differences between the [111] displacements of strings in the ideal isotropic solution for a screw dislocation, and their displacements after relaxation with (a) the M-derived string interaction laws and (b) the string interaction laws derived from the D-D potential. Differences for each string are plotted against its distance from the centre of the screw dislocation core in the (111) plane.

background level and the structure is close to the isotropic solution. Indeed, if a plot, similar to that produced using the M potential and shown in Figure 6.11b, were produced for the D-D potential, then it would look almost identical, except for some localised deviations around the dislocation line, very near to the symmetry-broken core. Figures 6.12b and 6.12c show the differential displacement maps for the two possible degenerate cores produced from the D-D interaction laws. The energy of these two configurations are identical, and hence we have the degeneracy associated with not having a single favoured core-configuration.

We found using additional CG minimisations that the degeneracy, or not, of the minimum energy screw core configuration was unaffected by the omission/inclusion of the second (U_2) or, in the case of the M potential, the third (U_3) nearest-neighbour string interactions. At the same time, simulations performed using the three different U_1 curves from DFT data (Figure 6.5), all produce the symmetrical non-degenerate core predicted by

DFT calculations for Fe (see, for example, [**226**, **228**]). This also indicates that the contributions due to the longer-range interactions are not important for the core structure. It is therefore safe to neglect the higher-order interactions when discussing the core structure of a screw dislocation, and from here onwards we only discuss the interaction of strings with their first nearest-neighbour strings described by U_1.

Concluding this section, we note that the *first* nearest-neighbour strings, together with the central string that they surround, contain all of the *first and second* nearest-neighbour *atoms* of an atom belonging to the central string (see Appendix D). They also include some, but not all, of the third and above, nearest-neighbour atoms. Hence our results show that only the interactions between the first and the second nearest-neighbour atoms influence the core structure of screw dislocations. This conclusion suggests that, when developing interatomic potentials for large-scale atomistic simulations, it may be possible to have a *very* short range of interaction (even shorter than current potentials like M, which extends to the sixth nearest-neighbour atoms), while still reproducing the correct core structure, and hence dynamic behaviour.

6.3.1 Shape of the U_1 curves

Simulations indicate that the absolute magnitudes of the energies in the U_1 curves are not important in determining the core structure, and that the curves can be re-scaled by any positive factor without altering the result. Shifting the curves by a constant value also has no effect because it is the relative energies of one part of the curve compared to another that are important. This alludes to the idea that it is the shape of a particular U_1 interaction law which determines the outcome of a simulation describing

the minimum-energy screw core structure. It is also worth noting that the choice of the Burgers vector length (and hence the lattice parameter a) is essentially arbitrary, and the argument of the U_1 law (*i.e.,* separation d) can be scaled to another Burgers vector length without altering the findings, provided that it is now applied to a crystal with the corresponding new structural parameter a.

What specific parameter characterizing the shape of a U_1 curve determines the nature of the equilibrium core structure? To answer this question we begin by looking at the U_1 potentials discussed above. Figure 6.14 shows the two interatomic potential-derived U_1 curves after shifting both to non-negative values of energy, and normalising them to a maximum energy magnitude of one. One of the DFT curves (single string U_1) is also shown in this shifted and re-scaled format. We see that the curves derived from the M interatomic potential and from DFT are very similar, and both produce a non-degenerate core, while the D-D-derived curve is somewhat broader about the peak at zero and results in a degenerate core.

Since all the curves in Figure 6.14 have the same basic cosine-like shape, it must be the subtle change occurring during the translation from the M and DFT curves to the D-D curve, that results in the profound change in the dislocation core structure. To study this we have performed a sequence of CG relaxations of screw core structures using a series of U_1 laws produced by linearly interpolating between the M and D-D curves. For example, a +0.5 interpolation corresponds to a curve that sits exactly half way (at each point) between the two base curves. In this way it is also possible to perform extrapolation outside of the region enclosed by the two curves.

We considered several different interpolated curves. For negative values

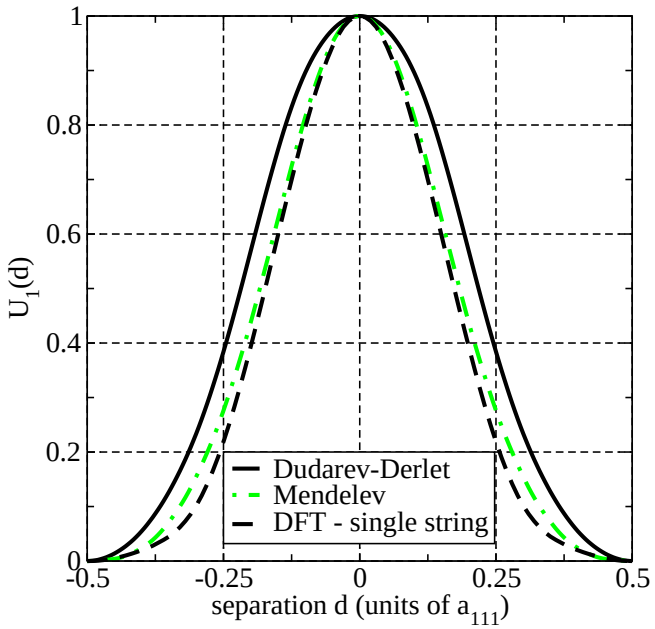


Fig. 6.14: Three U_1 potentials after normalising their minima to zero and scaling to a maximum of one.

of the interpolation constant, which in Figure 6.14 corresponds to a U_1 curve with a narrower peak than M, we found that the relaxed screw core remained non-degenerate and symmetric. This was not unexpected given that this region contains the DFT-derived U_1 curve. In the region between the two interatomic-potential-derived curves, where the interpolation constant varies between 0 and 1, we found that the screw core remains close to the isotropic elastic solution (*i.e.,* symmetric) up to around 75% (0.75 interpolation) of the way from M to D-D. Beyond this point the nature of the relaxed core abruptly changes to that of the symmetry-broken degenerate configuration seen for the D-D U_1 curve, and this symmetry-broken core remains the favoured one for all the U_1 curves extrapolated beyond (*i.e.,* broader than) D-D.

To see more clearly which type of core structure is favoured for a given inter-string interaction law we compute the relative energies of a sequence

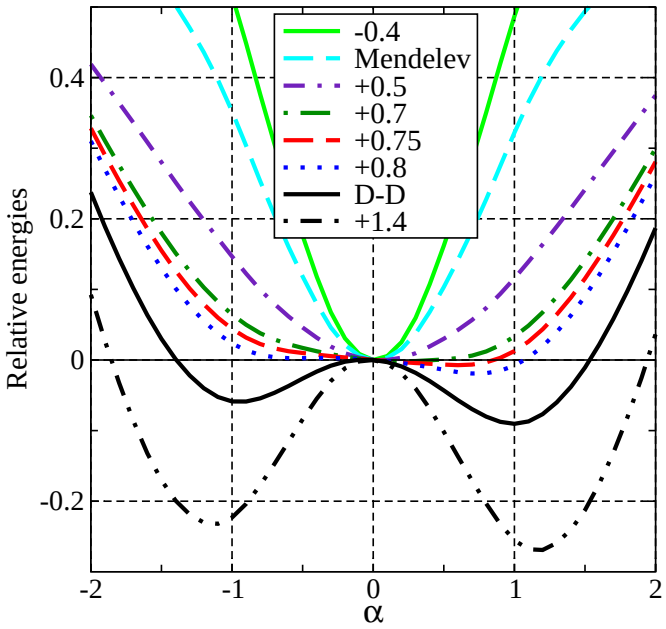


Fig. 6.15: Stability curves for various U_1 inter-string interaction laws. The numerical designation for a U_1 function in the legend refers to its interpolated distance from the M U_1 law ('zero') in the direction of the D-D law ('one'). α is a measure of symmetry breaking in the screw core with perfect symmetry at zero, and each curve in the chart shows how the energy of the screw core structure varies as a function of α for a given inter-string interaction U_1.

of string configurations, which were constructed by interpolating between a non-degenerate and degenerate core. Figure 6.15 shows, for several interpolated U_1 interaction laws, how the energy of a symmetric (non-degenerate) configuration ($\alpha = 0$) compares to progressively more symmetry-broken cores ($\alpha \neq 0$). Each curve in the graph is identified by the amount of interpolation (or extrapolation) between the M and D-D curves, as described above. Here the configuration parameter α describes the linear interpolation fraction between the string configuration corresponding to the isotropic elasticity solution for a screw core ($\alpha = 0$) in the given 40×40 string-lattice, and the configuration for the same set of strings containing a symmetry broken (degenerate) core at $\alpha = 1$. In this

case we have used the degenerate core produced from simulations using the D-D potential. This means that α, in this context, is a measure of symmetry-breaking in the core, with a perfectly symmetrical core at zero, and significantly symmetry-broken core at one.

Note that in Figure 6.15, there is an asymmetry about $\alpha = 0$, and, in particular, the energies of the $\alpha = -1$ configuration are slightly higher than those of the $\alpha = 1$ case. This is despite our earlier assertion that the energies of the two alternative degenerate cores are identical. The discrepancy here results from the way we have interpolated (and extrapolated) between the $\alpha = 1$ configuration and the isotropic solution at $\alpha = 0$. At long range, both the non-degenerate and degenerate core structures are identical. However, as Figure 6.13b shows, the string potential derived from the D-D potential does not produce a screw-core solution that is identical to the isotropic solution at large r - minor deviations do exist. This then is the origin of the asymmetry - the deviations should be the same for both possible degenerate cores, but for $\alpha = -1$ the interpolation produces the negative of these deviations. So at $\alpha = -1$ we do not quite have the minimum energy structure that the D-D potential would produce. By relaxing this solution under the D-D-U_1 law we find that the energy reduces to that of the $\alpha = 1$ configuration.

For each curve in Figure 6.15 the energy is calculated relative to the energy of the symmetric non-degenerate core at $\alpha = 0$, which is scaled to zero. Figure 6.15 shows that the M-derived U_1 curve, and curves near to it (negative or small positive interpolation from M), strongly favour configurations similar to the isotropic solution, with a pronounced global energy minimum at $\alpha = 0$ in the graph. However, for the D-D-derived inter-string interaction law and beyond, where the shape of the U_1 curve

becomes even broader than the D-D curve in Figure 6.14, the picture is entirely different. The non-degenerate configuration at $\alpha = 0$ is now a local maximum of energy, with local minima at two symmetry-broken configurations corresponding to $|\alpha| \sim 1$. The depth of the energy-wells is relatively large, implying that such inter-string interaction laws strongly favour a symmetry-broken dislocation core. The cross-over to favouring the symmetry-broken configuration occurs when the U_1 curve is taken approximately as a linear combination of $0.3U_1^{(M)} + 0.7U_1^{(D-D)}$ (*i.e.,* a 70% interpolation from M to D-D). For U_1 curves representing 0.7 to 0.8 interpolations from M (*i.e.,* almost equal to D-D) the energy curve (0.7, 0.75, and 0.8 are shown in Figure 6.15) has an almost flat profile around $\alpha = 0$, meaning that the symmetric core is quite unstable and could easily change configuration under the application of external stress.

We next investigate the particular features of the U_1 curve that are responsible for the transformation of the dislocation structure from the symmetric core to a symmetry-broken one. In Figure 6.16 we have plotted the first derivative of the inter-string interaction law, which corresponds to the forces acting between strings, for the scaled and normalised U_1 curves (Figure 6.14) derived from the M and the D-D interatomic potentials. The graph shows that the extrema (maximum and minimum) of these curves, which correspond to the inflexion points of the original U_1 curves, are further away from the origin for the D-D case in comparison with the M case. In the figure we have also plotted, as bars above the curves, the effective separations d between first nearest-neighbour strings in the [111] direction for an ideal screw dislocation core, defined by equation (6.1). In a perfect bcc lattice case the bars would all be merged at $\pm b/3$ ($= \pm 0.33$ in this scaled graph), whereas a screw dislocation structure is characterised by

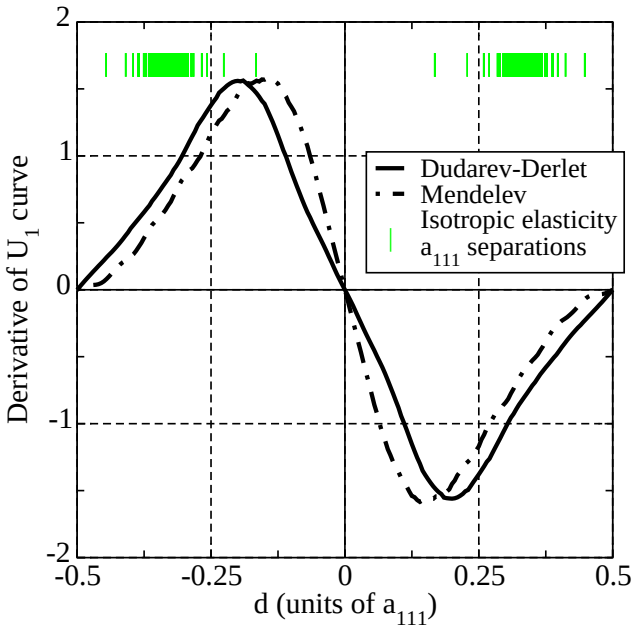


Fig. 6.16: The first derivatives of the U_1 curves derived from the M and D-D interatomic potentials for Fe. The bars above the curves show the relative separations for the [111] strings ('interaction distances') for the ideal isotropic elasticity solution of a screw dislocation, given by equation (6.1).

a spread of values of relative displacements of strings, although most of the values are still clustered around the perfect lattice positions of $\pm 1/3$. The maximum divergence from the perfect bcc case corresponds to the separations between strings immediately surrounding the core of the dislocation, with a minimum separation of $b/6$ (1/6 in the units of Figure 6.16) [**244**].

In Figure 6.16, for the M case, the string separations, indicated by the bars, *all* lie outside of the region about $d = 0$ bounded by the extremum points of the U_1 first derivative curve. In this outer region the second derivative of the U_1 curve is positive, resulting in a stable symmetrical core configuration, similar to the isotropic elasticity solution (6.1). On the other hand, for the D-D case there are strings nearest to the core that fall into

the 'region of instability' between the extrema of the first derivative of U_1. Under these circumstances the initial solution, defined by equation (6.1), loses its stability and evolves, *via* energy minimisation, towards a symmetry-broken core configuration.

For the linear combinations of the M- and D-D-derived U_1 potentials discussed previously in this section, the extremum points of the first derivative varies depending on the relative weights of the M and D-D contributions (*i.e.,* how much we have interpolated from M to D-D). For this family of curves we find that the symmetric core configuration loses its stability at approximately the point at which the inflexion points for a particular U_1 curve falls beyond the shortest inter-string interaction distance for the symmetric core configuration. This shortest distance is $b/6$ for the isotropic solution defined by equation (6.1), but is not exactly this for the family of curves discussed here. The reason for this is that the M-U_1 curve does not produce a symmetric core that is identical to the isotropic solution, *i.e.,* there are slight variations. Since M-U_1 was used to produce the interpolated interaction laws, it was always unlikely that they would adhere to the strict $b/6$ 1st-derivative extremum criteria. This observation agrees with the work of Takeuchi [**244**], who found, for model U_1 functions, that the cross-over to degeneracy did not always occur exactly where the 2nd-derivative of U_1 (and hence the 1st-derivative extrema) became zero at $b/6$.

6.3.2 Analytical representations for U_1

The analysis performed above indicates that an important criterion defining whether or not a given U_1 curve produces a symmetric non-degenerate screw core is the position of the inflexion points in its profile. This suggests

that it should be possible to define analytical representations for the string-potential curves, which have the required 'shape', and have adjustable parameters that can be varied to control the positions of the extremum points for the first derivative curves.

We have investigated three such functions in the present work. As can be seen in the earlier figures of derived U_1 curves (e.g. Figure 6.14), the basic profile we need is that of a cosine function. Thus the three functions presented below are constructed from a cosine base function, with different expressions for the argument of this function. We note that a basic cosine function of the form $(1/2)\cos(2\pi d/b) + (1/2)$, which has the same profile as $\cos(x)$ in the range between $-\pi$ and π, but instead remains non-negative and varies in the range $-b/2$ to $b/2$, produces a symmetry-broken core. The three functions that we consider in this study are:

$$U_1(d) = \frac{1}{2}\cos\left(\pi x^{\gamma}\right) + \frac{1}{2}, \qquad \text{where } x = \frac{2|d|}{b}, \tag{6.11}$$

$$U_1(d) = \frac{1}{2}\cos(\pi \sin(\beta\pi x)) + \frac{1}{2}, \qquad \text{where } x = \frac{2d}{b}, \tag{6.12}$$

$$U_1(d) = \frac{1}{2}\cos\left[\pi \frac{\tan^{-1}(\delta\pi x/2)}{\tan^{-1}(\delta\pi/2)}\right] + \frac{1}{2}, \text{ where } x = \frac{2d}{b}. \tag{6.13}$$

Each of the functions (6.11)-(6.13) has a parameter (γ, β, or δ, respectively) that can be varied in order to change the way the cosine argument runs from $-\pi$ to π (with zero at $d = 0$). We vary the parameters and construct the α versus energy stability-curves to see what effect they have on the equilibrium core configuration. Note that in this case we define the $\alpha = 1$ configuration via the displacement function $Ar^{-3/2}\cos 3\theta$, where θ is the same as in equation (6.1), r is the distance of a string from the screw core, and $A = 0.312$. With this function, the displacements from the isotropic solution are 0.2 Å near the core, as seen in the results from the

D-D potential (see Figure 6.13(b)), but tail off rapidly after this. We felt that using a specific displacement field to describe the symmetry-broken core was more appropriate than relying on the core defined by an interatomic potential, which may or may not be correct.

The three graphs in Figure 6.17 present the results of the 'α-stability analysis' for the functions defined by equations (6.11)-(6.13). In Figure 6.17a, we see that for the case (6.11), where the argument of the cosine is a power law, the change from a symmetric core to a symmetry-broken core occurs at $\gamma \approx 0.99$, with interactions corresponding to $\gamma < 0.99$ producing a generally symmetric core.

With a sine function as the argument in (6.12), the equilibrium core is symmetry-broken below $\beta = 0.35$, at which point there is an abrupt change to favouring the symmetric core (see Figure 6.17b). It is worth noting for this function, that the choice $\beta = 0.45$ in equation (6.12) results in a curve similar to the U_1 derived from the M-interatomic potential, and, as expected, this curve favours the non-degenerate core.

Finally, for the function given by equation (6.13), Figure 6.17c shows that the symmetric non-degenerate core is favoured when $\delta > 0.175$, while for smaller positive values of δ the simulations predict a symmetry-broken core.

Earlier, we discussed the idea that the position of the inflexion points in the cosine-like U_1 curves, which correspond to the zero roots of the curve's second derivative, seems to be the main criteria determining whether a function favours a degenerate or non-degenerate core structure. In particular, our studies suggested that whether these inflexions are greater or smaller (in magnitude) than the minimum separation distance in the isotropic solution, which is $b/6$ or $1/6$, controls whether the symmetric core

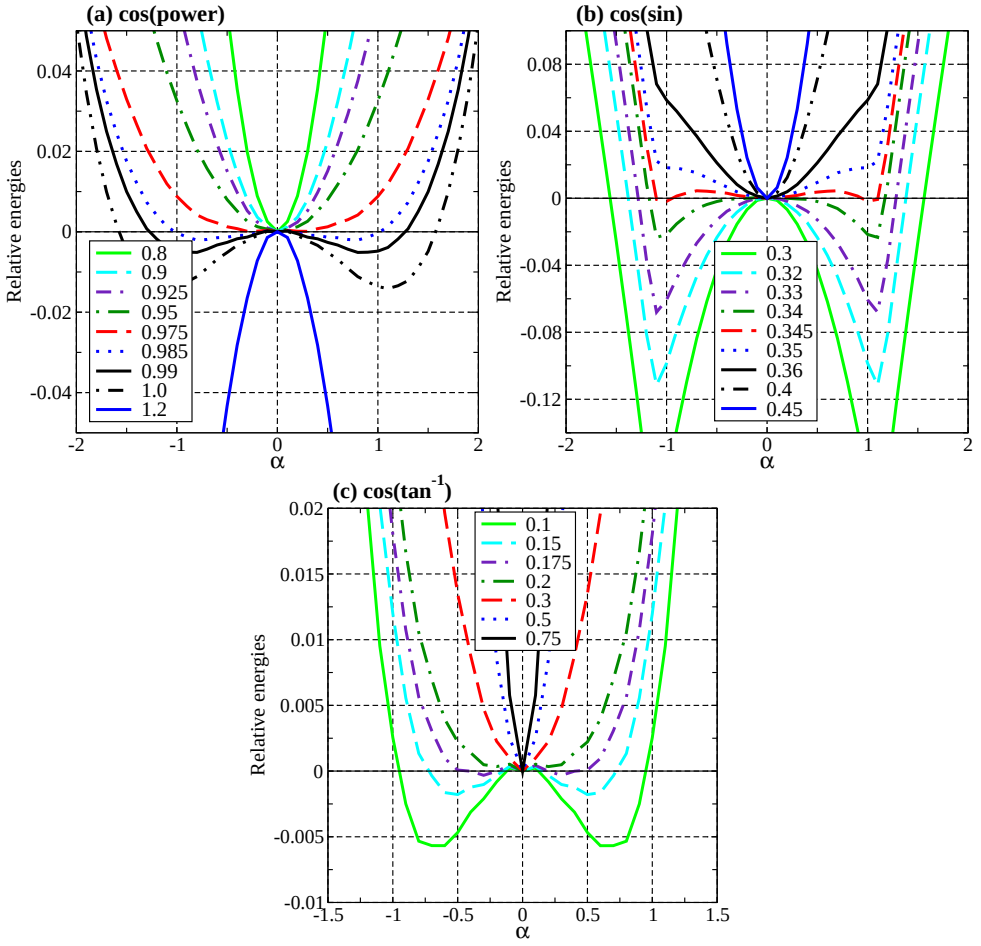


Fig. 6.17: Stability curves for various versions of the U_1 inter-string interaction laws defined by (a) the cos(power) function of equation (6.11), (b) the cos(sin) law of (6.12), and (c) the cos(tan^{-1}) expression of (6.13). The numerical designation for a U_1 function in the legend refers to the value of the varying parameter for each function defined by equations (6.11)-(6.13). α is a measure of symmetry breaking in the screw core, and each curve in the chart shows how the energy of the screw core structure varies as a function of α for a given inter-string interaction U_1.

is stable or unstable, respectively. However, as was noted by Takeuchi [**244**], there are other factors to consider. For the three functions discussed here we find that the zero-point of the second derivative, relative to the minimum isotropic separation, is not necessarily a reliable indicator for the transition in behaviour. It appears that the curvature in the first derivative near the inflexion points (e.g. in Figure 6.16) is also important. When the curvature is high in these regions, as it is in the M and D-D cases shown in Figure 6.16, then the symmetric core does become unstable when the inflexion points move beyond the minimum isotropic separation. On the other hand, when the first derivative peaks are broader, as is the case for the three functions (6.11)-(6.13), the symmetric core can remain stable until the set of second-smallest isotropic displacements fall inside the inflexion points.

6.4 The Peierls barrier

If a screw dislocation moves through a bcc lattice as a straight line, its energy, taken as a function of its position in the lattice, is a periodic function with minima corresponding to the soft-core configurations, separated by energy barriers that the dislocation has to overcome to move from one energy minimum configuration to another. This energy barrier is known as the Peierls barrier [**256**]. The height of the Peierls barrier (defined in this way) increases linearly as a function of the length of the dislocation line, and, for a sufficiently long dislocation, the mode of motion changes. Instead of moving as a straight line, the dislocation starts forming the so-called double-kinks, where only a short section of the dislocation line initially moves over the Peierls barrier, before dragging the remainder over the barrier. Whilst the details of this double-kinks mechanism cannot be

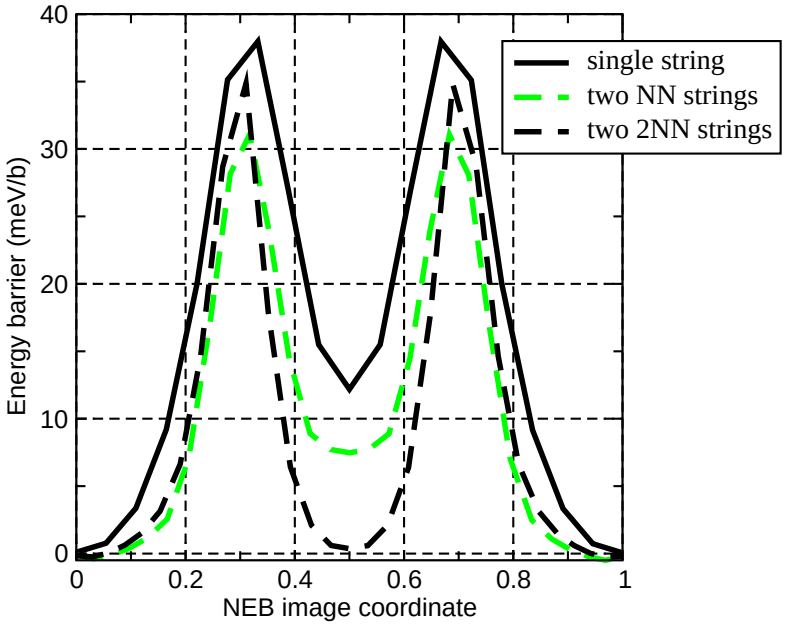


Fig. 6.18: The shape of pathways describing the transition of a straight screw dislocation over a Peierls energy barrier evaluated for the three U_1 curves derived from the DFT data shown in Figure 6.5.

derived from the model of rigid strings considered here, it is still possible to use the model to investigate the structure of the Peierls barrier for a straight dislocation.

Figure 6.18 shows the shapes of the Peierls energy pathways corresponding to the transition of a dislocation over a barrier, per unit length, evaluated for the three different U_1 laws, derived from the DFT data, shown in Figure 6.5. The transition pathways were investigated using a 2-dimensional nudged-elastic-band (NEB) method [**79**] (see section 2.3) applied to a lattice of strings. The initial and final configurations were taken as two fully relaxed easy-core (see section 6.3) configurations for a screw dislocation. The position of the cores in the two configurations were displaced by a single 'jump-distance' from one another, which in this case was $\sqrt{2/3}a$ in the $[11\bar{2}]$ direction, where $a = 2b/\sqrt{3}$ is the lattice

parameter. Thus the screw dislocations 'sit' in adjacent Peierls valleys, with a Peierls energy barrier between them. Since only the [111] positions of the strings differed between the two configurations, the NEB calculations were performed with only the [111] coordinates of image configurations treated as variables.

Initially, a series of image configurations were created along a linear pathway in the multi-dimensional space of displacements of strings $\{u_1, u_2, \ldots, u_N\}$ between the initial and final configurations. Testing determined the appropriate number of images for a given pathway, but 19 or 29 images were suitable in most cases. This initial pathway was then relaxed until it converged to the minimum energy pathway representing the 'shape' of the Peierls barrier for a particular interaction law.

The barriers shown in Figure 6.18 all have a double peak structure, with a deep trough between the two peaks. The heights of the peaks in all three cases are in reasonable agreement with the barrier height found in recent DFT calculations for screw dislocations [**212**]. However, the shape of the barriers is significantly different. The energy pathway found in [**212**] is described by a function with a single hump, with the middle configuration close to the hard-core structure. However, in our string-based approach we find that the minimum-energy pathway diverts from the linear path and does not go through the hard-core configuration. The low-energy configuration preferred at the middle of the barrier (*i.e.,* in the trough) is shown in the differential displacement map of Figure 6.19b, which is almost the same for all three DFT barriers shown in Figure 6.18. The intermediate configuration is not only spread between the two original core positions (shown in Figures 6.19a and 6.19c, respectively), but is also extended in the $[1\bar{1}0]$ direction, and is not centred on the hard-core position between the

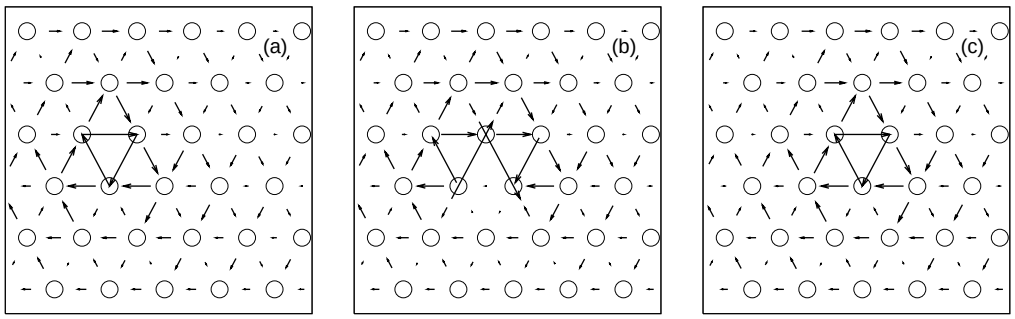


Fig. 6.19: Differential displacement maps of the lattice structure at different points along a DFT-derived Peierls energy pathway. (a) and (c) represent the initial and the final equilibrium screw dislocation core structures, and (b) is the structure corresponding to the middle of the transition pathway.

initial and the final soft-core configurations.

Since all three DFT-derived U_1 curves predict essentially the same height for the Peierls barrier, we see that the longer-range (beyond the NN) string interactions, responsible for the differences between the curves in Figure 6.5, do not seem to be significant enough to have any bearing on the results in this case. However, there is some difference in the energy of the middle configuration (Figure 6.19b) for the three cases. The trough is the deepest (to the extent that its half-way point is even lower than the initial and the final equilibrium screw configurations) for the case where the U_1 interaction law is derived from the two-2NN DFT data curve shown in Figure 6.5.

Figure 6.20 displays the Peierls energy pathway simulated for the M U_1 inter-string interaction law. It shows the same double peak shape as for the pathways simulated using the DFT-derived U_1 curves. Note that in all these simulations we use the original U_1 curves with no normalisation applied. Also shown in Figure 6.20 is the result of an atomistic NEB calculation performed using the original M potential. The shape of the

barrier for our string model is close to that obtained from the atomistic calculations (see also, for example, [**212**]), although the height is different. The peaks are higher for the string-model, but on this meV scale the difference is not great, and could be the result of small contributions from higher-order interactions that are not present in the string-model, or even slight displacements of atoms in the (111)-plane (*i.e.,* string 'bending') during translation of the dislocation.

We do not discuss fully the fairly complex transition pathways between the symmetry-broken dislocation core configurations found for the D-D-derived U_1 inter-string interaction law. These are unlikely to resemble the situation in a real bcc metal since DFT calculations now indicate that the non-degenerate core is the correct one [**225**, **226**]. However, we have performed NEB calculations using D-D-U_1 and found that the transition occurs via multiple peaks. Some of the peaks involve rotation of the non-symmetric core, where the symmetric configuration sits at the top of the peak, and others represent the translation between adjacent Peierls valleys.

Concluding this section we reiterate that the heights of the Peierls barriers found using the inter-string interaction laws derived from the DFT data (~ 35 meV/b) are in good agreement with the Peierls barriers found in large-scale supercell DFT calculations [**212**]. At the same time the shape of transition pathways differ, with the string-based models (both from DFT and interatomic potential curves) invariably predicting double-hump (or double-peak) structures, while direct DFT calculations favour fairly smooth one-hump pathways. We do not, as yet, see what causes this difference, although it may be the case that longer-range or non-linear interactions need to be taken into account. Given that interatomic potentials already

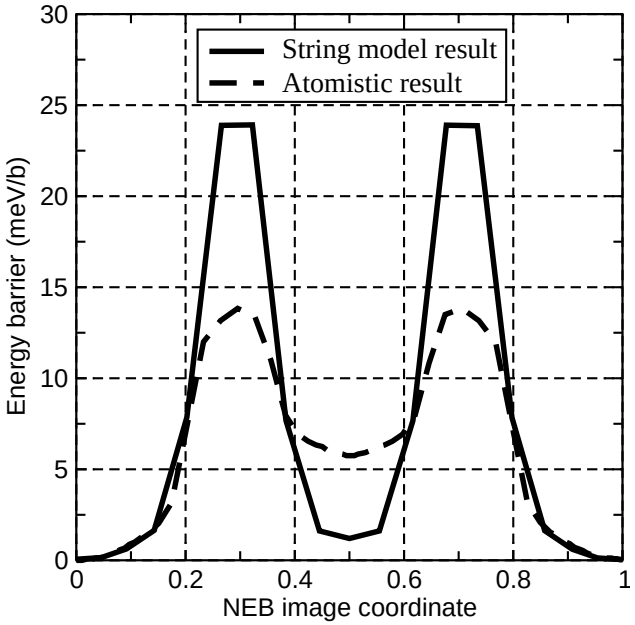


Fig. 6.20: The shape of the Peierls energy transition pathway evaluated both for the original atomistic Mendelev potential, and for the U_1 interaction law derived from it.

include these at a low level, but still predict a different Peierls barrier to direct DFT calculations, it seems that these interactions may need to be relatively strong to stiffen the lattice surrounding the core and prevent the non-linear transition pathway (*i.e.,* sideways 'slip') between adjacent Peierls valleys.

6.5 Conclusions and further work

We have presented a new method for investigating the structure and transition pathways for screw dislocations in Fe and other bcc metals. The MSFK model [**180**], considered here in the limit where the strings are taken as non-deformable [**244**, **245**], uses the fact that the presence of a screw dislocation in a crystal has practically no effect on the positions of atoms in the plane perpendicular to the direction of the screw's Burgers vector. As a

consequence, it is possible to treat the dislocation structure by considering the [111] strings of atoms as single objects, which are displaced relative to each other as a whole in the [111] direction.

The inter-string interaction laws were constructed from numerical string-displacement data evaluated using both DFT and semi-empirical potentials. Density functional data show that inter-string interactions are short-range and do not spread far beyond the first nearest-neighbour inter-string separation distance. Our study shows that it is the shape, and not the magnitude, of the first nearest-neighbour string-interaction law that determines the nature of the screw core structure. One of the critical factors appears to be the location of inflection points on the curve representing the first nearest-neighbour string interaction law. This criterion has already been successfully applied by Chiesa *et al.* [**230**], as part of a fitting algorithm, to help refine and improve the parameterization for a semi-empirical magnetic potential for bcc Fe. This advancement of understanding in the construction of interatomic potentials is a vital step in ensuring the future accuracy of materials modelling at the atomistic level, and there is no reason why it cannot be applied to, in particular, the other bcc transition metals.

We have also analyzed the Peierls migration pathways for screw dislocations predicted by the MSFK model. The heights of the Peierls barriers found using the inter-string interaction laws derived from the DFT data are in good agreement with the Peierls barriers found in direct DFT calculations. Agreement is also found in the comparison of the Peierls barriers found in the string-based and atomistic calculations from interatomic potentials. The shape of the transition pathways differ, with the string-based models and atomistic simulations invariably predicting

double-peak or -hump pathway structures, whereas large-scale DFT simulations predict smoother one-hump transition pathways. The next step in this area of research is to understand the reasons behind this disagreement, and hopefully develop criteria that can be reliably used to produce the correct transition pathway using interatomic potentials.

If the direct DFT calculations of Peierls barrier for screw dislocations are reliable then the difference between these and our results, and those of others (see for example Ventelon *et al.* [**212**]), is a cause for concern. In particular, it suggests that dynamic behaviour of screw dislocations predicted by atomistic simulations may not be correct, even if they are performed using a potential which predicts the correct zero Kelvin structure of the dislocation. It remains to be seen how important these zero temperature, zero stress barriers are in determining the behaviour at finite temperature and stress, particularly in view of the results obtained in chapter 5, where we found that the barrier was reduced under the influence of applied stress.

Our intention in developing the MSFK model further is to introduce an extra parameter in the calculations. This parameter will define how the distance between adjacent atoms in the same [111] string can be stretched or compressed. In this sense it describes the stiffness of the 'spring' joining two atoms (see for example the work of Rodney and Proville [**224**]). This extension should allow us to investigate the structure and formation of kinks, which we can compare directly with atomistic simulations of kinks performed by us and others (see for example Ventelon *et al.* [**216**]), and this may be one way in which we can investigate the significance of the shape of the Peierls barrier.

7. CONCLUSIONS

Nuclear fusion has the potential to alleviate many of the issues and concerns surrounding the world's future energy production demands, both in terms of availability and environmental impact. However, the success or failure of making fusion a commercial reality will rely heavily on the ability of scientists and engineers to develop *advanced* materials that can perform adequately under the extreme conditions that will occur in fusion reactors. Whilst it may still be several decades before fusion is able to make a significant contribution to the energy-landscape of human civilization, in the near-term new materials must also be available for the next generation of fission power stations. These, as well as 'filling the gap' between the present and a time when fusion reactors come online, will also provide a suitable test environment for improving materials performance.

Atomistic simulations have an important role to play in the design of new materials. They can be used to test theoretical concepts and help explain experimental observations, and thus bridge the gap between theory and experiment.

In the present work we have focused on materials that are being considered for structural components of both experimental reactor and future power stations. In particular, bcc transition metals, because of their desirable neutron-shielding properties, will almost certainly be the major constituents of many fusion components. Of these, Fe, as part of steels, is the chief candidate bcc metal and the main focus of the current work,

although many of the conclusions and techniques discussed will be equally applicable to the other metals. We have also studied W, which, with its high melting point and good erosion resistance, is being considered for components that will experience the most challenging conditions in a reactor, particularly those in the first-wall and high-thermal flux regions of the divertor (see Figure 1.2). Of the rest, Cr, as a significant fraction of many steels, must also be studied as a matter of urgency (both singly and as FeCr-alloy), although as an immediate extension to much of the work in this thesis, we should aim to repeat the simulations with all of the remaining bcc metals to explore both the similarities and differences to Fe (and W).

The thesis was split into two parts. Firstly we have explored the structure and evolution of vacancy and interstitial dislocation loop defects. These are commonly produced in damage cascades in irradiated metals, and their accumulation and evolution under neutron-irradiation is likely to be a serious issue for the integrity, and therefore lifetime, of components in a fusion device. In chapter 3 we found, using molecular static relaxations, that, regardless of the interatomic potential used, there was a critical size criteria controlling the formation of vacancy dislocation loops in both Fe and W. This observation, together with knowledge that spherical clusters of vacancies are the lowest energy configuration at any size, offers an explanation for the apparent (relative) rarity of vacancy dislocation loops in irradiated bcc metals compared to the near one-to-one ratio of loop production per displacement cascade in fcc metals such as Cu [**123**].

Specifically, for clusters smaller than the critical size, which varies according to the interatomic potential but is around 50 vacancies for $\frac{1}{2}\langle 111\rangle$-type loops in Fe, we find that dislocation loops are highly unstable,

and can easily transform at finite temperature into planar voids (or open loops or vacancy platelets) and subsequently into spherical voids. Only above the critical size, when a planar void becomes less favourable than the equivalent (closed) loop, can dislocation loops exist at equilibrium, although even then they are metastable compared to spherical voids. Experimental observations of irradiated Fe by Yao *et al.* [**123**], and others, are in apparent agreement with our findings. They find that the smallest vacancy loops detected in experiments are at least 2 nm in diameter, which corresponds well to the critical size in the simulations. At the same time, there is recent evidence from experiment [**127**] that a large number of spherical voids may indeed be produced under irradiation, forming a void 'sea', which is the predicted behaviour according to simulations.

While vacancy defects may only be formed on rare occasions in irradiated bcc metals, their accumulation could still have an impact, and so it is important to understand their post-formation evolution. In chapter 4, we characterised the finite temperature diffusivity of these vacancy defects in both Fe and W. In particular, we measured the relative diffusion of interstitial and vacancy defects of the same size. Our results indicated that vacancy dislocation loops are indeed less mobile than their interstitial counterpart (as was shown in earlier simulations [**155**]), but also that their diffusivities are in fact of the same order of magnitude. This suggests that while vacancy loops will have greater residence times than interstitial loops, they will still migrate out of a system, for example to surfaces or grain boundaries, on relatively short timescales. This conclusion illustrates the need, in experiment, for care when using post-irradiation counts of vacancy defects in materials to judge the response of that material to irradiation, since it will not only be interstitial loops that are lost from the system,

some of the vacancy loops will have also migrated out.

Also in chapter 4 we performed simulations that demonstrate that it is possible to observe the coherent motion of groups of similar $\frac{1}{2}\langle 111\rangle$ dislocation loops, which recent experiments by Yao *et al.* [**178**] have shown occurs on a regular basis as a prequel to coalescence. Our preliminary findings suggest that groups of loops migrate more slowly than isolated loops, although it is not clear whether this reduction is a function of the total number of point defects (either interstitials or vacancies), or whether it is merely controlled by the interaction of the elastic strain fields of the loops and therefore a constant for a given loop separation.

In Part II of the thesis, we studied screw dislocations. As the rate-limiting carriers of plastic deformation in bcc metals, the structure, mobility, and general behaviour of these defects (particularly their interaction with fast moving edge dislocations) will largely determine the response of components to the high stresses (and temperatures) expected in fusion reactors. We began, in chapter 5, by measuring the velocity response at a range of applied stresses of $\frac{1}{2}\langle 111\rangle$ screw dislocations moving at finite temperature in Fe. Our comprehensive study, performed at a range of temperatures using MD, revealed the presence of two distinct mobility regimes. At lower stresses, we observed an exponential velocity increase with increasing stress, which is characteristic of the thermally-activated kink-pair mechanism of screw dislocation motion. Meanwhile, above a given transition stress, which decreased with increasing temperature, the velocities of the screw dislocations became linearly increasing with stress.

For the low stress regime a single exponential law was fitted to the data at all temperatures and all stresses below the transition stress. This *mobility function* should prove invaluable in dislocation dynamics

simulations of screw dislocations in a wide variety of circumstances, especially in combination with other parameters controlling dislocation interactions, *etc.* As an extension to this work it will be interesting to compare these results, for pure Fe, with results obtained from the recently developed potentials for FeCr-alloy, which is a closer approximation to the steels that will be used in fusion components.

The results from these large-scale MD simulations were obtained using an interatomic potential [**82**] for Fe that is perhaps the most valid, as far as $\frac{1}{2}\langle 111\rangle$ screw dislocations are concerned, of those currently available. In chapter 6 we described a multi-string Frenkel-Kontorova (MSFK) model that is able to reproduce the screw dislocation core structure predicted by interatomic potentials, using interaction laws derived from them. We then apply this model to explain why only one of the potentials in common usage [**82**] produces the correct core structure at zero Kelvin. We also use data from density functional calculations to confirm that the model, which represents [111] strings of atoms as non-deformable objects able to move in 1D (the [111] direction) only, is valid in the core-structure context. Consequently, the model offers a simple technique for use in the development of interatomic potentials to guarantee that the correct core structure will be predicted.

However, we also show that a correct core configuration does not ensure that the translation of the screw between adjacent equilibrium positions will be reproduced accurately. In particular, we find that, while density functional calculations suggest a single-hump Peierls barrier [**212**], both interatomic potentials and our DFT-based MSFK model produce a double-hump barrier. In future work we intend to investigate this issue and, in particular, focus on developing criteria to guarantee that the correct

behaviour is produced by interatomic potentials.

In summary, we have studied the structure and behaviour of various types of defects in bcc transition metals. In particular, our simulations in Part I shed light on the experimental observations of dislocation loops produced during irradiation of Fe and W. Meanwhile the simulations and modelling in Part II have taken important steps towards improving the accuracy with which screw dislocations, and ultimately plastic deformation, is modelled in Fe and other bcc transition metals.

APPENDIX

A. THE BCC METAL STRUCTURE

The body-centred cubic (bcc) structure is a Bravais lattice, and can therefore be defined via a matrix of non-overlapping *primitive* unit cells each containing a single atom [**168**]. However, it is more convenient to represent the structure as being made up of *conventional* unit cells [**168**] having the symmetric and cubic structure shown in Figure A.1. In particular this *non primitive* [**168**] unit cell is a cube with an atom at each vertex and a 9th atom at the geometric centre of the cube - the 'body-centre' atom. Strictly speaking, each of these unit cells only contains two unique atoms, namely a single corner atom and the body-centre atom. All other atoms are obtained by translating the unit cell in directions parallel to the sides of the cube, and thus belong to adjacent unit cells. The lattice parameter a defines the dimensions of this cubic unit cell. As the coordinate axis in Figure A.1 demonstrates, the convention is that the edges of the 'bcc cube' are orientated along the normal Cartesian axes specified in vector-index notation as ([100],[010],[001])$\equiv (x, y, z)$.

In any of these three coordinate directions atoms are arranged in two sets of alternative {100}-type planes, one set corresponding to the 'corner' atoms in Figure A.1, and the other containing all the body-centre atoms. Thus, as mentioned in section 3.2.1, the stacking sequence of, say (001) planes, is ABAB.... Also, we can see that the magnitude of the Burgers vector for defects with stacking faults in any $\langle 100 \rangle$ direction is equal to the lattice parameter a.

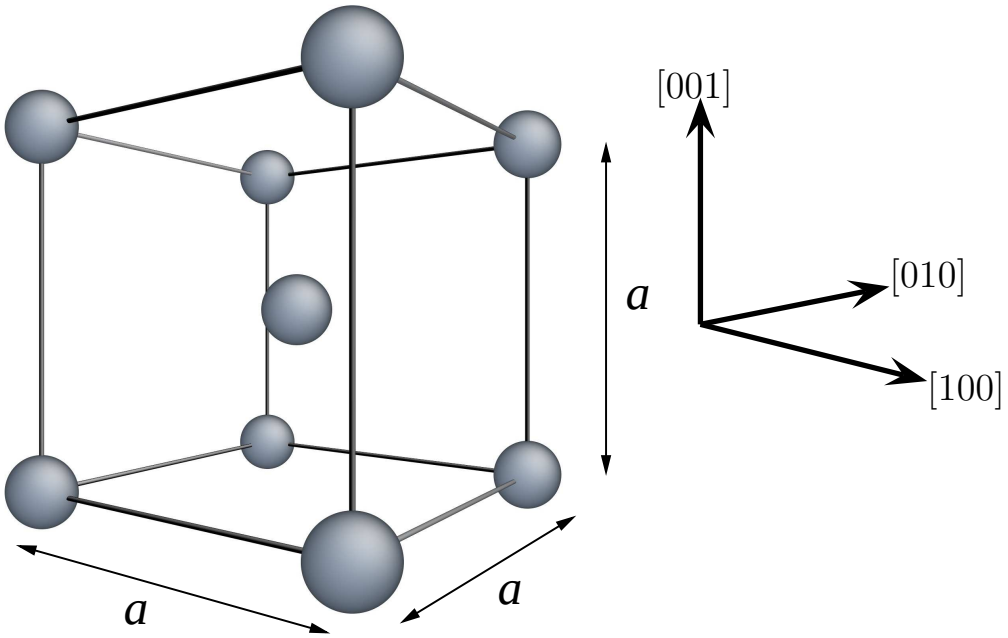


Fig. A.1: The bcc unit cell.

For void defects, like those considered in chapter 3, we are interested in the volume per atom, which is a close approximation of the formation volume of a single vacancy. We use this to estimate the volume, and therefore diameter, of a spherical void. Since a unit cell contains two unique atoms, it is clear that the volume per atom is half of the volume of each cell or $a^3/2$. Finally, for $\langle 001 \rangle$ dislocation loops the diameter is calculated using, as a base unit, the area occupied by a single atom in a $\{100\}$ plane. In fact, we consider the area occupied by, for example [001] strings in (001) planes. Similar to the case of the atomic volume, which applies to all of the vacancy defects considered in this thesis, the area per atom in a $\{100\}$ plane is half the area of a single face of the bcc cube or $a^2/2$.

A.1 A Coordinate system with $z = [111]$

In the bcc lattice structure the close-packed directions (*i.e.,* the directions in which the distance between atoms is shortest) are the $\langle 111 \rangle$-type directions, which correspond to the diagonals of the bcc unit cell (see Figure A.1). Stacking faults in these directions are generally the most energetically favourable, and thus the most interesting to study. It is convenient to work in a coordinate system where a $\langle 111 \rangle$ direction forms one of the coordinate axes. In this thesis we have used [111] as the z axis in the rotated system, with $x = [1\bar{1}0]$ and $y = [11\bar{2}]$. Figure A.2 shows how these three coordinate axes (labelled (x', y', z') in the figure) relate to the normal axes, which lie along the edges of the bcc cube.

Figure A.3 illustrates the 6-atom 'unit cell' building-block of this coordinate system. It has dimensions of $\sqrt{2}a$ in $x' = [1\bar{1}0]$, $\sqrt{6}a$ in $y' = [11\bar{2}]$, and $\sqrt{3}a/2$ in $z' = [111]$. In these units the six atoms shown in red in the figure have the following positions.

1. (0,0,0)
2. $\left(\frac{1}{2}, \frac{1}{6}, \frac{2}{3}\right)$
3. $\left(0, \frac{1}{3}, \frac{1}{3}\right)$
4. $\left(\frac{1}{2}, \frac{1}{2}, 0\right)$
5. $\left(0, \frac{2}{3}, \frac{2}{3}\right)$
6. $\left(\frac{1}{2}, \frac{5}{6}, \frac{1}{3}\right)$

The distance between atoms in the [111] closed-packed direction is equal to $\sqrt{3}a/2$. This is the magnitude of the Burgers vector for stacking faults (*i.e.,* defects) in this direction. Since this is half of the diagonal of the original bcc unit cell, the Burgers vector is often referred to as $\frac{1}{2}\langle 111 \rangle$. As we can see from the definition of the six-atom '[111] unit cell' there are three unique types of (111) plane in the [111] direction, giving an ABCABC... stacking sequence. Thus in section 3.2.1 dislocation loops are created by adding three extra planes in the [111] direction.

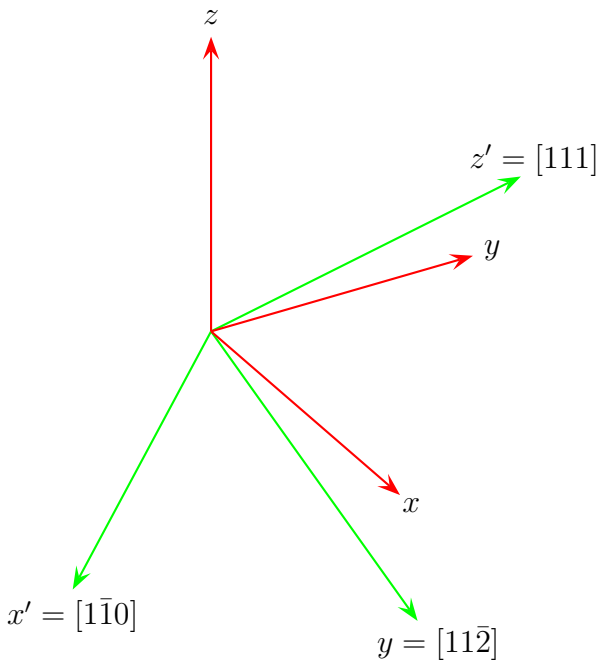


Fig. A.2: The $([1\bar{1}0], [11\bar{2}], [111])$ coordinate axes (green) relative to the axes of the normal (x, y, z) coordinate system (red).

To see the area occupied by each atom (or [111] string) in the (111) atomic plane consider Figure 6.2 of chapter 6 (page 204), which shows the distribution of [111] atomic strings. In the triangular matrix of positions the distance between atoms/strings in the $[11\bar{2}]$ direction (base of 'triangles') is $a/\sqrt{6}$, and in the $[1\bar{1}0]$ direction the separation is $\sqrt{2}a$. The unique area corresponding to each atom or string is twice the area of the triangular base unit, and is thus equal to $a^2/\sqrt{3}$.

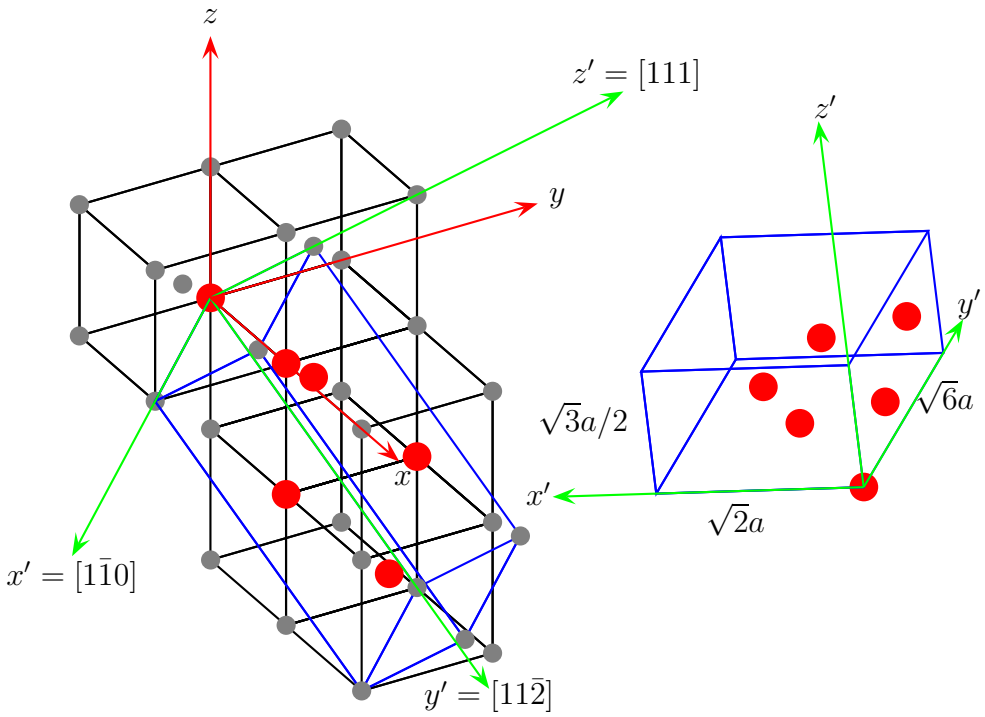


Fig. A.3: Correspondence of the normal bcc unit cell to the unit cell building-block of the $([1\bar{1}0], [11\bar{2}], [111])$ coordinate system. Each unit cell has 6 unique atoms (in red in both pictures).

B. HANDBOOK OF ACTIVATION DATA

In chapter 1 we discuss the calculation of activation properties using the FISPACT inventory code, and neutron cross-section and decay data, which are all part of the European Activation System (EASY) [**16**]. As a demonstration of the huge potential of this system we have used it to produce a set of fusion-relevant benchmark results for each of the naturally occurring elements in the periodic table. The data from this exercise, which was performed using the 2003 version of EASY, has been collated into a *Handbook of Activation Data* [**17**, **257**].

The data presented in the handbook for each element contains the following:

- A short table of basic properties, including a list of its naturally occurring isotopes and their abundances, as well as some important thermodynamic properties [**257**]. Table B.1 shows the data for Fe.

- Activation properties; The important radionuclides produced by irradiating 1 kg of the pure element for 5 years in the neutron flux expected for the first wall of a fusion reactor are tabulated. The table is split into data for six categories, one for each of: specific activity - a measure of the activity in the material; decay power (heat) - the amount of heat production due to decay processes; gamma dose - the contact dose rate from a semi-infinite slab of material; ingestion and inhalation doses - the doses received by an average person over a

50-year period from intake; clearance index - the numerical determination for the safe disposal of a material (a clearance index of one or less is safe). For each category, data are presented at six different decay times (cooling time after irradiation) from zero to 100,000 years, and for each time the total activity is given along with the percentage contributions of the important radionuclides to this total [**257**]. See table B.2 for Fe's activation properties.

- Pathway Analysis; The production pathways for each nuclide shown in the activation properties table are shown for four different incident-neutron energies (see table B.3), which were chosen to give a broad picture of an element's reaction behaviour under neutron irradiation [**257**]. Radionuclides are listed in order of increasing half-life, and the percentage contribution from a given pathway to the amount of each daughter radionuclide produced is shown for each energy. For example, in table B.3, which shows the production pathways from pure Fe, we see that Mn56, which beta-decays into Fe56 with a half-life of 2.579 hours, is produced at the three lowest energy neutron irradiations by a single reaction pathway starting from Fe54 (5.845% of naturally occurring Fe). The pathway proceeds via a neutron-capture and γ-emission (n,γ) to Fe55, which then β^+-decays to Mn55, and then Mn56 is produced by another (n,γ) reaction. However, at the highest energy (close to the energy of a fusion neutron) the production is dominated by a (n,p) reaction directly from the most abundant isotope of Fe, Fe56. Note that '&' in the table indicates that the generic pathway shown is actually a set of very similar pathways. As well as the direct reaction shown, the pathway may also include short-lived isomeric states of the nuclides in

italics, which then decay back to the ground-state.

- Activation graphs; For each of the six activation properties there is a graph showing how the element responds after four different irradiation conditions. The four conditions are first-wall, blanket, and shield fluxes for conceptual fusion power plants, with irradiation times of 5, 5, and 25 years, respectively, and also a 1 year DD irradiation flux and spectrum for the vacuum vessel of the JET experimental reactor [**17**]. The order given here represents the order of decreasing activity (*i.e.,* greatest in first wall, lowest in JET) - see the example for the specific activity of Fe shown in figure B.1 for more details. The cooling times range from 1×10^{-6} years to 1×10^{6} years, and we can see in Figure B.1 how the activity level evolves and falls with time. This gives important information about how long a material must be stored before it can be disposed of safely. The error bars shown in the figure are generated using the uncertainty estimates calculated by FISPACT.

- Importance Diagrams; These diagrams are designed to present activation results that are independent of neutron spectra [**257**]. They show the regions of the neutron irradiation energy versus decay (cooling) time space where individual radionuclides contribute more than 50% of the total activity for a given quantity. In the handbook an importance diagram is produced for each of the six activation quantities shown in the activation properties table (see above), but here we only show the gamma dose rate diagram for Fe in Figure B.2. This shows, for example, that at almost all neutron energies, Co60 is the predominant active radionuclide at long timescales - beyond

around 3 years. This may be significant when it comes to the disposal of Fe-based materials, although, as indicated by the activation tables (table B.2), the activity levels are very low by the time Co60 dominates. A full description of importance diagrams can be found in [**258**].

- Transmutation calculations; The final graph presented for each element displays the transmutation (burn-up) of a pure sample during 5 years of the neutron irradiation expected at the first wall of a fusion power plant. Figure B.3 displays the transmutation results for Fe, while 1.4 shows the burn-up of W. Both these graphs are reproduced exactly as they appear in [**17**], where all transmutation results are presented as weight parts per million (wppm) concentrations. In Figure 1.5 for W and Figure B.4 for Fe, we recalculate the concentrations of each element for all times, and this time present them in atomic parts per million (appm). This representation is particularly useful when investigating the production of low atomic mass elements, such as Hydrogen and Helium, as wppm concentrations of such elements can give the misleading impression that their production is very low compared to the higher atomic mass elements around the starting material (in the periodic table).

  Note that FISPACT is only able to estimate uncertainties in the radiological quantities, which it does using the cross-section and half-life errors provided in the data libraries. Thus, error bars are included in the specific-activity graph of Fe shown in Figure B.1. To minimise the computation time to calculate these errors it only considers the uncertainty in the production of the top 20 radionuclides for a given activation property [**15**], and thus does not

consider errors in the production of stable nuclides at all. This means that it is currently not possible to give error estimates for the transmutation results presented in Figures 1.4, 1.5, B.3, and B.4.

The handbook also has summary tables, for around 750 radionuclides, showing which elements produce them in significant quantities under neutron irradiation. 1341 n-capture reactions are also summarised, with details such as cross-section uncertainty, data source, and the radionuclides that rely on a particular reaction for their major production chains. Further information about the data in the handbook can be found in the introduction to the book itself, as well as in [**257**]. In conclusion, the 544 pages of activation data contained in the handbook represent a substantial reference source that can be useful in a wide variety of situations, including the design and validation of components for fusion devices. The full handbook is available online at
http://www.ccfe.ac.uk/techdocs/ukaea-fus-509.pdf.

Tab. B.1: General properties of Fe from [**17**]

Atomic number	26	Isotopes	Isotopic abundances /%
Crustal abundance / wppm	5.63×10^4	Fe54	5.845
Melting point / K	1811	Fe56	91.754
Boiling point / K	3134	Fe57	2.119
Density / kgm^{-3}	7874	Fe58	0.282
Thermal conductivity / $\mathrm{Wm}^{-1}\mathrm{K}^{-1}$	80.2		
Electrical resistivity / m	9.71×10^{-8}		
Coefficient of thermal expansion / K^{-1}	1.18×10^{-5}		
Crystal structure	bcc		
Number of stable isotopes	4		
Mean atomic weight	55.845		

Tab. B.2: The activation properties table for 5-year, first-wall irradiation of Fe in a fusion device. Six activation properties are shown along with their levels at each of 6 cooling times after irradiation. For each decay time the percentage contribution from different radionuclides are shown [**17**].

Act	**0**	**10^{-5} y**	**10^{-2} y**	**1 y**	**100 y**	**10^5 y**	**Heat**	**0**	**10^{-5} y**	**10^{-2} y**	**1 y**	**100 y**	**10^5 y**
Bq kg^{-1}	6.81E14	6.73E14	4.82E14	3.51E14	9.35E7	2.02E7	kW kg^{-1}	8.65E-2	8.39E-2	7.60E-3	3.39E-3	1.89E-10	1.82E-11
Fe55	62.15	62.91	87.66	93.54			Mn56	89.97	90.59				
Mn56	28.25	27.93					Mn54	7.89	8.14	89.07	89.45		
Mn54	7.45	7.54	10.44	6.42			Fe55	0.46	0.48	5.24	9.14		
Cr51	1.20	1.22	1.55				Fe59	0.38	0.39	4.09	0.03		
Co60	0.02	0.02	0.03	0.03	0.27	0.01	Co60	0.06	0.06	0.70	1.38	55.30	3.36
H3				0.01	77.68		H3					35.19	
Mn53					22.04	99.97	Mn53					9.49	96.44
Dose	**0**	**10^{-5} y**	**10^{-2} y**	**1 y**	**100 y**	**10^5 y**	**Ing**	**0**	**10^{-5} y**	**10^{-2} y**	**1 y**	**100 y**	**10^5 y**
Sv h^{-1}	1.07E5	1.05E5	1.17E4	5.06E3	1.84E-4	5.54E-6	Sv kg^{-1}	2.28E5	2.26E5	1.79E5	1.25E5	4.69E-3	7.75E-4
Mn56	88.67	88.61					Fe55	61.40	61.71	78.05	86.86		
Mn54	10.26	10.49	93.28	96.63			Mn56	21.14	20.75				
Fe59	0.49	0.51	4.28	0.04			Mn54	15.83	15.91	20.01	12.83		
Fe55	0.11	0.11	0.97	1.74			Fe59	1.24	1.25	1.50	0.01		
V52	0.10	0.04					Co60	0.19	0.19	0.24	0.31	18.16	0.65
Co60	0.09	0.09	0.78	1.59	97.52	19.05	H3					65.03	
Mn52	0.06	0.06	0.32				Mn53					13.18	78.39
Mn53					2.48	80.90	Fe60					3.62	20.95
Inh	**0**	**10^{-5} y**	**10^{-2} y**	**1 y**	**100 y**	**10^5 y**	**Clear**	**0**	**10^{-5} y**	**10^{-2} y**	**1 y**	**100 y**	**10^5 y**
Sv kg^{-1}	4.36E5	4.35E5	4.11E5	2.90E5	2.82E-2	1.55E-3		5.17E11	5.08E11	1.70E11	7.66E10	8.97E2	4.17E1
Fe55	74.80	74.89	79.14	87.14			Mn56	66.43	66.06				
Mn54	17.46	17.48	18.37	11.65			Mn54	32.69	33.28	98.40	98.08		
Mn56	5.30	5.18					Fe55	0.27	0.28	0.83	1.43		
Fe59	1.44	1.44	1.44	0.01			Fe59	0.10	0.10	0.29			
Co60	0.91	0.91	0.93	1.20	27.54	2.94	Co60	0.08	0.08	0.25	0.49	93.12	11.75
H3					66.97		Cr51	0.05	0.05	0.15			
Mn53					3.95	70.40	H3					2.70	
Fe60					1.53	26.61	Mn53					4.18	88.16

Tab. B.3: Radioactive isotope production pathway analysis for Fe. Radionuclides are listed in order of increasing half-life, and the important production pathways at each of 4 neutron irradiation energies are shown along with percentage contributions [**17**].

Nuclide	$T_{1/2}$	Pathway	0.26 eV	148 eV	37.6 keV	14.7 MeV
Mn56	2.579 h	Fe54(n,γ)Fe55(β^+) Mn55(n,γ)Mn56	100.0	100.0	100.0	
		Fe56(n,p)Mn56				98.9
		Fe57(n,d)Mn56				0.7
		Fe57(n,2n)Fe56(n,p)Mn56				0.4
Fe59	44.502 d	Fe56(n,γ)Fe57(n,γ)Fe58(n,γ)Fe59	67.1	0.3		
		Fe57(n,γ)Fe58(n,γ)Fe59	17.9	2.7	2.5	
		Fe58(n,γ)Fe59	15.0	97.0	97.4	98.5
Mn54	312.3 d	Fe54(n,p)Mn54	100.0	100.0	100.0	40.6
		Fe56(n,2n)Fe55(β^+)Mn55(n,2n)Mn54				37.5
		Fe56(n,d)Mn55(n,2n)Mn54				19.0
		Fe56(n,2n)Fe55(n,2n)Fe54(n,p)Mn54				0.6
Fe55	2.735 y	Fe54(n,γ)Fe55	100.0	100.0	100.0	
		Fe56(n,2n)Fe55				98.7
		Fe57(n,2n)Fe56(n,2n)Fe55				0.2
Co60	5.272 y	&Fe56(n,γ)Fe57(n,γ)Fe58(n,γ)Fe59(β^-)Co59(n,γ) *Co60*	42.2			
		&Fe58(n,γ)Fe59(β^-)Co59(n,γ)*Co60*	38.3	98.4	99.1	99.7
		&Fe57(n,γ)Fe58(n,γ)Fe59(β^-)Co59(n,γ)*Co60*	19.5	1.5	0.9	
H3	12.33 y	Fe54(n,X)H1(n,γ)H2(n,γ)H3	90.8	95.1	99.3	
		Fe54(n,γ)Fe55(n,X)H1(n,γ)H2(n,γ)H3	2.5			
		Fe56(n,X)H3				38.8
		Fe56(n,2n)Fe55(n,X)H3				28.9
		Fe57(n,X)H3				10.5
		Fe56(n,2n)Fe55(β^+)Mn55(n,X)H3				7.8
		Fe56(n,d)Mn55(n,X)H3				4.7
		Fe54(n,X)H3				4.3
		Fe54(n,d)Mn53(n,X)H3				1.9
		Fe56(n,α)Cr53(n,X)H3				1.4
Ni63	99.0 y	&Fe58(n,γ)Fe59(β^-)Co59(n,γ)*Co60*(n,γ)Co61(β^-) Ni61(n,γ)Ni62(n,γ)Ni63	55.0	88.9	84.6	76.6
		&Fe56(n,γ)Fe57(n,γ)Fe58(n,γ)Fe59(β^-)Co59(n,γ) *Co60*(n,γ)Co61(β^-)Ni61(n,γ)Ni62(n,γ)Ni63	15.4			
		&Fe57(n,γ)Fe58(n,γ)Fe59(β^-)Co59(n,γ)*Co60*(n,γ) Co61(β^-)Ni61(n,γ)Ni62(n,γ)Ni63	12.9	0.5	0.4	
		&Fe58(n,γ)Fe59(β^-)Co59(n,γ)*Co60*(β^-)Ni60(n,γ) Ni61(n,γ)Ni62(n,γ)Ni63	9.5	10.3	10.9	11.1
		Fe58(n,γ)Fe59(n,γ)Fe60(n,γ)Fe61(β^-)Co61(β^-) Ni61(n,γ)Ni62(n,γ)Ni63	2.0		4.0	11.8
		&Fe56(n,γ)Fe57(n,γ)Fe58(n,γ)Fe59(β^-)Co59(n,γ) *Co60*(β^-)Ni60(n,γ)Ni61(n,γ)Ni62(n,γ)Ni63	1.9			
		&Fe57(n,γ)Fe58(n,γ)Fe59(β^-)Co59(n,γ)*Co60*(β^-) Ni60(n,γ)Ni61(n,γ)Ni62(n,γ)Ni63	1.9			
Fe60	1.5 10^6 y	Fe56(n,γ)Fe57(n,γ)Fe58(n,γ)Fe59(n,γ)Fe60	48.5			
		Fe58(n,γ)Fe59(n,γ)Fe60	32.1	100.0	100.0	96.1
		Fe57(n,γ)Fe58(n,γ)Fe59(n,γ)Fe60	19.3			
		&Fe58(n,γ)Fe59(β^-)Co59(n,γ)*Co60*(n,p)Fe60				3.3
Mn53	3.68 10^6 y	Fe54(n,d)Mn53				95.0
		Fe54(n,2n)Fe53(β^+)Mn53				2.1
		Fe54(n,p)Mn54(n,2n)Mn53				1.1

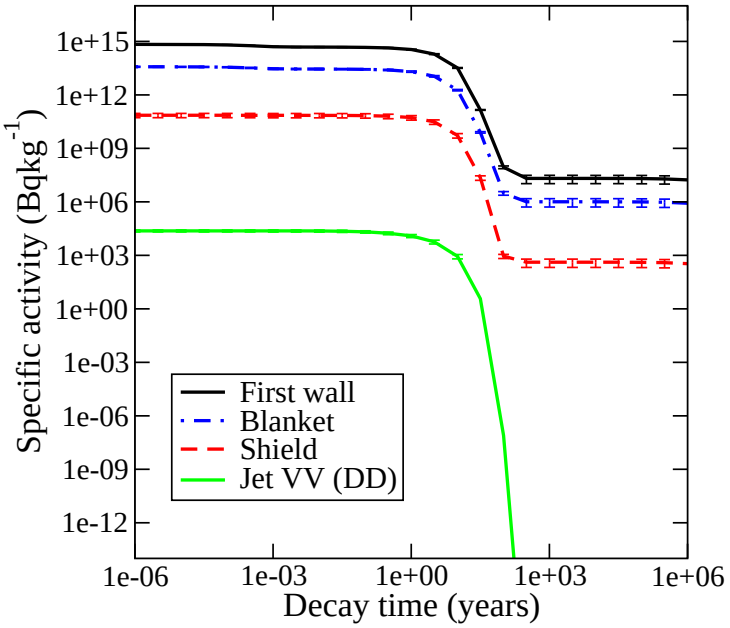


Fig. B.1: The specific activity graph for Fe under four different irradiation conditions. The three highest activity levels correspond to irradiation conditions in different regions of a conceptual fusion power plant [**8**]. The fourth curve corresponds to the activity generated for irradiation in the vacuum vessel wall of JET from a Deuterium-Deuterium plasma. See [**17**] for more details.

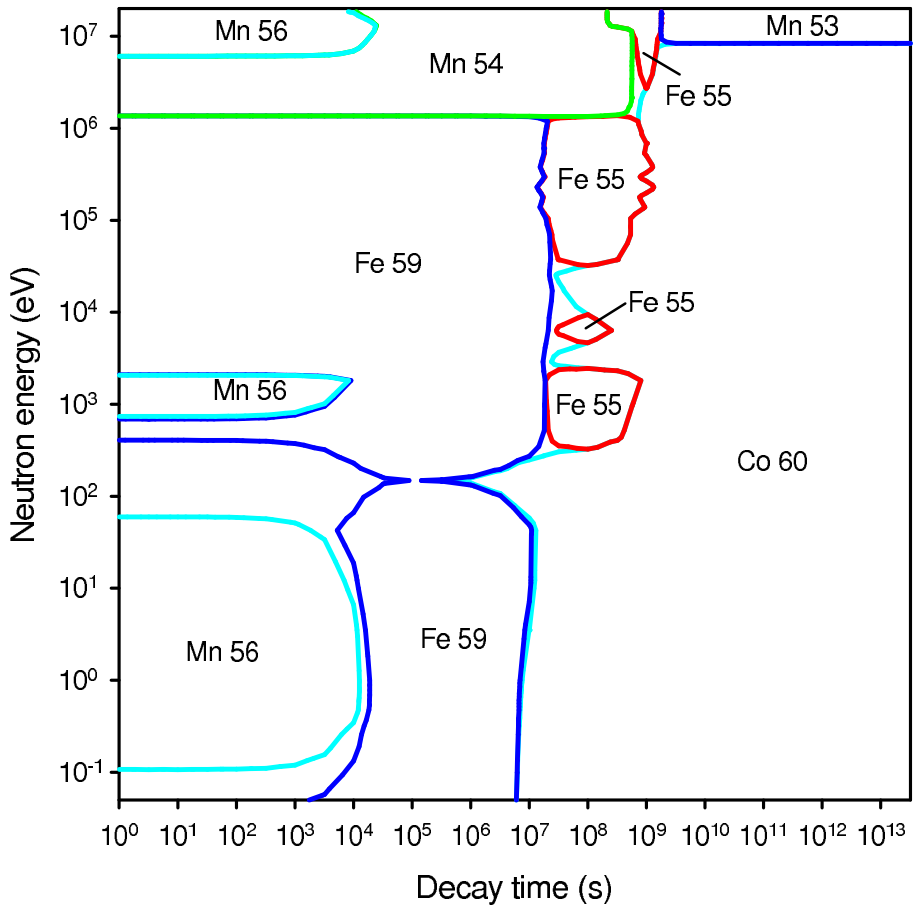


Fig. B.2: The gamma-dose-rate importance diagram for neutron-irradiated Fe from [**17**].

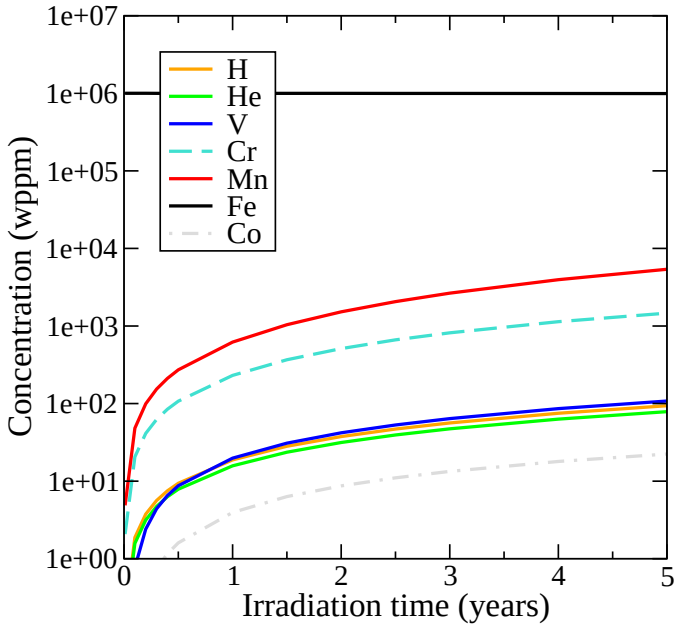


Fig. B.3: The transmutation (burn-up) of pure Fe as a result of exposure to the neutron flux expected in the first wall of a fusion power plant for five years [**17**]. Element concentrations at a particular time are given in wppm.

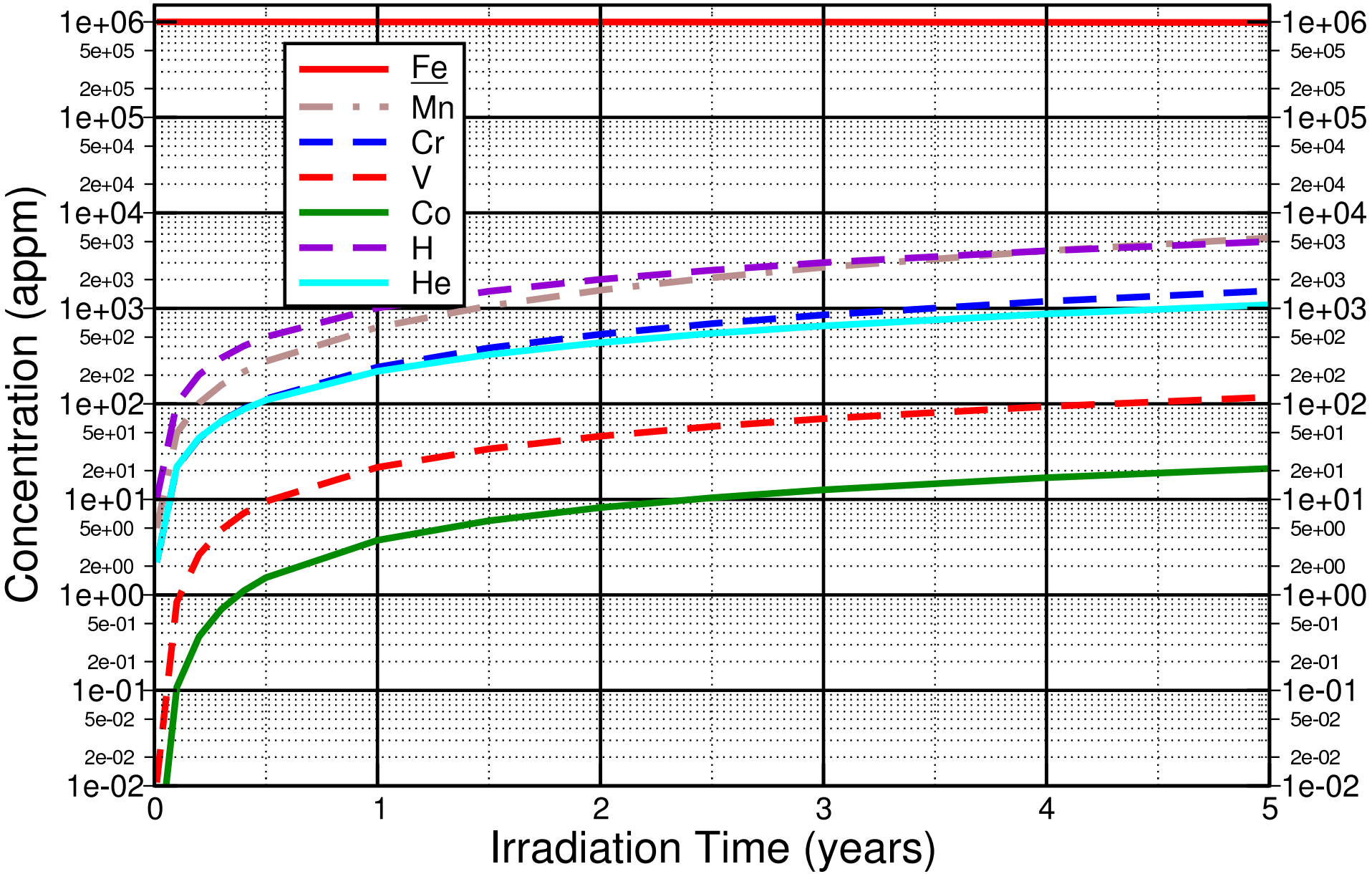


Fig. B.4: The transmutation (burn-up) of pure Fe as a result of exposure to the neutron flux expected in the first wall of a fusion power plant for five years [**17**]. In this expanded graph concentrations are given in appm. For more details see [**20**].

C. ADDITIONAL DERIVATIONS

C.1 The derivative of $\dot{\mathbf{s}}_i^T \mathbf{G} \dot{\mathbf{s}}_i$

In deriving the Parrinello-Rahman (PR) equations of motion (see section 2.1.4) for the particle positions we seek:

$$\frac{\partial}{\partial \dot{\mathbf{s}}_i} \left(\dot{\mathbf{s}}_i^T \mathbf{G} \dot{\mathbf{s}}_i \right).$$

In summation notation this is equivalent to

$$\begin{aligned} \frac{\partial}{\partial \dot{\mathbf{s}}_i} \sum_{m=1}^{3} \sum_{n=1}^{3} \dot{s}_i^m g^{mn} \dot{s}_i^n &= \left[\frac{\partial}{\partial \dot{s}_i^k} \sum_{m=1}^{3} \sum_{n=1}^{3} \dot{s}_i^m g^{mn} \dot{s}_i^n \right], \quad \text{for } k = 1, 2, 3 \\ &= \left[\sum_m \sum_n \left(\frac{\partial \dot{s}_i^m}{\partial \dot{s}_i^k} g^{mn} \dot{s}_i^n + \dot{s}_i^m g^{mn} \frac{\partial \dot{s}_i^n}{\partial \dot{s}_i^k} \right) \right], \end{aligned}$$

using the product rule. The derivatives in the above are only non-zero when m or n are equal to k. Therefore

$$\begin{aligned} \frac{\partial}{\partial \dot{\mathbf{s}}_i} \left(\dot{\mathbf{s}}_i^T \mathbf{G} \dot{\mathbf{s}}_i \right) &= \left[\sum_n g^{kn} \dot{s}_i^n + \sum_m \dot{s}_i^m g^{mk} \right] \\ &= \left[2 \sum_n g^{kn} \dot{s}_i^n \right] \\ &= 2 \mathbf{G} \dot{\mathbf{s}}_i. \end{aligned} \tag{C.1}$$

Above we have used the fact that:

$$\mathbf{G} = [g^{mn}] = \left[\sum_k (h^T)^{mk} h^{kn}\right] = \left[\sum_k h^{km} h^{kn}\right], \quad \text{for } m, n = 1, 2, 3, \quad \text{(C.2)}$$

since $(h^T)^{nm} = h^{mn}$, which gives that $g^{nm} = g^{mn}$.

C.2 The derivative $\partial r_{ij}/\partial \mathbf{s}_l$

In the formalism by Parrinello and Rahman [**65**] we have, by definition, for the elements of the column vector $\mathbf{r}_i$

$$r_i^n = (\mathbf{h}\mathbf{s}_i)^n = \sum_m h^{nm} s_i^m, \quad \text{(C.3)}$$

where h^{nm} is the nth row, m^{th} column element of the 3×3 box matrix $\mathbf{h}$. Therefore

$$\begin{aligned} r_{ij}^2 &= \|\mathbf{h}\mathbf{s}_i - \mathbf{h}\mathbf{s}_j\|^2 \\ &= \sum_{n=1}^{3} \left(\sum_{m=1}^{3} h^{nm} (s_i^m - s_j^m) \right)^2 \\ &= \sum_{n=1}^{3} \sum_{m=1}^{3} \sum_{k=1}^{3} h^{nm} h^{nk} (s_i^m - s_j^m)(s_i^k - s_j^k) \\ &= \sum_{n=1}^{3} \left(\sum_{m=1}^{3} h^{nm} (s_i^m - s_j^m) \right) \left(\sum_{k=1}^{3} h^{nk} (s_i^k - s_j^k) \right), \end{aligned}$$

This can be expressed as the product of a row vector with a column vector whose elements are $\sum_m^3 h^{nm}(s_i^m - s_j^m)$ and $\sum_k^3 h^{nk}(s_i^k - s_j^k)$, respectively. Clearly the latter is equal to the column vector $\mathbf{h}(\mathbf{s}_i - \mathbf{s}_j)$, whilst the former

is the row vector transpose of this:

$$\begin{aligned} r_{ij}^2 &= \left(\mathbf{h}(\mathbf{s}_i - \mathbf{s}_j)\right)^T \mathbf{h}(\mathbf{s}_i - \mathbf{s}_j) \\ &= (\mathbf{s}_i - \mathbf{s}_j)^T \mathbf{h}^T \mathbf{h}(\mathbf{s}_i - \mathbf{s}_j) \\ &= (\mathbf{s}_i - \mathbf{s}_j)^T \mathbf{G}(\mathbf{s}_i - \mathbf{s}_j), \end{aligned} \tag{C.4}$$

where $\mathbf{G} = \mathbf{h}^T\mathbf{h}$ and using the $(\mathbf{AB})^T = \mathbf{B}^T\mathbf{A}^T$ law for matrix multiplication [**259**, p. 47].

To differentiate the square root of equation (C.4) with respect to the column vector $\mathbf{s}_l$ we can make use of the summation notation used previously:

$$\begin{aligned} \frac{\partial r_{ij}}{\partial \mathbf{s}_l} &= \left\{ \frac{\partial}{\partial s_l^1} \left(\sum_{m=1}^{3} \sum_{k=1}^{3} g^{mk} (s_i^m - s_j^m)(s_i^k - s_j^k) \right)^{\frac{1}{2}}, \ \ldots, \ \ldots \right\}^T \\ &= \frac{1}{2} \frac{1}{r_{ij}} \left\{ \sum_m g^{m1} (s_i^m - s_j^m)(\delta_{il} - \delta_{jl}) + \right. \\ &\qquad \left. \sum_k g^{1k} (s_i^k - s_j^k)(\delta_{il} - \delta_{jl}), \ \ldots, \ \ldots \right\}^T, \end{aligned}$$

using the product rule and the fact that non-zero elements only occur when $l = i$ or $l = j$. For each element of the derivative vector the two terms can be combined by changing superscripts, and using $g^{nm} = g^{mn}$ from earlier, as appropriate, to give

$$\frac{\partial r_{ij}}{\partial \mathbf{s}_l} = \frac{1}{r_{ij}} (\delta_{il} - \delta_{jl}) \left\{ \sum_m g^{1m} (s_i^m - s_j^m), \ \ldots, \ \ldots \right\}^T,$$

where δ_{ij} is the Kronecker-Delta function whose value is one if $i = j$ and zero otherwise. Clearly each element w of the column vector $\partial r_{ij}/\partial \mathbf{s}_l$

contains the element-wise summation (*i.e.,* dot product) of the wth row of $\mathbf{G}$ multiplied with the elements of the column vector $(\mathbf{s}_i - \mathbf{s}_j)$. This observation allows us to express the derivative as the product of matrices and vectors:

$$\begin{aligned}\frac{\partial r_{ij}}{\partial \mathbf{s}_l} &= \frac{1}{r_{ij}}(\delta_{il} - \delta_{jl})\big((\text{rows of } \mathbf{G}) \times (\text{elements of } (\mathbf{s}_i - \mathbf{s}_j))\big)^T \\ &= \frac{1}{r_{ij}}(\delta_{il} - \delta_{jl})\mathbf{G}(\mathbf{s}_i - \mathbf{s}_j) \qquad \text{(C.5)} \\ &= \frac{1}{r_{ij}}(\delta_{il} - \delta_{jl})\mathbf{h}^T\mathbf{h}(\mathbf{s}_i - \mathbf{s}_j). \qquad \text{(C.6)}\end{aligned}$$

C.3 The Parrinello-Rahman equation of motion for $\ddot{\mathbf{h}}$

Evaluating (2.11) with $\mathcal{L}$ as defined in (2.9), for the box matrix $\mathbf{h}$, we get:

$$\frac{1}{2}W\frac{\mathrm{d}}{\mathrm{d}t}\left(\frac{\partial}{\partial\dot{\mathbf{h}}}\mathrm{Tr}[\dot{\mathbf{h}}^T\dot{\mathbf{h}}]\right) - \frac{\partial}{\partial\mathbf{h}}\left(\frac{1}{2}\sum_{i=1}^{N} m_i\dot{\mathbf{s}}_i^T\mathbf{G}\dot{\mathbf{s}}_i - \sum_{i=1}^{N}\sum_{j>i}^{N}\phi(r_{ij}) - p_{\text{ext}}\Omega\right) = 0. \qquad \text{(C.7)}$$

$\mathrm{Tr}[\ldots]$, or Trace, of a matrix is the sum of its diagonal elements, and

$$\begin{aligned}\dot{\mathbf{h}}^T\dot{\mathbf{h}} &= \left[\sum_{l=1}^{3}(\dot{h}^T)^{ml}\dot{h}^{ln}\right] \quad \text{for } n, m = 1, 2, 3 \\ &= \left[\sum_{l=1}^{3}\dot{h}^{lm}\dot{h}^{ln}\right],\end{aligned}$$

where $\dot{h}^{nm}$ is an element of the time derivative of $\mathbf{h}$. Therefore

$$\begin{aligned}\frac{\partial}{\partial\dot{\mathbf{h}}}\mathrm{Tr}[\dot{\mathbf{h}}^T\dot{\mathbf{h}}] &= \frac{\partial}{\partial\dot{\mathbf{h}}}\left(\sum_{m=1}^{3}\sum_{l=1}^{3}(\dot{h}^{lm})^2\right)\\ &= \left[\sum_{m=1}^{3}\sum_{l=1}^{3}\frac{\partial(\dot{h}^{lm})^2}{\partial\dot{h}^{pq}}\right] \quad \text{for } p,q=1,2,3\\ &= \left[2\dot{h}^{pq}\right]\\ &= 2\dot{\mathbf{h}}. \end{aligned} \tag{C.8}$$

In the second part of equation (C.7) we are calculating derivatives with respect to $\mathbf{h}$. The first to be evaluated is

$$\begin{aligned}\frac{\partial}{\partial\mathbf{h}}\left(\frac{1}{2}\sum_{i=1}^{N}m_i\dot{\mathbf{s}}_i^T\mathbf{G}\dot{\mathbf{s}}_i\right) &= \frac{1}{2}\left[\sum_{i=1}^{N}m_i\sum_{k=1}^{3}\sum_{m=1}^{3}\sum_{n=1}^{3}\frac{\partial}{\partial h^{pq}}\left(\dot{s}_i^k h^{nk}h^{nm}\dot{s}_i^m\right)\right] \quad \text{(using (C.2))}\\ &= \frac{1}{2}\left[\sum_{i=1}^{N}m_i\left(\sum_{m=1}^{3}\dot{s}_i^q h^{pm}\dot{s}_i^m+\sum_{k=1}^{3}\dot{s}_i^k h^{pk}\dot{s}_i^q\right)\right] \quad \text{(by product rule)}\\ &= \left[\sum_{i=1}^{N}\sum_{m=1}^{3}m_i h^{pm}\dot{s}_i^m\dot{s}_i^q\right]\\ &= \sum_{i=1}^{N}m_i\left[\sum_{m=1}^{3}h^{pm}\dot{s}_i^m\right]\dot{\mathbf{s}}_i^T\\ &= \sum_{i=1}^{N}m_i\mathbf{h}\dot{\mathbf{s}}_i\dot{\mathbf{s}}_i^T. \end{aligned} \tag{C.9}$$

Now consider

$$\frac{\partial}{\partial\mathbf{h}}\left(\sum_{i=1}^{N}\sum_{j>i}^{N}\phi(r_{ij})\right).$$

By the chain rule we obtain:

$$\sum_{i=1}^{N}\sum_{j>i}^{N}\phi'(r_{ij})\frac{\partial r_{ij}}{\partial\mathbf{h}}. \tag{C.10}$$

Proceeding as for $\partial r_{ij}/\partial \mathbf{s}_i$ we find $\partial r_{ij}/\partial \mathbf{h}$ via:

$$\begin{aligned}
\frac{\partial r_{ij}}{\partial \mathbf{h}} &= \left[\frac{\partial}{\partial h^{pq}}\left(\sum_{n=1}^{3}\sum_{m=1}^{3}\sum_{k=1}^{3} h^{nm}h^{nk}(s_i^m - s_j^m)(s_i^k - s_j^k)\right)^{\frac{1}{2}}\right] \quad \text{for } p,q = 1,2,3, \\
&= \left[\frac{1}{2}\frac{1}{r_{ij}}\left(\sum_k h^{pk}(s_i^q - s_j^q)(s_i^k - s_j^k) \right.\right. \\
&\qquad \left.\left. + \sum_m h^{pm}(s_i^m - s_j^m)(s_i^q - s_j^q)\right)\right] \qquad \text{(by the product rule)} \\
&= \left[\frac{1}{r_{ij}}\sum_k h^{pk}(s_i^k - s_j^k)(s_i^q - s_j^q)\right],
\end{aligned}$$

which we see is equal to the pth element of $\mathbf{h}(\mathbf{s}_i - \mathbf{s}_j) \times$ the qth element of $(\mathbf{s}_i - \mathbf{s}_j)$, giving

$$\frac{\partial r_{ij}}{\partial \mathbf{h}} = \frac{1}{r_{ij}}\mathbf{h}(\mathbf{s}_i - \mathbf{s}_j)(\mathbf{s}_i - \mathbf{s}_j)^T. \tag{C.11}$$

Finally, for the derivative of $p_{\text{ext}}\Omega$ with respect to $\mathbf{h}$ we start by expressing $\Omega = \det \mathbf{h}$ in a more appropriate form:

$$\begin{aligned}
\frac{\partial}{\partial \mathbf{h}} p_{\text{ext}}\Omega &= p_{\text{ext}}\frac{\partial}{\partial \mathbf{h}}\det \mathbf{h} \\
&= p_{\text{ext}}\frac{\partial}{\partial \mathbf{h}}\left(\sum_{n=1}^{3} h^{mn}C_{mn}\right) \quad \text{for } m = 1, 2, \text{ or } 3,
\end{aligned} \tag{C.12}$$

where C_{mn} is the cofactor of h^{mn} defined via the minor M_{mn} as:

$$C_{mn} = (-1)^{m+n}M_{mn}.$$

Note that in the above expression for $\det \mathbf{h}$ the n and m are interchangeable (keeping n in the summation) because the determinant can be found either *row-wise* (as above) or *column-wise* where m and n are reversed [**254**, chapter 6, Kreyszig]. Here the minor M_{nm} is the determinant

of the sub-matrix of $\mathbf{h}$ obtained from $\mathbf{h}$ by deleting the nth row and m^{th} column [**254**].

In (C.12) m is arbitrary and so can certainly be chosen to be equal to, for example, the p of a h^{pq} element of $\mathbf{h}$. Hence

$$\begin{aligned}\frac{\partial}{\partial \mathbf{h}} p_{\text{ext}}\Omega &= p_{\text{ext}}\left[\frac{\partial}{\partial h^{pq}}\left(\sum_{n=1}^{3} h^{pn}C_{pn}\right)\right] \\ &= p_{\text{ext}}\left[\sum_{n=1}^{3}\frac{\partial}{\partial h^{pq}}\left(h^{pn}(-1)^{p+n}M_{pn}\right)\right] \\ &= p_{\text{ext}}\left[\left((-1)^{p+q}M_{pq}\right)\right],\end{aligned}$$

since, by definition, M_{pq} is independent of h^{pq}. Noting the formula for the inverse of a square matrix, as given in [**254**, pg 353], we see that

$$\frac{\partial}{\partial \mathbf{h}} p_{\text{ext}}\Omega = p_{\text{ext}} \det \mathbf{h}\left(\mathbf{h}^{-1}\right)^{T} = p_{\text{ext}}\Omega\left(\mathbf{h}^{T}\right)^{-1}, \tag{C.13}$$

where $\mathbf{h}^{-1}$ is the inverse matrix of $\mathbf{h}$. Above we have used $(\mathbf{A}^{T})^{-1} = (\mathbf{A}^{-1})^{T}$ from [**259**, pg 63].

We now have all the necessary components to construct the equation of motion for the 9 degrees of freedom associated with $\mathbf{h}$. Substituting (C.8), (C.9), (C.10) combined with (C.11), and (C.13) into equation (C.7), and evaluating the required time derivative, gives

$$W\ddot{\mathbf{h}} - \left(\sum_{i=1}^{N} m_i \mathbf{h}\dot{\mathbf{s}}_i\dot{\mathbf{s}}_i^{T} - \sum_{i=1}^{N}\sum_{j>i}^{N}\frac{\phi'(r_{ij})}{r_{ij}}\mathbf{h}(\mathbf{s}_i-\mathbf{s}_j)(\mathbf{s}_i-\mathbf{s}_j)^{T} - p_{\text{ext}}\Omega\left(\mathbf{h}^{T}\right)^{-1}\right) = 0. \tag{C.14}$$

Defining a new matrix $\boldsymbol{\pi}$ as:

$$\Omega\boldsymbol{\pi} = \sum_{i=1}^{N} m_i \mathbf{h}\dot{\mathbf{s}}_i\dot{\mathbf{s}}_i^{T}\mathbf{h}^{T} - \sum_{i=1}^{N}\sum_{j>i}^{N}\frac{\phi'(r_{ij})}{r_{ij}}\mathbf{h}(\mathbf{s}_i-\mathbf{s}_j)(\mathbf{s}_i-\mathbf{s}_j)^{T}\mathbf{h}^{T},$$

which is equivalent to equation 2.11 of [**65**], we obtain, in accordance with 2.10 of [**65**],

$$W\ddot{\mathbf{h}} = (\boldsymbol{\pi} - p_{\text{ext}})\boldsymbol{\sigma}. \tag{C.15}$$

Here $\boldsymbol{\sigma} = \Omega(\mathbf{h}^T)^{-1}$.

D. CORRESPONDENCE BETWEEN NEAREST NEIGHBOUR STRINGS AND ATOMS

In chapter 6 we consider a multi-string Frenkel-Kontorova model based on the interaction of neighbouring [111] strings of atoms in a bcc lattice. Here we summarise the relationship between the [111] nearest-neighbour strings (NNSs) surrounding a central string and the nearest-neighbour atoms (NNAs) surrounding an atom of this string. Figure 6.2 (page 204) demonstrates the distribution of [111] strings in the (111) plane about a central string, while Appendix A explains how atoms are distributed in a bcc lattice. Using this understanding we have analyzed which NNAs are contained within a given NNS (Table D.1) and vice-versa (Table D.2). In the tables we also show the relative distances from the central string or atom to the given NNS or NNA (in units of the lattice parameter a), respectively, together with the number of such objects.

Tab. D.1: Description of the relative distances to nearest-neighbour strings and the nearest-neighbour atoms they contain.

NNS	Number of such strings	Distance from core string	Which atoms do they contain?
Core string	1	0	1st, 5th, 10th NNAs
1st	6	$\frac{2}{\sqrt{6}}a$	1st, 2nd, 3rd, 4th, 7th, 9th NNAs
2nd	6	$\sqrt{2}a$	3rd, 4th, 8th NNAs
3rd	6	$\frac{4}{\sqrt{6}}a$	4th, 5th, 6th, 7th, 10th NNAs
4th	12	$\sqrt{\frac{14}{3}}a$	7th, 8th, 9th, 10th NNAs
5th	6	$\sqrt{6}a$	9th NNAs

Tab. D.2: Description of the relative distances to nearest-neighbour atoms and the nearest-neighbour strings they are in.

NNA	Number of such atoms	Distance from core atom	Which strings are they in?
1st	8	$\frac{\sqrt{3}}{2}a$	2 in core string 6 in 1st NNSs
2nd	6	a	6 in 1st NNSs
3rd	12	$\sqrt{2}a$	6 in 1st NNSs 6 in 2nd NNSs
4th	24	$\frac{\sqrt{11}}{2}a$	6 in 1st NNSs 12 in 2nd NNSs 6 in 3rd NNSs
5th	8	$\sqrt{3}a$	2 in core string 6 in 3rd NNSs
6th	6	$2a$	6 in 3rd NNSs
7th	24	$\frac{\sqrt{19}}{2}a$	6 in 1st NNSs 6 in 3rd NNSs 12 in 4th NNSs
8th	24	$\sqrt{5}a$	12 in 2nd NNSs 12 in 4th NNSs
9th	24	$\sqrt{6}a$	6 in 1st NNSs 12 in 4th NNSs 6 in 5th NNSs
10th	20	$3\frac{\sqrt{3}}{2}a$	2 in core string 6 in 3rd NNSs 12 in 4th NNSs

E. CORRECTION TO THE DIFFUSION COEFFICIENT D

In Chapter 4 we calculate the diffusion coefficient D for a migrating dislocation loop using equation (4.7). In this equation the position of the loop appears in its corrected form $\tilde{z}$, which is defined via equation (4.6). Originally, it was thought that the correction (for drift) given by (4.6) did not alter the calculated values of D [**111**]. In this case, D is approximated as:

$$D \approx \frac{\tilde{z}^2(\tau)}{2\tau}, \tag{E.1}$$

However, an analysis by Derlet [**260**] revealed that, for a distribution where the value of D was known in advance, the drift correction (4.6) resulted in an underestimation of D by a factor of three. Thus, in (4.7), the right-hand-side of the equation is multiplied by three to correct for the systematic error.

To derive the correction factor directly, we start from the over-damped Langevin equation for a loop (or particle) diffusing in 1-dimension [**261**]:

$$\frac{\mathrm{d}z}{\mathrm{d}t} = \sqrt{2D}\xi(t), \tag{E.2}$$

where $\xi(t)$ is a random variable satisfying the time-averaged condition $\langle \xi(t)\xi(t') \rangle = \delta(t - t')$, with $\delta(x)$ the Dirac Delta function.
Integrating (E.1) gives

$$z(t) = \sqrt{2D} \int_0^t \xi(\tau)\mathrm{d}\tau,$$

and thus,

$$\langle z(t)z(t')\rangle = 2D\int_0^t\int_0^{t'}\delta(\tau-\tau')\mathrm{d}\tau'\mathrm{d}\tau. \tag{E.3}$$

For this equation there are two cases to consider:

1. if $t < t'$ then
$$\int_0^{t'}\delta(\tau-\tau')\mathrm{d}\tau' = 1$$
because $\forall\tau$ there exists a τ' satisfying $0 \le \tau' \le t$, such that $\tau - \tau' = 0$. (*i.e.,* using the fact that the definite integral of $\delta(x)$ can be viewed as being equal to one provided the range of the integral includes zero.)

2. if $t > t'$ then there are a further two cases:
$$\int_0^{t'}\delta(\tau-\tau')\mathrm{d}\tau' = \begin{cases} 0 & \text{if } \tau > t' \quad (\textit{i.e.}, \forall\tau', (\tau-\tau') \neq 0), \\ 1 & \text{if } \tau < t'. \end{cases}$$
Note that we also consider the result of the above integral to be zero if $\tau = t'$.

Applying these cases to (E.3) gives us that

$$\begin{aligned}\langle z(t)z(t')\rangle &= 2D\begin{cases}\displaystyle\int_0^{t'}1\mathrm{d}\tau + \int_{t'}^{t}0\mathrm{d}\tau & = t', \quad \text{for } t > t' \\ \displaystyle\int_0^{t}1\mathrm{d}\tau & = t, \quad \text{for } t' > t\end{cases} \\ &= 2D\,\min\{t,t'\}.\end{aligned} \tag{E.4}$$

Now let us consider the time-averaged square displacement of the corrected defect position, using the integral equivalent of equation (4.6):

$$\tilde{z}(t) = z(t) - \frac{2}{t}\int_0^t z(\tau)\mathrm{d}\tau. \tag{E.5}$$

Applying (E.4), we obtain

$$\begin{aligned}
\langle \tilde{z}^2(t)\rangle &= \langle z^2(t)\rangle - \frac{4}{t}\int_0^t \langle z(\tau)z(t)\rangle \mathrm{d}\tau \\
&\qquad + \frac{4}{t^2}\int_0^t \left(\int_0^t \langle z(\tau)z(\tau')\rangle \mathrm{d}\tau'\right)\mathrm{d}\tau \\
&= 2Dt - \frac{8D}{t}\int_0^t \min\{\tau,t\}\mathrm{d}\tau \\
&\qquad + \frac{8D}{t^2}\int_0^t \left(\int_0^t \min\{\tau,\tau'\}\mathrm{d}\tau'\right)\mathrm{d}\tau \\
&= 2Dt - \frac{8D}{t}\int_0^t \tau \mathrm{d}\tau \\
&\qquad + \frac{8D}{t^2}\int_0^t \left[\int_0^\tau \tau' \mathrm{d}\tau' + \int_\tau^t \tau \mathrm{d}\tau'\right]\mathrm{d}\tau \\
&= -2Dt + \frac{8D}{t^2}\int_0^t \left[\frac{\tau^2}{2} + \tau(t-\tau)\right]\mathrm{d}\tau \\
&= -2Dt + \frac{8}{3}Dt \\
&= \frac{1}{3}\,2Dt.
\end{aligned}$$

Thus,

$$D = 3\frac{\langle \tilde{z}^2(t)\rangle}{2t}, \tag{E.6}$$

which leads to equation (4.7) for the effective diffusion coefficient of a given defect trajectory.

LIST OF FIGURES

1.1 Schematics of the Deuterium-Tritium fusion reaction. The resulting neutron carries 14.1 MeV of the excess energy. 3

1.2 Diagrams of the planned ITER experiment [**3**, **4**]. The device dwarfs all previous fusion experiments (see the human scale indicator in the bottom right-hand corner of the main diagram). The plasma is contained within the toroidal vacuum vessel (see expanded view) using magnetic confinement. The first wall and blanket must function as both a neutron shield and heat sink to absorb the generated power, and, in a commercial reactor, would also need to breed Tritium fuel. © ITER organization. 6

1.3 The neutron spectrum of energies incident on the primary mirror of an equatorial diagnostic port being designed as part of the ITER experiment. Calculations performed using MCNP version 4C3 [**11**]. 10

1.4 The transmutation (burn-up) of pure W as a result of exposure to the 1×10^{15} neutrons $\mathrm{cm}^{-2}\mathrm{s}^{-1}$ neutron flux expected in the first wall of a fusion power plant for five years. The concentration of each element in the system, as it is burnt-up or created, is given in weight parts per million (wppm). Data taken from the *Handbook of Activation Data Calculated Using EASY-2003* [**17**, pg 431] © United Kingdom Atomic Energy Authority. 13

1.5 The transmutation (burn-up) of pure W as a result of exposure to the 1×10^{15} neutrons $\mathrm{cm}^{-2}\mathrm{s}^{-1}$ neutron flux expected in the first wall of a fusion power plant for five years. In this graph concentrations are given in atomic parts per million (appm). Calculated Using EASY-2003 [**19**]. For more details see [**20**] © 2010 United Kingdom Atomic Energy Authority. 15

3.1 Evolution of defect distribution during annealing at 600K using kMC. (reproduced from [**142**]) 60

3.2 Formation energies of vacancy (E_{vac}) and Self-Interstitial atom (SIA) (E_{SIA}) clusters simulated with a MBP. (reproduced exactly from [**148**]) 62

3.3 Loop construction methods: Open loops created by removing a disc of atoms from a perfect lattice; Closed loops created by inserting atoms (the red layer) outside of the disc radius. The Burgers vector is the vertical direction in these diagrams. . . . 67
3.4 Formation energy of 121-vacancy or -SIA loops and 137-vacancy voids as a function of the number of atoms in the periodic simulation cell. . . . 68
3.5 Variation in formation energy of spherical voids and various $\frac{1}{2}\langle 111\rangle$ loop defects in Fe under the Dudarev-Derlet [**105**] magnetic potential. Plotted as a function of defect size (number of SIAs/vacancies). The lines represent continuous interpolations between the discrete data points found using atomistic simulations. . . . 70
3.6 Variation in formation energy of various $\frac{1}{2}\langle 111\rangle$ loop defects in Fe under the Dudarev-Derlet [**105**] magnetic potential. Plotted as a function of loop diameter. . . . 71
3.7 Difference between formation energies of closed and open $\frac{1}{2}\langle 111\rangle$ vacancy loops in Fe as a function of diameter (D-D potential). 72
3.8 Heating of 26-vacancy closed and open loops: Final energy of remaining defect(s) after 1 ns heating at each temperature. Change in energy indicates a transformation in the defect structure. . . . 74
3.9 The temperature-driven configurational changes of a cluster of 26 vacancies in Fe, originally arranged as either a closed or open loop. Only atoms around the vacancy defects are shown. Bulk atoms are invisible. At 400K the closed loop becomes 'open'. The spherical void is formed by 1000K, while the evaporation begins at 1500K. . . . 75
3.10 61-vacancy closed dislocation loop heating: variation in formation energy as a function of heating temperature before relaxation. The formation energy, and hence the defect, remained stable almost up to the melting temperature. . . . 77
3.11 Variation in formation energy, as predicted by the Mendelev [**82**] potential, of spherical voids and various $\frac{1}{2}\langle 111\rangle$ loop defects in Fe. Plotted as a function of defect size. . . . 79
3.12 Theoretical curves for the formation energy of $\frac{1}{2}\langle 111\rangle$ loops and spherical voids in Fe. Also shown are the simulation data from Figure 3.5, as well as improved fits (see text) to the data (solid lines). . . . 82

3.13 The binding energy of $\frac{1}{2}\langle 111\rangle$ loop defects and spherical voids as a function of size. Calculated using equations (3.8) and (3.10). 84
3.14 Variation in formation energy of $\langle 001\rangle$ mesoscopic vacancy and interstitial dislocation loops, and spherical voids in Fe plotted as a function of the number of individual defects forming the loop or a void (D-D potential). 86
3.15 Difference between formation energies of closed and open $\langle 001\rangle$ vacancy loops in Fe as a function of diameter (D-D potential). The switch from positive to negative difference occurs at around the 28 Å diameter loop-size. 87
3.16 Comparison of formation energies for mesoscopic vacancy loops with different Burgers vectors in Fe, as predicted by the D-D magnetic potential for Fe. 89
3.17 Comparison of formation energies of (a) $\frac{1}{2}\langle 111\rangle$ and (b) $\langle 001\rangle$ vacancy loops of different shape in Fe (D-D potential). 91
3.18 Formation energy of 211-vacancy or -SIA loops and 259-vacancy voids as a function of the number of W atoms in the periodic simulation cell. 94
3.19 (a)$\frac{1}{2}\langle 111\rangle$ defect energies in W as a function of size; (b)Variation of difference between closed and open $\frac{1}{2}\langle 111\rangle$ vacancy loop energies in W as a function of diameter (closed minus open). . . 95
3.20 Formation energy as a function of defect size of $\langle 001\rangle$ loop defects in W 97
3.21 Weak-beam dark field contrast image of Fe8%Cr irradiated with Fe^{+} ions at 300 ^{o}C - see main text and [**127**] for more details. The scale indicator shows that the defects seen are very small. 99

4.1 Relaxed structures of various $\frac{1}{2}\langle 111\rangle$ mesoscopic dislocation loops in W: (a) 199-vacancy closed loop - view in the (111) plane; (b) as (a) but looking down the [111] axis of the defect; (c) 199-atom interstitial loop (in-plane view); (d) as (c) but axial view. 111
4.2 Variation of maximum strain through $\frac{1}{2}\langle 111\rangle$ closed vacancy and interstitial loops in W. 113
4.3 Motion of a sub-critical $\frac{1}{2}\langle 111\rangle$ closed vacancy loop (26-vacancy) at 400K in Fe. The graph shows how the centre-of-mass (COM) of the defect varied in time. 117

4.4 1D motion in the $z = [111]$ direction of a 61-vacancy closed $\frac{1}{2}\langle 111\rangle$ loop in Fe during finite temperature MD simulations. Defect position was computed every 0.1 ps for each temperature. 120
4.5 Variation in the (a) $x = [1\bar{1}0]$ and (b) $y = [11\bar{2}]$ positions of the 61-vacancy loop in Fe during a 400K MD simulation. . . . 121
4.6 Variation in the $z = [111]$ position of the 187-SIAs $\frac{1}{2}\langle 111\rangle$ loops in W during simulations at finite temperature. 122
4.7 1D motion in the [111] direction of a 61-atom interstitial $\frac{1}{2}\langle 111\rangle$ loop in Fe during finite temperature MD simulations. 124
4.8 Variation in the [111] squared displacement of the 61-vacancy loops in Fe during simulations at finite temperature. 124
4.9 Plot of calculated diffusion coefficients as a function of temperature for 19.2 Å diameter (61 vacancies/self-interstitials) $\frac{1}{2}\langle 111\rangle$ loops in Fe. The fitted curve for each set of data has a linear $D = CT$ form, as suggested by Zepeda-Ruiz *et al.* [**174**]. The green points for each set of data at 500K represents the result for an extended simulation of 20 ns (compared to the 2 ns of the primary results). 128
4.10 Plot of calculated diffusion coefficients as a function of temperature for 37.1 Å diameter (187 vacancies/self-interstitials) $\frac{1}{2}\langle 111\rangle$ loops in W. The fitted curve for each set of data has a exponential form. 131
4.11 Logarithmic plot of diffusion coefficients as a function of $1/k_BT$ for 19.2 Å diameter (61 vacancies/self-interstitials) $\frac{1}{2}\langle 111\rangle$ loops in Fe. 134
4.12 Logarithmic plot of diffusion coefficients as a function of $1/k_BT$ for 37.1 Å diameter (187 vacancies/self-interstitials) $\frac{1}{2}\langle 111\rangle$ loops in W. 135
4.13 Plot of calculated diffusion coefficients as a function of temperature for 31.1 Å diameter (185 vacancies/self-interstitials) $\langle 001\rangle$ loops in Fe. The fitted curve for each set of data has an exponential form. 138
4.14 Frames of video recording dynamic observations of ultra-high-purity Fe irradiated using 150 keV Fe^+ at 570K. The loop is seen to 'hop' between the first and second frames. Reproduced from [**127**]. 140
4.15 1D hopping of a $\frac{1}{2}\langle 111\rangle$ loop in ultra-high-purity Fe under the electron beam at 300°C after irradiation. Reproduced from [**127**]. 140

4.16 Comparison between diffusion of a 61-vacancy $\frac{1}{2}\langle 111\rangle$ loop in Fe at 500K with periodic boundary conditions and no free surfaces, and with free surfaces above and below the defect (approximately 50 Å away). 143
4.17 Initial positions of three 19-SIA interstitial $\frac{1}{2}\langle 111\rangle$ loops in Fe. The view in the (111) plane in picture (a) shows them lined up along $[1\bar{1}0]$, while the view looking along $[11\bar{2}]$ shown in (b) illustrates their random displacement in [111]. 146
4.18 Trajectories of three 19-SIA $\frac{1}{2}\langle 111\rangle$ loops in Fe at 500K, all contained within the same simulation cell. 148
4.19 Final positions of three 19-SIA loops after 6.5 ns of simulation time at 500K. (a) shows a close-up of the relative orientation of the three loops, while (b) displays their positions in full simulation box. Note that in this (relatively) high temperature simulation, the defects appear extended in the [111] direction because the strain fields cause additional atoms to have energies significantly above the average. 149
4.20 A second simulation of three 19-SIA interstitial loops migrating coherently at 500K. 150

5.1 Example secondary glide planes (red) and associated motion directions (green) of the $([1\bar{1}0], [11\bar{2}], [111])$ coordinate system. The primary glide direction is either $[1\bar{1}0]$ or $[11\bar{2}]$. In the figure the $y = [111]$ Burgers vector direction is pointing out of the page. For the $(11\bar{2})$ glide plane the secondary glide plane shown is $(10\bar{1})$, while for the $(1\bar{1}0)$ primary glide plane the $(2\bar{1}\bar{1})$ is the secondary shown. 164
5.2 Temperature dissipation in a Fe lattice equilibrated to 100K. The ΔT increases in temperature mimic the effect of the localised heating caused by the passage of a screw dislocation. . 167
5.3 The simulation set-up used to measure the velocity response of a $\frac{1}{2}\langle 111\rangle$ screw dislocation to applied stress at finite temperature. 169
5.4 Motion of the dislocation at 300K in pure Fe under the influence of a range of applied stress σ_A values. The applied stresses are given in MPa. 173
5.5 Example of the procedure used to measure the velocity from each simulation trajectory. The velocity is measured as the gradient of the straight-line fit to the steady-state motion. The simulation conditions in this case were 300K under applied stress of 800 MPa. 176

5.6 The variation of the measured dislocation velocity at each simulation temperature as a function of the applied stress σ_A. . . 177
5.7 Example simulation snapshot (not to scale in z) of the kinked screw dislocation (red atoms) at 300K with an applied stress of 300 MPa. Surface atoms are also shown (grey). 178
5.8 Simulation snapshot for a screw dislocation moving at 300K under an applied stress of 800 MPa. Debris is clearly visible in the wake of the screw dislocation. 188
5.9 Realisation of the fitted functions at (a) 100K, (b) 200K, (c), 300K, and (d) 500K. The original data are shown together with the fits to each regime. 190

6.1 Atomic scale structure of a $\mathbf{b} = (a/2)[111]$ screw dislocation in a bcc transition metal viewed in the [111] direction parallel to the dislocation line (a), and in the $[1\bar{1}0]$ direction normal to the dislocation line (b). The six atomic strings shown in lighter colour form the core of the dislocation. In (a) the positions of [111] strings in the (111) plane are unchanged compared to the perfect lattice, but in (b) the mismatch between atomic rows normal to the Burgers vector are clear [**250**]. 200
6.2 bcc lattice viewed in the [111] direction. It forms a hexagonal two-dimensional lattice of atomic strings. The strings are displaced with respect to each other in the [111] direction (normal to the plane of the image), forming three subsets (or phases), where one of the atoms in the string subset shown in white is situated in the plane of the lattice. One atom of the grey string subset is situated $b/3$ above the plane of the image, whereas one atom of the black string subset is situated $b/3$ below the plane of the image, where b is the magnitude of the Burgers vector $\mathbf{b} = (a/2)[111]$. The circles indicate the 1st, 2nd, and the 3rd (for the components of the inter-string interaction law U_1, U_2, and U_3, respectively) nearest-neighbours of the central string. 204
6.3 Curves, evaluated using density functional calculations described in the text, showing how the total energy of the system (per Burgers vector distance) changes if (i) the central string shown in Figure 6.2 is translated through the lattice parallel to itself in the [111] direction, (ii) two nearest-neighbour strings are translated in the [111] direction, and (iii) the translation involves two second nearest-neighbour strings. 205

6.4 These curves show data taken from Figure 6.3 and scaled by the factor of 1/3, 1/5, and 1/6, respectively. The fact that the re-scaled curves cannot be told apart over a large range of variation of displacement u suggests that the interactions between the strings that are further apart than the first nearest-neighbour distance are relatively weak. 207
6.5 The three effective nearest-neighbour inter-string interaction potentials $U_1(d)$ derived from the DFT data shown in Figure 6.4 using the Fourier deconvolution procedure described in the text. 209
6.6 Variation in system energy as a single [111] string moves through a stationary perfect lattice of Fe by one $\mathbf{b} = (a/2)[111]$ period. Results of calculations performed using the two interatomic potentials are shown together with the DFT data from Figure 6.3. 211
6.7 Total energy increases resulting from the [111] displacement of single or groups of [111] strings in an otherwise perfect bcc Fe lattice. (a) and (c) show results from the D-D potential. (b) and (d) are for the M potential. (a) and (b) display the absolute energy change, while (c) and (d) show the scaled energy changes (see text). The scaling ratios are 3:5:6:7 for (single):(two NN):(two 2NN):(row), respectively. In (c) and (d) the four curves are indistinguishable, which demonstrates the dominance of U_1 over higher order terms. 212
6.8 The U_1 curves corresponding to the two interatomic potentials described in the text. 215
6.9 The second nearest-neighbour inter-string interaction U_2 curves evaluated using the interatomic potentials. Note the difference in the absolute scale between the curves shown in this plot, and the U_1 curves shown in Figure 6.8. 216
6.10 The U_3 curve evaluated using the Mendelev *et al.* [**82**] many-body interatomic potential. 216
6.11 The [111] string configurations for (a) the perfect bcc Fe lattice and (b) the symmetric non-degenerate core structure found for the inter-string interaction law derived from the M interatomic potential. Note that (b) is practically indistinguishable from the isotropic elasticity solution for a screw dislocation (equation (6.1)). 218

6.12 Differential displacement maps of the screw dislocation cores produced by the inter-string potentials derived from the (a) M and (b,c) D-D interatomic potentials. $[1\bar{1}0]$ is the vertical direction, with $[11\bar{2}]$ horizontal. The energies of the two configurations shown in (b) and (c) are virtually identical. . . 220
6.13 The differences between the [111] displacements of strings in the ideal isotropic solution for a screw dislocation, and their displacements after relaxation with (a) the M-derived string interaction laws and (b) the string interaction laws derived from the D-D potential. Differences for each string are plotted against its distance from the centre of the screw dislocation core in the (111) plane. 221
6.14 Three U_1 potentials after normalising their minima to zero and scaling to a maximum of one. 224
6.15 Stability curves for various U_1 inter-string interaction laws. The numerical designation for a U_1 function in the legend refers to its interpolated distance from the M U_1 law ('zero') in the direction of the D-D law ('one'). α is a measure of symmetry breaking in the screw core with perfect symmetry at zero, and each curve in the chart shows how the energy of the screw core structure varies as a function of α for a given inter-string interaction U_1. 225
6.16 The first derivatives of the U_1 curves derived from the M and D-D interatomic potentials for Fe. The bars above the curves show the relative separations for the [111] strings ('interaction distances') for the ideal isotropic elasticity solution of a screw dislocation, given by equation (6.1). 228
6.17 Stability curves for various versions of the U_1 inter-string interaction laws defined by (a) the cos(power) function of equation (6.11), (b) the cos(sin) law of (6.12), and (c) the $\cos(\tan^{-1})$ expression of (6.13). The numerical designation for a U_1 function in the legend refers to the value of the varying parameter for each function defined by equations (6.11)-(6.13). α is a measure of symmetry breaking in the screw core, and each curve in the chart shows how the energy of the screw core structure varies as a function of α for a given inter-string interaction U_1. 232
6.18 The shape of pathways describing the transition of a straight screw dislocation over a Peierls energy barrier evaluated for the three U_1 curves derived from the DFT data shown in Figure 6.5.234

6.19 Differential displacement maps of the lattice structure at different points along a DFT-derived Peierls energy pathway. (a) and (c) represent the initial and the final equilibrium screw dislocation core structures, and (b) is the structure corresponding to the middle of the transition pathway. 236
6.20 The shape of the Peierls energy transition pathway evaluated both for the original atomistic Mendelev potential, and for the U_1 interaction law derived from it. 238

A.1 The bcc unit cell. 249
A.2 The $([1\bar{1}0], [11\bar{2}], [111])$ coordinate axes (green) relative to the axes of the normal (x, y, z) coordinate system (red). 251
A.3 Correspondence of the normal bcc unit cell to the unit cell building-block of the $([1\bar{1}0], [11\bar{2}], [111])$ coordinate system. Each unit cell has 6 unique atoms (in red in both pictures). 252

B.1 The specific activity graph for Fe under four different irradiation conditions. The three highest activity levels correspond to irradiation conditions in different regions of a conceptual fusion power plant [**8**]. The fourth curve corresponds to the activity generated for irradiation in the vacuum vessel wall of JET from a Deuterium-Deuterium plasma. See [**17**] for more details. 260
B.2 The gamma-dose-rate importance diagram for neutron-irradiated Fe from [**17**]. 261
B.3 The transmutation (burn-up) of pure Fe as a result of exposure to the neutron flux expected in the first wall of a fusion power plant for five years [**17**]. Element concentrations at a particular time are given in wppm. 262
B.4 The transmutation (burn-up) of pure Fe as a result of exposure to the neutron flux expected in the first wall of a fusion power plant for five years [**17**]. In this expanded graph concentrations are given in appm. For more details see [**20**]. 263

LIST OF TABLES

5.1 Values of the transition stress, σ_d and linear-regime parameters at each simulation temperature. Also shown are the friction coefficients $\mathcal{B}$, defined by equation (5.7). 187

B.1 General properties of Fe from [**17**] 258
B.2 The activation properties table for 5-year, first-wall irradiation of Fe in a fusion device. Six activation properties are shown along with their levels at each of 6 cooling times after irradiation. For each decay time the percentage contribution from different radionuclides are shown [**17**]. 258
B.3 Radioactive isotope production pathway analysis for Fe. Radionuclides are listed in order of increasing half-life, and the important production pathways at each of 4 neutron irradiation energies are shown along with percentage contributions [**17**].259

D.1 Description of the relative distances to nearest-neighbour strings and the nearest-neighbour atoms they contain. 273
D.2 Description of the relative distances to nearest-neighbour atoms and the nearest-neighbour strings they are in. 274

BIBLIOGRAPHY

[1] S. J. Zinkle, M. Victoria, and K. Abe, 2002, *J. Nucl. Mater.*, **307–311** 31–42

[2] D. MacKay, 2009, *Sustainable Energy - without the hot air* (UIT Cambridge Ltd, Cambridge); available online at www.withouthotair.com

[3] ITER Technical Basis, Document G A0 FDR 1 01-07-13 R1.0, 2001

[4] R. Aymar, P. Barabaschi, and Y. Shimomura, 2002, *Plasma Phys. Control. Fusion*, **44** 519–565

[5] Taken from the UK fusion website: www.fusion.org.uk

[6] K. Ehrlich, R. Bullough, A. Kelly, J. Sheffield, P. Vandenplas, C. Windsor, E. A. Little, T. N. Todd, I. Cook, and R. J. Hawryluk, 1999, *Phil. Trans. R. Soc. Lond. A*, **357** 595–623

[7] D. J. Ward, I. Cook, Y. Lechon, and R. Saez, 2005, *Fusion Eng. Des.*, **75–79** 1221–1227

[8] D. Maisonnier, I. Cook, P. Sardain, L. Boccaccini, L. De Pace, L. Giancarli, P. Norajitra, and A. Pizzuto, 2006, *Fusion Eng. Des.*, **81** 1123–1130

[9] D. Maisonnier, I. Cook, P. Sardain, L. Boccaccini, E. Bogusch, L. De Pace, R. Forrest, L. Giancarli, S. Hermsmeyer, C. Nardi, P. Norajitra, A. Pizzuto, N. Taylor, and D. Ward, 2005, *Fusion Eng. Des.*, **75–79** 1173–1179

[10] R. Gröger, *Development of Physically Based Plastic Flow Rules for Body-Centred Cubic Metals with Temperature and Strain Rate Dependencies*, PhD thesis, University of Pennsylvania, 2007

[11] J. F. Briesmeister, Ed., MCNP - A General Monte Carlo N-Particle Transport Code - Version 4C, LA-13709-M, Los Alamos National Laboratory, 2000

[12] R. A. Forster, L. J. Cox, R. F. Barrett, T. E. Booth, J. F. Briesmeister, F. B. Brown, J. S. Bull, G. C. Geisler, J. T. Goorley, R. D. Mosteller, S. E. Post, R. E. Prael, E. C. Selcow, and A. Sood, 2004, *Nucl. Instr. Meth. Phys. Res. B*, **213** 82–86

[13] MCNP - A General Monte Carlo N-Particle Transport Code, version 5. Volume I: Overview and Theory, LA-UR-03-1987, Los Alamos National Laboratory, 2005

[14] R. A. Forrest, FISPACT-2007: User manual, UKAEA FUS 534, 2007

[15] R. A. Forrest and M. R. Gilbert, FISPACT-2005: User manual, UKAEA FUS 514, 2005

[16] R. A. Forrest, The European Activation System: EASY-2007 Overview, UKAEA FUS 533, 2007

[17] M. R. Gilbert and R. A. Forrest, Handbook of Activation Data Calculated Using EASY-2003, UKAEA FUS 509, 2004

[18] G. A. Cottrell, 2004, *J. Nucl. Mater.*, **334** 166–168

[19] R. A. Forrest, The European Activation File: EAF-2003 overview, UKAEA FUS 484, 2002

[20] M. R. Gilbert, Transmutation and He production in W and W-alloys, CCFE-R(10)01, 2010

[21] I. Cook, R. L. Miller, and D. J. Ward, 2002, *Fusion Eng. Des.*, **63–64** 25–33

[22] D. Hull and D. J. Bacon, 2001, *Introduction to Dislocations* (Butterworth-Heinemann, Oxford)

[23] Y. I. Frenkel and T. A. Kontorova 1938; see Phys. Z. Sowietunion **13** 1, Zh. Eksp. Teor. Fiz. **8** 89, and Zh. Eksp. Teor. Fiz. **8** 1340

[24] M. P. Allen and D. J. Tildesley, 2004, *Computer Simulation of Liquids* (Oxford University Press)

[25] F. Ercolessi, *A molecular dynamics primer*, Spring College in Computational Physics, ICTP, Treiste, June 1997

[26] P. M. Derlet, *moldyPSIs (version 1.0)* Computer modelling and experiments, Paul Scherrer Institute, Switzerland, 2006; A Fortran95 serial molecular dynamics/statics program

[27] P. S. de Laplace, 1951, *A Philosophical Essay on Probabilities* (Dover); English translation of the French 1819 edition

[28] D. C. Rapaport, 2004, *The Art of Molecular Dynamics Simulation* (Cambridge University Press)

[29] N. Metropolis, A. W. Rosenbluth, M. N. Rosenbluth, A. H. Teller, and E. Teller, 1953, *J. Chem. Phys.*, **21** 1087–1092

[30] B. J. Alder and T. E. Wainwright, 1957, *J. Chem. Phys.*, **27** 1208–1209

[31] B. J. Alder and T. E. Wainwright, 1959, *J. Chem. Phys.*, **31** 459–466

[32] B. J. Alder and T. E. Wainwright, 1960, *J. Chem. Phys.*, **33** 1439–1451

[33] B. J. Alder, S. P. Frankel, and V. A. Lewinson, 1955, *J. Chem. Phys.*, **23** 417–419

[34] W. W. Wood and F. R. Parker, 1957, *J. Chem. Phys.*, **27** 720–733

[35] J. B. Gibson, A. N. Goland, M. Milgram, and G. H. Vineyard, 1960, *Phys. Rev.*, **120** 1229–1253

[36] G. H. Vineyard, 1957, *J. Phys. Chem. Solids*, **3** 121–127

[37] G. H. Vineyard, 1958, *Phys. Rev.*, **110** 999–1010

[38] A. Rahman, 1964, *Phys. Rev.*, **136** 405–411

[39] J. Naghizadeh and S. A. Rice, 1962, *J. Chem. Phys.*, **36** 2710–2720

[40] A. Eisenstein and N. S. Gingrich, 1942, *Phys. Rev.*, **62** 261–270

[41] L. Verlet, July 1967, *Phys. Rev.*, **159** 98–103

[42] L. Verlet, January 1968, *Phys. Rev.*, **165** 201–214

[43] J. P. Hansen and L. Verlet, 1969, *Phys. Rev.*, **184** 151–161

[44] R. P. Feynman, R. B. Leighton, and M. Sands, 1963, *The Feynman Lectures on Physics*, volume 1 (Addison-Wesley); Chapter 9 – "Newton's Laws of Dynamics"

[45] R. W. Hockney, 1970, *Methods Comput. Phys.*, **9** 136–211

[46] D. Potter, 1972, *Computational Physics* (Wiley)

[47] W. C. Swope, H. C. Anderson, P. H. Berens, and K. R. Wilson, 1982, *J. Chem. Phys.*, **76** 637–649

[48] S. Plimpton, 1995, *J. Comp. Phys.*, **117** 1–19

[49] S. Plimpton, P. Crozier, and A. Thompson; LAMMPS homepage at Sandia
http://lammps.sandia.gov/index.html

[50] C. W. Gear, The numerical integration of ordinary differential equations of various orders, ANL 7126, Argonne National Laboratory, 1966

[51] C. W. Gear, 1967, *Math. Comp.*, **21** 146–156

[52] C. W. Gear, 1969, *Math. Comp.*, **23** 119–125

[53] C. W. Gear, 1971, *Numerical initial value problems in ordinary differential equations* (Prentice-Hall, Englewood Cliffs, NJ)

[54] M. Parrinello and A. Rahman, 1980, *Phys. Rev. Lett.*, **45** 1196–1199

[55] D. Fincham and B. J. Ralston, 1981, *Comput. Phys. Commun.*, **23** 127–134

[56] S. M. Thompson, 1983, *CCP5 Quarterly*, **8** 20–28

[57] B. Quentrec and C. Brot, 1973, *J. Comp. Phys.*, **13** 430–432

[58] R. W. Hockney, S. P. Goel, and J. W. Eastwood, 1974, *J. Comp. Phys.*, **14** 148–158

[59] P. Schofield, 1973, *Comp. Phys. Comm.*, **5** 17–23

[60] D. E. Knuth, 1968, *Fundamental Algorithms*, volume 1 of *The Art of Computer Programming* (Addison-Wesley, Reading, MA)

[61] R. W. Hockney and J. W. Eastwood, 1981, *Computer simulation using particles* (McGraw-Hill)

[62] S. Nosé, 1984, *Molec. Phys.*, **52** 255–268

[63] W. G. Hoover, 1985, *Phys. Rev. A*, **31** 1695–1697

[64] H. C. Andersen, 1980, *J. Chem. Phys.*, **72** 2384–2393

[65] M. Parrinello and A. Rahman, 1981, *J. Appl. Phys.*, **52** 7182–7190

[66] M. Parrinello and A. Rahman, 1982, *J. Chem. Phys.*, **76** 2662–2666

[67] C. L. Cleveland, 1988, *J. Chem. Phys.*, **89** 4987–4993

[68] R. M. Wentzcovitch, 1991, *Phys. Rev. B*, **44** 2358–2361

[69] L. D. Landau and E. M. Lifshitz, 2004, *Course of Theoretical Physics, Volume 1: Mechanics* (Elsevier, Oxford) 3rd edition

[70] H. Goldstein, C. Poole, and J. Safko, 2002, *Classical Mechanics* (Pearson Education - Addison-Wesley, San-Francisco) 3rd edition

[71] M. R. Hestenes and E. Stiefel, 1952, *J. Res. Nat. Bur. Standards*, **49** 409–436

[72] M. R. Hestenes, The conjugate gradient method for solving linear systems, In *Proceedings of Symposia on Applied Mathematics*, volume VI, Numerical Analysis, pages 83–102 (McGraw-Hill, New York) 1956

[73] E. Polak, 1971, *Computational Methods in Optimization; A Unified Approach* (Academic Press, London); section 2.3

[74] R. Fletcher and C. M. Reeves, 1964, *Comput. J.*, **7** 149–154

[75] E. Polak and G. Ribière, 1969, *Rev. Fr. Inform. Rech. Oper.*, **16** 35–43

[76] W. H. Press, S. A. Teukolsky, W. T. Vetterling, and B. P. Flannery, 2007, *Numerical Recipes, The Art of Scientific Computing* (Cambridge University Press, New York) 3rd edition

[77] W. H. Press, S. A. Teukolsky, W. T. Vetterling, and B. P. Flannery, 1992, *Numerical Recipes, Example Book [FORTRAN]* (Cambridge University Press, New York) 2nd edition

[78] H. Jónsson, G. Mills, and K. Jacobsen, *Classical and Quantum Dynamics in Condensed Phase Sumulations*, chapter 16, pages 385–404 (World Scientific, Singapore) 1998; edited by B. J. Berne, G. Cicotti, and D. F. Coker

[79] G. Mills and H. Jónsson, 1994, *Phy. Rev. Lett.*, **72** 1124–1127

[80] G. Henkelman and H. Jónsson, 2000, *J. Chem. Phys.*, **113** 9978–9985

[81] A. E. Carlsson, 1990, *Solid State Phys.*, **43** 1–91

[82] M. I. Mendelev, S. Han, D. J. Srolovitz, G. J. Ackland, D. Y. Sun, and M. Asta, 2003, *Philos. Mag.*, **83** 3977–3994

[83] M. W. Finnis and J. E. Sinclair, 1984, *Philos. Mag. A*, **50** 44–55

[84] M. S. Daw and M. I. Baskes, 1984, *Phys. Rev. B*, **29** 6443–6453

[85] V. Rosato, M. Guillopè, and B. Legrand, 1989, *Philos Mag. A*, **59** 321–336

[86] G. J. Ackland, D. J. Bacon, A. F. Calder, and T. Harry, 1997, *Philos. Mag. A*, **75** 713–732

[87] M. S. Daw and M. I. Baskes, 1983, *Phys. Rev. Lett.*, **50** 1285–1288

[88] F. Ercolessi, M. Parrinello, and E. Tosatti, 1988, *Philos. Mag. A*, **38** 213–226

[89] K. W. Jacobsen, J. K. Nørskov, and M. J. Puska, 1987, *Phys. Rev. B*, **35** 7423–7442

[90] B. J. Lee and M. I. Baskes, 2000, *Phys. Rev. B*, **62** 8564–8567

[91] B. J. Lee, M. I. Baskes, H. Kim, and Y. K. Cho, 2001, *Phys. Rev. B*, **64** 184102

[92] M. I. Baskes, J. S. Nelson, and A. F. Wright, 1989, *Phys. Rev. B*, **40** 6085–6100

[93] M. I. Baskes, 1992, *Phys. Rev. B*, **46** 2727–2742

[94] F. Ducastelle and F. Cyrot-Lackmann, 1970, *J. Phys. Chem. Solids*, **31** 1295–1306

[95] D. G. Pettifor, 1979, *Phys. Rev. Lett.*, **42** 846–850

[96] D. G. Pettifor, 1987, *Solid State Phys.*, **40** 43–92

[97] D. G. Pettifor, 1995, *Bonding and structure of molecules and solids* (Oxford University Press)

[98] M. Mrovec, D. Nguyen-Manh, D. G. Pettifor, and V. Vitek, 2004, *Phys. Rev. B*, **69** 094115

[99] J. A. Moriarty, 1990, *Phy. Rev. B*, **42** 1609–1628

[100] F. H. Streitz, J. N. Glosli, and M. V. Patel, 2006, *Phys. Rev. Lett.*, **96** 225701

[101] C. J. Wu, P. Söderling, J. N. Glosli, and J. E. Klepeis, 2009, *Nat. Mater.*, **8** 223–228

[102] M. Finnis, 2003, *Interatomic forces in condensed matter* (Oxford University Press)

[103] F. Cleri and V. Rosato, 1993, *Phys. Rev. B*, **48** 22–33

[104] G. J. Ackland, G. Tichy, V. Vitek, and M. W. Finnis, 1987, *Philos. Mag. A*, **56** 735–756

[105] S. L. Dudarev and P. M. Derlet, 2005, *J. Phys.: Condens. Matter*, **17** 7097–7118

[106] H. Hasegawa and D. G. Pettifor, 1983, *Phys. Rev. Lett.*, **50** 130–133

[107] G. Liu, D. Nguyen-Manh, B. G. Liu, and D. G. Pettifor, 2005, *Phys. Rev. B*, **71** 174115

[108] C. C. Fu, F. Willaime, and P. Ordejón, 2004, *Phys. Rev. Lett.*, **92** 175503

[109] C. C. Fu, J. Dalle Torre, F. Willaime, J. L. Bocquet, and A. Barbu, 2005, *Nat. Mater.*, **4** 68–74

[110] P. M. Derlet and S. L. Dudarev, 2007, *Prog. Mater. Sci.*, **52** 299–318

[111] P. M. Derlet, D. Nguyen-Manh, and S. L. Dudarev, 2007, *Phys. Rev. B*, **76** 054107

[112] Yu. N. Osetsky, A. G. Mikhin, and A. Serra, 1995, *Philos. Mag. A*, **72** 361–381

[113] Yu. N. Osetsky and A. Serra, 1996, *Philos. Mag. A*, **73** 249–263

[114] M. Ludwig, D. Farkas, D. Pedraza, and S. Schmauder, 1998, *Modelling Simul. Mater. Sci. Eng.*, **6** 19–28

[115] A. Caro, M. Caro, E. M. Lopasso, P. E. A. Turchi, and D. Farkas, 2006, *J. Nucl. Mater.*, **349** 317–326

[116] A. Caro, D. A. Crowson, and M. Caro, 2005, *Phys. Rev. Lett.*, **95** 075702

[117] A. Caro, M. Caro, E. M. Lopasso, and D. A. Crowson, 2006, *Appld. Phys. Lett.*, **89** 121902

[118] L. Malerba, D. Terentyev, P. Olsson, R. Chakarova, and J. Wallenius, 2004, *J. Nucl. Mater.*, **329–333** 1156–1160

[119] J. Wallenius, P. Olsson, C. Lagerstedt, N. Sandberg, R. Chakarova, and V. Pontikis, 2004, *Phys. Rev. B*, **69** 094103

[120] J. H. Shim, H. J. Lee, and B. D. Wirth, 2006, *J. Nucl. Mater.*, **351** 56–64

[121] K. Arakawa, M. Hatanaka, E. Kuramoto, K. Ono, and H. Mori, 2006, *Phys. Rev.Lett.*, **96** 125506

[122] K. Arakawa, K. Ono, M. Isshiki, K. Mimura, M. Uchikoshi, and H. Mori, 2007, *Science*, **318** 956–959

[123] Z. Yao, M. Hernández-Mayoral, M. L. Jenkins, and M. A. Kirk, 2008, *Philos. Mag.*, **88** 2851–2880

[124] M. Hernández-Mayoral, Z. Yao, M. L. Jenkins, and M. A. Kirk, 2008, *Philos. Mag.*, **88** 2881–2897

[125] M. R. Gilbert, S. L. Dudarev, P. M. Derlet, and D. G. Pettifor, *Stability of open and collapsed vacancy type clusters in bcc iron*, pages 726–728, September 2006; In the proceedings of the 3rd International Multiscale Materials Modelling Conference, Freiburg, Germany

[126] M. R. Gilbert, S. L. Dudarev, P. M. Derlet, and D. G. Pettifor, 2008, *J. Phys.: Condens. Matter*, **20** 345214

[127] M. R. Gilbert, Z. Yao, M. A. Kirk, M. L. Jenkins, and S. L. Dudarev, 2009, *J. Nucl. Mater.*, **386–388** 36–40

[128] C. H. Woo, A. A. Semenov, and B. N. Singh, 1993, *J. Nucl. Mater.*, **206** 170–199

[129] C. H. Woo, 1999, *J. Computer-Aided Mater. Des.*, **6** 247–275

[130] M. N. Shabrov and A. Needleman, 2002, *Modelling Simul. Mater. Sci. Eng.*, **10** 163–183

[131] C. A. English and M. L. Jenkins, 1987, *Mater. Sci. Forum*, **15-18** 1003–1022

[132] M. L. Jenkins, M. A. Kirk, and W. J. Phythian, 1993, *J. Nucl. Mater.*, **205** 16–30

[133] M. L. Jenkins and M. A. Kirk, 2001, *Characterization of Radiation Damage by Transmission Electron Microscopy*, Microscopy & Materials Science (Institute of Physics, Bristol and Philadephia)

[134] M. L. Jenkins, A. C. Nicol, and M. A. Kirk, 2001, *Mat. Res. Soc. Symp. Proc.*, **650** R1.3

[135] F. Von Häussermann, 1972, *Philos. Mag.*, **25** 583–598

[136] W. Jäger and M. Wilkens, 1975, *Phys. Stat. Sol.(a)*, **32** 89–100

[137] M. L. Jenkins, C. A. English, and B. L. Eyre, 1978, *Philos. Mag. A*, **38** 97–114

[138] M. Horiki, T. Yoshiie, M. Iseki, and M. Kiritani, 1999, *J. Nucl. Mater.*, **271-272** 256–260

[139] M. Horiki, T. Yoshiie, Q. Xu, M. Iseki, and M. Kiritani, 2000, *J. Nucl. Mater.*, **283-287** 282–285

[140] C. C. Matthai and D. J. Bacon, 1985, *J. Nucl. Mat.*, **135** 173–180

[141] T. Diaz de la Rubia, 1996, *Annu. Rev. Mater. Sci.*, **26** 613–649

[142] N. Soneda and T. Diaz de la Rubia, 1998, *Philos. Mag. A*, **78** 995–1019

[143] J. R. Beeler, 1983, *Radiation Effects Computer Experiments* (North-Holland, Amsterdam)

[144] D. Bacon, A. Calder, F. Gao, V. Kapinos, and S. Wooding, 1995, *Nucl. Instrum. Meth.*, **102** 37–46

[145] R. E. Stoller, 1996, *J. Nucl. Mater.*, **233-237** 999–1003

[146] N. Soneda, S. Ishino, and T. Diaz de la Rubia, 2001, *Philos. Mag. Lett.*, **81** 649–659

[147] A. F. Calder, D. J. Bacon, A. V. Barashev, and Yu. N. Osetsky, 2008, *Philos. Mag. Lett.*, **88** 43–53

[148] M. A. Puigvi, Yu. N. Osetsky, and A. Serra, 2003, *Philos. Mag.*, **83** 857–871

[149] Yu. N. Osetsky, D. J. Bacon, A. Serra, B. N. Singh, and S. I. Golubov, 2000, *J. Nucl. Mater.*, **276** 65–77

[150] J. P. Hirth and J. Lothe, 1992, *Theory of Dislocations* (Krieger Publishing); Reprint of 2nd edition (first published in 1982)

[151] D. Kulikov, L. Malerba, and M. Hou, 2006, *Philos. Mag.*, **86** 141–172

[152] R. A. Johnson, 1967, *Philos. Mag.*, **16** 553–564

[153] Grace-5.1.20, Copyright P. J. Turner and the Grace Development Team (2006). Maintained by E. Stambulchik. http://plasma-gate.wiezmann.ac.uk/Grace/

[154] C. Björkas and K. Nordlund, 2007, *Nucl. Instr. and Meth. B*, **259** 853–860

[155] Yu. N. Osetsky, D. J. Bacon, and A. Serra, 1999, *Philos. Mag. Lett.*, **79** 273–282

[156] P. Van Zwol, P. M. Derlet, H. Van Swygenhoven, and S. L. Dudarev, 2007, *Surf. Sci.*, **601** 3512–3520

[157] D. J. Bacon, R. Bullough, and J. R. Willis, 1970, *Philos. Mag.*, **22** 31–45

[158] S. L. Dudarev, R. Bullough, and P. M. Derlet, 2008, *Phys. Rev. Lett.*, **100** 135503

[159] GNUPLOT, Version 4.0, Copyright 2004 T. Williams, C. Kelly *et al.* http://www.gnuplot.info/

[160] M. J. S. Spencer, A. Hung, I. Snook, and I. Yarovsky, 2002, *Surf. Sci.*, **513** 389–398

[161] Yu. N. Osetsky, A. Serra, B. N. Singh, and S. I. Golubov, 2000, *Philos. Mag. A*, **80** 2131–2157

[162] B. C. Masters, 1965, *Philos. Mag.*, **11** 881–893

[163] E. A. Little and B. L. Eyre, 1973, *Metal Sci.*, pages 100–102

[164] E. A. Little and B. L. Eyre, 1973, *J. Microscopy*, **97** 107–111

[165] D. Nguyen-Manh, A. P. Horsfield, and S. L. Dudarev, 2006, *Phys. Rev. B*, **73** 020101

[166] M. Eldrup, B. N. Singh, S. J. Zinkle, T. S. Byun, and K. Farrell, 2002, *J. Nucl. Mater.*, **307–311** 912–917

[167] M. Eldrup and B. N. Singh, 2003, *J. Nucl. Mater.*, **323** 346–353

[168] N. W. Ashcroft and N. D. Mermin, 1976, *Solid State Physics* (Thomas Learning, London)

[169] T. S. Hudson, S. L. Dudarev, M-J. Caturla, and A. P. Sutton, 2005, *Philos. Mag.*, **85** 661–675

[170] D. N. Seidman and K. Stiller, 2009, *Mater. Res. Soc. Bulletin*, **34** 717–721

[171] A. F. Calder and D. J. Bacon, 1993, *J. Nucl. Mater.*, **207** 25–45

[172] Yu. N. Osetsky, D. J. Bacon, A. Serra, B. N. Singh, and S. I. Golubov, 2003, *Philos. Mag.*, **83** 61–91

[173] R. Landauer and J. A. Swanson, 1961, *Phys. Rev.*, **121** 1668–1674

[174] L. A. Zepeda-Ruiz, J. Rottler, B. D. Wirth, R. Car, and D. J. Srolovitz, 2005, *Acta Mater.*, **53** 1985–1994

[175] J. Marian, B. D. Wirth, A. Caro, B. Sadigh, G. R. Odette, J. M. Perlado, and T. Diaz de la Rubia, 2002, *Phys. Rev. B*, **65** 144102

[176] B. D. Wirth, G. R. Odette, D. Maroudas, and G. E. Lucas, 2000, *J. Nucl. Mater.*, **276** 33–40

[177] D. A. Terentyev, L. Malerba, and M. Hou, 2007, *Phys. Rev. B*, **75** 104108

[178] Z. Yao, M. L. Jenkins, and M. A. Kirk 2009; private presentation of recent experimental observations

[179] Yu. N. Osetsky, A. G. Mikhin, and A. Serra, 1995, *Philos. Mag. A*, **72** 361–381

[180] S. L. Dudarev, 2003, *Philos. Mag.*, **83** 3577–3597

[181] A. Einstein, 1926, *Investigations on the Theory of Brownian Movement* (Methuen, London); pg. 9

[182] R. Kubo, 1966, *Reports on Progress in Physics*, **29** 255–284

[183] S. L. Dudarev, 2008, *C. R. Physique*, **9** 409–417

[184] M. W. Guinan, R. N. Stuart, and R. J. Borg, 1977, *Phys. Rev. B*, **15** 699–710

[185] S. Chandrasekhar, 1943, *Rev. Mod. Phys.*, **15** 1–89

[186] S. L. Dudarev 2008; private communication, unpublished

[187] M. Hiratani and H. M. Zbib, 2002, *J. Eng. Mater. Technol.*, **124** 335–341

[188] Yu. N. Osetsky, A. Serra, and V. Priego, 2000, *J. Nucl. Mater.*, **276** 202–212

[189] P. B. Hirsch, In *5th International Conference on Crystallography*, pages 1–139 (Cambridge University Press) 1960

[190] J. M. Burgers, 1939, *Proc. Kon. Ned. Akad. Wetenschap*, **42** 378–382

[191] L. Hollang, *Purification Process and Characterization of Ultra Pure Metals*, pages 305–348 (Springer) 2002; Eds. Y. Waseda and M. Isshiki

[192] U. K. Kocks, A. S. Argon, and M. F. Asby, 1975, *Prog. Mater. Sci.*, **19** 1–291

[193] V. Vitek, 2004, *Philos. Mag.*, **84** 415–428

[194] A. Seeger, 1956, *Philos. Mag.*, **1** 651–661

[195] Z. S. Basinski and J. W. Christian, 1960, *Aust. J. Phys.*, **13** 299–308

[196] A. Seeger and B. Šesták, 1971, *Scripta Metall.*, **5** 875–882

[197] A. Seeger, 1981, *Z. Metallkde.*, **72** 369

[198] D. Brunner and J. Diehl, 1991, *Phys. Stat. Sol.(a)*, **124** 155–170

[199] A. Seeger, 2002, *Z. Metallkde.*, **93** 760–777

[200] J. A. Moriarty, V. Vitek, V. V. Bulatov, and S. Yip, 2002, *J. Computer-Aided Mater. Des.*, **9** 99–132

[201] W. Xu and J. A. Moriarty, 1998, *Comput. Mater. Sci.*, **9** 348–356

[202] L. Hollang, M. Hommel, and A. Seeger, 1997, *Phys. Stat. Sol.(a)*, **160** 329–354

[203] D. Brunner and J. Diehl, 1991, *Phys. Stat. Sol.(a)*, **124** 455–464

[204] D. Brunner and J. Diehl, 1991, *Phys. Stat. Sol.(a)*, **125** 203–216

[205] A. Seeger, 1995, *J. Phys. IV France*, **5** C7–45

[206] V. I. Alshits and V. L. Indenbom, *Mechanisms of dislocation drag*, volume 7, pages 43–111 (North-Holland, Amsterdam) 1986; in *Dislocations in Solids*, Ed. F. R. N. Nabarro

[207] V. I. Alshits and R. K. Kotowski, 1975, *Phys. Stat. Sol.(b)*, **68** K171–174

[208] J. Chang, W. Cai, V. Bulatov, and S. Yip, 2002, *Comp. Mater. Sci.*, **23** 111–115

[209] J. Marian, W. Cai, and V. V. Bulatov, 2004, *Nat. Mater.*, **3** 158–163

[210] C. Domain and G. Monnet, 2005, *Phys. Rev. Lett.*, **95** 215506

[211] J. Chaussidon, M. Fivel, and D. Rodney, 2006, *Acta Mater.*, **54** 3407–3416

[212] L. Ventelon and F. Willaime, 2007, *J. Computer-Aided Mater. Des.*, **14** 85–94

[213] G. Simonelli, R. Pasianot, and E. J. Savino in *Materials Theory and Modelling*, edited by Jeremy Broughton, Paul Bristowe, and John Newsam, Mater. Res. Soc. Symp. Proc. Proceedings No. 291 (Materials Research Society, Warrendale, 1993), p. 567

[214] W. A. Spitzig and A. S. Keh, 1970, *Acta Metall.*, **18** 611–622

[215] E. Kuramoto, Y. Aono, and K. Kitajima, 1979, *Scripta Metall.*, **13** 1039–1042

[216] L. Ventelon, F. Willaime, and P. Leyronnas, 2009, *J. Nucl. Mater.*, **386–388** 26–29

[217] D. A. Terentyev and L. Malerba, 2008, *Comp. Mat. Sci.*, **43** 855–866

[218] D. R. Lide, editor, 2004, *CRC Handbook of Chemistry and Physics* (CRC Press, Boca Raton, Florida) 85th edition

[219] D. Rodney and L. Proville, 2009, *Phys. Rev. B*, **79** 094108

[220] A. H. W. Ngan and M. Wen, 2001, *Phys. Rev. Lett.*, **87** 075505

[221] J. Marian 2009; private communication.

[222] J. D. Eshelby, 1956, *Proc. Phys. Soc.*, **69B** 1013

[223] G. Leibfried, 1950, *Z. Phys.*, **127** 344–356

[224] D. Rodney and L. Proville, 2008, *Phys. Rev. B*, **78** 104115

[225] S. Ismail-Beigi and T. Arias, 2000, *Phys. Rev. Lett.*, **84** 1499

[226] S. L. Frederiksen and K. W. Jacobsen, 2003, *Philos. Mag.*, **83** 365–375

[227] F. Shimizu, S. Ogata, H. Kimizuka, T. Kano, J. Li, and H. Kaburaki, 2007, *Journ. Earth Simulator*, **7** 17–21

[228] H. Kaburaki, F. Shimizu, S. Ogata, M. Yamaguchi, T. Kano, H. Kimizuka, and M. Itakura, 2007, *Ann. Rep. Earth Simulator Center*, pages 235–237 Chapter 3

[229] M. R. Gilbert and S. L. Dudarev, 2010, *Philos. Mag.*, **90** 1035–1061

[230] S. Chiesa, M. R. Gilbert, S. L. Dudarev, P. M. Derlet, and H. Van Swygenhoven, 2009, *Philos. Mag.*, **89** 3235–3243

[231] T. E. Mitchell, R. A. Foxall, and P. B. Hirsch, 1963, *Philos. Mag.*, **8** 1895–1920

[232] A. W. Sleeswyk, 1963, *Philos. Mag.*, **8** 1467–1486

[233] F. Kroupa and V. Vitek, 1964, *Chech. J. Phys.*, **B14** 337–346

[234] V. Vitek and F. Kroupa, 1968, *Chech. J. Phys.*, **B18** 464–470

[235] P. B. Hirsch and Y. Q. Sun, 2003, *Trans. Roy. Soc. South Africa*, **58** 129

[236] J. Li, C. Z. Wang, J. P. Chang, W. Cai, V. V. Bulatov, K. M. Ho, and S. Yip, 2004, *Phys. Rev. B*, **70** 104113

[237] T. Harry and D. J. Bacon, 2002, *Acta Mater.*, **50** 195–208

[238] T. Harry and D. J. Bacon, 2002, *Acta Mater.*, **50** 209–222

[239] G. J. Ackland and R. Thetford, 1987, *Philos. Mag. A*, **56** 15–30

[240] P. W. Ma, W. C. Liu, C. H. Woo, and S. L. Dudarev, 2007, *J. Appl. Phys.*, **101** 073908

[241] M. Mrovec, R. Gröger, A. G. Bailey, D. Nguyen-Manh, C. Elsässer, and V. Vitek, 2007, *Phys. Rev. B*, **75** 104119

[242] D. Nguyen-Manh, M. Mrovec, and S. P. Fitzgerald, 2008, *Materials Transactions, Japanese Institute of Metals*, **49** 2497–2506

[243] M. S. Duesbery and V. Vitek, 1998, *Acta Mater.*, **46** 1481–1492

[244] S. Takeuchi, 1979, *Philos. Mag. A*, **39** 661–671

[245] H. Suzuki, *Fundamental Aspects of Dislocation Theory*, volume 1, pages 253–272 1970; Eds. J. A. Simmons, R. de Wit, and R. Bullough, National Bureau of Standards Special Publication 317

[246] N. I. Medvedeva, Yu. N. Gornostyrev, and A. J. Freeman, 2005, *Phys. Rev. B*, **72** 134107

[247] Z. Chen, N. Kioussis, N. Ghoniem, and T. Hasebe, 2008, *Phys. Rev. B*, **77** 014103

[248] S. P. Fitzgerald and D. Nguyen-Manh, Higher-order Frenkel-Kontorova modelling of crowdions, In *Electron Microscopy and Multiscale Modeling, EMMM-2007*, pages 93–101 (AIP) 2008; Eds. A. Avilov, S. L. Dudarev, and L. D. Marks, American Institute of Physics Conference Proceedings CP999

[249] S. P. Fitzgerald and D. Nguyen-Manh, 2008, *Phys. Rev. Lett.*, **101** 115504

[250] S. L. Dudarev 2008; private communication, published as part of [**229**]

[251] E. Clouet, L. Ventelon, and F. Willaime, 2009, *Phys. Rev. Lett.*, **102** 055502

[252] G. Kresse and J. Hafner, Phys. Rev. B**47**, 558–561 (1993); G. Kresse and J. Furthmuller, ibid. **54**, 11169 (1996); G. Kresse and D. Joubert, ibid. **59**, 1758 (1999).

[253] J. P. Perdew, K. Burke, and M. Ernzerhof, 1996, *Phys. Rev. Lett.*, **77** 3865–3868

[254] E. Kreyszig, 1999, *Advanced Engineering Mathematics* (John Wiley & Sons, Inc., New York) 8th edition

[255] V. Vitek, R. C. Perrin, and D. K. Bowen, 1970, *Philos. Mag. A*, **21** 1049–1073

[256] R. Peierls, 1940, *Proc. Phys. Soc.*, **52** 34–37

[257] M. R. Gilbert and R. A. Forrest, 2006, *Fusion Eng. Des.*, **81** 1511–1516

[258] R. A. Forrest, 1998, *Fusion Eng. Des.*, **43** 209–235

[259] W. K. Nicholson, 1993, *Linear Algebra with Application* (PWS Publishing Company, Boston) 3rd edition

[260] P. M. Derlet 2010; private communication, unpublished

[261] S. L. Dudarev, M. R. Gilbert, K. Arakawa, H. Mori, Z. Yao, M. L. Jenkins, and P. M. Derlet, 2010, *Phys. Rev. B*, **81** 224107